

**The Dynamics of Ventilated Partial Cavities over a Wide Range of Reynolds  
Numbers and Quantitative 2D X-ray Densitometry for Multiphase Flow**

by

**Simo A. Mäkiharju**

A dissertation submitted in partial fulfillment  
of the requirements for the degree of  
Doctor of Philosophy  
(Mechanical Engineering)  
in The University of Michigan  
2012

Doctoral Committee:

Professor Steven L. Ceccio, Co-Chair  
Professor Marc Perlin, Co-Chair  
Professor Armin W. Troesch  
Assistant Professor Eric Johnsen

© Simo A. Mäkiharju 2012  
All Rights Reserved

To Family and Friends

## **ACKNOWLEDGMENTS**

I would like thank the Office of Naval Research and the Great Lakes Maritime Research Institute for sponsoring the research.

I also wish to thank the members of my dissertation committee, especially professors Steven Ceccio and Marc Perlin for all their advice on practical experimental setup design to reviewing this dissertation. I also thank my other committee members Armin Troesch and Eric Johnsen for agreeing to be my committee in the first place, and for reading through the hundreds of pages of this dissertation. Additionally, I wish to thank professor Zoran Filipi for originally being on my committee, and professor William Schultz for providing research opportunities and for his guidance during my first year of Ph.D. studies at University of Michigan.

I'm also thankful to the staff members at UM, especially Kent Pruss, Bill Kirkpatrick and Melissa McGeorge, who provided the technical and administrative support for the numerous experiments. I wish to acknowledge the crucial help given by the entire staff of the LCC. Without the assistance, technical skills, and patience of these individuals the experiments discussed in this thesis would not have been possible. I wish to thank David Foster, Bob Etter, and Chris Chesnakas for all their help with the preparation for and implementation of the LCC experimental campaigns, and for approving the gate I designed to be used at the LCC.



I would like to thank my colleagues Alex Mychkovsky, Harish Ganesh, Andrew Wiggins, Deniz Akcabay, Sarah Schinasi, Bu-Geun Paik, Andre Pinheiro, Natasha Chang, Brian Elbing, Kerry Lay, Ryo Yakushiji, Steven Zalek, and Joel Hartenberger for their collaboration.

I also want to thank the numerous M.Sc., B.Sc. and visiting students who I had the privilege to work with: Richard Mooney, Justin Kahl, Eloi Desrippes, Barazer Aymeric, Aymeric Leboulanger, Camille Bon, Thomas Ferretti, Arthur de Lavernette, and Christopher Haddad.

I especially want to thank, Professor Celine Gabillet who graciously borrowed the optical probes used in this work, taught us how to use them and processed much of the data, which we will use for our upcoming joint publication.

All my friends and relatives, especially my father Juhani, grandmother Sylvi, great uncle Mauno and great aunt Tellervo, have been extremely supportive throughout my studies, and have made it easier for me to pursue a Ph.D.

My lovely wife, Heather, deserves special credit for tolerating my frequent trips to Memphis, late nights at the lab and for sometimes even helping me in the lab ...when it was the weekend and I couldn't drag any of my colleagues to the lab.

I'd also like to thank my undergraduate advisor Piroz Zamankhan for getting me involved with serious research at an early stage in my academic career at the Lappeenranta University of Technology in Finland, and my M.Sc. advisor at the Ohio State University, Seppo Korpela, for his career guidance and for teaching me to become a better researcher.

## TABLE OF CONTENTS

<b>DEDICATION.....</b>	<b>ii</b>
<b>ACKNOWLEDGMENTS .....</b>	<b>iii</b>
<b>LIST OF FIGURES .....</b>	<b>x</b>
<b>LIST OF TABLES .....</b>	<b>xxx</b>
<b>LIST OF APPENDICES .....</b>	<b>xxxii</b>
<b>NOMENCLATURE.....</b>	<b>xxxii</b>
<b>ABSTRACT.....</b>	<b>xxxvi</b>
<b>CHAPTER 1</b>	
<b>Introduction.....</b>	<b>1</b>
1.1 Partial cavity drag reduction.....	2
1.2 X-ray densitometry.....	4
<b>CHAPTER 2</b>	
<b>High Reynolds Number Partial Cavity Drag Reduction Experiments .....</b>	<b>6</b>
2.1 Background – concept of air lubrication .....	7
2.2 Determining the cavity shape .....	11
2.3 Mechanisms at the cavity closure.....	14
2.4 The large scale model.....	16
2.5 Test facility.....	19
2.6 The dependent and independent variables of interest .....	21
2.7 Specialized instrumentation .....	22
2.7.1 Traversing probes.....	25
2.7.2 The video system .....	28

2.8 About the experiments.....	29
2.9 Results – steady flow.....	35
2.9.1 About the cavity surface .....	39
2.9.2 Cavity closure .....	40
2.9.3 Effect of beach geometry .....	41
2.10 Results – unsteady flow.....	42
2.11 Comparison to another air lubrication technique .....	53
2.12 Discussion.....	55
2.13 References for Chapter 2 .....	57

### **CHAPTER 3**

#### **Scaling of Partial Cavity Drag Reduction and Attendant Air Entrainment. 60**

3.1 Dimensionless parameters.....	60
3.2 Low Reynolds number experiments.....	64
3.3 Inlet flow conditions.....	68
3.4 Comparison of air entrainment at different size scales .....	69
3.5 Effect of Weber number at small scale and low Reynolds number .....	76
3.6 Effect of Reynolds number.....	80
3.7 Discussion .....	81
3.8 References for Chapter 3.....	82

### **CHAPTER 4**

#### **Air Lubrication Energy Cost-Benefit Analysis ..... 83**

4.1 Example calculations.....	88
4.2 Discussion .....	91
4.3 References for chapter 4.....	93

## CHAPTER 5

<b>Time Resolved X-Ray Densitometry .....</b>	<b>94</b>
5.1 Introduction .....	95
5.2 Physical principles of x-ray densitometry .....	96
5.2.1 Void fraction of a two phase flow.....	97
5.2.2 Beam hardening .....	101
5.3 Test facility.....	109
5.4 X-ray source and imager .....	111
5.4.1 Shielding.....	118
5.5 Void fraction measurement accuracy.....	119
5.5.1 Void fraction accuracy in theory.....	119
5.5.2 Calibration procedure for the sub-range of the void fractions .....	122
5.5.3 Experiment for measured versus actual void fraction.....	122
5.6 Temporal resolution .....	125
5.6.1 Time constant of the imager system .....	125
5.6.2 Time dependence of the x-ray source .....	129
5.7 Spatial resolution and positional accuracy .....	132
5.7.1 Focal spot blur.....	132
5.7.2 Noise .....	134
5.7.3 The camera resolution.....	135
5.7.4 Scatter .....	135
5.7.5 Imaging – characterizing the spatial frequency response .....	137
5.7.6 Veiling glare.....	141
5.7.7 Correcting for veiling glare.....	143

5.7.8 Distortion .....	150
5.7.9 Image intensifier and lens distortions .....	151
5.7.10 Non-parallel beam paths.....	154
5.7.11 Non-parallel beam path correction.....	156
5.7.12 Empirically determined resolution.....	166
5.8 Discussion .....	167
5.9 References for Chapter 5 .....	169
 <b>CHAPTER 6</b>	
<b>A Ventilated Partial Cavity Downstream of a Backward Facing Step .....</b>	<b>172</b>
6.1 Experimental setup.....	173
6.2 Description of the single phase flow .....	176
6.3 Optical probes and high speed video.....	182
6.4 High speed video .....	196
6.5 X-ray measurements.....	201
6.6 Comparison of the results.....	207
6.7 Discussion .....	220
6.8 References for Chapter 6.....	222
 <b>CHAPTER 7</b>	
<b>Conclusions.....</b>	<b>223</b>
7.1 Achievements and contributions .....	223
7.1.1 Partial cavity drag reduction.....	223
7.1.2 X-ray densitometry .....	224
7.2 Future work .....	226
7.2.1 Partial cavity drag reduction.....	226

7.2.2 X-ray densitometry .....	227
7.3 References for Chapter 7 .....	229
<b>Appendices</b> .....	<b>230</b>

## LIST OF FIGURES

Figure 2.1 – a) Simplified view of the experimental setup and resulting free surface shape. b) Example of a typical undular jump shape from Ohtsu *et al.* (2001). The vertical red line indicates the typical cavity length encountered in our experiments. In the figure,  $h_1$  is the water depth  $H$  here,  $h_{\max}$  is the height of the first crest, and  $B$  is the channel width. In our experiments  $L_c/h_1 \sim 7.5$ , width to depth  $B/h_1 \sim 2.5$  and Reynolds number based on depth at step  $\sim 7 \times 10^6$ ; therefore the shape is not expected to match well..... 12

Figure 2.2 – Froude number regions of hydraulic jumps adapted from White (2001). In the experiments discussed in this thesis, the flow is in the undular or weak jump regions..... 13

Figure 2.3 – Simplified view of the stationary cavity closing on the beach, where the free surface terminates near or at the crest of the beach. .... 14

Figure 2.4 – Conceptual sketch of potential cavity closure events leading to shedding of gas. The upper illustration depicts the pinching mechanism, the lower the re-entrant jet process, where the red arrow moving upstream represents the re-entrant jet..... 15

Figure 2.5 – Profile of the gate and model in the LCC's test section. The depth of the water below the BFS is 1.23 m. The mid-body of the plate is 18.4 cm thick, and at the step the plate is 36.2 cm thick. The origin of the coordinate system is at the base of the 17.8 cm tall BFS, as detailed in table 2.2. For clarity, the axes are shown shifted to the side and not at the true location of the origin. Insert: Detailed view of the cavity-terminating beach, shown in grey. .... 17

Figure 2.6 – Boundary layer velocity profile measured with the LDV. In the legend, BL refers to base line conditions where no gas is injected, and INJ refers to conditions where gas is injected.  $\delta$  is the 99% boundary layer thickness. (Modified version of figure by Dr. Brian Elbing. Reproduced with permission)..... 18

Figure 2.7 – Photo showing the top half of the U. S. Navy's W. B. Morgan Large Cavitation Channel located in Memphis, Tennessee. For scale, note the three people walking next to the tunnel on the left side of the image. .... 20

Figure 2.8 – Sketch of the LCC showing the dimensions and main features. Flow is clock-wise. The boxes at the corners of the tunnel represent the turning vanes. The tunnel has flow straighteners, not shown, upstream of the contraction. .... 20

Figure 2.9 – 3D drawing of the model as seen from below with the measurement and instrument locations indicated. The detailed locations are given in table 2.2. ....	22
Figure 2.10 – Photo of traverse T1 when the traverse was at $y \sim 10$ cm. The probes are from the left: Pitot-tube, point electrode, and time-of-flight electrode pair. ....	27
Figure 2.11 – Sketch of the traversing probes. All the probes had a 3.2 mm outer diameter and are shown in the enlarged view of the figure. The probes are from the left: Pitot-tube, point electrode, and time-of-flight electrode pair. The upper sketch shows the mechanism, enclosure, and the plate that mounted into the model.....	28
Figure 2.12 – Sketch of the step, recess and beach on the model shows in the following two figures. ....	31
Figure 2.13 – Looking upstream inside the cavity under the model, as seen through a side window at mid cavity. The drops seen in the foreground are on the tunnel window. ....	31
Figure 2.14 – Cavity under the model as seen through a side window at mid cavity. Camera is looking downstream. Again, drops can be seen in the foreground ( <i>i.e.</i> on the window). ....	32
Figure 2.15 – Time series of images showing the cavity initially filling from base of the step to the top. The recirculation area behind the BFS filled first, and then the cavity progressed downstream, when the supplied gas flux was sufficient. Modified version of figure from Lay <i>et al.</i> (2010). ....	33
Figure 2.16 – Air flux requirements for establishment and maintenance gas flux is indicated by the blue circles and red squares, respectively. The large variation in gas flux for $Fr > 0.75$ may be due to both unsteady cavity flow and variation of freestream conditions. ....	38
Figure 2.17 – Time averaged void fraction profiles shown by the squares and circles from profiles of traverses $T_1$ and $T_2$ , respectively, compared to the average local cavity thicknesses measured from the video (diamonds). The horizontal error bars show the uncertainty, $\pm 7$ mm, of the video data. ....	39
Figure 2.18 – The cavity closure as seen from below. The round disk immediately to the right of the cavity closure that is delineated with a white circle is the fourth force balance. The green dashed curve surrounds a small cloud being shed from the cavity. The white arrow indicates the flow direction.....	40
Figure 2.19 – Air flux requirements for different beach positions. The minimum establishment and maintenance gas flux required is indicated by the blue and red symbols, respectively. ....	42



- Figure 2.20 – Excess air requirements versus a measure of perturbation amplitude (standard deviation of the cavity pressure divided by its mean). Given the finite test time, the gas requirements were found within a ~20% excess gas flux range. The true minimum flux lies somewhere between the last point where the cavity held and the first flux where the cavity was lost. The legend names these points accordingly as “Held” and “Lost”. In comparison, the ratio of required establishment to maintenance flux in steady flow was typically around 4..... 43
- Figure 2.21 – Time traces of the experiment with the oscillating gate where the cavity was not lost. The errorbars shown around the local mean values represent one standard deviation. From the bottom figure the cavity closure can clearly be seen to move upstream of force balance FB4, then past FB3, and finally past FB2 prior to reversing a brief moment later. For the case shown:  $Hc \sim 17.0$  cm,  $pc \sim 6400$  Pa,  $U = 5.46$  m/s,  $Fr = 0.57$ ,  $tcycle = 15.7$  seconds and  $q \sim 0.025$ . The non-dimensional values (\* superscripts) are defined in the text..... 45
- Figure 2.22 – Time traces of an unsteady case where the cavity was lost. In these time traces the force balance readings clearly indicate the loss. (The plot of  $U *$  ends prematurely due to the limited recording time of the LDV system.) For the case shown:  $Hc \sim 17.0$  cm,  $pc \sim 6400$  Pa,  $U = 5.46$  m/s,  $Fr = 0.57$ ,  $tcycle = 15.7$  seconds  $q \sim 0.022$ ..... 46
- Figure 2.23 – Cavity closure position oscillations and the low-pass filtered gate flap angle.  $Fr = 0.57$ .  $L(t^*)$  notes the instantaneous closure position, which was visible within the camera's field of view. Subscripts min and max define the minimum and maximum closure position within the field of view. Subscript FB refers to the closure position at the spanwise coordinate of the force balances. (Figure by Mr. Andrew Wiggins. Reproduced with permission.)..... 48
- Figure 2.24 – Approximate area of the beach where shapes sketched in figures 2.25 to 2.30 occur..... 48
- Figure 2.25 – Stage I, closure near upstream end of the beach. Upstream of the cavity closure ~20 cm from the beach's leading edge. Closure begins to exhibit violent churning and three-dimensional disturbances. Ridges of wave patterns on the free surface are visible. The thickness of the closure edge is greater than for other stages. Air loss occurs through staggered and fairly regular cloud shedding. The spanwise correlation length of the clouds is fairly short (<10cm) and shedding occurs at ~30Hz. (Figure by Mr. Andrew Wiggins. Reproduced with permission.) ..... 49
- Figure 2.26 – Stage II, uniform growth. The cavity grows with spanwise uniformity. The trailing edge of the cavity has become thinner and assumed a glassy scalloped appearance. The volume of air loss has noticeably decreased. The clouds shed are long in the spanwise direction. (Figure by Mr. Andrew Wiggins. Reproduced with permission.)..... 49

Figure 2.27 – Stage III, rapid growth. The cavity approaches the beach flat and the edge continues to thin. Long spanwise narrow “fingers” and other spanwise non-uniformities appear. The fingers are spaced approximately 16 cm apart and extend to 50 cm in length. This stage is short lived. (Figure by Mr. Andrew Wiggins. Reproduced with permission.) ..... 50

Figure 2.28 – Stage IV, maximum cavity length. The cavity now extends almost the full length of the beach flat. The cavity edge shape fluctuates rapidly. There is erratic shedding of wide, but short, clouds. (Figure by Mr. Andrew Wiggins. Reproduced with permission.)..... 50

Figure 2.29 – Stage V, beginning of the retreat. Necking of the fully extended closure region initiates near the sidewall resulting in substantial variations in closure position. (Figure by Mr. Andrew Wiggins. Reproduced with permission.) ..... 51

Figure 2.30 – Stage VI, rapid retreat. The extended part of the closure region detaches and divides. The cavity edge retreats to the position of Stage I with relative spanwise uniformity. (Figure by Mr. Andrew Wiggins. Reproduced with permission.) ..... 51

Figure 2.31 – A conceptual comparison of ALDR and PCDR. Top: The air layer is thin, and can be of the order of the boundary layer thickness. All gas is carried downstream, and the layer is established and lost at the convective time scale. Bottom: The partial cavity requires a recess with a streamlined closure surface. Typical time scale to fill or empty the cavity of gas is orders of magnitude larger than the flow’s convective time scale. .... 53

Figure 2.32 – Comparison of the air requirements per unit span for PCDR and ALDR. The solid lines represent best fits to the data (for PCDR from 5.48 to 7.46 m/s, for ALDR from 6.79 to 12.45 and 15.26 m/s for smooth and rough surfaces, respectively). For PCDR the large variation in gas flux for  $U > 7.2$  m/s may be due to both unsteady cavity flow and variation of freestream conditions. .... 54

Figure 3.1 – The “Mini-LCC” water tunnel located at the University of Michigan’s Marine Hydrodynamics Laboratory. Flow is left-to-right through the test section as seen in this view. The blue arrow points to the test section, and also indicates the flow direction. .... 64

Figure 3.2 – Three dimensional view of the gate, plate and starboard window in the ..... 65

Figure 3.3 – Photo of the model and gate in the test section of the MLCC during early stages of cavity growth. In addition to the free surface of the cavity behind the BFS, we also have a second free surface above the plate and originating from the leading edge of the gate. The second free surface terminated in the tunnel’s diffuser *via* a hydraulic jump. .... 66

Figure 3.4 – a) Close up of the boundary layer trip, which comprised of ~140 micron particle roughness elements randomly distributed along the leading edge and was longitudinally 5 cm wide from the leading edge. b) Close-up photo of the beach region, where the beach starts at the 0-label. .... 67

Figure 3.5 – Required air fluxes with and without the boundary layer trip at the leading edge. The results indicate that the trip had no significant effect on the air entrainment. Based on accuracy of the velocity measurement, the Froude number is accurate within +/- 0.035. For  $Fr = 0.4$ , experimented for the non-tripped case only, both the establishment and maintenance fluxes were below the flow meter’s scale. Thus we merely know that the required flux at  $Fr = 0.4$  was greater than zero, but below  $10^{-3.4}$ . Also, for all establishment fluxes at the lower  $Fr$ , which do not have a corresponding data point for the maintenance flux, it was below the range of flow meters,  $<10^{-3.4}$ , but larger than zero. .... 68

Figure 3.6 – Cavity closure at high Reynolds number in the LCC.  $U = 5.9$  m/s, run # 423,  $Fr = 0.62$ ,  $We = 9.0 \times 10^4$  and  $Re = 5.5 \times 10^7$ . Flow is from right to left. We can observe the continuous shedding of gas clouds from the closure. Image recorded through ~2 m of liquid and 0.1 m of acrylic; hence clarity of image is somewhat lacking. .... 70

Figure 3.7 – Cavity closure in the MLCC.  $U = 2.27$  m/s,  $Fr = 0.89$ ,  $We = 940$  and  $Re = 1.5 \times 10^6$ . Flow is from right to left. .... 71

Figure 3.8 – Cavity closure in the MLCC.  $U = 1.25$  m/s,  $Fr = 0.49$ ,  $We = 285$  and  $Re = 8.0 \times 10^5$ . Flow is from right to left. The closure was often more two-dimensional than seen in this figure, where a portion of the cavity is just about to shed a pocket of air. .... 71

Figure 3.9 – Small scale cavity experiments closures at a different instance in time than in the two previous figures. It should be noted that there is no continuous shedding of bubbles at the lower speed, and it appears that the surface tension force is sufficiently high relative to other forces to retain the closure. .... 72

Figure 3.10 – Cavity free surface profile at various Froude numbers for the MLCC experiments. Vertical coordinate,  $y/H_{step}$ , measured to within +/- 0.1, with potential bias error or -0.1, and  $x/L_{cav}$  measured to within +/- 0.02. .... 73

Figure 3.11 – Non-dimensionalized critical gas flux as a function of Froude number at different size scales. For all MLCC establishment fluxes at the lower  $Fr$ , which do not have a data point for the maintenance flux, this was below the range of the flow meters ( $<10^{-3.4}$ ), but larger than zero. .... 74

Figure 3.12 – a) Side view  $U \sim 1.4$  m/s,  $Fr \sim 0.58$  in the MLCC. b) Oblique view of the same cavity. c) Close up of the establishing cavity’s closure at the LCC, where in a

similar $Fr \sim 0.6$ flow the establishing cavity would shed large clouds continually as shown .....	75
Figure 3.13 – Surface tension of the water in the MLCC flow loop as a function of Triton X-100 concentration.....	76
Figure 3.14 – Required cavity maintenance gas flux as a function of surface tension. Surface tension measurement +/- 0.002 N/m.....	77
Figure 3.15 – Required cavity maintenance and establishment gas flux as a function of surface tension at $U = 1.45$ m/s.....	78
Figure 3.16 – Required cavity maintenance and establishment gas flux as a function of surface tension at $U = 1.75$ m/s.....	78
Figure 3.17 – Required cavity maintenance and establishment gas fluxes for two different values of surface tension. For all establishment fluxes at the lower $Fr$ , which do not have a data point for the maintenance flux, this was below the range of the flow meters ( $<10^{-3,4}$ ), but larger than zero. ....	79
Figure 3.18 – Critical dimensionless gas fluxes as a function of Reynolds number.....	80
Figure 4.1 – Typical contributions of different components of ship’s resistance as a function of Froude number as commonly reported in the literature. ....	84
Figure 4.2 – Required volumetric flow rate per unit span to achieve an air layer on a smooth surface ( $\triangleright$ and $\triangleleft$ ), on a rough surface ( $\star$ ), to establish a partial cavity ( $\circ$ ) and to maintain a partial cavity ( $\square$ ). Solid lines are curve fits given in equations 4.7a-d. The wide error bars at the two highest PCDR test speeds are due to variation of the free stream conditions and uncertainty of the velocity measurement performed using LDV in optically semi-opaque bubbly flow.....	87
Figure 4.3 – The M/V American spirit is a cargo ship operating on the U.S. Great Lakes. $L= 306$ m, $w= 32$ m and midsummer draft 8.8 m (American Steamship Company).88	88
Figure 4.4 – Estimates of the potential net energy savings for a ship similar to the M/V American Spirit. ....	90
Figure 5.1 – Mass attenuation coefficient, $\mu/\rho$ , of water as a function of photon energy plotted on a log-log scale. Figure based on data by Hubbell and Seltzer (2004). ..	102
Figure 5.2 – Sketch of the general shape of detective quantum efficiency of x-ray image intensifiers with Cesium Iodine (CsI) input phosphors behind an aluminum/glass vacuum envelope, $0.2 \text{ g/cm}^2$ phosphor. Based on data from Thirlwall (1998). ....	103

- Figure 5.3 – a) X-ray source’s spectrum from a tungsten target simulated using SpecCalc by Poludniowski *et al.* (2009). This is a lightly filtered Bremsstrahlung spectrum, with the characteristic radiation spikes at the atom’s lower shell electron binding energies. b) The photon energy spectra can be “shaped” by filtering with a highly attenuating material. Green - original spectra, Blue - spectra filtered/hardened with a 0.64 mm thick steel plate. Red – spectra after passing through the test section. . 106
- Figure 5.4 – Illustration of the reduction of error when the void fraction is computed using the ratio of the energy from a polychromatic beam with or without pre-hardening. a) Relative and b) absolute errors in void fraction, as a function of the actual void fraction. .... 108
- Figure 5.5 – The University of Michigan’s 9” water tunnel before construction of the new platform. A 12 ft x 18 ft test stand capable of accommodating the lead shielding’s weight and size was designed by the author. The white arrow shows the direction of the flow and also points to the test section. .... 110
- Figure 5.6 – Sketch of the new test section. The green lines indicate the interior contours on the centerline and the blue arrow shows the flow direction..... 110
- Figure 5.7 – Schematic of the x-ray system’s key components. The control panel is used to set the x-ray tube’s current, voltage and duration of exposure. The II field size is set by a three position toggle-switch (not shown), while software running on the PC is used to set the camera’s exposure settings, which include resolution, frame rate, exposure time, and number of post trigger frames to be captured. A push-button switch is used to trigger the exposure, which can only occur if all the interlocks are engaged. Once an exposure begins, a stepped down AC voltage signal is sent to the trigger unit (Stanford Research Systems model DG535 delay generator), which after a specified delay sends a TTL signal to the high speed camera. .... 112
- Figure 5.8 – a) Side elevation view of the x-ray densitometry system showing the source enclosure on the right, test section in the middle and imager enclosure on the left. The red cone indicates the x-ray cone beam originating from the source. b) View from an oblique angle. Note the "large" (>70 cm) distance between the test section and the imager. This space provides an "air gap" which reduces the amount of scatter reaching the imager. The source is housed in a separate enclosure and its distance to the test section can be adjusted. The further the source is, the lower the beam intensity, which goes as  $1/(\text{distance})^2$ , but the beam will encounter more of the domain with a shallower angle (see section 5.7.10). .... 113
- Figure 5.9 – a) The x-ray source is shown in its enclosure. The red arrows indicate the vertical adjustment mechanism, which is connected on a horizontal slide at the bottom of the enclosure. b) The image intensifier with the high speed optical camera. Together these components form the "imager". Both source and imager are housed in the custom lead enclosure designed for easy access to the test section. c)

The x-ray control panel, manual switch and warning lights on the high voltage generator. ....	115
Figure 5.10 – Photo and a diagram of a rotating anode x-ray tube insert, Varian G-1092. Image from the G-1092’s data sheet by Varian. The cathode is colored blue and the anode red, to make it easier to identify them. Both are housed in a vacuum. To generate the x-rays, electrons are freed at the cathode and then accelerated to the focal spot on the anode, by up to a 150 kV electrical potential difference. ....	116
Figure 5.11 – A sketch showing the main components of a generic image intensifier with a right angle adapter and a high-speed imager mounted to it. This sketch is a retouched version of one posted on Alternative Vision Corporation’s web-page ( <a href="http://www.alt-vision.com/medical_imaging_optics.htm">http://www.alt-vision.com/medical_imaging_optics.htm</a> ). ....	117
Figure 5.12 – Assuming $\Delta I = \pm 0.5$ , $I_w = 6$ and $I_a = 240$ . True void fraction (blue curve) and uncertainty envelope (within red lines), as a function of the pixel's grey scale value. ....	121
Figure 5.13 – Assuming $\Delta I = \pm 1$ , $I_w = 6$ and $I_a = 240$ . True void fraction (blue curve) and uncertainty envelope (within red lines), as a function of the pixel's grey scale value. ....	121
Figure 5.14 – The experimental setup for the void fraction comparison. The containers between were filled and emptied in different combinations, thus providing varying, but known, void fractions within the accuracy of container thickness ( <i>i.e.</i> uncertainty of water thickness along the beam path). ....	123
Figure 5.15 – Comparison of void fraction based on container thicknesses versus the measured void fraction. The circles are measurement results and the solid line is the curve these points would ideally be on. From measurement, 200 frames and a 60,000 pixel area averaged to get a single value for the void fraction for comparison. ....	123
Figure 5.16 – Relative error in void fraction based on container thicknesses versus the measured void fraction. From measurement, 200 frames and a 60,000 pixel area averaged to get a single value for the void fraction for comparison. ....	124
Figure 5.17 – Time averaged image of the case for which the following figures present the area averaged time traces. There were no transient events in the test section; hence for an ideal system the next figure should show a step function. ....	126
Figure 5.18 – Time traces of spatially averaged mean intensity, and standard deviation of intensity. The vertical units are the pixel's grey scale values, and each frame was recorded 1 ms apart. The ordinate values are averages over the entire exposure of the respective quantity. ....	127

Figure 5.19 – Expanded view of the time traces of the spatially averaged mean intensity shown in figure 5.18. There is a ripple present due to noise, which was not evident in fig. 5.18. The ordinate values are averages over the entire exposure of the respective quantity. ....	128
Figure 5.20 – Time trace of average intensity. Note that ~0.5 GSV drift occurred even after the first 100 ms (100 frames). The blue lower line is the spatial mean intensity. ....	130
Figure 5.21 – Time trace of average intensity. The recording was started several dozen milliseconds after the start of the exposure, so that a longer time trace of the slow drift would be visible. Note that ~0.5 GSV drift occurred even after the first 100 ms (100 frames). The blue upper line is the mean intensity.....	131
Figure 5.22 – Penumbra with the same source focal spot size, but with different source to object distance (SOD) and source to imager distance (SID) ratios. (The SID/SOD ratio is also called the object’s magnification.) .....	133
Figure 5.23 – Probable angle of scatter for different photon energies. From Seibert and Boone (2005). Note how at higher energies, forward scatter becomes more probable. (Reprinted with permission.) .....	136
Figure 5.24 – a) Sharp edged 1.6 mm thick lead sheet placed directly onto the II's input screen is visible in the bottom left quadrant of the image. The shadow in the middle is cast by the model used in the experiments described in Chapter 6. To check the relative locations of the source, object and imager, two lead spheres were placed between the source and the object and their shadows appear at the top of the figure. b) The ESF determined by plotting the intensity normal to the lead sheet. c) LSF, calculated using eqn. 5.32, with a 6.46 pixel full width half max. ....	140
Figure 5.25 – Veiling glare caused by scatter of x-ray and visible photons in the imaging system (II and lenses). A glow over 10 mm wide is clearly seen near the edge of plate, which produced a sharp discontinuity in attenuation. Faint pixel lines caused by the camera are also visible. ....	141
Figure 5.26 – A trace of intensity through all air minus that through all water in the test section, at a random streamwise location of the edge shown in figure 5.25. The edge is at ~2 mm, and at that point the GSV on the vertical axis should drop rapidly to zero, and rise to some constant value to the left. The shape of the curve beyond 25 mm is due to geometry of the object in the test section.....	142
Figure 5.27 – Edge spread function obtained experimentally compared to various curve fits, some of whose forms can have a physical interpretation (Barney Smith 2006). ....	145

- Figure 5.28 – a) Relative intensity normal to the edge of the lead sheet (as shown in figure 5.24a) for the original and deconvolved image. Ideally the result should be a Heaviside step function. b) An expanded view clearly showing the improvement. Additionally visible is that the higher frequency ripple was not smeared by the deconvolution. In this case the ripple may have been just noise, but in other situations it could contain information. .... 147
- Figure 5.29 – A photograph of the aluminum calibration plate that was machined with 3.3 mm holes regularly spaced 12.7 mm apart. 15 cm long parallel rods were additionally used because, based on geometry their projections could be employed to determine the relative location of the source with respect to the imager..... 152
- Figure 5.30 – a) X-ray image of the bottom part of the calibration plate shown in figure 5.29 before distortion correction. Colors are inverted so that low attenuation regions appear black. b) Part of the same image after the feature recognition algorithm is applied and the image dewarped. A small amount of distortion remains at the extreme right edge because the model obscured the markers, but this area is not of interest..... 153
- Figure 5.31 – Upper figure shows an ideal case where a perfect 2D void fraction distribution is projected onto the imager by parallel beams. The bottom figure illustrates the actual situation. (Although the beam originates from a finite size focal spot, here it is simplified as a point.) The ‘one’ parallel beam still projects a ‘perfect’ image onto the imager, but beams with higher angles project an increasingly smeared and stretched projection of the void fraction distribution as is indicated by the slightly stretched rectangles with grey fill. .... 155
- Figure 5.32 – Sketch showing the origin (red dot) and labeling of the grid. The origin is at the  $(x, y)$ - location of the central beam path from the source normal to the model. .... 157
- Figure 5.33 – Sketch of the beam paths in the  $(z,y)$  - plane. .... 158
- Figure 5.34 – Location calibration target (glowing blue) located on the source’s side of the test section. The target has 16 lead spheres in two different  $z$ -planes, two different  $y$ -planes and four different  $x$ -planes. The relative positions of the lead spheres are known precisely, as they are in pockets machined into the plastic frame by a CNC mill. Flow is from right-to-left through the test section..... 161
- Figure 5.35 – Sketch of the setup to find the relative source location. All the dimensions shown on the right, except  $z_{II}$ ,  $y_a$  and  $y_b$  can be measured directly from the II image, and used to determine the remaining dimensions needed..... 162
- Figure 5.36 – Simulated void fraction distribution ( $x$ ), and distorted void fraction distributions that would be observed in the imager plane due to non-parallel beam paths. Circles are “perfect” projections, and red plus-signs are projections with +/- 0



to 0.5 % random noise in void fraction measurement, mimicking the type of errors a real image might have. ....	164
Figure 5.37 – Reconstructed void fraction distribution (x) using eqn. 5.56. In the absence of noise (o) the non-distorted void fraction distribution is recovered within the round off error accumulated during the simulation. However, the data which had noise (+) did not return the actual distribution, but rather the noise produced a large error of increasing magnitude as the reconstruction progressed away from the center beam path. ....	165
Figure 5.38 – X-ray image of a standard-resolution test tool in the flow domain. The numbers in the image give the grid spacing in units of lines per inch. ....	167
Figure 6.1 – Schematic of the model in the test section. The red arrows indicate the x- and y-coordinate axis, and the origin is located at the base of the step. The free surface forming gate was located immediately upstream of the model. Flow is from right to left as indicated by the arrow. ....	173
Figure 6.2 – Cavity viewed from the side (a) and from below at an oblique angle (b). The photos have a different downstream field of view as can be seen by the different location of the step. ....	174
Figure 6.3 – Instrument locations. The coordinate axis are as shown in figure 6.1, and the origin is located at the base of the step. ....	175
Figure 6.4 – Time averaged PIV velocity profiles immediately upstream of the step. The solid blue and green curves show the theoretical turbulent and laminar velocity profiles. The red curve shows a laminar BL measured without a trip. The crosses and circles show the boundary layers obtained with various trips, and finally the + - signs show the TBL with the trip which was used for these experiments. ....	177
Figure 6.5 – Time averaged PIV velocity field immediately after the backward facing step. The black lines on the top are sketched to indicate location of the step and model test surface at $y = 0$ mm. The red dashed line indicates the location from which the velocity profile shown in the next figure is taken from. ....	178
Figure 6.6 – Time averaged streamwise velocity component 61 mm downstream of the step. The measured velocity near the wall may be incorrect due to reflection of laser light and particle images from the wall. Here position 0.0 mm is measured from the model’s test surface downstream of the step. ....	179
Figure 6.7 – Time averaged PIV velocity field in vicinity of probe position #2 after the backward facing step. The black line on the top indicates the location of the model test surface at $y = 0$ mm. The red dashed line indicates the location from which the velocity profile shown in the next figure is taken from. ....	180

- Figure 6.8 – Time averaged PIV velocity field at approximately the second optical probe position. Velocity is normalized by the free stream speed at the backward facing step. .... 181
- Figure 6.9 – Left: a dual fiber optical probe with 10 micron tips. Right: a dual fiber optical probe with 30 micron tips suited for use in bi-directional multiphase flow. .... 182
- Figure 6.10 – Void fraction distributions from optical probe at position #1. Flow speed was 1.8 m/s and ventilation rate  $7.87 \times 10^{-6} \text{ m}^3/\text{s}$ . The blue and black points are based on data provided by the upstream and downstream tips, respectively. The small scattered markers were based on data averaged over 30 seconds, and the thicker markers connected by lines are the combined averages, representing averaging over  $\sim 3$  minutes and 30 seconds. Number of bubbles detected varied from 24 at  $y = 15.9 \text{ mm}$  to 309 at  $y = 7.8 \text{ mm}$ , and decreasing to 90 at  $y = 1.7 \text{ mm}$ . The orange line indicates the location beyond which optical probe data was not recorded to avoid risking the probe tips touch the model surface. .... 184
- Figure 6.11 – Void fraction distributions from optical probe at position #1. Flow speed was 1.8 m/s and ventilation rate  $2.2 \times 10^{-5} \text{ m}^3/\text{s}$ . The blue and black points are based on data provided by the upstream and downstream tips, respectively. The small scattered markers were based on data averaged over 30 seconds, and the thicker markers connected by lines are the combined averages, representing averaging over  $\sim 3$  minutes and 30 seconds. The orange line indicates the location beyond which optical probe data was not recorded to avoid risking the probe tips touch the model surface. .... 185
- Figure 6.12 – Void fraction distributions from optical probe at position #1. Flow speed was 1.8 m/s and ventilation rate  $3.93 \times 10^{-5} \text{ m}^3/\text{s}$ . The blue and black points are based on data provided by the upstream and downstream tips, respectively. The small scattered markers were based on data averaged over 30 seconds, and the thicker markers connected by lines are the combined averages, representing averaging over  $\sim 3$  minutes and 30 seconds. The orange line indicates the location beyond which optical probe data was not recorded to avoid risking the probe tips touch the model surface. .... 186
- Figure 6.13 – Void fraction distributions from optical probe at position #1. Flow speed was 2.0 m/s and ventilation rate  $7.87 \times 10^{-6} \text{ m}^3/\text{s}$ . The blue and black points are based on data provided by the upstream and downstream tips, respectively. The small scattered markers were based on data averaged over 30 seconds, and the thicker markers connected by lines are the combined averages, representing averaging over  $\sim 3$  minutes and 30 seconds. The orange line indicates the location beyond which optical probe data was not recorded to avoid risking the probe tips touch the model surface. .... 187

Figure 6.14 – Void fraction distributions from optical probe at position #1. Flow speed was 2.0 m/s and ventilation rate  $2.2 \times 10^{-5} \text{ m}^3/\text{s}$ . The blue and black points are based on data provided by the upstream and downstream tips, respectively. The small scattered markers were based on data averaged over 30 seconds, and the thicker markers connected by lines are the combined averages, representing averaging over ~3 minutes and 30 seconds. The orange line indicates the location beyond which optical probe data was not recorded to avoid risking the probe tips touch the model surface. .... 188

Figure 6.15 – Void fraction distributions from optical probe at position #1. Flow speed was 2.0 m/s and ventilation rate  $3.93 \times 10^{-5} \text{ m}^3/\text{s}$ . The blue and black points are based on data provided by the upstream and downstream tips, respectively. The small scattered markers were based on data averaged over 30 seconds, and the thicker markers connected by lines are the combined averages, representing averaging over ~3 minutes and 30 seconds. The orange line indicates the location beyond which optical probe data was not recorded to avoid risking the probe tips touch the model surface. .... 189

Figure 6.16 – Void fraction distributions from optical probe at position #2. Flow speed was 1.8 m/s and ventilation rate  $7.87 \times 10^{-6} \text{ m}^3/\text{s}$ . The blue and black points are based on data provided by the upstream and downstream tips, respectively. The small scattered markers were based on data averaged over 30 seconds, and the thicker markers connected by lines are the combined averages, representing averaging over ~3 minutes and 30 seconds. Number of detected bubbles varied from over 900 at the peak and decaying towards zero far from the plate. The orange line indicates the location beyond which optical probe data was not recorded to avoid risking the probe tips touch the model surface. .... 190

Figure 6.17 – Void fraction distributions from optical probe at position #2. Flow speed was 1.8 m/s and ventilation rate  $2.2 \times 10^{-5} \text{ m}^3/\text{s}$ . The blue and black points are based on data provided by the upstream and downstream tips, respectively. The small scattered markers were based on data averaged over 30 seconds, and the thicker markers connected by lines are the combined averages, representing averaging over ~3 minutes and 30 seconds. The orange line indicates the location beyond which optical probe data was not recorded to avoid risking the probe tips touch the model surface. .... 191

Figure 6.18 – Void fraction distributions from optical probe at position #2. Flow speed was 1.8 m/s and ventilation rate  $3.93 \times 10^{-5} \text{ m}^3/\text{s}$ . The blue and black points are based on data provided by the upstream and downstream tips, respectively. The small scattered markers were based on data averaged over 30 seconds, and the thicker markers connected by lines are the combined averages, representing averaging over ~3 minutes and 30 seconds. The orange line indicates the location beyond which optical probe data was not recorded to avoid risking the probe tips touch the model surface. .... 192

Figure 6.19 – Void fraction distributions from optical probe at position #2. Flow speed was 2.0 m/s and ventilation rate  $7.87 \times 10^{-6} \text{ m}^3/\text{s}$ . The blue and black points are based on data provided by the upstream and downstream tips, respectively. The small scattered markers were based on data averaged over 30 seconds, and the thicker markers connected by lines are the combined averages, representing averaging over  $\sim 3$  minutes and 30 seconds. The orange line indicates the location beyond which optical probe data was not recorded to avoid risking the probe tips touch the model surface. .... 193

Figure 6.20 – Void fraction distributions from optical probe at position #2. Flow speed was 2.0 m/s and ventilation rate  $2.2 \times 10^{-5} \text{ m}^3/\text{s}$ . The blue and black points are based on data provided by the upstream and downstream tips, respectively. The small scattered markers were based on data averaged over 30 seconds, and the thicker markers connected by lines are the combined averages, representing averaging over  $\sim 3$  minutes and 30 seconds. The orange line indicates the location beyond which optical probe data was not recorded to avoid risking the probe tips touch the model surface. .... 194

Figure 6.21 – Void fraction distributions from optical probe at position #2. Flow speed was 2.0 m/s and ventilation rate  $3.93 \times 10^{-5} \text{ m}^3/\text{s}$ . The blue and black points are based on data provided by the upstream and downstream tips, respectively. The small scattered markers were based on data averaged over 30 seconds, and the thicker markers connected by lines are the combined averages, representing averaging over  $\sim 3$  minutes and 30 seconds. The orange line indicates the location beyond which optical probe data was not recorded to avoid risking the probe tips touch the model surface. .... 195

Figure 6.22 – The high speed camera setup, where side view was measured. The mirror seen in the figure, as indicated by the arrow, was used to record the bottom view as well as to reflect light sometimes when a second high power Arri-studio light was used. .... 196

Figure 6.23 – Still photograph from a 1000 fps movie showing the bubbles near probe position #2 as viewed from below. The dashed lines are spaced on average 2.54 cm apart..... 197

Figure 6.24 – Image showing the bubbles as viewed from the side in the vicinity of probe position #2..... 197

Figure 6.25 – Dimensions of the bubbles which were determined for the bottom and side views. .... 198

Figure 6.26 – Scatter plot of the bubble speed versus major axis diameter..... 198

Figure 6.27 – Bubble size histogram. .... 199

Figure 6.28 – Bubble axis diameter ratio histogram, showing that most bubbles were slightly elliptical.....	199
Figure 6.29 – Bubble speed histogram. ....	200
Figure 6.30 – Image showing the instantaneous beam intensity distribution behind the backward facing step.....	201
Figure 6.31 – False color image of the instantaneous void fraction calculated without any distortion or glare correction.....	202
Figure 6.32 – Time averaged light intensity field.....	203
Figure 6.33 – Time averaged void fraction calculated from the data presented in image 6.32, and from the reference images taken with void fractions zero and one.....	203
Figure 6.34 – The root mean square deviation of the void fraction weighted by the mean void fraction to highlight the area of large fluctuation with significant void fractions. This result is valuable as it clearly shows the size of the area where the cavity is oscillating, and enables a quantitative definition of the mean oscillations.....	204
Figure 6.35 – Void fraction distribution corrected for some of the veiling glare and geometric distortion .....	206
Figure 6.36 – One frame of a movie where each frame represented a mere 1 ms. $Q_{inj} = 2.2 \times 10^{-5} \text{ m}^3/\text{s}$ , $U = 1.8 \text{ m/s}$ . Some random light spots on the background are noise 10 pixels wide. A 2D median filter was applied to reduce noise in the animation. The void fraction through a single 5 mm bubble should be 2.4%. We can see that the size of the bubbles visible and the void fraction through the center are as expected. ....	207
Figure 6.37 – Comparison at flow speed of 1.8 m/s and ventilation rate of $7.87 \times 10^{-6} \text{ m}^3/\text{s}$ . Void fraction distribution approximately 267 mm downstream of the step. The blue and black optical probe data points are averaged over 30 seconds. Thick lines are averages over 3min 30sec. Cyan crosses are uncorrected x-ray void fraction results averaged over ~1 second. Red crosses are points based on video. ....	210
Figure 6.38 – Comparison at flow speed of 1.8 m/s and ventilation rate of $2.2 \times 10^{-5} \text{ m}^3/\text{s}$ . Void fraction distribution approximately 267 mm downstream of the step. The blue and black optical probe data points are averaged over 30 seconds. Thick lines are averages over 3min 30sec. Red crosses are veiling glare corrected x-ray void fraction results averaged over ~1 second.....	211
Figure 6.39 – At flow speed of 1.8 m/s and ventilation rate of $2.2 \times 10^{-5} \text{ m}^3/\text{s}$ . Void fraction distributions at multiple streamwise locations showing the streamwise evolution of the void fraction distribution. Where $x_{OP}$ was approximately 267 mm	

downstream of the step. X-ray averaged over ~1 second. (From x-ray recording #53)	212
.....	212
Figure 6.40 – Comparison at flow speed of 1.8 m/s and ventilation rate of $2.2 \times 10^{-5} \text{ m}^3/\text{s}$ . Void fraction distribution approximately 64 mm downstream of the step. The blue and black optical probe data points are averaged over 30 seconds. Thick lines are averages over 3min 30sec. Green and red crosses are veiling glare uncorrected and corrected x-ray void fraction results, respectively. X-ray averaged over ~1 second. Distance specified is $y$ as measured from the test surface. ....	213
Figure 6.41 – Comparison of cavity at step, for $U = 1.8 \text{ m/s}$ and $Q_{inj} = 2.2 \times 10^{-5} \text{ m}^3/\text{s}$ . Void 6 mm downstream of presumed probe location. Distance specified is $y$ as measured from the test surface. ....	214
Figure 6.42 – Comparison of cavity at step, for $U = 1.8 \text{ m/s}$ and $Q_{inj} = 2.2 \times 10^{-5} \text{ m}^3/\text{s}$ . Void 6 mm downstream of presumed probe location. Distance specified is $y$ as measured from the test surface. Same as figure 6.41, except the squares show an approximation of the void fraction which would be measured by the x-ray due to the distortion caused by non-parallel beam paths, if the center beam was to be located at $y = 0 \text{ mm}$ and at the streamwise location, $x$ , of the optical probe. ....	215
Figure 6.43 – Void fraction profiles downstream of the step for $U = 1.8 \text{ m/s}$ and $Q_{inj} = 2.2 \times 10^{-5} \text{ m}^3/\text{s}$ . No veiling glare correction has been employed. Streamwise evolution of void fraction is observed easily, as the peak void fraction monotonically decreases with distance from the step. First profile is taken approximately 10 mm from the step. Each curve represents the profile 10 mm apart. ....	216
Figure 6.44 – Void fraction profiles downstream of the step for $U = 1.8 \text{ m/s}$ and $Q_{inj} = 2.2 \times 10^{-5} \text{ m}^3/\text{s}$ , with veiling glare correction employed. Streamwise evolution of void fraction is observed easily, as the peak void fraction monotonically decreases with distance from the step. First profile is taken approximately 10 mm from the step. Each curve represents the profile 10 mm apart. The veiling glare correction could cause the calculated void fraction to “undershoot” returning negative values, which given the physical constraints were converted into zero. ....	217
Figure 6.45 – Cavity at step, for $U = 1.8 \text{ m/s}$ and $Q_{inj} = 2.2 \times 10^{-5} \text{ m}^3/\text{s}$ . a) Void fraction calculated based on uncorrected images. b) Void fraction change due to the correction. Note that the color bar now spans only 0 to 40%. c) Void fraction distribution after deconvolution using veiling glare PSF from eqn. 6.2. Note: due to a plotting error in the software, what should be a solid blue region was left empty. (Inspection of the void fraction distribution showed the void fraction to be zero in this region.) ....	219
Figure A.1 – Flow is from left to right. $U = 1 \text{ m/s}$ , $Fr = 1.1$ . Old version of the gate with the flap at a 22.5 degree angle. ....	231

Figure A.2 – Oblique view of the gate and free surface. $U = 2.5$ m/s, $Fr = 2.7$ ( $Fr$ -scaled for LCC: 9.4 m/s), old version of the gate in fully vertical position. The pitot used to measure the flow speed and its foil shaped support can be seen in the middle of the image. The frothy region near the aft of the test section is due to water draining down from hoses that connected the volume in front of the gate to the end of the test section, allowing air accumulating in front of the gate to be removed. ....	232
Figure A.3 – At low speed and moderate fill levels a condition was observed where there was a free surface upstream as well as downstream. The green dots on the top of the diffuser correspond to electrical impedance probes used to observe water level and detected splashing. ....	233
Figure A.4 – At slightly higher speeds up to around 1.5 m/s no free surface was observed upstream and no constant splashing of water was detected at the electrodes. The free surface in the diffuser probably wasn't as smooth as in the sketch, but at least no large splashes hitting the top of the diffuser occurred. ....	233
Figure A.5 – Three steps of loss of free surface: At 1.5-2.4m/s rapid splashing was detected at the back two and three electrodes. As speed was increased closer two 3 m/s splashing was indicated at almost all electrodes. Once at this condition, it seems that any significant increase of speed leads to a loss of free surface. Once the free surface was lost the back 2-3 electrodes curiously enough indicated no water and often no splashing. This would indicate that a topology of the type shown in the last sketch may be occurring. ....	233
Figure A.6 – The old version of the gate in the MLCC and a loss of cavity. ....	234
Figure A.7 – Looking upstream inside the LCC's test section. Leica measurement station seen in the middle of the image. ....	235
Figure A.8 – Location of the gate. We can see that the gate has three mounting points using the existing front most diagonal windows on both port and starboard sides, and a third window opening in the ceiling of the tunnel. ....	236
Figure A.9 – FEA model of the gate viewed from below. Figure by Dr. Wang. ....	237
Figure A.10 – FEA model of the gate viewed from above. Figure by Dr. Wang. ....	237
Figure A.11 – FEA model of the gate viewed from the side with the flap at 25 degrees with respect to the flow. Figure by Dr. Wang. ....	238
Figure A.12 – FEA model of the gate viewed from the side with the flap at 90 degrees with respect to the flow. Figure by Dr. Wang. ....	238
Figure A.13 – Pressure and void fraction contours from CFD. ....	239

Figure A.14 – The location of the gate and HiPlate. ....	240
Figure A.15 – To get the gate into the test section it had to be tilted by over 45 degrees. Once in the test section, it was lowered onto a cart and the crane disconnected so that the chains could be repositioned for the final lift into position, during which the chains upstream went through the window on the LCC’s ceiling upstream of the test section. ....	241
Figure A.16 – Gate in the test section with the flap at 0 degrees with respect to the horizon. The gate’s hinge was covered by a flexible spring steel sheet which slid in and out of the slot upstream, always providing a smooth flow surface and minimizing water leakage through the hinge. ....	242
Figure A.17 – The flap can be seen through the right window and the displaced water surface through the left. ....	242
Figure A.18 – Looking upstream towards the gate. The gate’s flap and piston are clearly visible. The green hoses seen in the image are 4” drain lines with pneumatic valves used to divert the air water mixture skimmed from in front of the gate to the back of the test section where the mixture could be discarded without disturbing the flow in the test section, but without loss of water from the flow loop. ....	243
Figure A.19 – Looking downstream the free surface can be seen to have become flat and free of major perturbations, providing a suitable surface for free surface testing. The hydraulic jump which terminated the free surface in this case was just after the test section and can partially be seen. ....	244
Figure A.20 – The streamwise velocity, $U$ , was fairly uniform and vertical velocity, $V$ , was practically zero as it should. (The data from all four profiles overlaps.) The highest point are on the free surface and it is possible that they are erroneous. ....	245
Figure A.21 – Flow speed vs. RPM at various initial fill levels and gate angles, with a free surface and without the HiPlate. Note the bends and dips which occur when the flow topology changed in the test section or diffuser. ....	246
Figure A.22 – The required pump power versus flow rate for different flap angles and initial fill levels. The approximate power measurement was provided by the LCC’s control system. ....	247
Figure A.23 – The blue circles in the figure below show all the velocities actually measured with the LDV (with the PCDR HiPlate and beach in base position). Depending on the curve fit chosen, two shown for example, the velocity expected at the highest pump PRM had large variation. ....	248



Figure B.1 – The PCDR model, with flow direction indicated by the arrow. The HiPlate model was outfitted with a 7" tall nose at the leading edge and an adjustable beach at the aft. ....	251
Figure B.2 – View of the 7" step with slot d in use. In these experiments, the slot at the base of the step, a, was always used. ....	252
Figure B.3 – PCDR model with some of the instrumentation locations indicated. ....	253
Figure B.4 – The height and angle of the beach could be adjusted by varying the location of the load blocks, which held the beach using the LCC's aluminum windows. To adjust the beach, sealing plates covering the opening were removed from the outside, chain hoists used to suspend the beach and varying the thickness of load blocks under the beach's load-pins in the windows. ....	254
Figure B.5 – Sketch of the beach showing clearly how it mounts into the holes in the LCC's windows. ....	255
Figure B.6 – Drawing of the HiPlate with the beach. ....	256
Figure B.7 – Drawing showing the dimensions of the beach, and its location in the "base" configuration when beach flat is at zero degrees and 3.5" below the HiPlate surface. ....	256
Figure B.8 – View of the structure beneath the beach, for the first design analyzed. In this initial design the round instrument locations were not in two rows and the load pins were found to be too weak as shown in the following. ....	257
Figure B.9 – Plot of the beach's structural factor of safety to yield. ....	258
Figure B.10 – The lowest factor of safety was found to be at the base of the load-pins, which were subsequently thickened and a chamfer was added to the base of the pins. ....	258
Figure B.11 – The expected deflection of the beach. Under the highest loads envisioned, the beach could have deflected as much as 5 mm. ....	259
Figure C.1 – The traverse mechanism shown in detail. Note the flexible shaft coupling inside the enclosure and the shaft exiting the enclosure through three seals, which are not shown in this drawing. ....	261
Figure C.2 – A drawing where the top of the traverse is made transparent to reveal detail. ....	262
Figure C.3 – A close up of the point electrode. The thicker support is 1/8" in diameter, the excitation was provided by the electrode at the very tip and the sensing was done	

via the middle conducting copper color ring seen between the black and white insulating material.....	263
Figure C.4 – Time trace of the point electrode signal as a single bubble passes by. (Figure by Desrippes Eloi and Barazer Aymric) .....	264
Figure C.5 – Time trace of the point electrode signal multiple bubbles passe by. (Figure by Desrippes Eloi and Barazer Aymric) .....	264
Figure C.6 – Circuit diagram of the EIM setup. $V_{ref}$ is what is connected to the Va input on the lock in amplifiers front panel. ....	265
Figure C.7 – The error caused by assumption that $V_1 = V_s$ . ....	267
Figure C.8 – Left: The traverse mechanism. Right: optical probe (used to obtain results shown in in Chapter 6) below the test surface mounted on its brass support. The probe’s reflection can be seen in the test surface.....	268

## LIST OF TABLES

Table 2.1 – Independent variables and possible ranges.....	21
Table 2.2 – Coordinates of the measurement and instrument locations. The origin of the coordinate system is located at the base of the BFS, at the injector location, with y-axis pointing in the direction of gravity and the x-axis pointing downstream. *On the beach the instruments are mounted flush with the local surface and as before $y(x)$ is the distance normal to the model surface from the instrument's mean position. ....	23
Table 2.3 – The six beach positions tested. ....	41
Table 3.1 – Dimensionless groups.....	62
Table 3.2 – Parameter ranges of the experiments.....	63
Table 6.1 – Volume flow rates of air based on the flow meter, optical probe, video and x-ray measurements. For the x-ray measurements the void fraction was integrated from $y = 0$ to 25 mm. Additional measurement and data processing is needed for x-ray at view #2 for $U = 2.0$ m/s, hence those data are not available in present table. ....	208

## LIST OF APPENDICES

### APPENDIX A

<b>Gate Design and Testing</b> .....	<b>230</b>
A.1 Initial design and development.....	231
A.2 FEA of gate structure .....	237
A.3 Final gate design and gate's position .....	240
A.4 First test of the gate in the LCC .....	241
A.5 LCC with the gate and HiPlate.....	248
A.6 The variables considered in the testing .....	249

### APPENDIX B

<b>The PCDR Model</b> .....	<b>251</b>
B.1 The beach design .....	254
B.2 References for Appendix B .....	260

### APPENDIX C

<b>Traversing Probes</b> .....	<b>261</b>
C.1 The traverse mechanism.....	261
C.2 The electrical impedance sensors .....	262

### APPENDIX D

<b>Codes used in Chapter 4</b> .....	<b>269</b>
--------------------------------------	------------

### APPENDIX E

<b>Point Spread Functions and Solutions to Equations in Chapter 5</b> .....	<b>277</b>
---	------------

## NOMENCLATURE

$A$	Cross-sectional area	[m <sup>2</sup> ]
$a$	Bubble major axis diameter	[m]
$b$	Bubble minor axis diameter	[m]
$D$	Draft	[m]
$E$	Energy	[J]
$f$	Frequency	[Hz]
$F$	Force	[N]
$Fr$	Froude number, $U/(gL_c)^{1/2}$	[ ]
$g$	Gravitational acceleration $\sim 9.81$	[m/s <sup>2</sup> ]
$H$	Water depth	[m]
$H_{\text{BFS}}$	Height of the BFS (0.18/0.013 m)	[m]
$H_c$	Cavity thickness at mid cavity	[m]
$I$	Intensity	[ ]
$I_0$	Original intensity/number of photons	[ ]
$I$	Transmitted intensity/number of photons	[ ]
$k$	Ratio of specific heats, 1.4 for air	[ ]
$L_c$	Cavity length (9.25/0.66 m)	[m]
$L$	Length	[m]
$\dot{m}$	Mass flow rate	[kg/s]
$N$	Total number of materials	[ ]

$P$	Power	[W]
$p$	Pressure	[Pa]
$Q_{\text{det}}$	Detection efficiency	[ ]
$q$	Air flux divided by speed, modes width and step height	[ ]
$Q_c$	Volume flow rate of gas at $p_c$ and $T_c$	[m <sup>3</sup> /s]
$Re$	Reynolds number, $UL_c/\nu$	[ ]
$St$	Strouhal number, $fL_{\text{shed}}/U$	[ ]
$t$	Time	[s]
$t$	Thickness of domain in beam path	[m]
$T$	Temperature	[°C]
$U$	Free stream velocity at the BFS	[m/s]
$V$	Photon energy	[eV]
$W$	Spanwise width of the model	[m]
$We$	Weber number, $\rho U^2 d/\sigma$	[ ]
$x_n$	Mass thickness of material n	[kg/m <sup>2</sup> ]
$x$	Streamwise coordinate	[m]
$y$	Coordinate normal to the test surface	[m]
$z$	Spanwise coordinate	[m]

### ***Greek Letters***

$\alpha$	Volumetric void fraction	[ ]
$\beta$	Angle with respect to horizon	[degrees]
$\sigma$	Surface tension	[N/m]

$\delta$	Boundary layer thickness ( $U = 99\%$ of $U$ free stream)	[m]
$\eta$	Efficiency	[ ]
$\rho$	Density	[kg/m <sup>3</sup> ]
$\sigma$	Cavitation number, usually $2(p_c - p_{\text{vapor}})/\rho_w U^2$	[ ]
$\tau$	Stress	[N/m <sup>2</sup> ]
$\theta$	Momentum thickness	[m]
$\nu$	Kinematic viscosity	[m <sup>2</sup> /s]
$\mu$	Dynamic viscosity	[kg m/s]
$\mu_n/\rho_n$	Mass attenuation coefficient of material n	[m <sup>2</sup> /kg]

### ***Subscripts***

atm	Atmosphere
a	Air
B	Beach
BFS	Backwards Facing Step
C	Cavity
D	Drag
g	Gas, glass/acrylic
G	Gate's flap
ref	Reference point
l	Liquid
m	Mixture
n	Material designator (air, water, mix, <i>etc.</i> )

v	Vapor
w	Water
0	Initial
$\infty$	Infinity or far away from surface, depending on context

***Acronyms***

ACS	Air cavity ship
ALDR	Air layer drag reduction
BDR	Bubble drag reduction
BFS	Backward facing step
FB	Force balance
GSV	Grey scale value (referring to value between 0 and 255 for 8-bit camera)
II	Image Intensifier
LCC	US Navy's W.B. Morgan Large Cavitation Channel, Memphis TN
MLCC	1:14.1 scale model of the LCC located at the University of Michigan
LDV	Laser Doppler velocimetry
OD	Outer diameter
PCDR	Partial cavity drag reduction
PIV	Particle image velocimetry
T	Traverse
ToF	Time of flight
2D	Two dimensional
3D	Three dimensional



## ABSTRACT

Ventilated partial cavity drag reduction is a technique that could potentially enable reduction of a ship's frictional drag, leading to a 5 to 20% net fuel savings, and thus providing economic and environmental benefits. Ventilated partial cavity drag reduction experiments were conducted using two geometrically similar experimental setups. First, experiments were performed at the world's largest re-circulating water channel, the U.S. Navy's Large Cavitation Channel (LCC), at Reynolds numbers to 80 million. For these experiments the LCC was adapted to allow free surface testing, which in itself was a major effort. The effect of the cavity closure geometry, and the cavity's robustness in the presence of global flow perturbations mimicking the effect of ambient waves were studied. Next, the experiments were reproduced at 1:14<sup>th</sup> size scale at Reynolds numbers of the order of one million, and in these small scale experiments the effect of Weber number was also investigated by reducing the surface tension by a factor of two. Results from these two sets of experiments were compared, and a potential scaling of required ventilation gas flux discussed. In addition the energy economics of the partial cavity drag reduction technique were analyzed. We can note that for partial cavities, the air entrainment is dominated by the cavity closure dynamics. To gain a better understanding of these dynamics, knowing the void fraction distribution, both spatially and temporally, would be very useful. In the cavity's closure region, as well as in most cavitating flows, any intrusive probe would perturb the flow greatly. X-ray densitometry offers a way to obtain a two dimensional time-resolved projection of the void fraction

distribution, and a quantitative measure of the void fraction along the beam paths. An x-ray densitometry system was developed for use with a pre-existing cavitation tunnel. The limitations of the x-ray system were investigated, methods to contend with the imaging artifacts found, and the measured void fraction profiles compared against those obtained employing dual fiber optical probes and high speed video.

## **CHAPTER 1**

### **Introduction**

“Science is built up of facts, as a house is built of stones,  
but an accumulation of facts is no more science than a heap of stones a house.”

- Jules Henri Poincare (1854 - 1912)

This dissertation covers two distinct, but connected topics. First an air lubrication technique, called partial cavity drag reduction is discussed. Chapter 2 presents results and analysis of a large scale partial cavity drag reduction experiment with Reynolds numbers of the order of 80 million, while Chapter 3 presents results and discusses a scaling based on experiment performed with a geometrically similar setup, but at 1:14<sup>th</sup> the scale. Finally, Chapter 4 considers the energy economics of the partial cavity drag reduction technique, concluding this first half of the dissertation.

Second, we discuss one particular experimental technique: x-ray densitometry. This technique can be used to gain further insight into the details of partial cavities, by providing a quantitative measure of void fraction throughout the flow domain without perturbing the flow in the cavity's closure region. Chapter 5 introduces the technique, and in Chapter 6 the technique is validated against optical probes and high speed video,

which are some of the more classical void fraction measurement techniques. In conclusion, Chapter 7 offers a summary, discussing the achievements and future work.

## **1.1 Partial cavity drag reduction**

Shipping is vital for global commerce, as it is generally one of the most economical and environmentally friendly transportation methods. Worldwide, shipping uses almost 10% of the world's annual oil production and is a significant source of pollution. In addition to the commercial shippers, the world's navies and innumerable cruise lovers need and want, respectively, shipping to be as economical as possible with minimal environmental harm. Since approximately 60% of a typical ship's propulsive power is required to overcome frictional drag, any technique that could significantly reduce a ship's frictional resistance might have a substantial impact both economically and environmentally.

Researchers over the past two centuries have proposed using air to "lubricate" a ship's hull as it passes through water, thus reducing frictional drag. *Air lubrication* is the general term used, but three distinct incarnations of air lubrication can be distinguished: 1) bubble, 2) air layer, and 3) partial cavity drag reduction. This dissertation will focus on partial cavity drag reduction, whilst also providing references to the other two techniques. It has been estimated that a successfully implemented partial cavity drag reduction technology could reduce a ship's net fuel consumption by 5 to 20%, and recent sea trials in Europe have shown this not to be just a laboratory phenomenon. A reduction of 5%, let alone anything approaching 20%, of a ship's fuel consumption would have major environmental and economic implications.

To develop partial cavity drag reduction into a widely adopted technique, implemented on large ships, more must be understood about its behavior under a variety of flow conditions. Currently, even the qualitative understanding of some of the relevant processes, such as air entrainment from the cavity closure, is lacking. The analysis and discussion in this dissertation are based on experimental data. The goal is to increase the understanding of the flow physics affecting partial cavity formation and stability, and to provide sufficient practical data to motivate additional experiments, should the data justify this.

In the present work, partial cavities were studied for several closure region geometries, under both steady and unsteady flow conditions. Minimal air requirements were established over a range of Reynolds numbers from 2 to 80 million. Detailed quantitative measurements were performed and used to study the underlying processes. We discuss scaling of the air requirement with geometry, Reynolds number, Froude number, Weber number, and the effect of periodic flow perturbations, characterized by a Strouhal number and relative amplitude of the pressure and velocity oscillations.

In the course of these experiments, several findings of practical importance were made. For air layers the use of a small backwards facing step, with height of the order of the boundary layer thickness, immediately upstream of the injection site was found to be important to facilitate the initial formation of the layer. Partial cavities in turn were found to be persistent even under perturbed flow conditions, as long as appropriate amounts of excess air was supplied to them.

The experiments were performed at facilities at the University of Michigan and at the U. S. Navy's Large Cavitation Channel. The latter is the world's largest water tunnel,

allowing experiments at near real world scales, while remaining in laboratory conditions. Besides the challenges offered by the need to adapt various measurement instrumentation, these experiments also required the multi year effort of design, development and implementation of an enhancement to the Large Cavitation Channel enabling it to be used for free surface testing.

## **1.2 X-ray densitometry**

To understand the dynamics of partial cavity closures, it would be particularly instructional to know the void fraction distribution as a function of space and time. Though, one of the most difficult challenges in any multiphase experiments is the measurement of void fraction. Many classical techniques are intrusive, perturbing the flow, and often only provide information from one point in space at a time. However, some of the techniques used in medical imaging have the key feature we seek of an ideal void fraction measurement technique. That is the capability to, without perturbing the flow, measure the spatial density distribution's two dimensional projection, as with conventional medical x-rays, or even the three dimensional distribution, as done in computed tomography. Hence it is not surprising that for several decades numerous fluid mechanics researchers have employed x-ray and gamma densitometry techniques. However, the speed of most flows of practical interest as well as the size of experimental setups, presents challenges because of the frame rates at which the flow should be imaged, and because of the large attenuation differences that can exist within small distances in the flow domain.

The work presented in this dissertation discusses an x-ray densitometry system developed to acquire space- and time-resolved quantitative void fraction data from an

existing water channel, where the flow domain was 21 cm laterally. Frame rates of the order of a kilohertz were required and void fraction within the domain ranged from 0 to 100%. Relevant work by previous researchers and basic challenges of the technique are discussed in Chapter 5, followed by, in Chapter 6, a comparison of the technique to more traditional methods of measuring void fraction (by means of high speed video and dual fiber optical probes).

In the spirit of Poincare's phrase; while no one dissertation alone builds a house, this dissertation hopefully provides a few stones in the right places with mortar on top for the stones to come.

## CHAPTER 2

### **High Reynolds Number Partial Cavity Drag Reduction Experiments**

In this chapter, based on the author's recent paper (Mäkiharju *et al.* 2010), we discuss ventilated partial cavity drag reduction (PCDR) experiments conducted at the U.S. Navy's W. B. Morgan Large Cavitation Channel (LCC). The LCC was operated with a free surface within the test section and diffuser to facilitate the removal of the injected air. The free surface was formed behind an actuated gate which was positioned immediately upstream of the LCC's test section. The gate, which could also be used to create large scale perturbations simulating the effect of waves, was a new feature designed by the author specifically for these experiments, and has now become an optional feature for tests at the LCC. Partial cavities were investigated at downstream distance based Reynolds numbers to 80 million. The test model was a 3.05 m wide and 12.9 m long flat plate with a 0.18 m backward-facing step (BFS) 2.01 m from the leading edge of the model. Thus the model thickness was 0.36 m over its forward portion and 0.18 m along its mid-body. The air used to form the cavity was injected at the base of the step, and filled a recess between the step and the "beach". The beach was a tilted plate having an adjustable slope, tilt and height above the test surface. The geometry in the region of the cavity closure (*i.e.* the beach geometry) was varied in an attempt to minimize the rate of air entrainment into the free stream and to assess PCDR's sensitivity



to the cavity closure geometry. Stable cavities with frictional drag reduction more than 95% were attained at best conditions.

## **2.1 Background – concept of air lubrication**

A significant percentage of a ship's propulsive power, about 60% in many cases, is needed to overcome the resistance caused by frictional drag. Throughout the last two centuries, various ways to reduce this component of drag have been proposed. These include injection of polymers, the use of riblets, compliant walls, electromagnetic methods, and various air lubrication techniques (Proc. of Int. Symp. on Seawater Drag Reduction 1998, 2005). A simple test to illustrate how air lubrication works is to run a thin, but sturdy, plate through air and then through water while keeping the widest area on the sides. The resistance is mostly due to frictional drag, and you can immediately observe that the resistance in air is much less than in water. This is because the dynamic viscosity (the natural resistance to flow) and density of air are much less than those of water. In fact, at the same speed the frictional drag for a flat plate is more than 500 times greater in water than it is in air.

Within the field of air lubrication there is a wide variety of techniques that have been suggested since the 19<sup>th</sup> century (Latorre 1997). Air lubrication can be divided into three main subcategories: Bubble Drag Reduction (BDR) (Kodama *et al.* 2000, Madavan *et al.* 1985); Air Layer Drag Reduction (ALDR) (Elbing *et al.* 2008); and Partial Cavity Drag Reduction (PCDR) (Butuzov 1967). A handful of ships today benefit from any form of air lubrication for friction drag reduction. Mitsubishi Heavy industries (Mizokami *et al.* 2010), Stena Bulk, Marin, and DK group have begun serious commercial development and are beginning to offer their versions of air lubrication to shipping companies.

However, further research and development is needed to make air lubrication a mature and widely adopted technique. Given the potential for a 5 to 20% net fuel savings, with an equivalent reduction in emissions, these techniques could have a significant environmental and economic impact.

This chapter focuses on ventilated partial cavity drag reduction, in which drag reduction is achieved by filling a recess that is much deeper than the ship-hull's boundary layer thickness, with gas. The frictional drag on the surface covered by gas is reduced greatly. This technique is also called air cavity drag reduction, but the terminology of specifying this as partial cavity is adopted as the cavity closes on the hull, and this is more consistent with terminology of natural cavitating flows. The same frictional drag reduction could also be achieved with a natural (*i.e.* cavitating) cavity. However, the operational speed range and draft of most vessels make ventilated cavities the only viable option, as the pressure in the cavity would not be sufficiently low to support a natural cavity.

To practically apply PCDR on a ship's hull, its bottom must have indentations, which are to be filled with gas. A backward facing step at the upstream edge and a gently downwards sloping closure at the recesses' downstream edge, trap the injected gas and allow for the formation of a steady ventilated partial cavity. This cavity could in principle have multiple streamwise waves along its free surface, or just a single partial wave. When operating within a design speed range(s), a properly designed closure will minimize the volume of gas lost from the cavity. To maintain the cavity, the volume of gas lost must be continuously replaced by supplying more gas to the cavity. When functioning properly,

the gas separates the hull surface from the water resulting in more than a 95% decrease in frictional drag for the surface inside the cavity.

Researchers in the former USSR studied PCDR for decades and developed several ships which utilize it (Butuzov 1967, Butuzov *et al.* 1999, Amromin and Mizine 2003). Ships utilizing PCDR are sometimes called air cavity ships (ACS). In the last decade, there has been renewed interest in air lubrication and many research groups have studied PCDR through numerical modeling (Amromin *et al.* 2006, Matveev 2003), small scale experiments (Arndt *et al.* 2009, Gokcay *et al.* 2004), and large scale experiments (Lay *et al.* 2010). Also, a recent review by Ceccio (2010) discusses some of the remaining research questions relevant to PCDR. Most recently Stena (Surveyor 2011) and Marin (Foeth 2011) have presented encouraging results from sea trials on reduced-scale models.

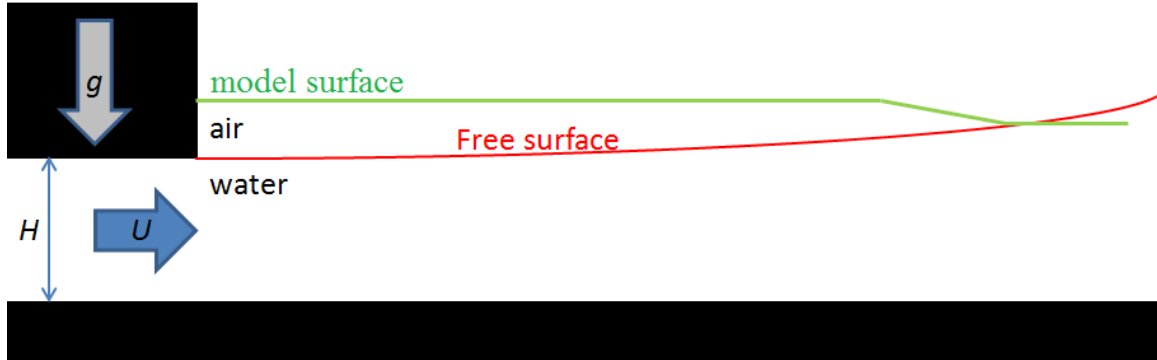
The ability to establish and maintain a cavity beneath a ship with minimal gas supply is of the utmost importance for PCDR to be economically viable, as the savings provided by reduced drag must significantly outweigh the energy and cost required to supply gas to the cavity. To minimize the gas requirement, proper cavity geometry, especially in the closure region, is critical. Kawanami *et al.* (1997) experimented with cloud cavitation control, and given the similarities to a partial cavity's closure region, similar techniques could be of interest for PCDR to reduce the gas entrainment and hence gas supply requirements. Arndt *et al.* (2009) and Amromin *et al.* (2006) provide a good basis for the cavity design. However, open questions remain about PCDR scaling to large ships, the effects of perturbations, the details of the cavity closure and design, and the ultimate cost benefit.

Calm conditions sometimes accompany river and lake shipping, while most ocean going ships operate in conditions where waves are omnipresent and the sea state can be severe; hence we also need to understand how PCDR performs under perturbed flow. Partial cavities in perturbed flows were studied in small scale experiments by Koprikova *et al.* (2008) and Arndt *et al.* (2009). However, no data have been available for Reynolds number,  $Re$ , based on downstream distance from air injector of over  $10^6$ , although  $Re$  for most ships is  $O(10^9)$ . The results included in this chapter are from experiments with  $Re$   $O(10^8)$ , which approaches full scale. The perturbations were generated by periodically oscillating the angle of the flap of the free surface forming gate. Due to these perturbations, the pressure and speed of the incoming flow varied by as much as  $\pm 5\%$ .

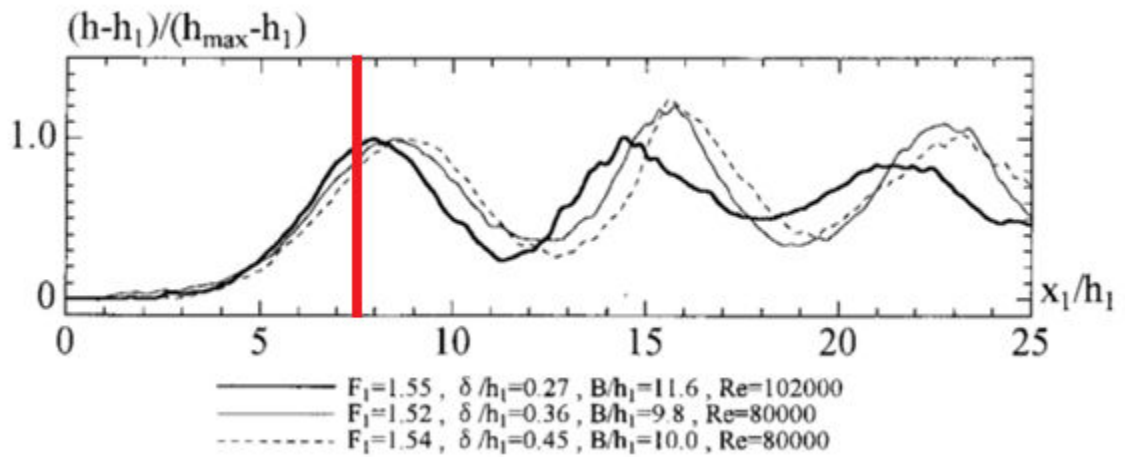
In the experiments reported here, the cavity gas flux, thickness, frictional loads, and pressures were measured over a range of flow speeds (4.4 to 7.5 m/s) and air injection fluxes (0 to 0.490 kg/s). The minimum air flux to establish and to maintain the cavity under steady conditions, as well as the flux required to maintain a cavity under perturbed conditions, were determined for various model beach geometries and flow speed. High speed video was used to visually record the unsteady three dimensional cavity closure, the overall cavity shape, and cavity oscillations. In Chapter 3 results are presented from steady conditions for a geometrically similar model, 1:14<sup>th</sup> scale, and potential scaling is discussed. In Chapter 4 we investigate the energy it takes to supply the gas compared to the savings, which is a pivotal consideration for the viability of PCDR and any other air lubrication method.

## 2.2 Determining the cavity shape

The PCDR experiment models were designed such that the cavity would be the longest achievable within the test facility. From the step to the crest of the beach the recess spanned 71.7% of the length of the models. The free surface downstream of the backward facing step separated tangentially, and closed on the beach at a shallow angle. The overall cavity shape in an unbounded downstream domain is expected to be that of a gravity wave. In deep water at 6.5 m/s a low amplitude (*i.e.* linear) gravity wave length,  $\lambda = 2\pi U^2/g$ , would be 27 m, while our nominal cavity length was 9.25 m (*i.e.* approximate 1/3<sup>rd</sup> of a gravity wavelength). The experiments were, however, conducted in a finite depth ( $H = 1.23$  m at step, 3.05 m total) water tunnel and based on the depth of the flow at the step, the flow was supercritical ( $Fr = U/\sqrt{gH} > 1$ ). Hence in the absence of the model surface downstream of the step, instead of a gravity wave we expect a weak or undular hydraulic jump, as sketched in figure 2.1a. Here the green line shows the model surface location and the red line the approximate shape the free surface would have in the absence of the model. Figure 2.2 details the typical classifications of hydraulic jumps. In these experiments we were mostly in the undular or weak jump region, as we had Froude numbers ranging from 1.4 to 2.7 based on upstream depth,  $H$ . (At the highest  $Fr$  we are transitioning into the oscillating jump region, which could cause the cavity to become more unstable. However, even in the absence of the partial cavity, the flow in the tunnel was becoming unstable at these speeds, and this limited the speed range of the experiments. Therefore, we are not able to determine whether the cavity would have been unstable at the highest speeds in shallow water simply due to the nature of the hydraulic jump, even in a perturbation free external flow.)



(a)



(b)

Figure 2.1 – a) Simplified view of the experimental setup and resulting free surface shape. b) Example of a typical undular jump shape from Ohtsu *et al.* (2001). The vertical red line indicates the typical cavity length encountered in our experiments. In the figure,  $h_1$  is the water depth  $H$  here,  $h_{\max}$  is the height of the first crest, and  $B$  is the channel width. In our experiments  $L_c/h_1 \sim 7.5$ , width to depth  $B/h_1 \sim 2.5$  and Reynolds number based on depth at step  $\sim 7 \times 10^6$ ; therefore the shape is not expected to match well.

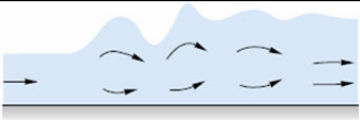
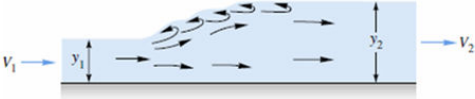
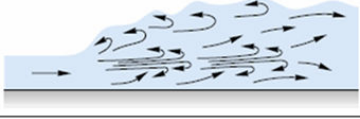
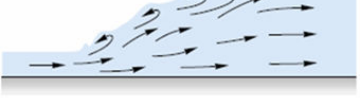
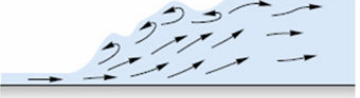
Type of Jump	Froude Number Range	Description	Energy Dissipation	
Undular jump	1.0 to 1.7	Standing-wave, or <i>undular</i> , jump about $4y_2$ long.	< 5 %	
Weak jump	1.7 to 2.5	Smooth surface rise with small rollers, known as <i>weak jump</i> .	5 to 15 %	
Oscillating jump	2.5 to 4.5	Unstable, <i>oscillating jump</i> ; each irregular pulsation creates a large wave which can travel downstream for miles, damaging earth banks and other structures. Not recommended for design condition.	15 to 45 %	
Steady jump	4.5 to 9.0	Stable, well-balanced, <i>steady jump</i> ; best performance and action, insensitive to downstream conditions. Best design range.	45 to 70 %	
Strong jump	> 9.0	Rough, somewhat intermittent <i>strong jump</i> , but good performance	70 to 80 %	

Figure 2.2 – Froude number regions of hydraulic jumps adapted from White (2001). In the experiments discussed in this thesis, the flow is in the undular or weak jump regions.

Despite the finite depth of the channel which caused the flow to be supercritical, it is assumed that while the overall cavity shape is affected, the air entrainment mechanisms and entrainment rates are representative of those one would find in an open water application of PCDR as the closure dynamics are presumably the same. Hence, the following discussion on cavity closure and gas shedding is expected to be applicable for a wide range of similar situations from dam spillway aerators (Chanson 1990, Mortensen *et al.* 2011) to cavities for drag reduction (Lay *et al.* 2010, Matveev 2003).

### 2.3 Mechanisms at the cavity closure

Typically the cavity closed on the sloped part of the surface just upstream of the crest of the beach, as shown in figure 2.3; however it sometimes also overshoot the beach thus openly venting gas from the cavity. (The tendency to overshoot was observed qualitatively to be exaggerated in the smaller scale experiments. Increasing the volume of gas in the cavity, and hence increasing the compliance of the cavity, might mitigate the tendency to overshoot the beach as the cavity could react more to perturbations by change in volume.) The tendency of the closure to overshoot the beach was also related to flow perturbations (Mäkiharju *et al.* 2010). Additionally it may also be induced by auto excitation of the cavity, as pressure pulsations from the closure feed the oscillation of the cavity surface, in turn moving the closure region. However, many conditions existed where the cavity was observed to never (or rarely) overshoot the beach, and air was lost *via* gas shedding from the relatively stationary closure. Therefore, the focus in the following discussion is on the nominally stationary closure, and how gas shedding from it might scale.

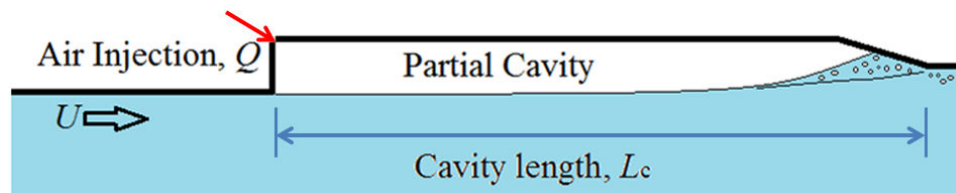


Figure 2.3 – Simplified view of the stationary cavity closing on the beach, where the free surface terminates near or at the crest of the beach.

The presence of an upstream boundary layer, with vortices and other structures, means that there will be a wide range of perturbations impinging on the free surface separating from the step. Hence, there may be a wide spectrum of short wave length and



low amplitude perturbation present at the cavity closure region, which have been observed visually to be present in the experiments at both the small and large scales. Additionally, the cavity surface has superimposed three dimensional waves originating from the lateral sides of the cavity (similar to discussed by Matveev 2007). On the cavity interface for the large scale experiments, the smaller waves had lengths approximately of the order of 10 cm. For each 10 cm horizontal, the beach had a vertical change of about 3 mm. Therefore, if the wave amplitude-to-length ratio was 1/30 or larger, the waves could be responsible for bubble “clouds” being shed due to pinching of the tail of the cavity as sketched in the upper graphic of figure 3.4. Alternatively, the dominant mechanism could be re-entrant jets, which is the case for natural cavities that exhibit the periodic shedding mechanism (Le *et al.* 1993). This alternative is shown schematically in the lower sketch of figure 2.4. A re-entrant jet would travel upstream and cause the shedding of a gas cloud (when it strikes a crest or simply collapses).



Figure 2.4 – Conceptual sketch of potential cavity closure events leading to shedding of gas. The upper illustration depicts the pinching mechanism, the lower the re-entrant jet process, where the red arrow moving upstream represents the re-entrant jet.

While both scenarios depicted in figure 3.4 seem reasonable, the experiments currently discussed do not yield sufficiently detailed information of the cavity closure to determine the prevailing mechanism. However, results from Lay *et al.* (2010) seemed to indicate Strouhal number (shedding frequency multiplied by shed cloud length and divided by the free stream speed) of  $\sim 0.3$  for the cloud shedding, which coincides with that typically observed for shedding associated with re-entrant jets. Additionally both mechanisms could coexist or one could dominate. If the re-entrant jet mechanism dominates, perhaps air loss could be decreased by obstacles strategically placed on the beach (Kawanami *et al.* 1997). However, if the "pinch-off" mechanism dominates, any obstacles could increase the air entrainment. Hence, along with better visualization and time resolved void fraction measurements, obstacle placement could be a useful method to determine which mechanism is dominant.

#### **2.4 The large scale model**

The test model, shown in figure 2.5, was a 3.05 m wide and 12.9 m long flat plate fitted with a 0.18 m tall backward-facing step and a "beach", a cavity-terminating composite surface, on the trailing portion of the model (shown in inset of figure 5.1). The height, streamwise slope and spanwise tilt of the beach were adjustable. The upstream part of the beach surface began 4.5 to 13.5 cm below the test surface and sloped down at an angle,  $\beta_B$ , which was adjustable between 0.4 and 2.8 degrees. The spanwise tilt of the beach was adjustable from 0 to 1.4 degrees. The mid-section of the beach surface, termed the "beach flat", was angled -1.7 degrees with respect to the first section and it could be positioned 9 to 18 cm below the model surface. Six beach configurations were tested in search of the optimal geometry. For the geometries tested, optimal was found to be

configuration P1 with no spanwise tilt, upstream beach section slope  $\beta_B$  at  $1.7^\circ$  from horizontal, and the beach flat horizontal and 9 cm from the model surface.

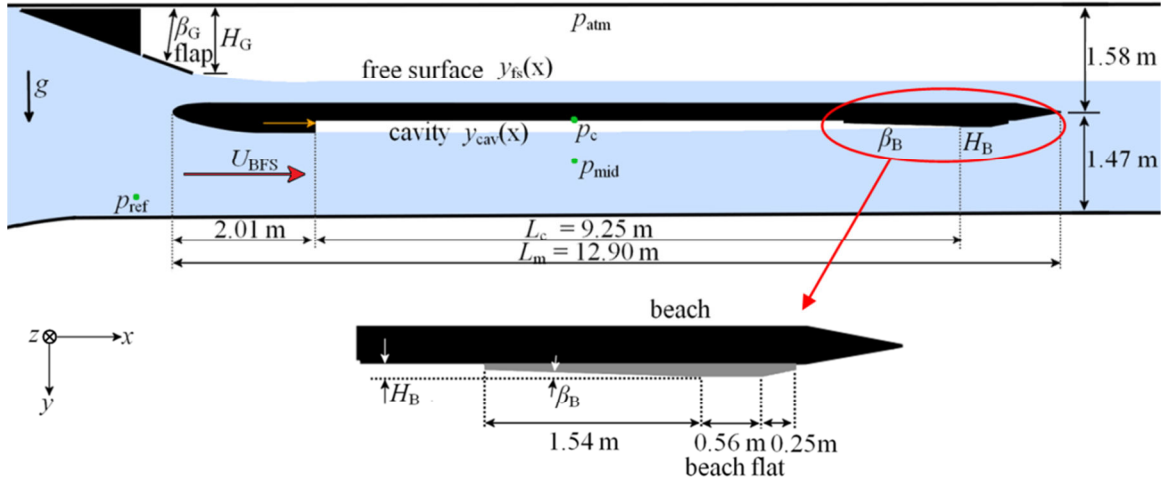


Figure 2.5 – Profile of the gate and model in the LCC's test section. The depth of the water below the BFS is 1.23 m. The mid-body of the plate is 18.4 cm thick, and at the step the plate is 36.2 cm thick. The origin of the coordinate system is at the base of the 17.8 cm tall BFS, as detailed in table 2.2. For clarity, the axes are shown shifted to the side and not at the true location of the origin. Insert: Detailed view of the cavity-terminating beach, shown in grey.

Air was injected at the base of the BFS, which was 2.01 m downstream of the model leading edge. The BFS and the beach trapped the ventilated partial cavity over the longitudinal mid-section of the model. The bottom of this model can be thought to represent a small section of a ship hull, as on an actual ship there would likely be multiple cavities in both the streamwise and spanwise directions, and some of the cavities could have multiple waves in the streamwise direction along their liquid-gas interfaces.

The leading edge of the model was roughened randomly to ensure that boundary layer transition occurred. Laser Doppler velocimetry (LDV) measurements, shown in

figure 2.6, were taken to confirm a turbulent boundary layer 20 cm upstream of the BFS, at LDV<sub>1</sub> – location given in table 2.2.

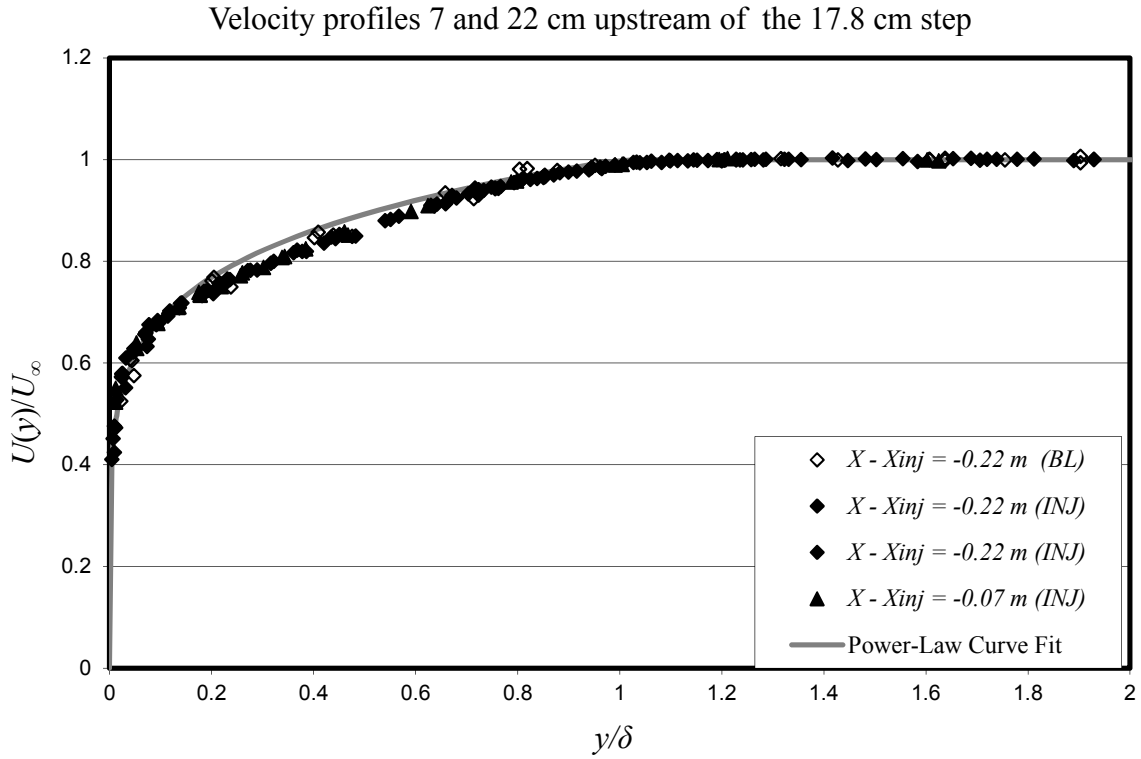


Figure 2.6 – Boundary layer velocity profile measured with the LDV. In the legend, BL refers to base line conditions where no gas is injected, and INJ refers to conditions where gas is injected.  $\delta$  is the 99% boundary layer thickness. (Modified version of figure by Dr. Brian Elbing. Reproduced with permission).

## 2.5 Test facility

The experiments were performed at the Large Cavitation Channel (LCC) described in Park *et al.* (2003) and Etter *et al.* (2005). The LCC, shown in figure 2.7 and 2.8, is the world's largest cavitation channel with a 3.05 m wide, 3.05 m tall and 13.1 m long test section. For these experiments the LCC was modified by the addition of a gate to facilitate the formation of a stable free surface within the test section and diffuser. (The gate designed by the author is discussed further in appendix A.) The free surface permitted air injected beneath the model to escape from the free surface downstream of the model, and then be removed from the tunnel without loss of water while the tunnel was operating. This minimized static pressure fluctuations and the accumulation of air in the tunnel's water during experiments. As a result the test run times were significantly increased relative to previous air injection studies performed at the LCC (Sanders *et al.* 2006, Elbing *et al.* 2008, Lay *et al.* 2010). The gate was attached to the inside ceiling of the LCC immediately upstream of the test section inlet and it projected downstream into the test section. It displaced the flow downwards creating a 0.44 m average flow depth above the model with a free surface in the test section (see figure 2.5). In most cases the free surface extended into the diffuser where it returned to its conjugate depth via a hydraulic jump. The gate spanned the test section width and extended down 0.97 m from the channel ceiling with at a gate-flap angle of 20°. The gate remains at the LCC as a new optional feature.

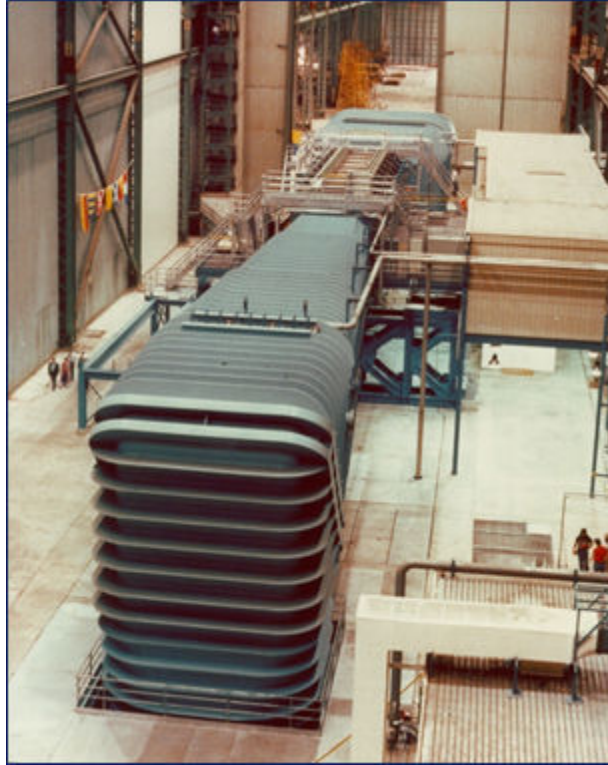


Figure 2.7 – Photo showing the top half of the U. S. Navy’s W. B. Morgan Large Cavitation Channel located in Memphis, Tennessee. For scale, note the three people walking next to the tunnel on the left side of the image.

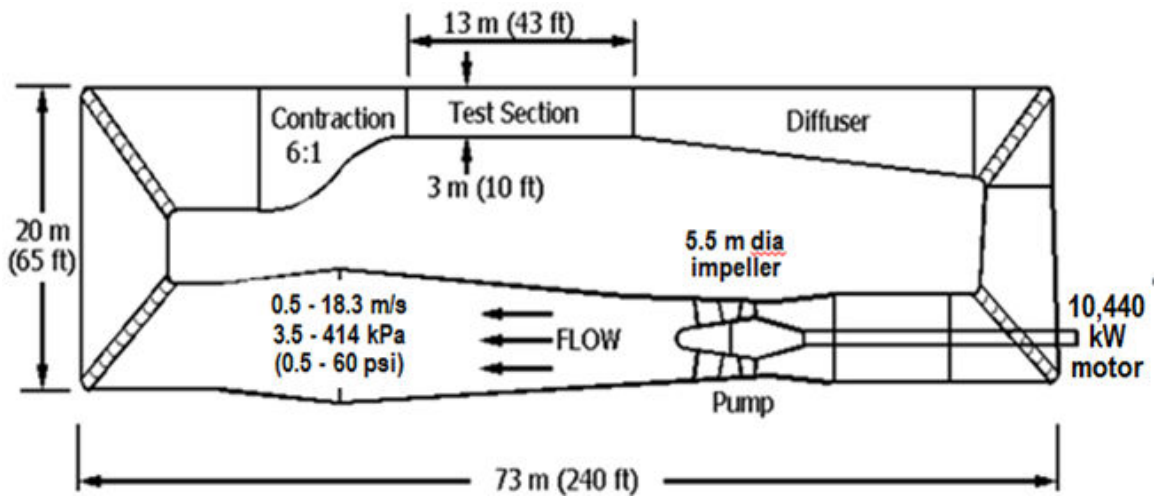


Figure 2.8 – Sketch of the LCC showing the dimensions and main features. Flow is clock-wise. The boxes at the corners of the tunnel represent the turning vanes. The tunnel has flow straighteners, not shown, upstream of the contraction.

## 2.6 The dependent and independent variables of interest

The main research questions were dependence of the required PCDR establishment and maintenance gas volume fluxes on the flow speed, beach geometry, and whether or not cavities could be maintained under perturbed condition. [*i.e.* attempt to determine  $Q_{\text{establish}}(U_{\infty}, \text{ geometry, disturbances})$  and the  $Q_{\text{maintain}}(U_{\infty}, \text{ geometry, disturbances})$ ]. The independent parameters for these experiments, as well as the ranges of parameters used, are listed in table 2.1.

Table 2.1 – Independent variables and possible ranges.

Variable		Approximate Range
$U_{\infty}$	free-stream speed [m/s]	5.0 to 7.5
$p_{\infty}$	free surface pressure in the LCC test section [Pa]	0
$H_F$	no-flow test section liquid fill height [m]	0.50 to 2.85
$\bar{\beta}_G$	mean gate angle [degrees]	0 to 90
$\Delta\beta_G$	gate oscillation amplitude [degrees]	0 to 20
$f_G$	gate frequency of sinusoidal oscillation [Hz]	0 to 0.5
$Q_A$	mass flow-rate of injected air [kg/s]	0 to 0.85
$H_B$	beach crest height [m]	0.09 to 0.19
$\beta_B$	beach angle [degrees]	-1.7 to +3.5

## 2.7 Specialized instrumentation

The flow diagnostics included gas mass flow meters, pressure transducers, electrical impedance probes, Pitot tubes, flow imaging systems, two component laser Doppler velocimeter, and force balances. The locations of instruments are shown in figure 2.9 and listed in table 2.2. The impedance probes and Pitot tubes were mounted on water proof traverses, designed by the author, at three downstream locations to measure void fraction, liquid-gas interface speed and dynamic pressure profiles. For perturbed flow, a TTL triggering circuit was used to synchronize the LDV data with the pressure, air flux, gate angle and force balance time traces.

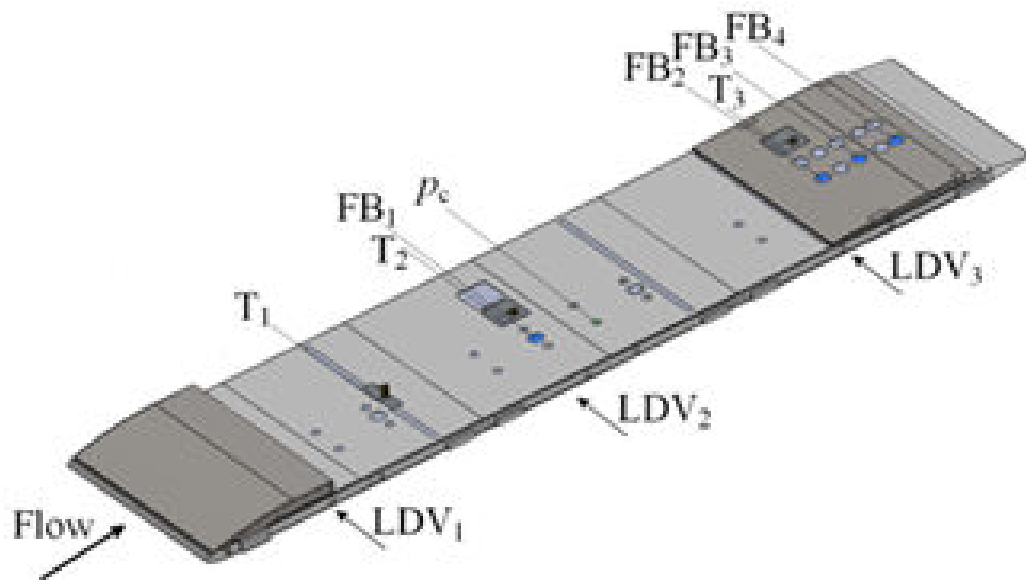


Figure 2.9 – 3D drawing of the model as seen from below with the measurement and instrument locations indicated. The detailed locations are given in table 2.2.



Table 2.2 – Coordinates of the measurement and instrument locations. The origin of the coordinate system is located at the base of the BFS, at the injector location, with y-axis pointing in the direction of gravity and the x-axis pointing downstream. \*On the beach the instruments are mounted flush with the local surface and as before  $y(x)$  is the distance normal to the model surface from the instrument's mean position.

Instrument/Object	$x$ [m]	$y$ [m]
Traverse 1	1.57	0.10...0.20
Traverse 2	3.86	0.10...0.20
Traverse 3	8.60	0.07...0.17*
Force Balance #1	3.93	0.00
Force Balance #2	8.58	0.07*
Force Balance #3	9.04	0.08*
Force Balance #4	9.56	0.09*
$p_{\text{ref}}$ pressure tap	-2.43	1.18
$p_{\text{cav}}$ pressure tap	4.60	0.00
$p_{\text{mid}}$ pressure tap	4.70	0.26
$LDV_{\text{ref}}$	-2.04	0.27
$LDV_1$	-0.22	0.00...0.16
$LDV_{\text{BFS}}$	-0.22	0.04
$LDV_2$	3.93	-0.16...0.36
$LDV_3$	7.86	0.00...0.21
Leading edge	-2.01	-0.09
BFS/Injector	0.00	0.18/0.00

The establishment of a cavity and its closure were observed visually, as well as from the electrical impedance probe and force balance readings. The measurement from the force balances reliably indicated when they were within the cavity, as this caused the reading to drop to near zero. The force balances were those used by Sanders *et al.* (2006), and Vishay 2310 amplifiers provided the excitation and the signal conditioning. The flush mounted Force Balance #1 in the cavity was normal to the flow and as such expected to

measure actual shear stress, while the balances mounted on the beach were inclined with respect to the flow and measured a force with contributions from stresses normal and tangential to the local surface orientation.

The gate's flap angle was measured using a VTI Technologies SCA121T-D03 dual axis inclinometer, with a manufacturer specified accuracy of  $\pm 0.1^\circ$ . The flap angle was adjusted and then locked, or articulated to generate perturbed flow, by a hydraulic piston with a 20 cm bore. The piston was custom fabricated by S&W Machine Works and powered by a 3000 psi hydraulic diesel power pack. The injected air's mass flow rate was measured using three Sierra Instruments 640S thermal mass flow meters (each located in a separate inflow pipe), which had manufacturer reported accuracies of  $\pm 1.5\%$  of full scale (0.490, 0.490, and 0.610 kilograms per second, kg/s). At multiple flow rates, below 0.120 kg/s, the total air flux indicated by the thermal gas thermal mass flow meters was compared to a reading from an Omega rotameter located in series upstream of the mass flow meters. The readings coincided to within the accuracy of the rotameter, which was  $\pm 0.002$  kg/s.

Differences in static pressure between the reference point (position listed in table 2.2) and atmospheric pressure, and between the reference point and cavity pressure were measured by Omega PX2300-DI10 and PX2300-DI5 wet-wet differential pressure transducers, respectively. The manufacturer specified accuracy of the pressure transducers were  $\pm 170$  and  $\pm 85$  Pa, respectively. The difference between the cavity pressure and free stream static pressure at the same streamwise coordinate was measured by an Omega Engineering PX760-06WCDI differential pressure transducer with manufacturer specified accuracy of  $\pm 3$  Pa. The outputs from the three pressure

transducers, mass flow meters, gate-flap tilt sensor, LCC monitoring sensors (tunnel motor frequency and water temperature) and force balances were simultaneously recorded *via* a National Instruments PCI DAQ board and a PC computer running LabView data acquisition software.

### 2.7.1 Traversing probes

To obtain profiles of the air-water interface speed,  $U_{\text{interface}}(x_i, y)$ , the void fraction,  $\alpha(x_i, y)$ , and the dynamic pressure,  $p_{\text{dynamic}}(x_i, y)$ , three probes were mounted onto traverses that could be positioned 0 to 20 cm normal to the model surface (in the y-direction). Figure 2.10 shows a photo of one of these traverses. During the PCDR tests, the traverse on the beach,  $T_3$ , could be remotely fully-retracted into a tight fitting plastic housing such that not part of it protruded beyond the beach surface. A position control better than  $\pm 0.2$  mm was used; the motion was achieved *via* a gear mechanism connected to a Yaskawa Sigma 5 SGMAV-04A3A61 motor with a 20 bit per revolution absolute encoder. The motors were controlled by SGD V-2R8F11A Yaskawa drives, with position prescribed by a LabView program (via Yaskawa Mechatrolink II JAPMC-NT110 PCI-card). Figure 2.11 shows the motor's watertight anodized aluminum enclosure and gear mechanism for one of the traverses. The enclosures, which the author designed, were slightly pressurized and instrumented to detect leaks. The probe positions were verified periodically with direct measurements using a caliper inside the LCC's test section. The measured and set position were always found to agree within the accuracy of the measurements, which using the 8-inch Mitutoyo caliper was  $\pm 0.2$  mm. The three traverses were identical and each had three probe instruments: point electrode, time-of-flight electrode pair, and a Pitot-tube. The probes were spaced 2.6 cm apart in the spanwise z-direction.

The time-of-flight (ToF) electrode pair, seen as the right-most probe in figure 2.11, consisted of five conducting rings spaced 5 mm apart on a 3.2 mm OD Garolite rod, with an elliptical rounded tip. The conducting rings were made by machining 0.5 mm wide grooves into the non-conducting Garolite rod, wrapping one loop of bare 32 gauge wire in the grooves, and then filling the rest of the groove with highly conductive silver epoxy. Then the rings were carefully re-machined and polished to ensure that the rod's surface was smooth and flat. The first, second and third rings formed the first electrode, with the second ring providing the excitation signal at frequency  $f_1$ . The second electrode was formed by the third, fourth and fifth rings, with the fourth ring providing the second excitation signal at frequency  $f_2$ . The return line connecting the first, third and fifth rings was shared, and the signals at different frequencies,  $f_1$  and  $f_2$ , were distinguished by lock-in-amplifiers (Stanford Research Systems SR830). The water-air interfacial speeds, were calculated by cross-correlating the signals from the two electrode pairs of the ToF probe.

The point electrode was made from 1.1 mm outer diameter (OD) rigid coaxial cable supported by a 3.2 mm OD brass rod. The tip of the coaxial cable was machined conically with an approximately  $60^\circ$  included angle. The center conductor and the shield of the coaxial cable formed the point electrode. All three point probes had volumes of influence that can be approximated as a sphere with radius between 1 and 2 mm. (The volume of influence was estimated based on the distance at which a non-conducting object near the probe causes a significant change in the signal. It should be noted that the signal is also dependent on the flow topology, as the signal indicates a void fraction of unity when any bubble fully surrounds the center electrode.)

Both the ToF and point electrode signals were converted into void fraction information by relating the electrical impedance of the mixture in the vicinity of the electrode to the void fraction (Ceccio and George, 1996). For the circuit used the expression derived in Appendix C is given by

$$\alpha = \frac{2(V_s - V_a)(V_m - V_w)}{V_s(3V_a - V_m - 2V_w) + 3V_mV_w - V_a(2V_m + V_w)} \quad (2.1)$$

The stagnation and static pressures from the pitot were used to calculate the flow speed as

$$u(x, y, t) = \sqrt{\frac{2(p_{stag} - p_{stat})}{\alpha\rho_a + (1 - \alpha)\rho_w}} \quad (2.2)$$

where  $\rho_a$  and  $\rho_w$  represent the mass density of air and water, respectively. The water temperature was measured by the LCC's instrumentation, and was found to be nearly constant at 25 °C during the experiments. Hence, the water density was taken to be a constant  $\rho_w = 997 \text{ kg/m}^3$ .

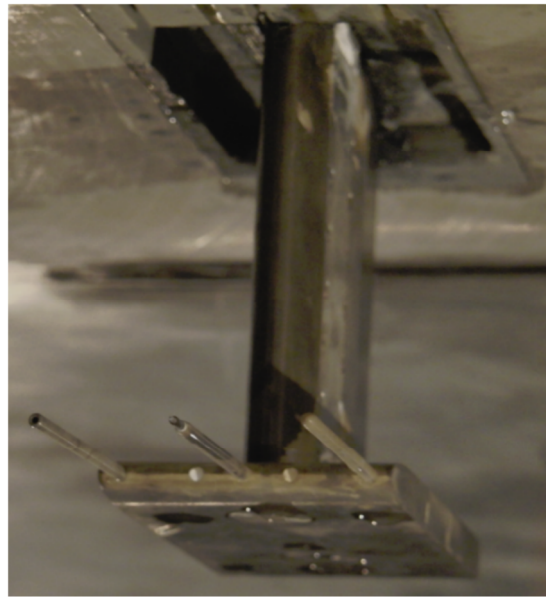


Figure 2.10 – Photo of traverse T1 when the traverse was at  $y \sim 10 \text{ cm}$ . The probes are from the left: Pitot-tube, point electrode, and time-of-flight electrode pair.

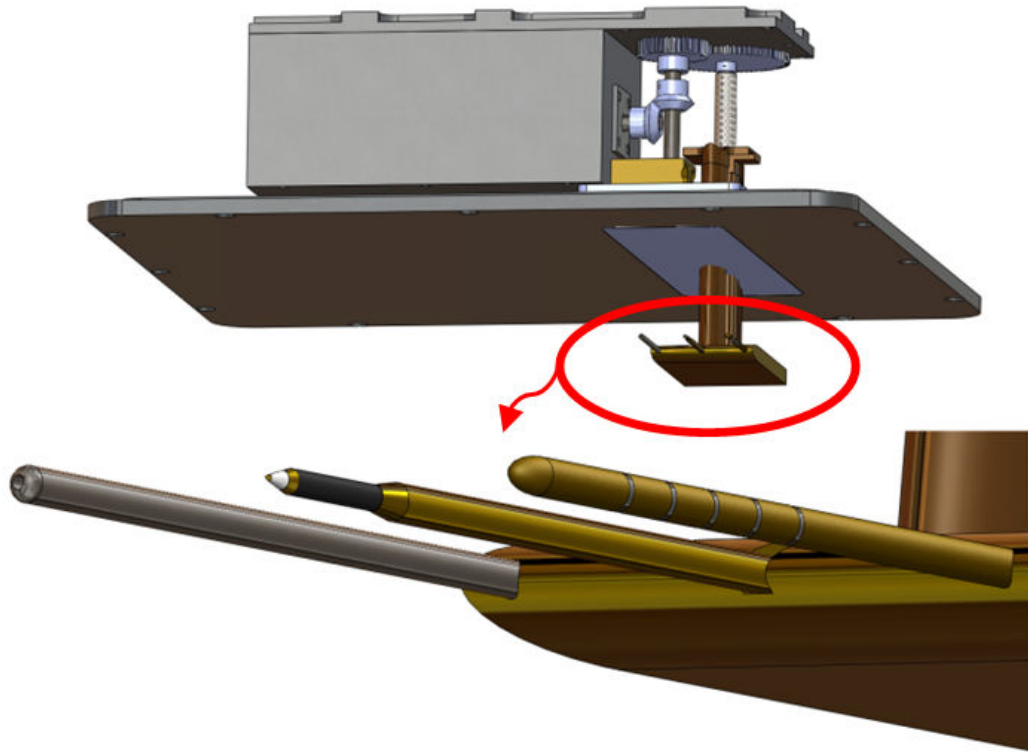


Figure 2.11 – Sketch of the traversing probes. All the probes had a 3.2 mm outer diameter and are shown in the enlarged view of the figure. The probes are from the left: Pitot-tube, point electrode, and time-of-flight electrode pair. The upper sketch shows the mechanism, enclosure, and the plate that mounted into the model.

### 2.7.2 The video system

Most of the experiments were continuously recorded with four synchronized Basler GigE-cameras, and for select conditions still images were taken with a Nikon D40 and Casio EX-F1 cameras. Additionally, for a half a dozen cases high-speed video was recorded using a Phantom V9.0 or Casio EX-F1 camera. The GigE cameras were connected to a Dell T7400 PC *via* two Intel® PRO/1000 GT quad port server adapter PCI-X network cards. Image acquisition was controlled by Norpix's Streampix 4 software. The images were stored on a 16 TB RAID (Redundant Array of Independent Disks), with 16 x 1TB WD RE3 hard drives in a 3U 16-bay PCI-E rack mount chassis,

controlled by a 3WARE 9650SE-16ML controller. The RAID was operated in 1+0 configuration to achieve the maximum data security as well as read/write performance required for high speed video streaming. Two of the Basler piA640-210gm 648x488 210 fps monochrome CCD cameras were equipped with wide angle lenses and mounted on the diagonal bottom chamfer of the LCC. Their field of view covered almost 80% of the cavity, from approximately 0.5 m downstream of the BFS to 1.2 m upstream of the beach's crest (beach flat). One Basler scA750-60gm 752x480 60 fps monochrome CCD camera recorded the cavity starting at the injector and a second identical 60 fps camera recorded the cavity closure on the beach. The images were used in determining the cavity shape, growth rate, rate of collapse, closure oscillation frequency and closure type. Test section and model features together with grid lines spanning the starboard test section wall from the step to the beach and spaced at one inch intervals vertically, were used to determine the cavity shape. From these images, the cavity shape could be resolved to within  $\pm 7$  mm for most cases.

## **2.8 About the experiments**

Both steady and perturbed flow conditions were investigated. The perturbations were generated by periodically oscillating the free-surface-forming gate's flap. These oscillations caused the static pressure in the cavity and streamwise speed of the incoming flow beneath the model to vary by as much as  $\pm 15\%$  and  $\pm 5\%$ , respectively. The geometry in the region of the cavity closure (*i.e.* the beach geometry) was also varied to investigate its effect on the rate of air entrainment and to assess PCDR's sensitivity to the cavity closure geometry. The optimal geometry was used exclusively for the perturbed flow experiments. Cavity gas flux, thickness, frictional loads and cavity pressures were

measured over a range of flow speeds and air injection gas volume fluxes. The minimum air flux to establish and to maintain the cavity was determined for each flow speed under steady conditions. The overall dynamics of perturbed cavities were observed extensively and the minimum air maintenance flux was determined for three different perturbations at three different free stream average speeds. High speed video was used comprehensively to record the unsteady three dimensional cavity closures, and the overall cavity shape oscillations.

We should note that the flow speed beneath the model before and beyond the BFS changed as the cavity was established, as the presence of the cavity, and injection of air itself, changed the losses in the LCC. Therefore, the flow speed at the BFS when the cavity was present was used as the characteristic flow speed. With this definition of the velocity, it corresponded roughly to the flow velocity below a ship hull wherein a cavity could be expected to behave similarly. That is, by considering the velocity at the BFS, for the same uniform free stream velocity and comparable turbulent boundary layer at the BFS on another model (or ship) with a similar cavity, in approximately two-dimensional flows, the cavity would be assumed to behave similarly and independently of the detailed upstream model (or ship) geometry.

Figure 2.12 shows a sketch of the model highlighting the locations depicted in figures 2.13 and 2.14. Figures 2.13 and 2.14 show a typical view into the cavity looking upstream and downstream from mid cavity, respectively. The model surface is clearly separated from the liquid flow and it is obvious that the frictional drag experienced by this surface is greatly reduced. The cavity surface is approximately flat and horizontal



until the closure region, where it curves down and closes typically immediately upstream of the crest of the beach.



Figure 2.12 – Sketch of the step, recess and beach on the model shows in the following two figures.

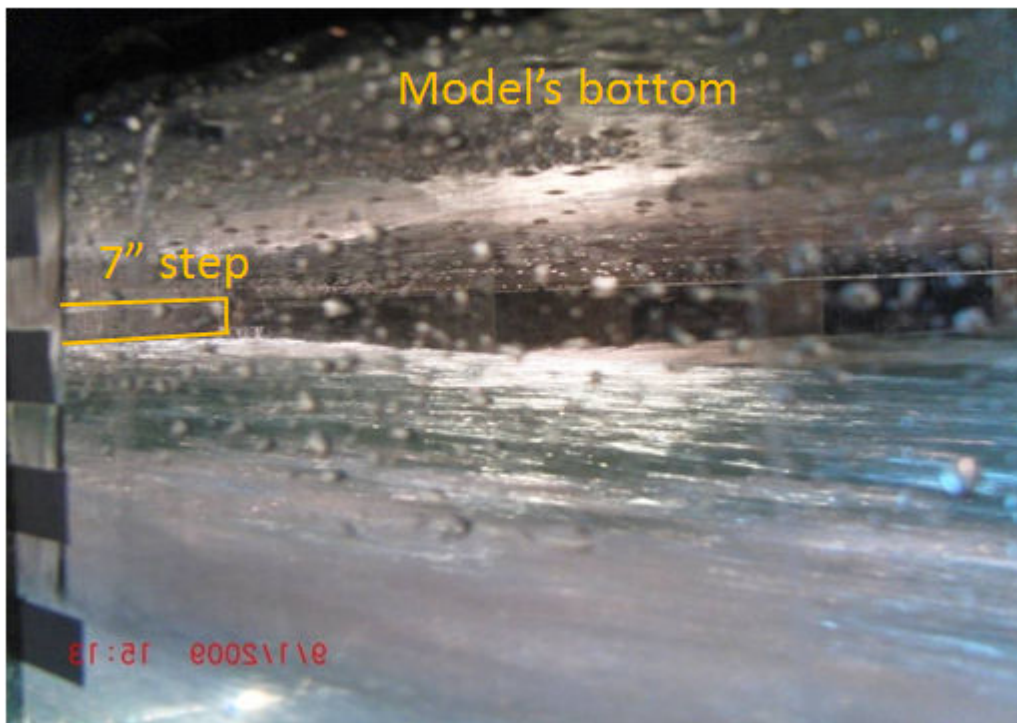


Figure 2.13 – Looking upstream inside the cavity under the model, as seen through a side window at mid cavity. The drops seen in the foreground are on the tunnel window.

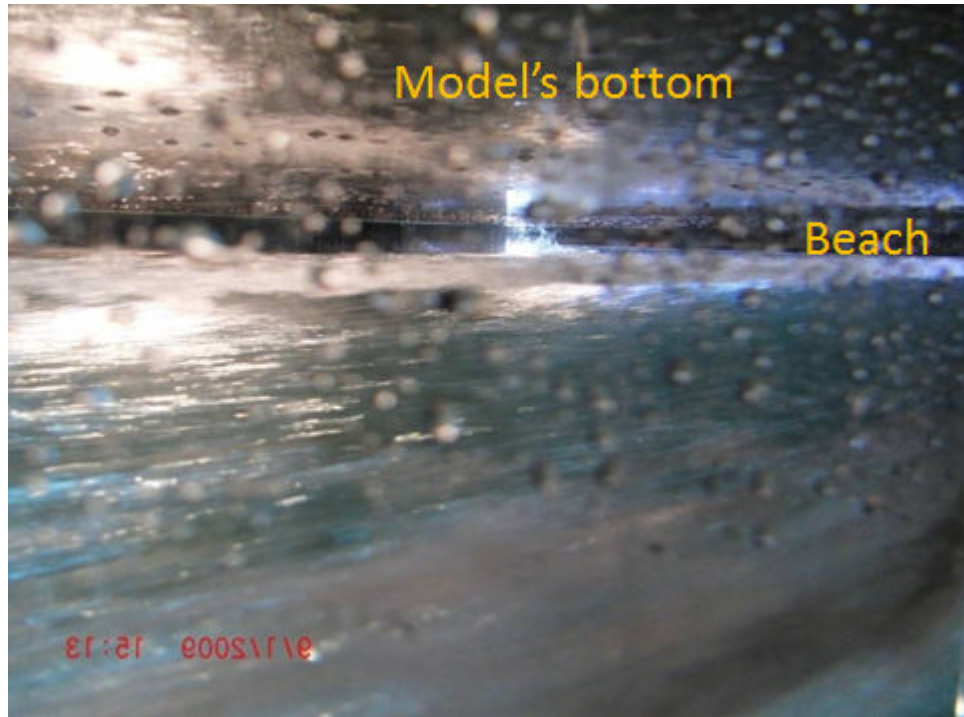


Figure 2.14 – Cavity under the model as seen through a side window at mid cavity. Camera is looking downstream. Again, drops can be seen in the foreground (*i.e.* on the window).

Figure 2.15 (from Lay *et al.* 2010) shows a time series of photos taken as the recirculation zone of the BFS fills with air. After the cavity has filled, its surface has a glassy appearance extending from the step to the beach.

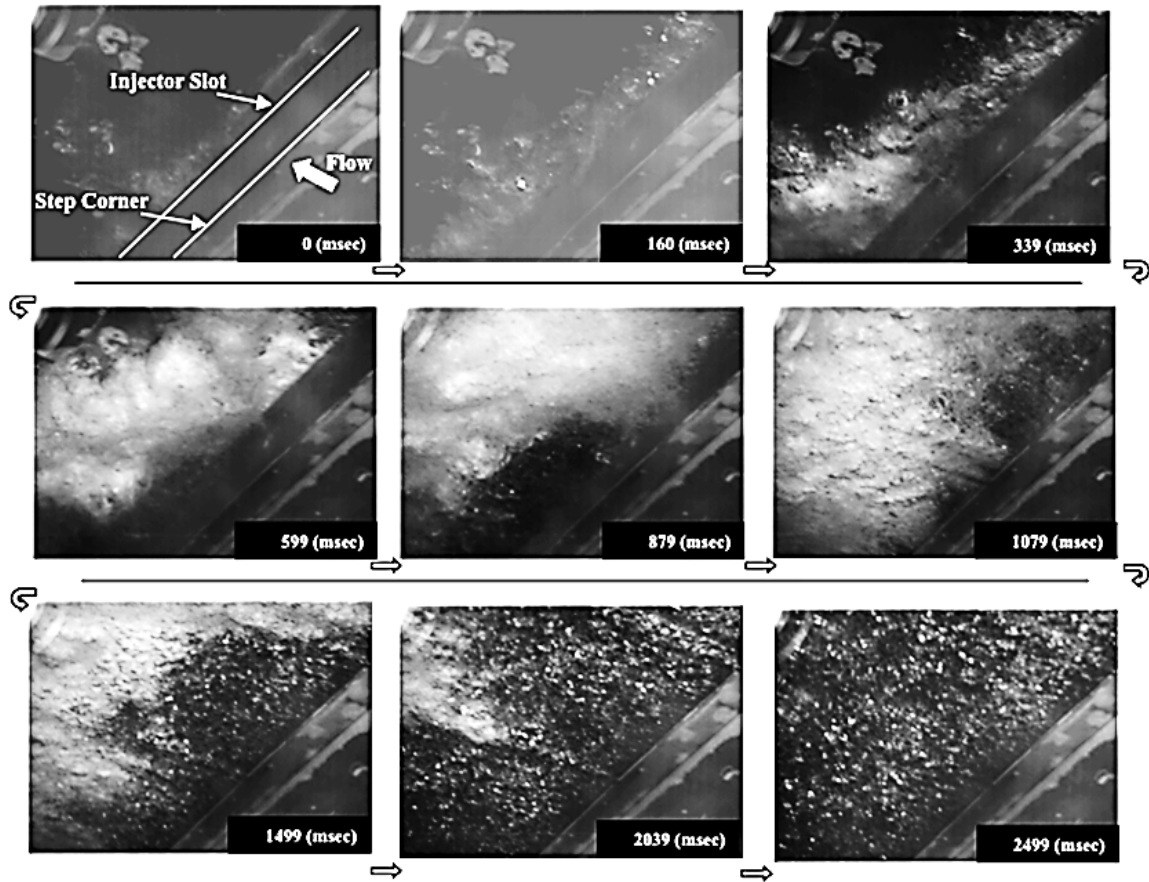


Figure 2.15 – Time series of images showing the cavity initially filling from base of the step to the top. The recirculation area behind the BFS filled first, and then the cavity progressed downstream, when the supplied gas flux was sufficient. Modified version of figure from Lay *et al.* (2010).

The gas flux required to establish and maintain a cavity depends on the density of the gas in the cavity, which is set by pressure inside the cavity (which for a ship would largely be determined by the draft) and temperature, cavity width, flow speed, upstream boundary layer, nominal cavity length (length of recess), and the details of the geometry at the cavity closure. Hence we can expect the required gas flux,  $q$ , to be dependent on at least the  $Fr$ ,  $Re$ , and beach geometry. In this thesis we define our gas flux as

$$q = \frac{Q}{UWH_{step}} \quad (2.3)$$

where  $Q$  is the volume flux of gas needed at cavity pressure and temperature. Thus,  $q$  is the gas volume flow rate non-dimensionalized by the free stream flow speed at the point of separation, the cavity cross-section width (span), and the height of the backward facing step. This equation implicitly includes the compressibility of an ideal gas *via* the definition of  $Q$ , and therefore the required value of  $q$  is already includes the effect of the cavity pressure on gas volume.

Besides being dependent on the draft,  $D$ , of the ship, the cavity pressure also depends on the vessel's speed and hull shape upstream of the cavity. If the pressure were to drop below vapor pressure, *i.e.* negative cavitation number, no air injection would be required as a natural cavity would be formed. The cavitation number here is defined as

$$\sigma = \frac{2(p_c - p_{vapor})}{\rho_w U^2} \quad (2.4)$$

This is a crucial parameter for natural cavitation and if we were near a natural cavitation region, it should be used to represent the cavity pressure,  $p_c$ . However, the pressure was considered explicitly, rather than in terms of the cavitation number, because for slow

moving deep draft ships, the cavity pressure is orders of magnitude larger than water's vapor pressure. Hence, for consideration in practical terms, it is clearer to explicitly include cavity pressure,  $p_c$ , in units of pressure. For a relatively slow moving ship  $p_c = \rho_w g D$ . The most significant effect of pressure (when  $p_c \gg p_{\text{vapor}}$ ) is to change the volume occupied by a given mass of gas, and this effect was incorporated into the definition of  $q$ .

The temperature of the gas in the cavity is assumed to approach the water temperature, which in these experiments remained steady at 25 °C. Therefore, it was assumed that the air and water viscosity experienced negligible variation. Thus, for a given flow speed and geometry the effect of *variation* in the Reynolds number was also assumed negligible for these experiments, but is believed to have a large effect when comparing results from various model scales to real world applications. A potential scaling with  $Re$ ,  $Fr$ , and the Weber,  $We$ , numbers is discussed in Chapter 3.

## **2.9 Results – steady flow**

The model's cavity length was chosen based on maximum model size fitting the test section and previous experience (Lay *et al.* 2010). The water depth,  $H$ , below the backward facing step was 1.23 m, which makes this flow situation somewhat different than the deep-water flow that ships usually encounter, as the flow is supercritical (*i.e.*  $Fr$  based on flow depth larger than unity). At lower than design speeds, the cavity did not reach the beach easily and closed on the model surface at large angles leading to excessive air loss from the cavity. As the gas flux was increased again for  $Fr$  lower than design speed, the cavity pressure increased slightly and the cavity grew in length, but the gas entrainment rate increased beyond the gas supply's capacity before the cavity reached the beach. For Froude number based on the cavity length and flow speed at the BFS,  $Fr =$

$U/(gL_c)^{1/2}$ , above 0.55 a cavity was established with ease and the minimum gas fluxes required to establish and maintain were measured. At flow speeds above  $\sim 7$  m/s with a free surface, the flow in the LCC became somewhat unstable, and the free surface (that closed in the diffuser) may have been moving, and began entraining excessive amounts of air. At these higher speeds, the air flux requirements increased in part due to flow speed, which lead to the cavity increasingly overshooting the beach, but at the highest speeds perhaps unsteadiness may also have contributed. Some of the unsteadiness could be contributed to the accumulation of air upstream of the gate and likely also at the highest point of the LCC's lower leg, at the highest test speeds. This air also had the tendency to randomly or periodically be expelled, causing unsteadiness. Besides potential perturbations from free stream conditions, we note that the Froude number based on flow depth under the cavity was such that an oscillating hydraulic jump may have been the flow's desired state. However, even in the absence of the cavity, the LCC performance with a free surface limits the highest flow speed of the experiments.

Some measured time traces of a cavity being established were shown and discussed in Mäkiharju *et al.* (2010). To find the minimum establishment flux, the gas flux was increased gradually until the cavity reached the beach. The cavity was considered established when the gas flux could be reduced without a decrease in the cavity length. This only occurred when the cavity closed on the beach. Once a stable cavity was established and the minimum establishment gas flux determined, the gas supply was terminated. Once all the air had left the cavity and the flow was at steady state, the minimum establishment gas flux was applied again to reconfirm that it would be sufficient to establish the cavity. Once the cavity was re-established and stable, so that

no measurable mean quantity was changing, the search for the minimum cavity maintenance flux was initiated. The gas flux was slowly decreased in steps. Once the cavity began retreating upstream, the previously used gas flux was designated as the minimum maintenance flux,  $q_{main}$ . Experiments where the cavity was maintained for tens of minutes were conducted. The results indicate that once a stable cavity was formed it remained, barring a change in gas flux or significant flow perturbations.

Using these procedures, the minimum establishment and maintenance gas fluxes were found for different flow speeds. The range of flow speeds was limited by the minimum and maximum  $Fr$  where our 0.490 kg/s gas supply could fill a cavity reaching the beach, and by the LCC's performance when operated with a free surface.

The minimum gas flux,  $q$ , required to establish and maintain the cavity was a function of the Froude number. However, for longer cavities it might be possible to have multiple operating regions, if a stable multi-wave cavity can be established.

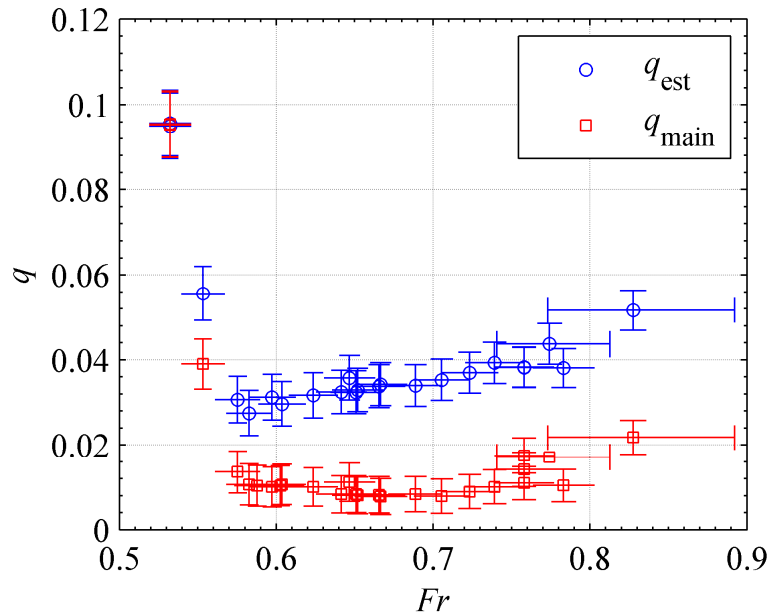


Figure 2.16 – Air flux requirements for establishment and maintenance are indicated by the blue circles and red squares, respectively. The large variation in gas flux for  $Fr > 0.75$  may be due to both unsteady cavity flow and variation of free stream conditions.

Figure 2.16 shows the minimum air fluxes,  $q_{est}$  and  $q_{main}$ , at the optimal beach position, P1. When the cavity reached the beach, air entrainment from the cavity closure decreased significantly. This is evident from the decrease in the amount of gas required to maintain the cavity. The gas flux required to reach the beach was influenced by the flow speed, cavity pressure, nominal cavity length, and beach geometry. (For a more streamlined beach front geometry,  $q_{est}$  would be expected to decrease, but remain larger than  $q_{main}$ .) The results suggest that for a single partial wave cavity, the gas flux requirements are lowest within a limited Froude number range, and increase disproportionately with flow speed outside this range.



### 2.9.1 About the cavity surface

When a stable cavity was present, the cavity interface had ripples superimposed onto a two dimensional wavy surface, as can be seen in figures 2.13, 2.14 and 2.15. These ripples were observed both visually and in the readings from the traversing probes. The height of the surface can be determined from video and the traverses' electrical impedance measurements for local void fraction. Figure 2.17 shows the time averaged void fraction profiles and compares the average interface location to that obtained from 60 fps videos, and it can be seen that the agreement is satisfactory.

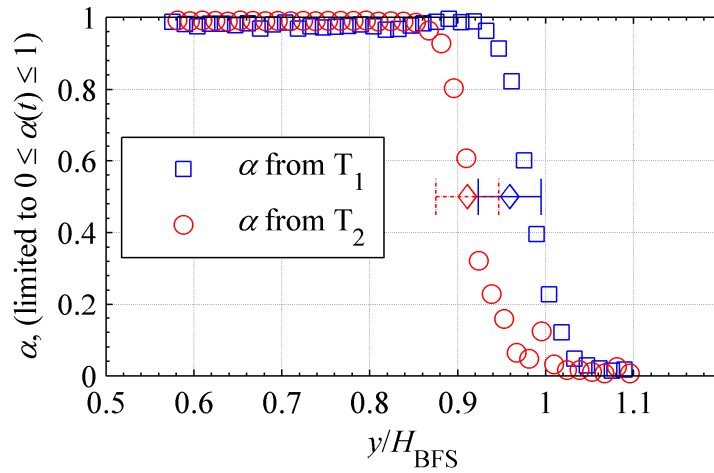


Figure 2.17 – Time averaged void fraction profiles shown by the squares and circles from profiles of traverses  $T_1$  and  $T_2$ , respectively, compared to the average local cavity thicknesses measured from the video (diamonds). The horizontal error bars show the uncertainty,  $\pm 7$  mm, of the video data.

It is important to note that despite the presence of ripples, no major loss of gas from the interface was observed. This suggests that all significant air loss occurs at the cavity closure, details of which then set the required minimum gas flux. The perturbations present at the cavity interface may, however, affect the dynamics of and hence the air loss from the closure.

### 2.9.2 Cavity closure

Air was lost mainly from the cavity closure apparently *via* re-entrant jets or by wave "pinch-off" that removed air-chunks from the cavity as sketched in figure 2.4. Figure 2.18 shows part of the cavity closure. The closure exhibits similarities to natural cavitation (cavity formed due to low pressure), where re-entrant jets are one of the important mechanisms leading to shedding of clouds of gas from the cavity (Callenaere *et al.*, 2001), and interestingly it was observed by Lay *et al.* (2010) that the gas cloud shedding from the closure was in the Strouhal number range encountered in natural cavitation.

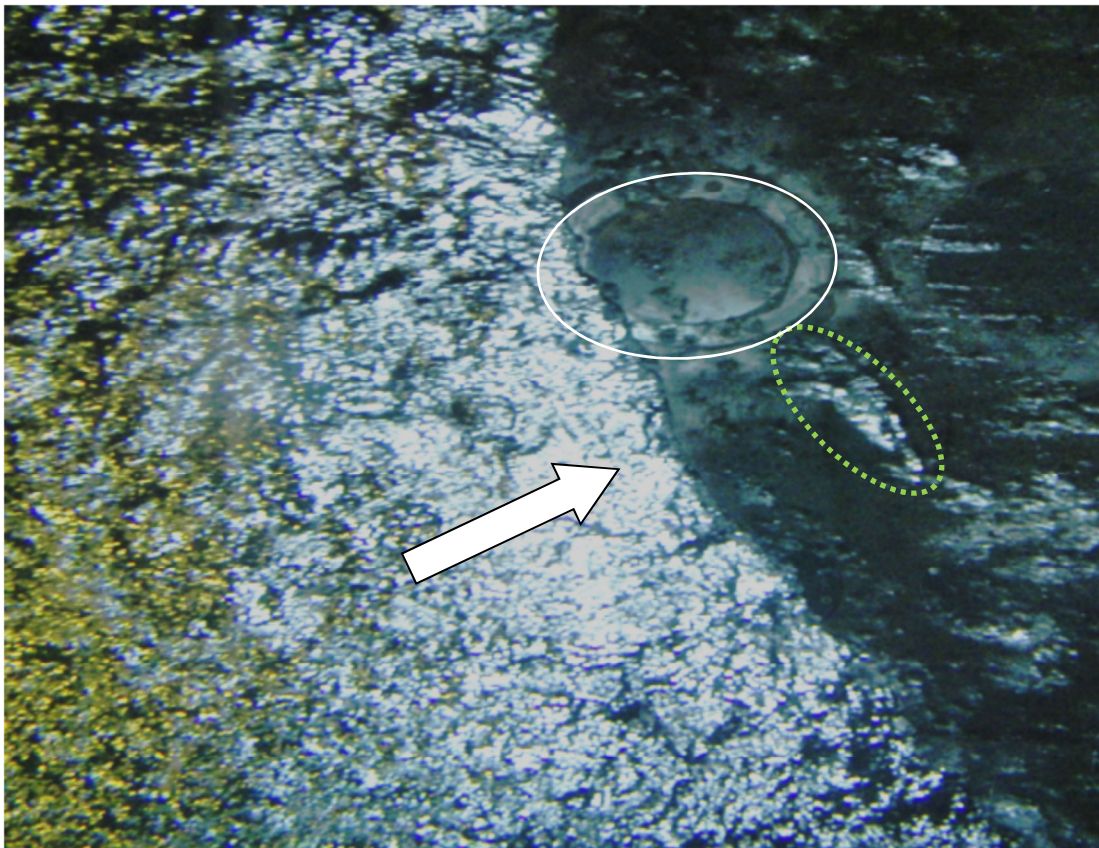


Figure 2.18 – The cavity closure as seen from below. The round disk immediately to the right of the cavity closure that is delineated with a white circle is the fourth force balance. The green dashed curve surrounds a small cloud being shed from the cavity. The white arrow indicates the flow direction.

### 2.9.3 Effect of beach geometry

The streamwise and spanwise angle of the beach could be variable, as well as the overall beach height. The geometry was fixed during the no-flow condition when the tunnel was mostly drained, enabling the removal of sealing plates on the windows which supported the beach and adjustment of the beach from the outside the tunnel. The beach geometries tested are listed in table 2.3.

Table 2.3 – The six beach positions tested.

	<b>Beach height</b> $H_B$ [cm]	<b>Streamwise</b> <b>angle, <math>\beta_B</math> [deg]</b>	<b>Spanwise tilt</b> <b>[deg]</b>
P1	0.09	1.7	0.0
P2	0.14	1.7	0.0
P3	0.115	1.7	0.0
P4	0.09	1.1	0.0
P5	0.09	1.7	1.4
P6	0.09	1.7	0.5

Stable cavities were achieved for all but position P5, in which the spanwise tilt was 1.4 degrees, bringing one side of the vertical upstream face of the beach 12.0 cm below the bottom of the cavity, while the other side was at 4.5 cm. This meant that the front edge on one side was lower than the crest of the beach (beach flat), which was 9.0 cm on the high side. Consequently, when trying to establish a cavity by filling the recess, the cavity on the low side terminated into the vertical face, while on the other side, instead of the cavity closing on the beach, air flowed freely from the cavity. If the upstream slope was free of the abrupt vertical face, the outcome might be more similar with that obtained with P6, where a 0.5 degree spanwise slope simply led to an angled

closure line on the beach and a slight increase in the required maintenance flux. A comparison of the establishment and maintenance fluxes for various beach positions is given in figure 2.19.

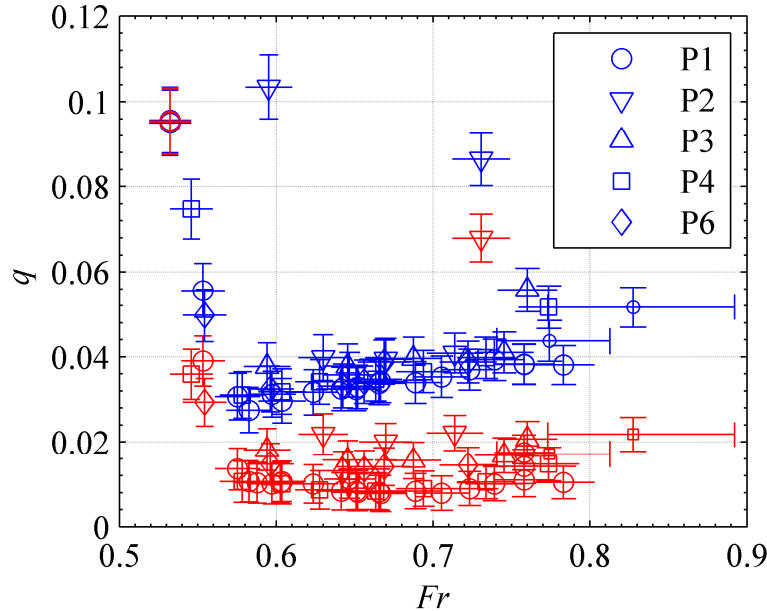


Figure 2.19 – Air flux requirements for different beach positions. The minimum establishment and maintenance gas flux required is indicated by the blue and red symbols, respectively.

## 2.10 Results – unsteady flow

To apply PCDR on ships, one must understand under what conditions flow perturbations of a given nature and magnitude lead to stable periodic oscillations of the cavity *versus* when they lead to increasing oscillation amplitude and eventual loss of the cavity. A cavity being maintained at  $q_{main}$  was found to tolerate only small external perturbations, whereas a cavity supplied with an excess gas flux was more robust and could tolerate larger perturbations. The perturbations were generated in a controlled way

by the oscillation's of the gate's flap. It was found that the larger the perturbations, the larger the required gas flux to maintain the cavity. However, for all the perturbations tested, the required perturbation-tolerant maintenance gas flux,  $q_{pert}$ , was always less than the minimum gas flux required to establish the cavity in steady flow at same  $Fr$ .

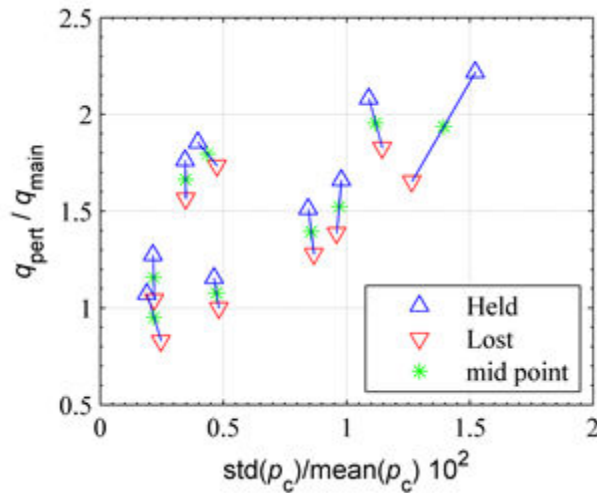


Figure 2.20 – Excess air requirements versus a measure of perturbation amplitude (standard deviation of the cavity pressure divided by its mean). Given the finite test time, the gas requirements were found within a  $\sim 20\%$  excess gas flux range. The true minimum flux lies somewhere between the last point where the cavity held and the first flux where the cavity was lost. The legend names these points accordingly as “Held” and “Lost”. In comparison, the ratio of required establishment to maintenance flux in steady flow was typically around 4.

Figure 2.20 shows how the air requirements increased for the perturbed flow. Given the time constraints on the experiments, as we only had a few days at the LCC to experiment with the unsteady conditions, the exact gas flux below which the perturbed cavity is lost was not found. Rather figure 2.20 presents the smallest flux which still maintained the cavity and the highest flux at which the cavity was lost. These are plotted against the normalized cavity pressure fluctuations, which in turn correspond also to the percentage by which the gas is compressed. However, as the mechanism of cavity loss during flow

perturbations is quite complex, no general relationship for the air requirement and the amplitude of the perturbation is implied. It should also be noted that the amplitude of the gate's flap's motion, and therefore the amplitude of the perturbations, could not be controlled independently from the perturbation frequency. However, we can conclude that by supplying an excess gas flux, a cavity can tolerate perturbations. The larger the amplitude of the perturbation, the larger the excess flux required within the conditions tested.

While the excess gas flux for a given perturbation is of great interest, it also can be useful to look in detail at the cavity behavior during the oscillations. Figure 2.21 shows typical time traces obtained during the strongest flow perturbations generated by periodic gate-flap oscillation, where the cavity still held at a gas flux of  $q \sim 0.025$ , which was approximately twice the gas flux required under steady conditions at this Froude number. With everything else held constant other than decreasing the excess flux to  $\sim 1.6$  times the required minimum maintenance flux for steady flow,  $q_{main}$ , the cavity was lost as seen in figure 2.22.

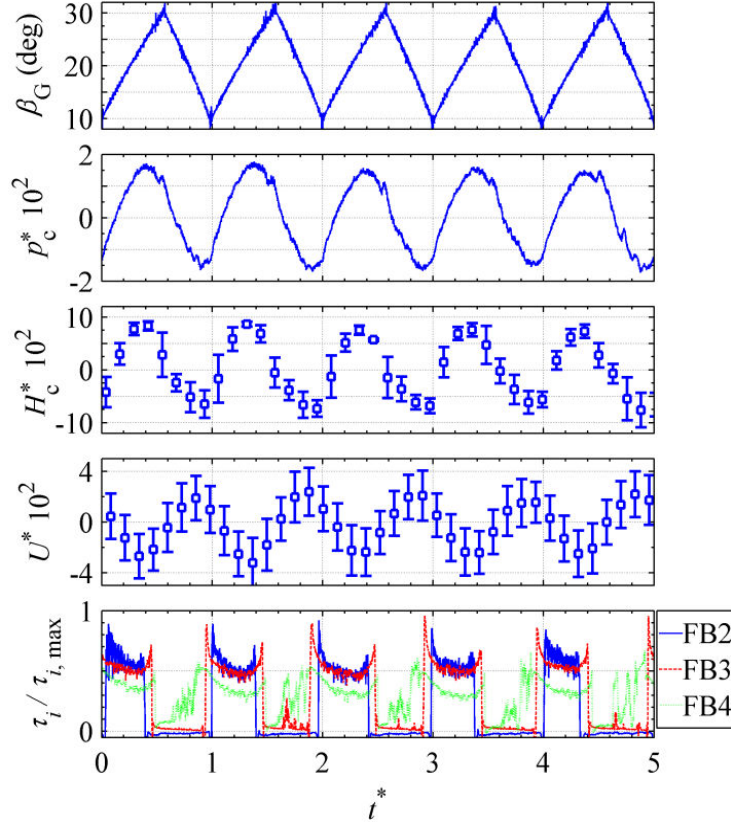


Figure 2.21 – Time traces of the experiment with the oscillating gate where the cavity was not lost. The errorbars shown around the local mean values represent one standard deviation. From the bottom figure the cavity closure can clearly be seen to move upstream of force balance FB4, then past FB3, and finally past FB2 prior to reversing a brief moment later. For the case shown:  $\overline{H}_c \sim 17.0$  cm,  $\overline{p}_c \sim 6400$  Pa,  $\overline{U} = 5.46$  m/s,  $Fr = 0.57$ ,  $t_{cycle} = 15.7$  seconds and  $q \sim 0.025$ . The non-dimensional values (\* superscripts) are defined in the text.

Here the dimensionless cavity pressure,  $p_c^* = (p_c(t) - \overline{p}_c)/(\overline{p}_c)$ , is related to the expected change in cavity volume due to pressure oscillations and the velocity fluctuations are normalized by the mean velocity  $U^* = (Fr(t) - \overline{Fr})/(\overline{Fr})$ . Mean quantities are denoted by an overbar. The cavity height fluctuations based on the hydrostatic pressure,  $H_c^* = (H_c(t) - \overline{H}_c)/\overline{H}_c$ , at mid cavity had a maximum amplitude of  $\sim 1.3$  cm, which is  $\sim 7.5\%$  of the cavity depth at the measurement location. In addition the



time scale,  $t^* = (t - t_0)/t_{cycle}$ , was normalized with the period of the oscillations,  $t_{cycle}$ , rather than with the convective time scale,  $t_{convective} = L_c/U$  ( $\sim 1.5$  sec).

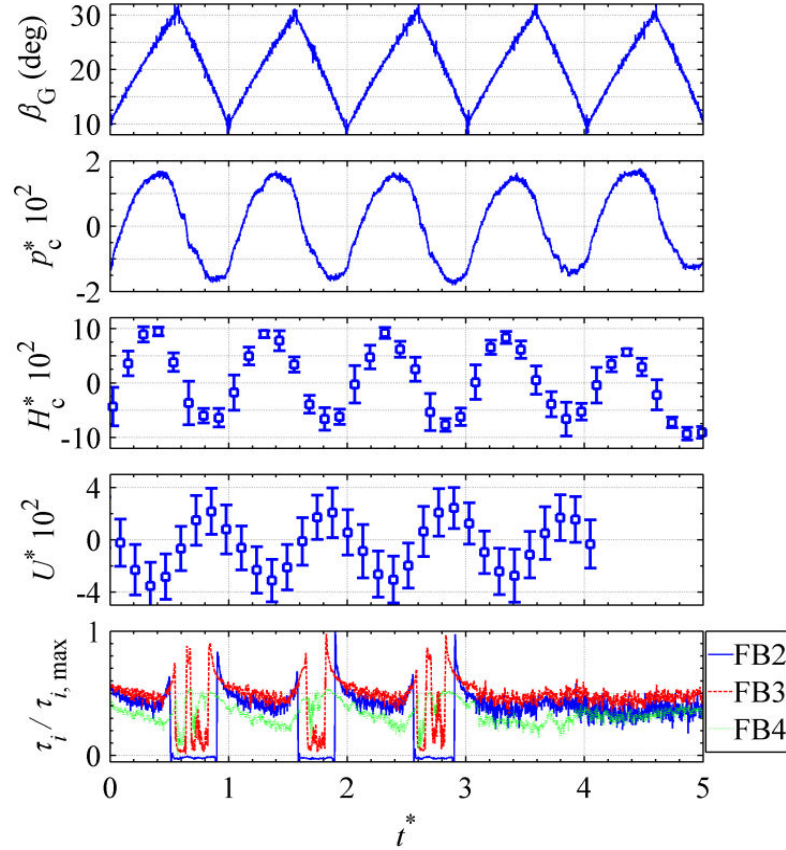


Figure 2.22 – Time traces of an unsteady case where the cavity was lost. In these time traces the force balance readings clearly indicate the loss. (The plot of  $U^*$  ends prematurely due to the limited recording time of the LDV system.) For the case shown:  $\overline{H_c} \sim 17.0$  cm,  $\overline{p_c} \sim 6400$  Pa,  $\overline{U} = 5.46$  m/s,  $Fr = 0.57$ ,  $t_{cycle} = 15.7$  seconds  $q \sim 0.022$ .

Several mechanisms by which flow perturbations lead to cavity loss could be suggested from the observations:

1. Large quantities of air can be lost when the cavity overshoots the beach.

The cavity returning upstream has a reduced volume and will be lost unless additional gas is supplied.



2. A cavity retreating upstream can "run out of beach" causing it to terminate on the vertical upstream face of the beach. This leads to the loss of large quantities of air, and to further retreat of the cavity. (The beach length on the test model was limited by the mechanical design of the adjustable beach. A beach designed to be stationary can be designed without this same limitation, *i.e.* without an abrupt vertical section.)
3. Increased cavity pressure causes the volume of gas to decrease. If the decreased volume is comparable to the volume of a cavity that has not yet been established, the compressed cavity will be lost unless additional gas is supplied.

Given the coupled nature of these suggested mechanisms, two or more could be expected to exert influence under any given condition, and they may be stages of the same cavity loss, rather than separate mechanisms.

In figure 2.23, we see a presentation of the cavity closure position and the gate angle as a function of time non-dimensionalized by the flap oscillation frequency. We can observe a phase lag of roughly 0.15 between the flap motion and closure position. The cavity position is based on analysis of footage from the downstream 60 fps Basler camera viewing the beach from beneath at an oblique angle. The simplified typical shape of the closure's edge during the distinguishable six stages of oscillations, that can be seen in figure 2.23, are described in figures 2.25 to 2.30. We can see that at times the closure is strongly three dimensional for the perturbed flow.

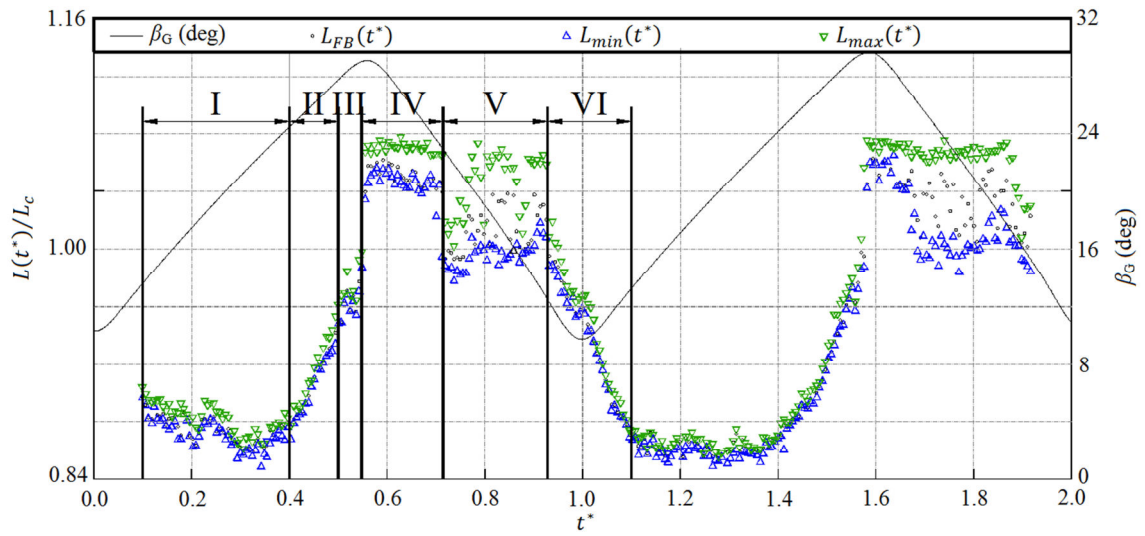


Figure 2.23 – Cavity closure position oscillations and the low-pass filtered gate flap angle.  $Fr = 0.57$ .  $L(t^*)$  notes the instantaneous closure position, which was visible within the camera's field of view. Subscripts min and max define the minimum and maximum closure position within the field of view. Subscript FB refers to the closure position at the spanwise coordinate of the force balances. (Figure by Mr. Andrew Wiggins. Reproduced with permission.)



Figure 2.24 – Approximate area of the beach where shapes sketched in figures 2.25 to 2.30 occur.

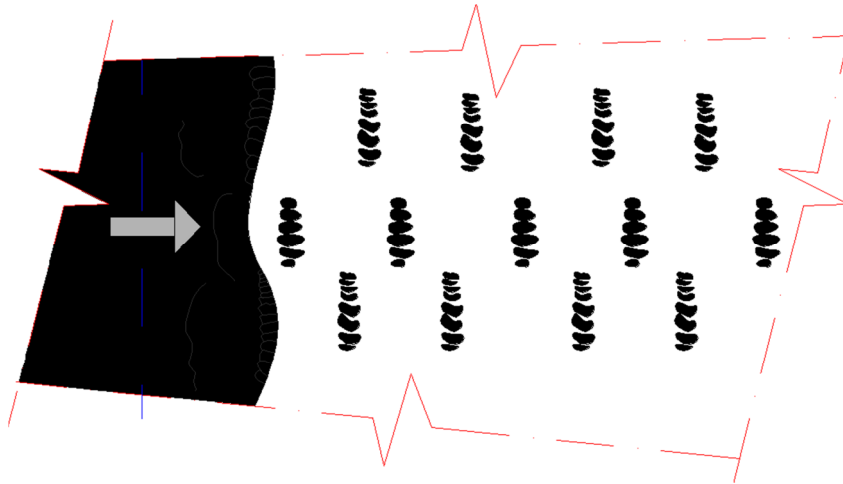


Figure 2.25 – Stage I, closure near upstream end of the beach. Upstream of the cavity closure  $\sim 20$  cm from the beach's leading edge. Closure begins to exhibit violent churning and three-dimensional disturbances. Ridges of wave patterns on the free surface are visible. The thickness of the closure edge is greater than for other stages. Air loss occurs through staggered and fairly regular cloud shedding. The spanwise correlation length of the clouds is fairly short ( $< 10$ cm) and shedding occurs at  $\sim 30$ Hz. (Figure by Mr. Andrew Wiggins. Reproduced with permission.)

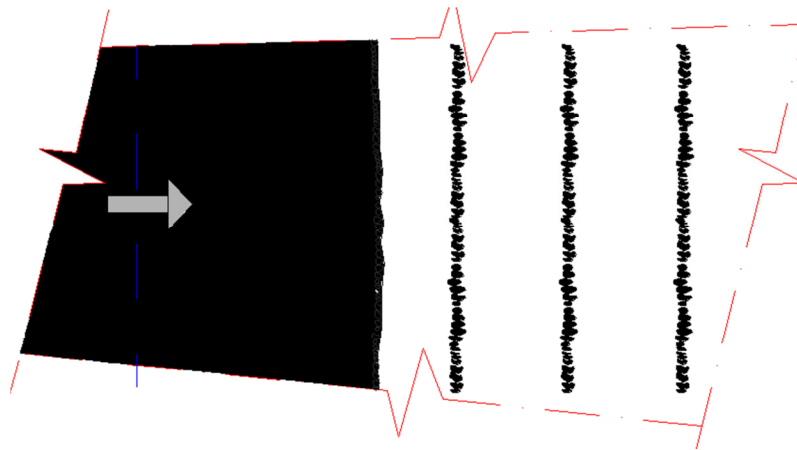


Figure 2.26 – Stage II, uniform growth. The cavity grows with spanwise uniformity. The trailing edge of the cavity has become thinner and assumed a glassy scalloped appearance. The volume of air loss has noticeably decreased. The clouds shed are long in the spanwise direction. (Figure by Mr. Andrew Wiggins. Reproduced with permission.)

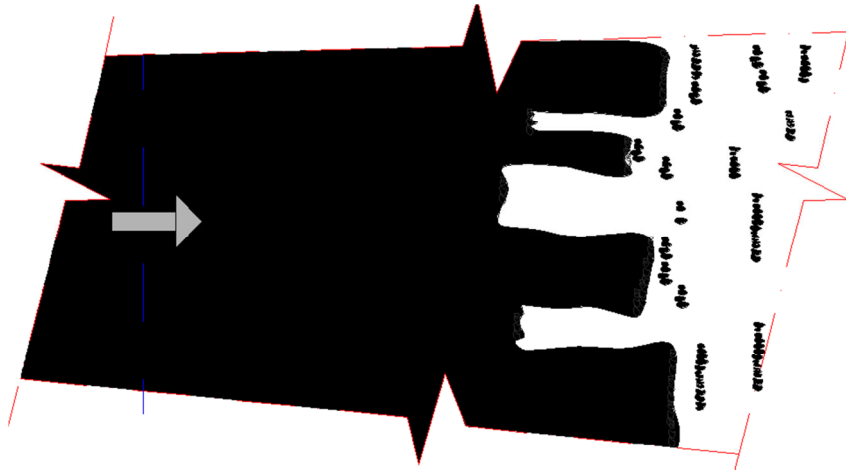


Figure 2.27 – Stage III, rapid growth. The cavity approaches the beach flat and the edge continues to thin. Long spanwise narrow “fingers” and other spanwise non-uniformities appear. The fingers are spaced approximately 16 cm apart and extend to 50 cm in length. This stage is short lived. (Figure by Mr. Andrew Wiggins. Reproduced with permission.)



Figure 2.28 – Stage IV, maximum cavity length. The cavity now extends almost the full length of the beach flat. The cavity edge shape fluctuates rapidly. There is erratic shedding of wide, but short, clouds. (Figure by Mr. Andrew Wiggins. Reproduced with permission.)



Figure 2.29 – Stage V, beginning of the retreat. Necking of the fully extended closure region initiates near the sidewall resulting in substantial variations in closure position. (Figure by Mr. Andrew Wiggins. Reproduced with permission.)

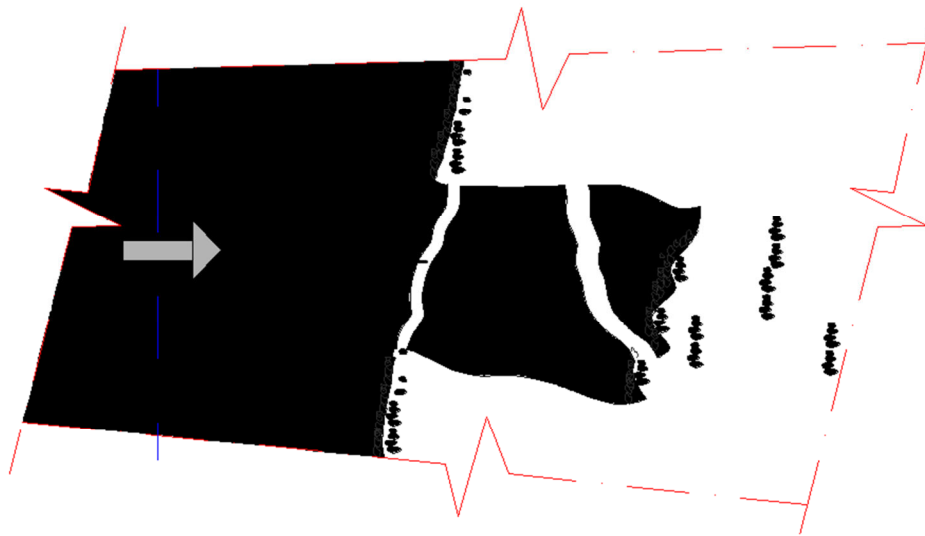


Figure 2.30 – Stage VI, rapid retreat. The extended part of the closure region detaches and divides. The cavity edge retreats to the position of Stage I with relative spanwise uniformity. (Figure by Mr. Andrew Wiggins. Reproduced with permission.)

In the presence of global flow perturbations, the slowly oscillating cavity closure often appeared similar to that observed for steady cavities. Limitations of the gate's piston's hydraulic system restricted the range of frequencies that could be imposed on the flow. Thus the oscillations had long time scales, compared to the convective time scale and the closure's cloud shedding time scale. The time scale of small cloud shedding during Stage I at the closure was approximately 0.03 sec, with a Strouhal (defined as the shedding frequency multiplied by the shed cavity length, and divided by the flow speed) number around 0.55, while the global perturbations were imposed at period  $O(10\text{sec})$ . As far as the closure is concerned the flow could perhaps be considered quasi-steady during the oscillations. However, the overall time scales for filling and retreating of a cavity are minutes, and in that sense if a cavity lost a significant amount of air during an oscillation the overall flow would not have been quasi steady for all conditions, and as seen in figure 2.22 the cavity sometimes endured multiple oscillations shrinking every time and eventually having insufficient gas to sustain itself as the closure region retreats upstream of the beach's edge.

## 2.11 Comparison to another air lubrication technique

To put the achievable drag reduction *versus* required gas flux in context, a comparison to another air lubrication technique will be instructional. Here we present a brief comparison to air layer drag reduction. When comparing ALDR and PCDR one should note that the frictional drag reduction on a surface covered by air for ALDR is defined to be >80% (Elbing *et al.* 2008), while for PCDR Lay *et al.* (2010) reported reduction in excess of 95%. However, PCDR requires a recess on the bottom of the hull, which, if the cavity is lost will likely introduce a drag penalty. Also, the closure region on the cavity may modify the hull's form drag adversely, even in the presence of the cavity. However, if a cavity is intentionally drained of gas, the increased form drag might even be beneficial if the goal is to stop the ship faster.

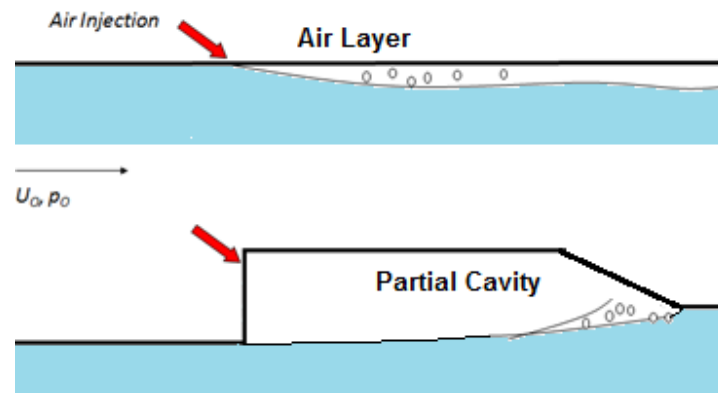


Figure 2.31 – A conceptual comparison of ALDR and PCDR. Top: The air layer is thin, and can be of the order of the boundary layer thickness. All gas is carried downstream, and the layer is established and lost at the convective time scale. Bottom: The partial cavity requires a recess with a streamlined closure surface. Typical time scale to fill or empty the cavity of gas is orders of magnitude larger than the flow's convective time scale.

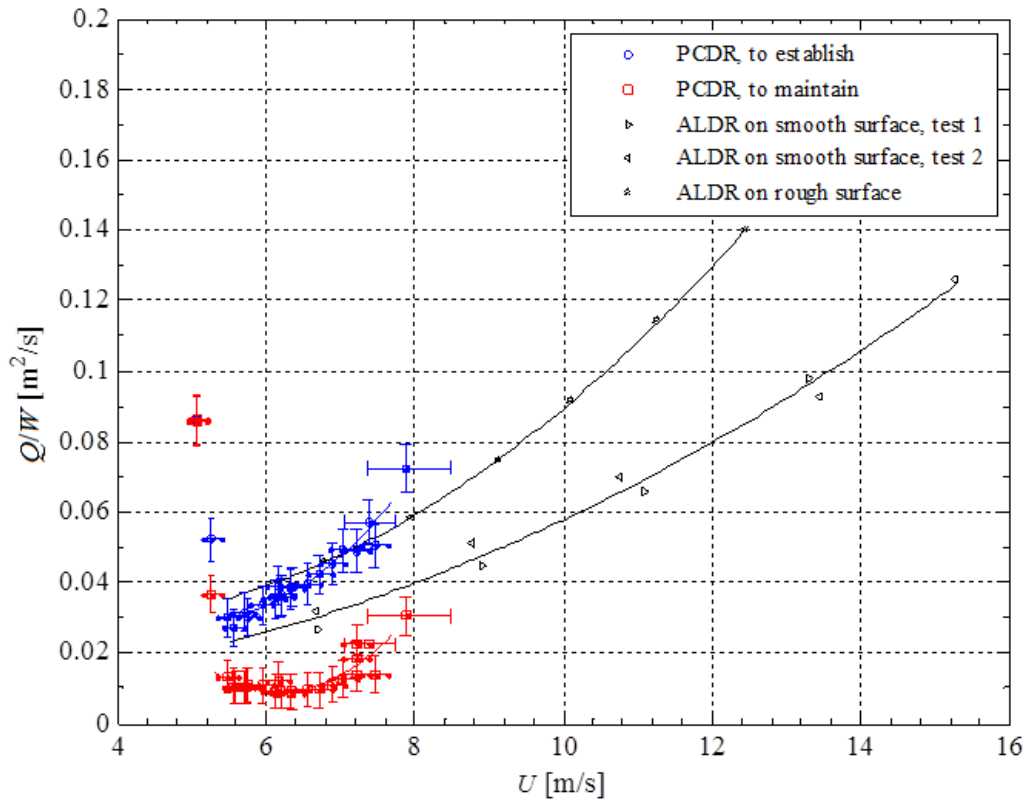


Figure 2.32 – Comparison of the air requirements per unit span for PCDR and ALDR. The solid lines represent best fits to the data (for PCDR from 5.48 to 7.46 m/s, for ALDR from 6.79 to 12.45 and 15.26 m/s for smooth and rough surfaces, respectively). For PCDR the large variation in gas flux for  $U > 7.2$  m/s may be due to both unsteady cavity flow and variation of freestream conditions.

A conceptual comparison of ALDR and PCDR is shown in figure 2.31, and the air requirements, with PCDR beach position P1, are compared in figure 2.32.

In its relatively narrower, optimal, range for the speed, PCDR seems to be more economical than ALDR, but outside the ideal speed range PCDR may be more costly or perhaps even unattainable. We also point out that retrofitting an old ship for ALDR would require fewer hull modifications than PCDR. Hence, PCDR would likely be better suited for new ships if they are to be operated mostly within the cavity’s design speed range, or perhaps ranges, if a multi-wave cavity can be shown to be practical.



## 2.12 Discussion

PCDR experiments with detailed measurements for Reynolds number to 80 million exhibiting the establishment and maintenance of steady, and unsteady partial cavities were completed. In these experiments the cavity was found to have an approximately 2 m/s optimal operating speed range. At very low speeds the cavity could not be established with the air supply available while at the highest test speeds the global flow conditions deteriorated to the point where a velocity measurement from the LDV was barely possible, and there was excessive variation in the results included in the figures showing the required gas fluxes. It remains to be seen whether these limitations are specific to these experiments. If there is a narrow operating speed range, dependent likely on the cavity length matching the length of recess, we hypothesize that a cavity accommodating multiple waves could have multiple ideal operating ranges.

These experiments showed that a cavity can be maintained even under globally perturbed flow conditions that mimic the effect of ambient waves. The cavity tolerated global flow perturbations when the gas flux was greater than the minimum required to maintain it, with larger perturbations requiring larger excess gas flux to maintain the cavity. However, for all the perturbed conditions tested, the required flux was always less than the gas flux required to establish the cavity under steady conditions at the mean test speed. In the presence of global perturbations, the closure was at times highly three-dimensional. The time scale of the small scale cloud shedding was found to be one to two orders of magnitude less than the time scale of the global perturbations.

An active flow control system could potentially improve the cavity's stability under perturbed flow conditions and help minimize the required gas flux. One can note from figure 2.22 that under some conditions the cavity loss is a slow process when

compared to the convective time scale. It was observed that if the gas flux is increased immediately upon cavity retreat, the cavity could be rapidly re-stabilized before it retreated far from the beach. Hence, active flow control combined with local upstream measurements, and even potentially scanning radar to detect incoming waves might prevent some cavity loss situations.

## 2.13 References for Chapter 2

Arndt, R.E.A, Hambleton, W.T., Kawakami, E. and Amromin E.L. "Creation and Maintenance of Cavities Under Horizontal Surfaces in Steady and Gust Flows" *Journal of Fluids Engineering*, vol. 131, 2009

Amromin, E. and Minize, I. "Partial Cavitation as Drag Reduction Technique and Problem of Active Flow Control" *Marine Technology*, Vol. 40, No. 3, pp. 181-188. 2003

Amromin, E., Kopriva, J., Arndt, R. E. A., and Wosnik, M. "Hydrofoil Drag Reduction by Partial Cavitation." *Journal of Fluids Engineering*, 128, pp. 931-936. 2006

Butuzov AA. "Artificial cavitation flow behind a slender wedge on the lower surface of a horizontal wall." *Fluid Dyn.* 3. pp.56–58. 1967

Butuzov, A., Sverchkov, A., Poustoshny, A. and Chalov, S., "State of art in investigations and development for the ship on the air cavities." *International Workshop on Ship Hydrodynamics*, China, pp. 1-14. 1999

Callenaere, M., Franc, J.-P., Michel, J.-M. and Riondet, M., 2001. "The cavitation instability induced by the development of a re-entrant jet." *Journal of Fluid Mechanics*, 444, pp. 223-256. 2001

Ceccio, S.L. and George D. L. "A Review of Electrical Impedance Techniques for the Measurement of Multiphase Flows" *Journal of Fluids Engineering*, vol. 118 Issue 2, pp. 391-399. 1996

Ceccio, S.L. "Friction Drag Reduction of External Flows with Bubble and Gas Injection," *Annual Review of Fluid Mechanics*, Vol. 42, pp. 183-203. 2010

Ceccio, S.L., Perlin, M. and Elbing, B.R., "A cost-benefit analysis for air layer drag reduction" *Int. Conf. On Ship Drag Reduction, SMOOTH-SHIPS*, Istanbul, Turkey. 2010b

Elbing, B.R., Winkel, E.S., Lay, K.A., Ceccio, S.L., Dowling, D.R. and Perlin, M. "Bubble-induced skin-friction drag reduction and the abrupt transition to air-layer drag reduction," *Journal of Fluid Mechanics*, 612, pp. 201-236. 2008

Etter, R.J., Cutbirth, J.M., Ceccio, S.L., Dowling, D.R. and Perlin, M., "High Reynolds number experimentation in the US Navy's William B Morgan Large Cavitation Channel." *Measurement Science and Technology*, 16, pp. 1701-1709. 2005

Foeth, E.-J. "Projects prove that air cavities reduce ship resistance." report, *MARIN's news magazine*, 16. August, 2011

Gokcay, S., Insel, M., and Odabasi, A.Y. "Revisiting artificial air cavity concept for high speed craft." *Ocean Engineering*, 31, pp. 253-267. 2004

Proceedings of the International Symposium on Seawater drag reduction. Newport, Rhode Island. 22-23 July, 1998

Proceedings of the 2nd International Symposium on Seawater drag reduction. Busan, Korea. 23-26 May, 2005

Kawanami, Y., Kato, H., Yamaguchi, H., Tanimura, M., & Tagaya, Y. "Mechanism and Control of Cloud Cavitation." Transactions of ASME, 119(December). 1997

Kodama, Y., Kakugawa, A., Takahashi, T., and Kawashima, H. "Experimental study on microbubbles and their applicability to ships for skin friction reduction." International Journal of Heat Fluid Flow, 21:582–88. 2000

Kopriva, J., Arndt, R.E.A., and Amromin, E. "Improvement of Hydrofoil Performance by Partial Ventilated Cavitation in Steady Flow and Periodic Gusts." Journal of Fluids Engineering, 130. 2008

Latorre, R., "Ship hull drag reduction using bottom air injection." Ocean Engineering, 24(2), pp. 161-175. 1997

Lay, K.A., Yakushiji, R., Mäkiharju, S., Perlin, M. and Ceccio, S.L. "Partial cavity drag reduction at high Reynolds numbers," Journal of Ship Research, v.54, n.2, pp. 109-119. 2010

Le, Q., Franc, J. P., & Michel, J. M. "Partial Cavities: Global Behavior and Mean Pressure Distribution. Journal of Fluids Engineering", 115(2), 243. doi:10.1115/1.2910131, 1993

Madavan, N.K., Deutsch, S., and Merkle, C.L. "Measurements of local skin friction in a microbubble modified turbulent boundary layer." Journal of Fluid Mechanics, 156:237–256, 1985.

Matveev, K.I., "On the limiting parameters of artificial cavitation." Ocean Engineering, 30, pp. 1179-1190, 2003.

Matveev, K. I. "Air-cavity ships are ready for a wider market." Speed at Sea, 13-16. February, 2003.

Matveev, K. I. "Three-dimensional wave patterns in long air cavities on a horizontal plane." Ocean Engineering, 34(13), 1882-1891. doi:10.1016/, 2006.08.015, 2007.

Mäkiharju, S., Elbing, B. R., Wiggins, A., Dowling, D. R., Perlin, M., & Ceccio, S. L. "Perturbed Partial Cavity Drag Reduction at High Reynolds Numbers". 28th Symposium on Naval Hydrodynamics (pp. 1-12). Pasadena, CA. 2010

Mizokami, S., Kawakita, C., Kodan, Y., Takano, S., Higasa, S., & Shigenaga, R. "Experimental Study of Air Lubrication Method and Verification of Effects on Actual Hull by Means of Sea Trial". Mitsubishi Heavy Industries Technical Review, 47(3), 41-47. 2010

Mortensen, J. D., Barfuss, S. L., & Johnson, M. C. "Scale effects of air entrained by hydraulic jumps within closed conduits." Journal of Hydraulic Research, 49(1), 90-95. doi:10.1080/00221686.2010.536695, 2011.

Ohtsu, I., Yasuda, Y., & Gotoh, H. "Hydraulic condition for undular-jump formations". Journal of Hydraulic Research, 39(2), 203-209, 2001.

Park J.T., Cutbirth J.M. and Brewer W.H., "Hydrodynamic performance of the Large Cavitation Channel (LCC)." Proc. 4th ASME–JSME Joint Fluids Engineering Conference, Honolulu, HI. 2003

Sanders, W. C., Winkel, E. S., Dowling, D. R., Perlin, M. and Ceccio, S. L. "Bubble friction drag reduction in a high-Reynolds number flat-plate turbulent boundary layer." Journal of Fluid Mechanics, 552, pp. 353-380. 2006

Surveyor. "Airship of the Sea". Surveyor, A Quarterly Magazine from AMS, 10-15. 2011

## CHAPTER 3

### Scaling of Partial Cavity Drag Reduction and Attendant Air Entrainment

To further our understanding of the underlying physical phenomena and to make predictions based on the model scale tests, we attempted to find scaling laws for partial cavity drag reduction. To facilitate the scaling, experiments were performed in a geometrically similar tunnel and with a geometrically similar model at a scale 1:14.1 smaller than those reported in Chapter 2. Before discussing the results from these experiments, we first discuss the pertinent variables and determine the relevant dimensionless groups.

#### 3.1 Dimensionless parameters

It has been confirmed by observation that all notable air loss occurs at the cavity closure (Mäkiharju *et al.* 2010), hence the critical air flux requirements are set by the physics of the cavity closure. The air entrainment from the closure has some similarity to plunging jets and breaking waves, and hence the following analysis is very similar to those done by many researchers investigating the aforementioned phenomena (for example: Kiger and Duncan, 2011). For the partial cavity closure, the relevant independent variables are free stream speed,  $U$ , gravity,  $g$ , densities of both fluids,  $\rho_w$  and

$\rho_g$ , viscosities of both water and gas,  $\mu_w$  and  $\mu_g$ , (although the gas in the experiments was always air, vapor could be treated similarly with the addition of effects from nearby collapsing vapor bubbles and phase change), surface tension,  $\sigma$ , nominal length of the cavity,  $L_c$ , (*i.e.* length of the recess), width of the model, and angle between the closure surface and the free stream,  $\beta_B$ . Additionally, it is postulated that the fluctuating velocity of the local disturbances,  $u$ , and length of these disturbances,  $\lambda$ , could be important. (Although these are dependent variables set by upstream flow conditions, when considering only the closure region they could be thought of as being independent.) The proper length scale at the closure would be the closure thickness,  $t_c$ , or the related wake thickness,  $\delta_c$ , but as these are directly set by the closure physics another relevant vertical length scale is employed. As the height difference between the backward facing step (BFS) and the beach was half the BFS height,  $H_{step}/2$ , we chose the height of the backward facing step  $H_{step}$  as the second vertical length scale, recognizing that it is not the physically significant scale. The cavity pressure at the minimal air fluxes is assumed to be essentially in equilibrium with the free stream pressure, and much higher than the vapor pressure,  $p_v$ . Therefore the effect of the cavitation number is not considered here, although it is the crucial parameter for similar natural cavities. This analysis is thus restricted to conditions where  $p_c \gg p_v$ . Therefore, we have

$$Q = f(U, g, \rho_l, \rho_g, \mu_l, \mu_g, \sigma, L_c, W, \beta_B, u', \lambda, H_{step}) \quad (3.1)$$

Now we have 13 independent parameters and three dimensions. Hence by using the PI-theorem we can reduce the non-dimensionalized air flux to be dependent on 10 dimensionless groups. One possible set of dimensionless groups is given by

$$q = f \left( Re, Fr, We, \frac{\rho_g}{\rho_l}, \frac{\mu_g}{\mu_l}, \frac{H_{step}}{L_c}, \frac{W}{L_c}, \beta_B, \frac{u'}{U}, \frac{\lambda}{L_c} \right) \quad (3.2)$$

where the non-dimensional groups are defined in table 3.1.

Table 3.1 – Dimensionless groups.

Group	Definition	Note
Dimensionless gas flux	$q = \frac{Q}{UWH_{step}}$	Gas flux divided by free stream speed, model span and step height to non-dimensionalize
Reynolds number	$Re = \frac{\rho_l U L_c}{\mu_l}$	Ratio of inertia to viscous forces
Froude number	$Fr = \frac{U}{\sqrt{gL_c}}$	Ratio of inertia to gravity forces
Weber number	$We = \frac{\rho U^2 H_{step}}{\sigma}$	Ratio of inertia to surface tension forces
Density ratio	$\frac{\rho_g}{\rho_l}$	For the small scale experiments $\sim 1/830$
Viscosity ratio	$\frac{\mu_g}{\mu_l}$	For both large and small scale experiments $\sim 0.018$
Non-dimensionalized step height	$\frac{H_{step}}{L_c}$	For both large and small scale experiments $\sim 0.019$
Non-dimensionalized cavity span	$\frac{W}{L_c}$	For both large and small scale experiments $\sim 0.33$
Angle of closure surface with respect to free stream direction at infinity	$\beta_B$	Fixed at $1.7^\circ$ for the small scale experiments
Fluctuation intensity	$\frac{u'}{U}$	
Non-dimensionalized length of disturbances	$\frac{\lambda}{L_c}$	Could be more meaningful to substitute $L_c$ with closure wake thickness, $t_c$ .



In the experiments reported in Chapter 2 and here, the key groups assume the range of values listed in table 3.2.

Table 3.2 – Parameter ranges of the experiments

	<b>Large Scale</b>	<b>Small Scale</b>
$Fr$	0.5 – 0.9	0.5 – 1.0
$We$	$(0.6 – 1.4) \times 10^5$	$(0.3 – 2.2) \times 10^3$
$Re$	$(4.6 – 6.9) \times 10^7$	$(0.9 – 1.6) \times 10^6$
$U$ [m/s]	5 – 7.5	1.3 – 2.5
$Q$ [m <sup>3</sup> /s]	$(0.3 – 2.6) \times 10^{-1}$	$(0.8 – 126) \times 10^{-6}$
$L_c$ [m]	9.25	0.66

The groups that were the same for both of the experiments include the density ratio of  $\sim 0.0012$ , viscosity ratio of  $\sim 0.018$ , non-dimensionalized step height  $\sim 0.019$ , and cavity span  $\sim 0.33$ . As these dimensionless values and the setup geometry were matched in both experiments, it was expected that a scaling in the following form might be possible:

$$q = f\left(Re, Fr, We, \frac{u'}{U}, \frac{\lambda}{L_c}\right) \quad (3.3)$$

Additionally, as properties of the disturbances ( $u'$  and  $\lambda$ ) are set by the upstream flow conditions, the turbulent boundary layer on the model upstream of the step, and free stream perturbations, which all depend presumably on  $Re$  and  $We$  already included [*i.e.*  $\frac{u'}{U}$  and  $\frac{\lambda}{L_c} = f(Re, Fr, We, TBL, \dots)$ ], and also as we have no measurements of the turbulent boundary layer (TBL) we further limit the search of scaling relationships to:

$$q = f(Re, Fr, We) \quad (3.4)$$

To proceed, we now need to compare the results from the different scales.

### 3.2 Low Reynolds number experiments

The “Mini-LCC” (MLCC) is the Large Cavitation Channel’s 1:14<sup>th</sup> scale model that resides at the University of Michigan’s Marine Hydrodynamics Laboratory. This facility enabled us to perform experiments at smaller scale while maintaining geometric similarity of the entire setup and matching the Froude numbers. While it was impossible to simultaneously also match the Reynolds and Weber numbers, we were able to vary the Weber number by a factor of two, independent of the other relevant parameters, by adding a surfactant.

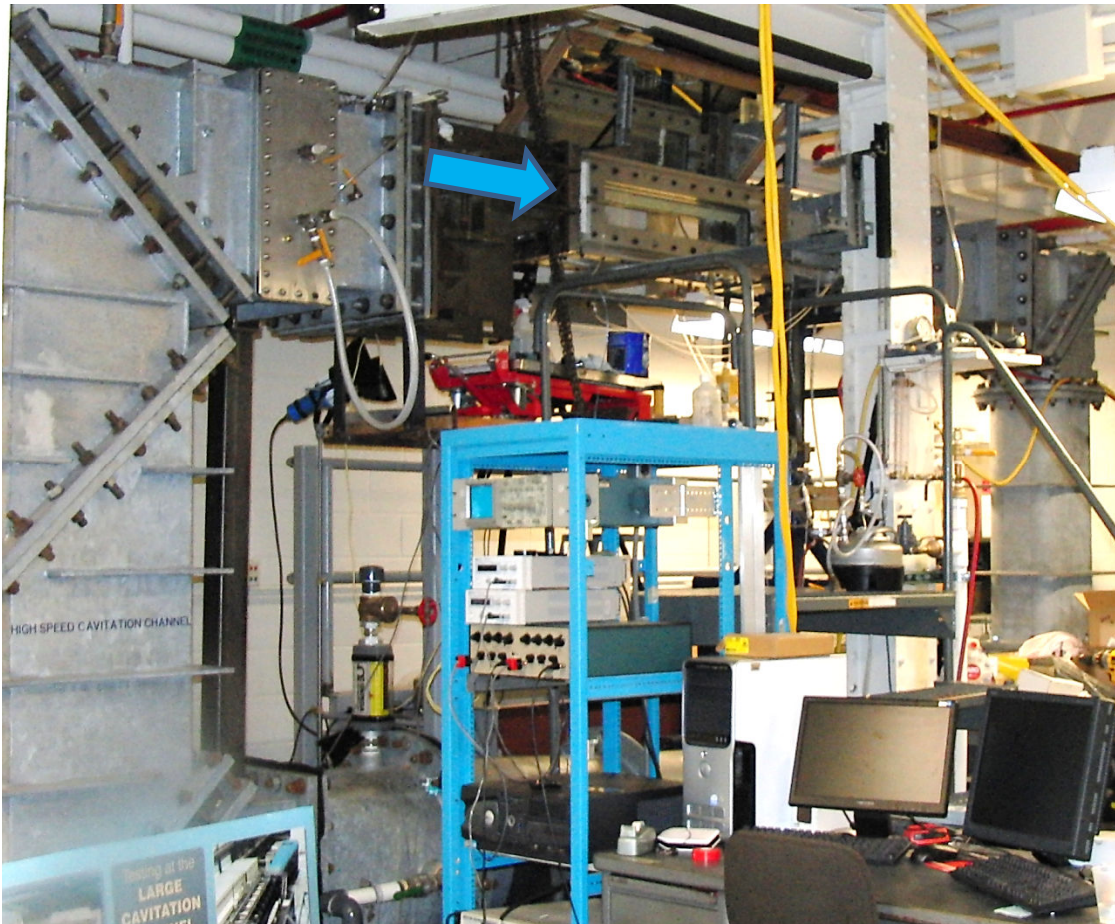


Figure 3.1 – The “Mini-LCC” water tunnel located at the University of Michigan’s Marine Hydrodynamics Laboratory. Flow is left-to-right through the test section as seen in this view. The blue arrow points to the test section, and also indicates the flow direction.

The MLCC shown in figure 3.1 differed from the LCC only through 1.20 m extensions included in both vertical legs to increase the hydrostatic pressure on the impeller. A drawing of the small scale model is shown in figure 3.2, while figure 3.3 shows the gate and model in the test section during the establishment of a cavity. Figure 3.4 shows a close up of the boundary layer trip at the leading edge and the beach, with lateral lines every 2.54 cm.

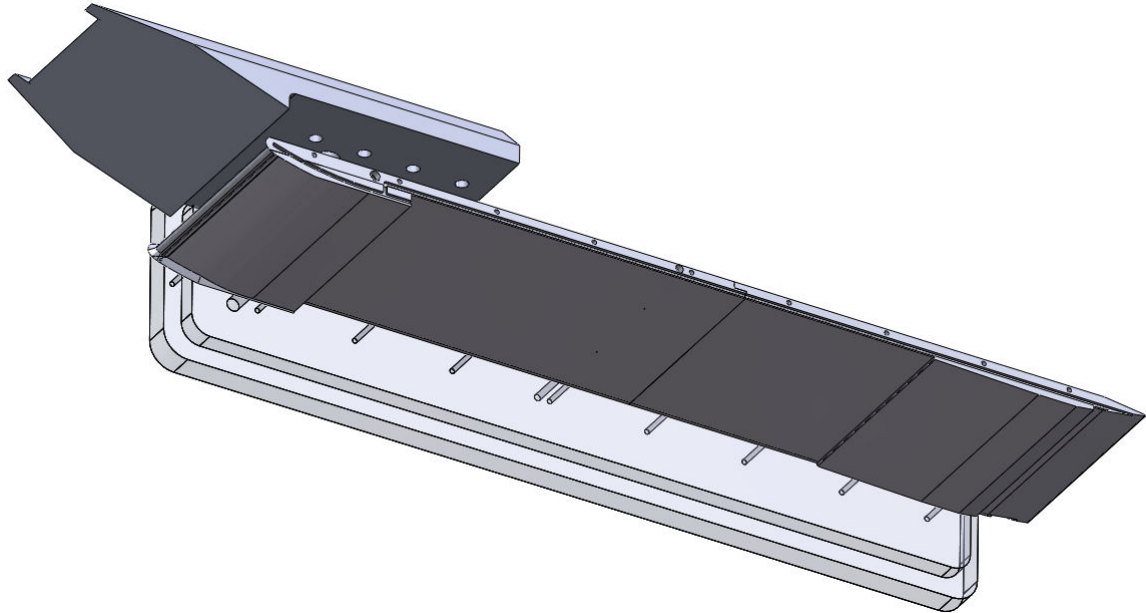


Figure 3.2 – Three dimensional view of the gate, plate and starboard window in the MLCC.

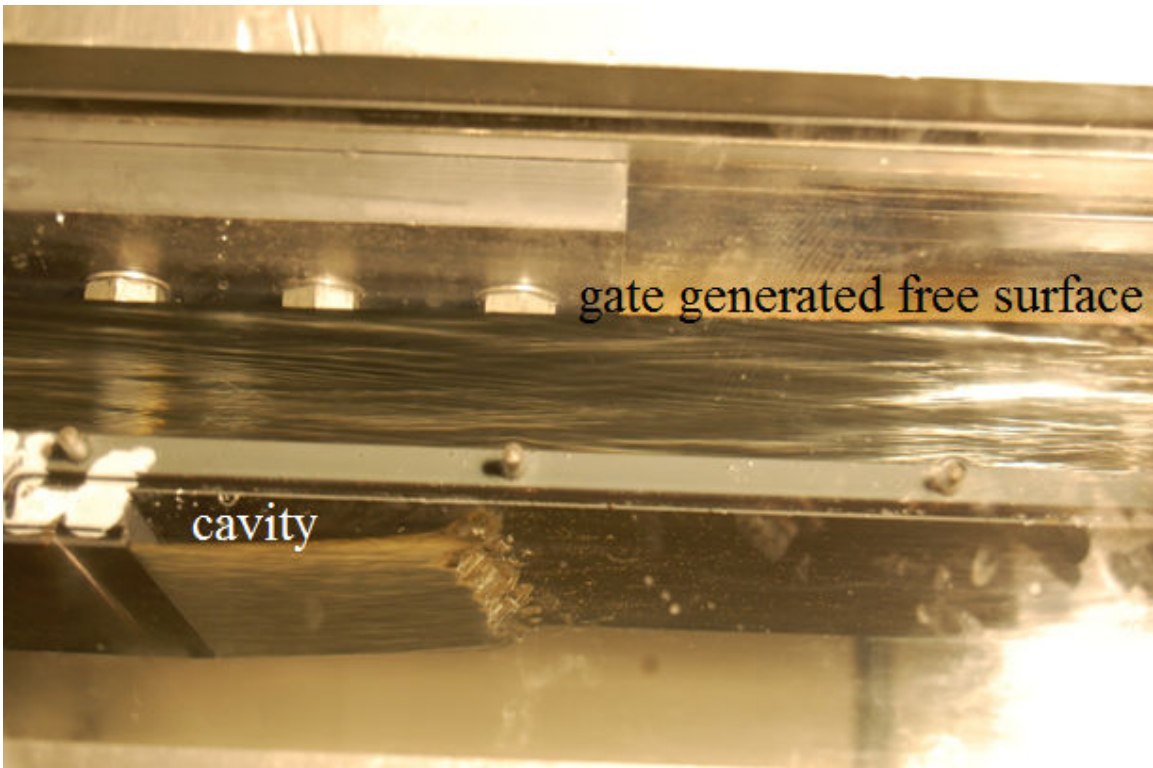
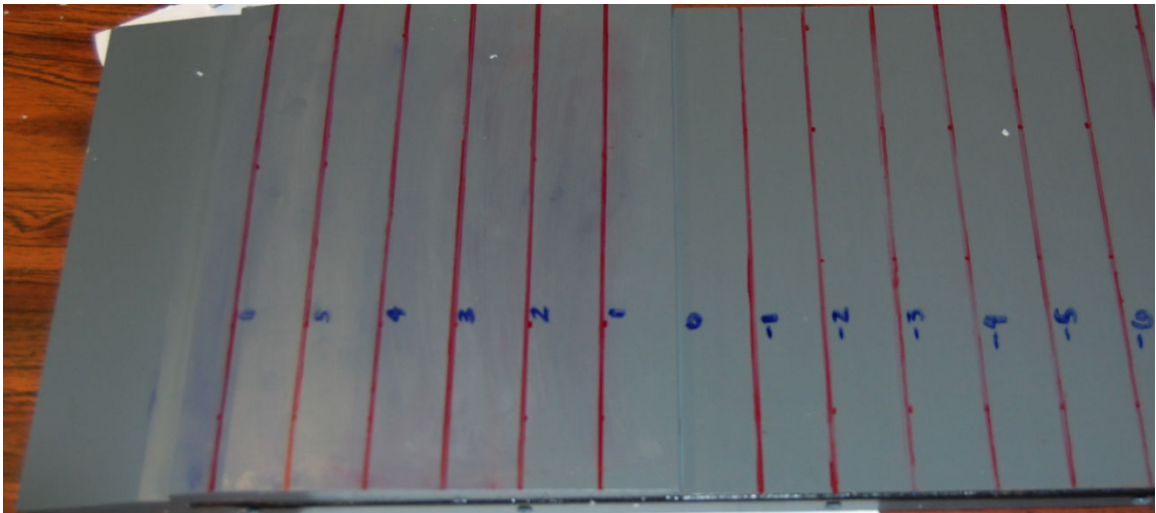


Figure 3.3 – Photo of the model and gate in the test section of the MLCC during early stages of cavity growth. In addition to the free surface of the cavity behind the BFS, we also have a second free surface above the plate and originating from the leading edge of the gate. The second free surface terminated in the tunnel's diffuser *via* a hydraulic jump.





(a)



(b)

Figure 3.4 – a) Close up of the boundary layer trip, which comprised of  $\sim 140$  micron particle roughness elements randomly distributed along the leading edge and was longitudinally 5 cm wide from the leading edge. b) Close-up photo of the beach region, where the beach starts at the 0-label.

### 3.3 Inlet flow conditions

The upstream boundary layer was not surveyed in the low Reynolds number experiments, unlike in the high Reynolds number experiments at the LCC. (For the LCC experiments, the turbulent boundary layer information was presented in Chapter 2). However, sensitivity of the cavity to the upstream boundary layer was investigated by first conducting the experiments with a nominally smooth surface at the leading edge and then repeating the experiments after addition of the boundary layer trip shown in figure 3.4a (randomly distributed 140 micron roughness elements).

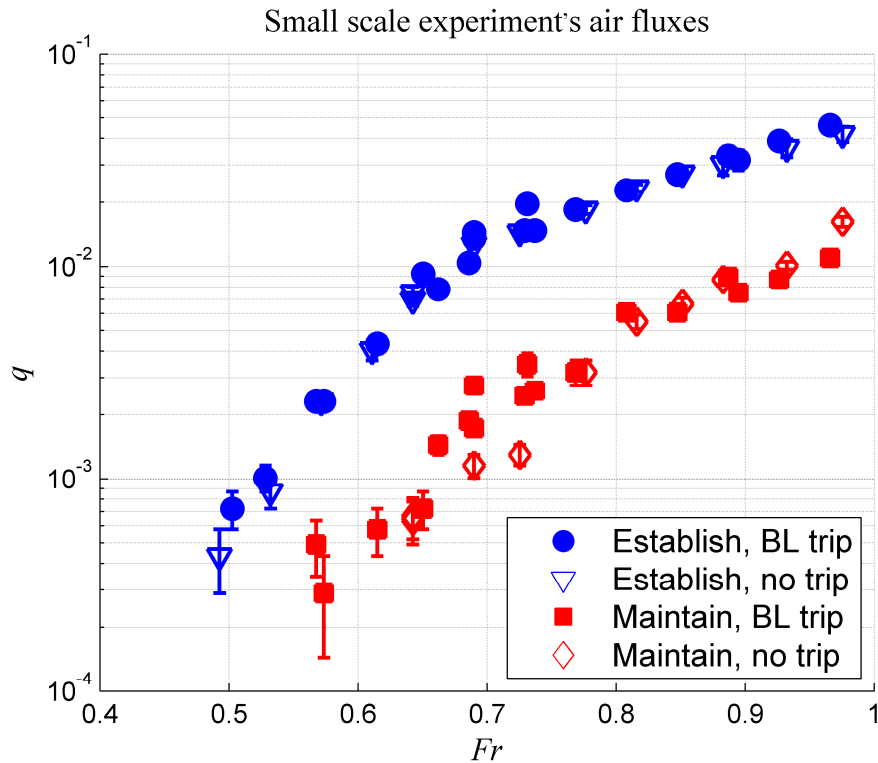


Figure 3.5 – Required air fluxes with and without the boundary layer trip at the leading edge. The results indicate that the trip had no significant effect on the air entrainment. Based on accuracy of the velocity measurement, the Froude number is accurate within  $\pm 0.035$ . For  $Fr = 0.4$ , experimented for the non-tripped case only, both the establishment and maintenance fluxes were below the flow meter's scale. Thus we merely know that the required flux at  $Fr = 0.4$  was greater than zero, but below  $10^{-3.4}$ . Also, for all establishment fluxes at the lower  $Fr$ , which do not have a corresponding data point for the maintenance flux, it was below the range of flow meters,  $< 10^{-3.4}$ , but larger than zero.

It is shown in figure 3.5 that the addition of the boundary layer trip had no clear observable effect on the required establishment or maintenance gas fluxes. Hence, the events in the closure region of the cavity would not seem to be acutely sensitive to modest changes of the upstream turbulent boundary layer. It could be speculated that by the time the free surface reaches the closure, it has “forgotten” the initial boundary layer from the step, similar to a turbulent jet far downstream having no memory of the specific orifice geometry. (Note that there were near zero flux conditions, where required flux was finite but below scale of the flow meters and no symbol is present in figure 3.5, as explained in the caption)

### **3.4 Comparison of air entrainment at different size scales**

The most notable difference qualitatively is the appearance of the cavity closure at the lowest Reynolds, Froude and Weber numbers. Figure 3.6 shows a close-up of the closure region as it typically appeared in the high Reynolds number LCC experiments. Small bubble clouds are being shed constantly, perhaps even periodically, as was observed in Lay *et al.* (2010). Figures 3.7 and 3.8 show the closure as it appeared in the small scale experiments with a larger and smaller  $Re$ , respectively, and it is immediately observable that while the higher Reynolds number cavity closure appears similar, the low Reynolds number case does not. In fact, were the flow speed further decreased, a seemingly zero flux closure would be observed, similar to that reported by Arndt *et al.* (2009) for a  $U < U_{crit}(Re)$ .

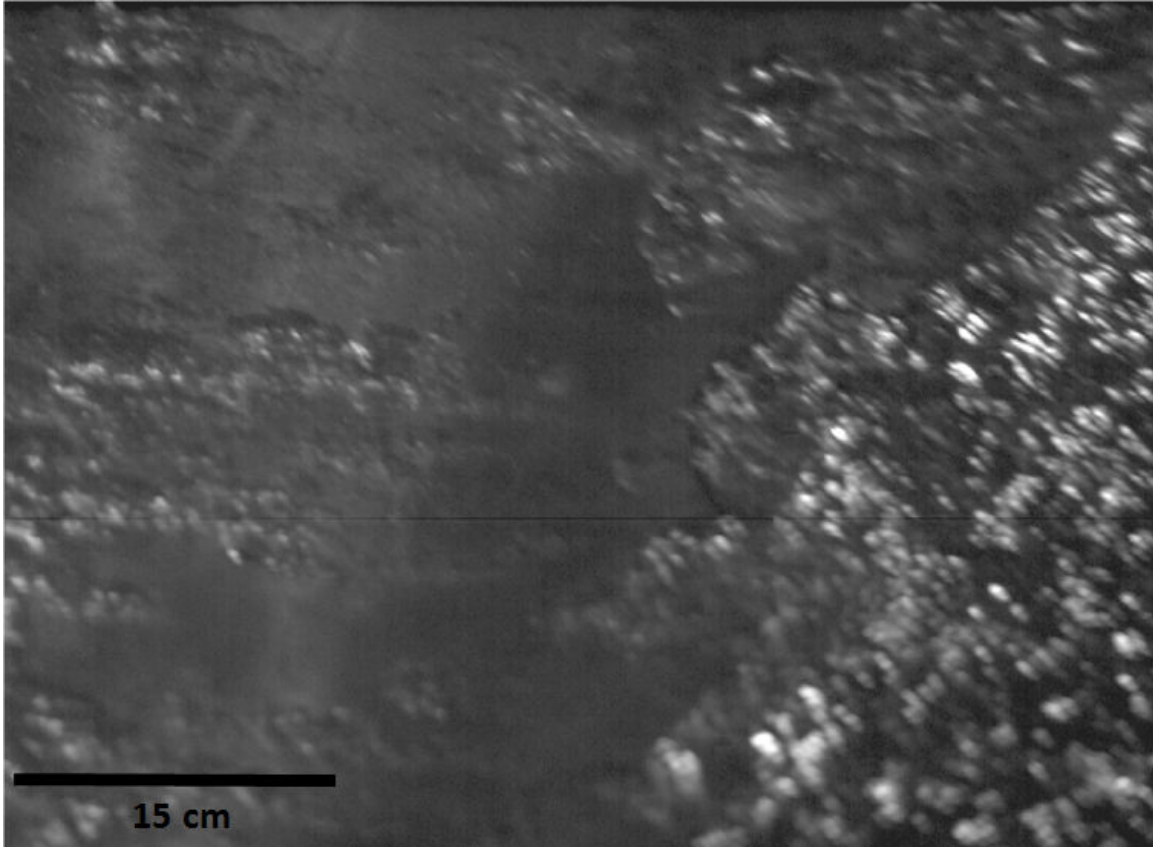


Figure 3.6 – Cavity closure at high Reynolds number in the LCC.  $U = 5.9$  m/s, run # 423,  $Fr = 0.62$ ,  $We = 9.0 \times 10^4$  and  $Re = 5.5 \times 10^7$ . Flow is from right to left. We can observe the continuous shedding of gas clouds from the closure. Image recorded through  $\sim 2$  m of liquid and 0.1 m of acrylic; hence clarity of image is somewhat lacking.



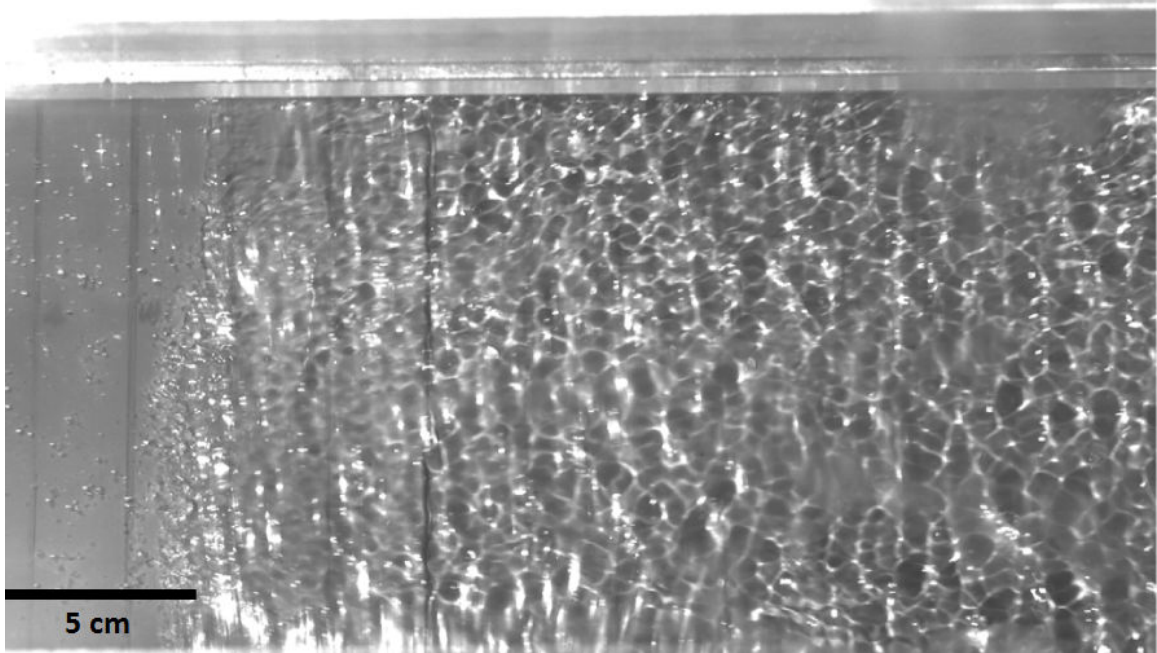


Figure 3.7 – Cavity closure in the MLCC.  $U = 2.27$  m/s,  $Fr = 0.89$ ,  $We = 940$  and  $Re = 1.5 \times 10^6$ . Flow is from right to left.

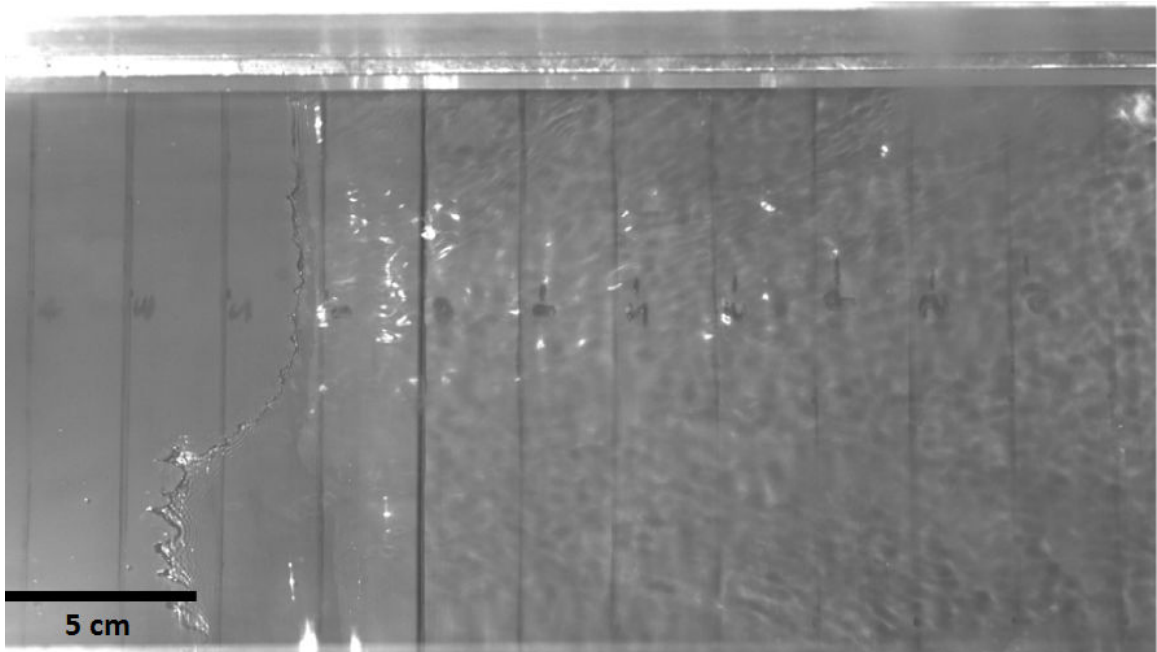


Figure 3.8 – Cavity closure in the MLCC.  $U = 1.25$  m/s,  $Fr = 0.49$ ,  $We = 285$  and  $Re = 8.0 \times 10^5$ . Flow is from right to left. The closure was often more two-dimensional than seen in this figure, where a portion of the cavity is just about to shed a pocket of air.

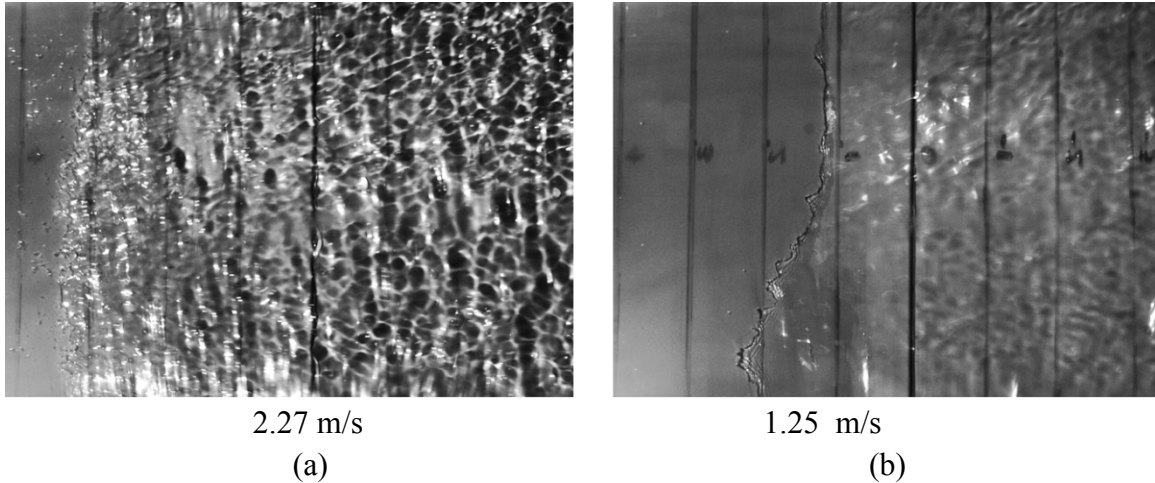


Figure 3.9 – Small scale cavity experiments closures at a different instance in time than in the two previous figures. It should be noted that there is no continuous shedding of bubbles at the lower speed, and it appears that the surface tension force is sufficiently high relative to other forces to retain the closure.

In the small scale experiment at the lower speeds air was lost by infrequent release of large gas pockets from the comparatively stationary closure with very few small bubbles shed (figure 3.9b). At the higher speeds (figure 3.9a) the situation was qualitatively similar to that observed in the large scale experiments shown in figure 3.6. There was constant shedding of small bubbles, with the occasional large oscillation of the cavity closure position leading to additional shedding of gas.

The cavity shape, however, seemed to scale better with Froude number. Figure 3.10 shows the small scale cavity shapes at various Froude numbers, which qualitatively agree with the cavity shapes observed at the LCC (matching within the large +/-10% error bars that stem from limited accuracy of measurements from video in the LLC and using a scale at the edge of the cavity in the MLCC).

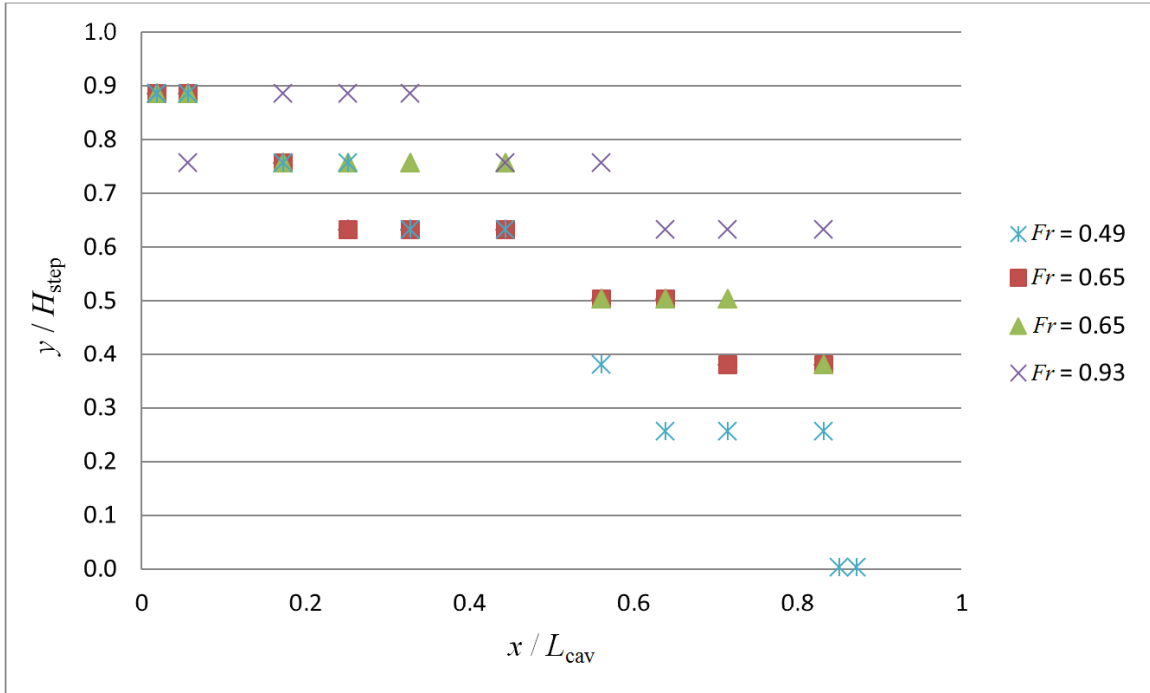


Figure 3.10 – Cavity free surface profile at various Froude numbers for the MLCC experiments. Vertical coordinate,  $y/H_{step}$ , measured to within  $\pm 0.1$ , with potential bias error or  $-0.1$ , and  $x/L_{cav}$  measured to within  $\pm 0.02$ .

A more quantitative comparison is given by comparing the required air fluxes at the two different scales as a function of Froude number. As in Chapter 2, the establishment flux which was required to form the cavity was always significantly higher than the maintenance flux required to sustain cavity after it had reached the beach. The results of the experiments are compared in figure 3.11.

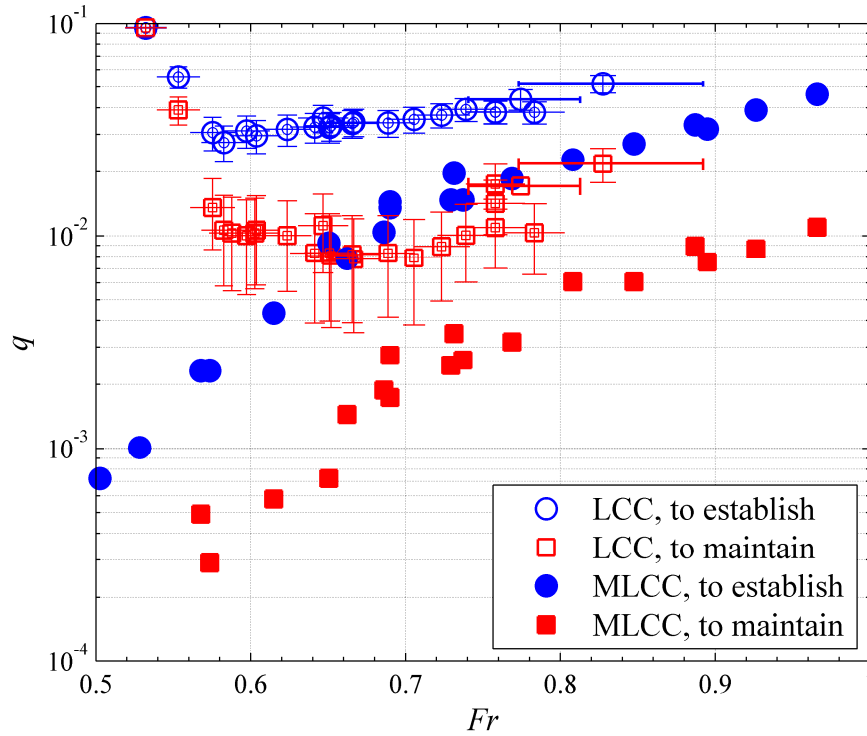
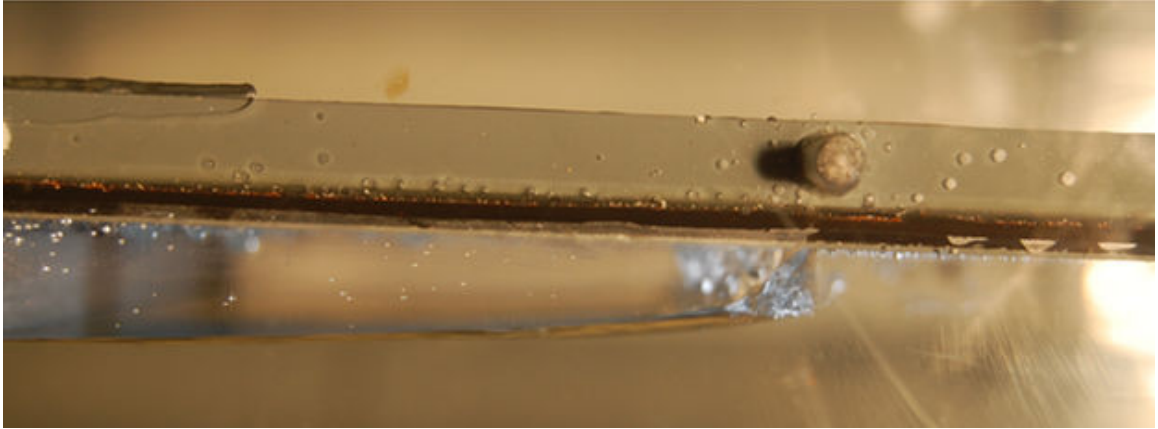
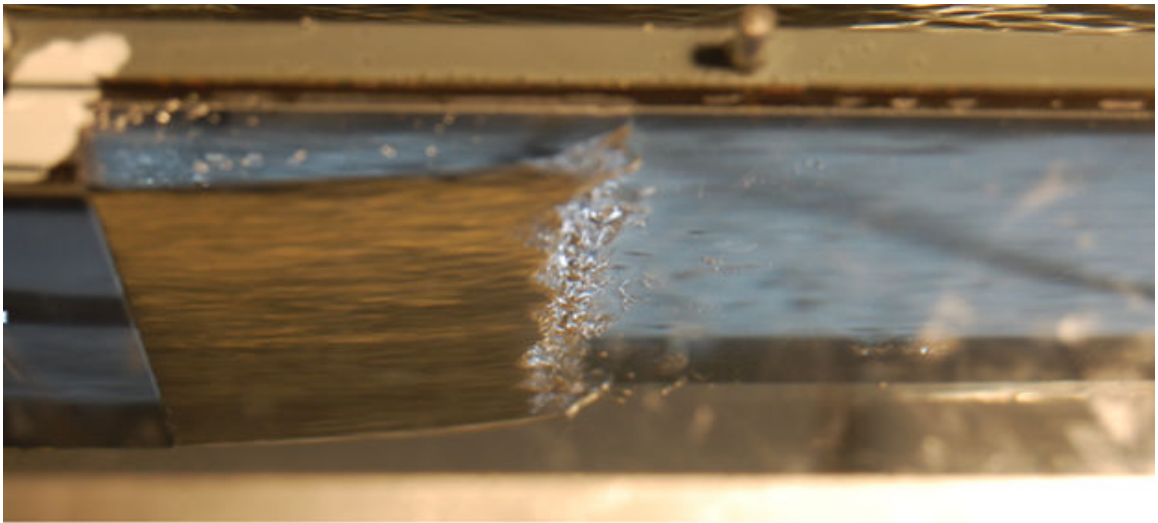


Figure 3.11 – Non-dimensionalized critical gas flux as a function of Froude number at different size scales. For all MLCC establishment fluxes at the lower  $Fr$ , which do not have a data point for the maintenance flux, this was below the range of the flow meters ( $<10^{-3.4}$ ), but larger than zero.

From results presented in figure 3.11, it can be seen clearly that non-dimensional air fluxes do not scale with Froude number alone. An especially large difference is observable at the lowest speeds. At the lowest speeds in the large scale experiments, the cavity was trying to close before reaching the beach leading to excessive gas cloud shedding. Dissimilarly, in the smaller scale at low speeds, the developing cavity had the appearance of a bubble, in that it seemed as the surface tension was retaining the cavity closure as seen in figure 3.12a, where few bubbles are being shed.



(a)



(b)



(c)

Figure 3.12 – a) Side view  $U \sim 1.4$  m/s,  $Fr \sim 0.58$  in the MLCC. b) Oblique view of the same cavity. c) Close up of the establishing cavity's closure at the LCC, where in a similar  $Fr \sim 0.6$  flow the establishing cavity would shed large clouds continually as shown

### 3.5 Effect of Weber number at small scale and low Reynolds number

To investigate the role of surface tension at the cavity closure, the Weber number was varied between 300 and 2200. The addition of Triton X-100, a soluble surfactant, enabled increasing the Weber number by a factor of two while keeping all other dimensionless parameters the same. The measured surface tension as a function of concentration is shown in figure 3.13. The surface tension was measured using the annular slide method developed by Lapham *et al.* (1999). The resulting surface tension versus concentration curve is as expected based on Winkel *et al.* (2004) and Liu and Duncan (2006).

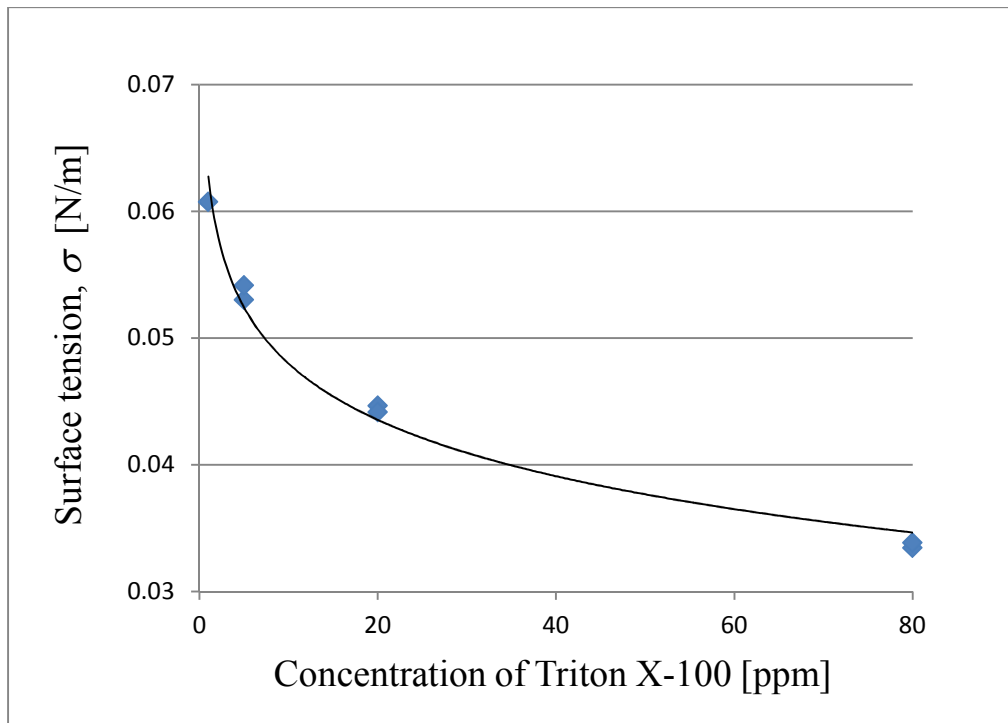


Figure 3.13 – Surface tension of the water in the MLCC flow loop as a function of Triton X-100 concentration.

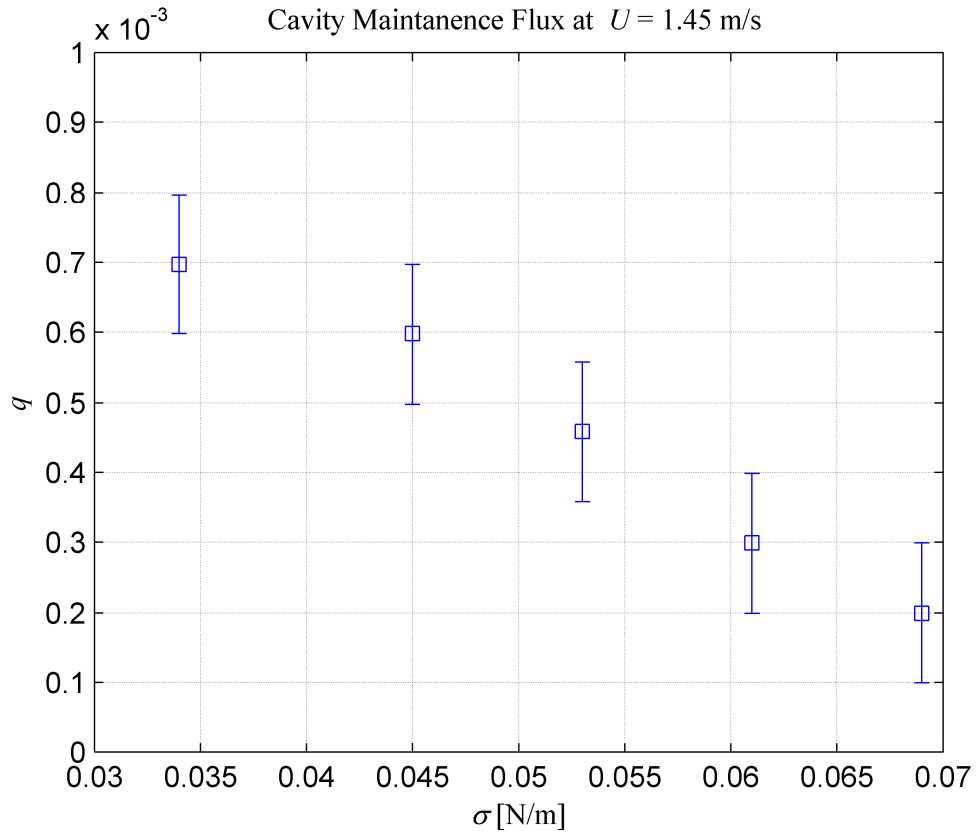


Figure 3.14 – Required cavity maintenance gas flux as a function of surface tension. Surface tension measurement +/- 0.002 N/m.

Figure 3.14 clearly shows that at least at the lowest test speed decreasing surface tension significantly increased the required air flux, as would be expected based on the assumption that the different cavity closure behavior observable in figure 3.9 is attributable to the relatively strong surface tension compared to the inertial and viscous forces trying to tear gas from the closure.

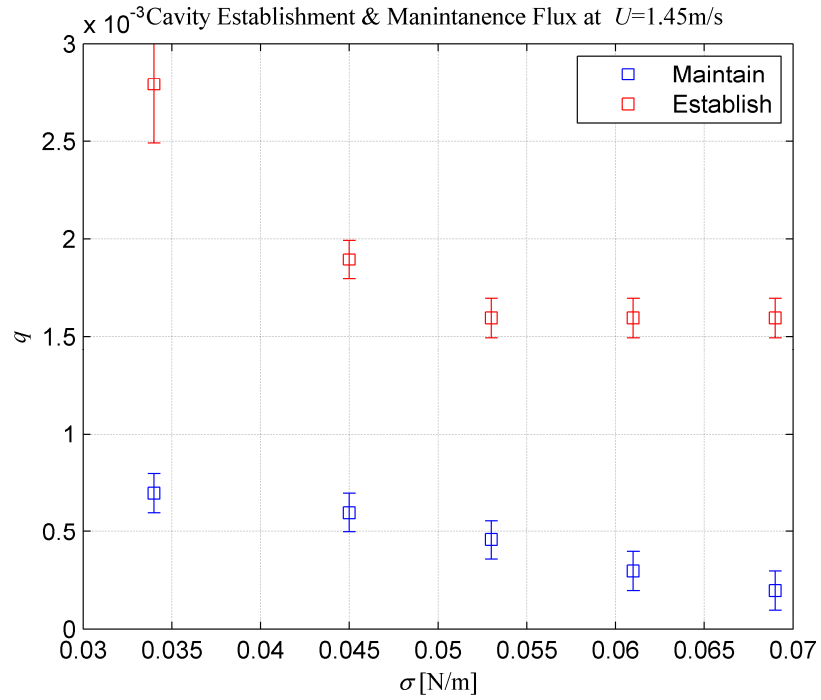


Figure 3.15 – Required cavity maintenance and establishment gas flux as a function of surface tension at  $U = 1.45$  m/s.

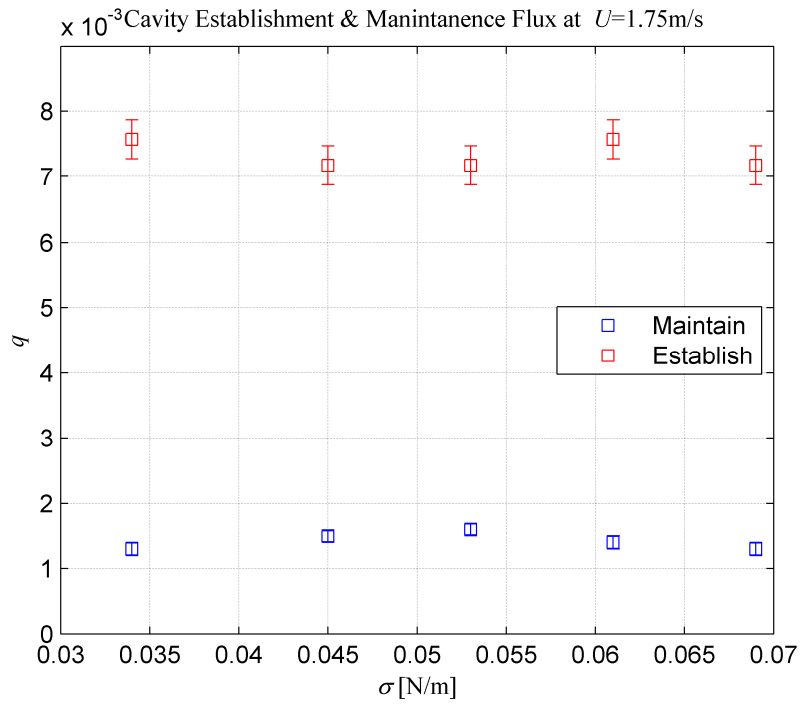


Figure 3.16 – Required cavity maintenance and establishment gas flux as a function of surface tension at  $U = 1.75$  m/s.



At 1.45 m/s (figure 3.15) reduction in surface tension by a factor of two (and hence increase of Weber number by a factor of two) had a significant effect on both the maintenance and establishment fluxes, but at the higher speed of 1.75 m/s there seems to be no clear significant effect as seen in figure 3.16.

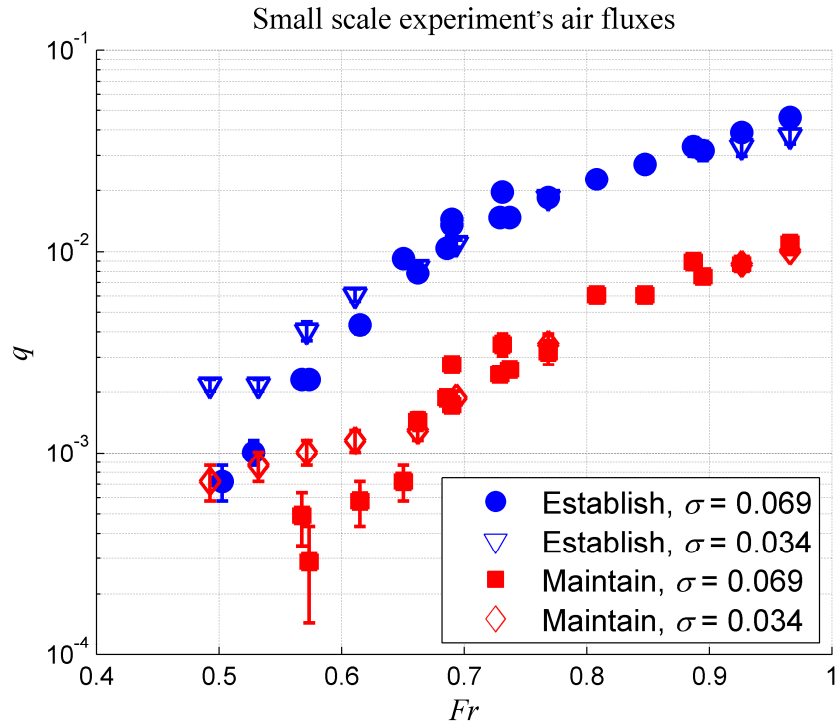


Figure 3.17 – Required cavity maintenance and establishment gas fluxes for two different values of surface tension. For all establishment fluxes at the lower  $Fr$ , which do not have a data point for the maintenance flux, this was below the range of the flow meters ( $<10^{-3.4}$ ), but larger than zero.

It seems that the effect of Weber number diminished as  $U$  increased, as the change in surface tension by a factor of two had no clear effect on the required gas fluxes. It is deduced that only at  $We < We_{critical}$  does surface tension play an important role in determining the entrained gas flux. After  $Fr \sim 0.7$ ,  $We \sim 600$ , there is no longer a significant observable change in figure 3.17 and hence we take  $We_{critical}$  to be  $\sim 600$ .

### 3.6 Effect of Reynolds number

The effect of Reynolds number on the closure behavior and hence the air entrainment could not be investigated comprehensively, as it was not possible to vary  $Re$  alone while keeping the other dimensionless parameters the same. However, figure 3.18 shows that beyond a Reynolds number of  $\sim 1.5$  million the gas fluxes are of the same order of magnitude, which is quite interesting given that the Reynolds number is still almost two orders of magnitude apart. This might suggest that a properly non-dimensionalized air flux could become independent of the Reynolds number at  $Re > Re_{critical}$ , similar to the drag coefficient on a flat plate, etc.

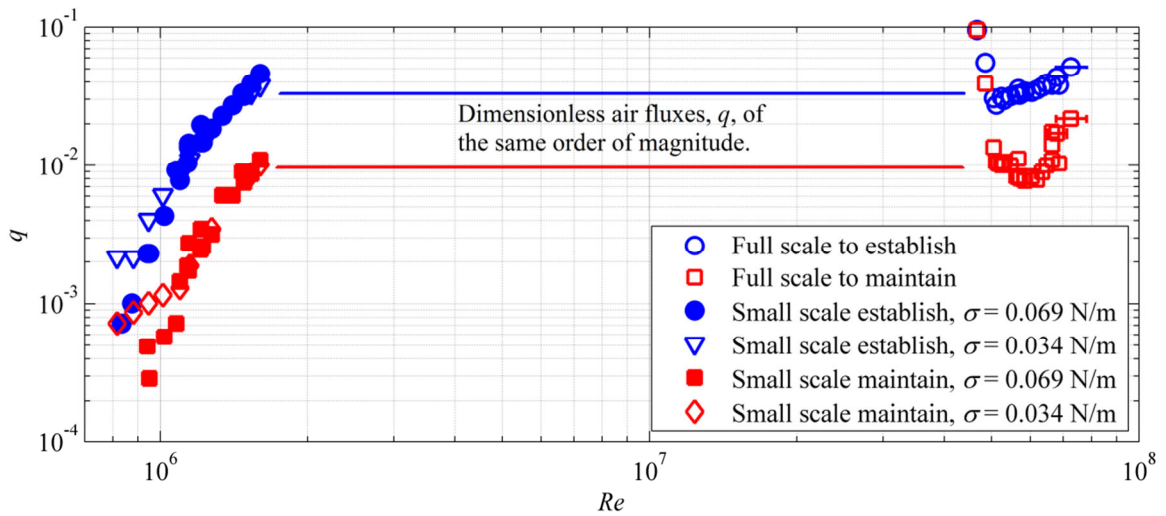


Figure 3.18 – Critical dimensionless gas fluxes as a function of Reynolds number.

### 3.7 Discussion

Air flux requirements of a stable ventilated partial cavity were examined for varying Froude, Reynolds, and Weber numbers employing two geometrically similar experimental setups a size scale factor of 1:14 apart. At both scales, all notable air loss occurred from the cavity closure. Results showed that in this closure region inertial, viscous and surface tension forces can all be important. For example, a change in surface tension will alter the required air flux for the lower Weber number flow conditions. At the lowest Reynolds numbers, there was an observable change in the gas entrainment mechanism. The gas entrainment rate was reduced greatly for lower Reynolds and lower Weber numbers. However, as the Weber number increased, the required air flux became insensitive to changes in Weber number up to a factor of two.

Additional experiments would be required to verify a proper scaling, but it appears that at  $Re > Re_{critical}$  and  $We > We_{critical}$  the required air flux may simply be a function of Froude number and cavity geometry alone,

$$q = q(Fr, geometry) \quad (3.5)$$

Scaling of air entrainment requires a detailed understanding of cavity closure dynamics, and hence our subsequent work was, and still is, focused on details of the air cavity closures. In Chapter 5 we describe a time resolved x-ray densitometry system developed to measure the two dimensional void fraction distribution in the cavity closure and in its wake. In Chapter 6 we present results using this system on a ventilated partial cavity, and compare to measurements using optical probes and high speed video.

### 3.8 References for Chapter 3

Arndt, R. E. A., Hambleton, W. T., Kawakami, E., & Amromin, E. L. "Creation and Maintenance of Cavities Under Horizontal Surfaces in Steady and Gust Flows". *Journal of Fluids Engineering*, 131(11), 111301. doi:10.1115/1.4000241, 2009.

Chanson, H. "Study of Air Demand on Spillway Aerator". *Journal of Fluids Engineering*, 112, 343, 1990.

Duncan, J. H., & Kiger, K. "Physics of Air Entraining Flows. Annual Review of Fluid Mechanics", 44(1), 110301100027072. doi:10.1146/annurev-fluid-122109-160724, 2011.

Liu, X., & Duncan, J. H. "An experimental study of surfactant effects on spilling breakers". *Journal of Fluid Mechanics*, 567, 433. doi:10.1017/S0022112006002011, 2006.

Lay, K. A., Yakushiji, R., Mäkiharju, S., Perlin, M., & Ceccio, S. L. "Partial Cavity Drag Reduction at High Reynolds Numbers". *Journal of Ship Research*, 54(2), 109-119, 2010.

Lapham, G. S., Dowling, D. R., & Schultz, W. W. "In situ force-balance tensiometry". *Experiments in Fluids*, 27(2), 157-166. doi:10.1007/s003480050340, 1999.

Mäkiharju, S., Elbing, B. R., Wiggins, A., Dowling, D. R., Perlin, M., & Ceccio, S. L. "Perturbed Partial Cavity Drag Reduction at High Reynolds Numbers". 28th Symposium on Naval Hydrodynamics (pp. 1-12). Pasadena, CA, 2010.

Winkel, E. S., Ceccio, S. L., Dowling, D. R., & Perlin, M. "Bubble-size distributions produced by wall injection of air into flowing freshwater, saltwater and surfactant solutions". *Experiments in Fluids*, 37, 802-810. doi:10.1007/s00348-004-0850-y, 2004.

White, F. M. "Fluid Mechanics, 5th edition" McGraw-Hill, 2001.

## CHAPTER 4

### Air Lubrication Energy Cost-Benefit Analysis

For any air lubrication technique to be considered for implementation, the potential net energy savings must be sufficient to justify the added complexity of the air supply system and the capital, operational and maintenance costs. We present an energy cost-benefit analysis for ALDR and PCDR, and discuss the results and some of the limitations of their validity. A more simplified cost-benefit analysis for ALDR has been previously provided by Ceccio *et al.* (2010). BDR is not considered, as the results available to date are dependent on bubble size distributions and BDR's frictional drag reduction effects persistence is likely not sufficient to make it viable (Elbing *et al.* 2008).

The air layer or partial cavity will only reduce the frictional drag on the area covered. It is assumed that the ship's form drag is not appreciably changed by the air injector, strakes or other appendages attached to the hull to achieve air lubrication. Assuming further that practically all of the ship's energy consumption is used for propulsion, the possible percentage net energy savings,  $\%E_{\text{saved}}$ , can be estimated by considering the ratio of net energy savings to total energy consumption

$$\frac{\%E_{\text{saved}}}{100} \cong \frac{\Delta t \cdot P_{\text{saved}}}{\Delta t \cdot P_D / \eta_{\text{prop}}} \quad (4.1)$$

where  $P_{\text{saved}}$  is the net power savings,  $P_D$  is the power required to overcome the ship's total drag,  $\eta_{\text{prop}}$  is the propeller efficiency and the increments of time,  $\Delta t$ , cancel. The net energy savings can be estimated by considering the reduction in power required to overcome frictional drag and the power required to supply the gas, yielding

$$P_{\text{saved}} = \frac{P_D f_{FD}}{\eta_{\text{prop}}} \frac{A_{\text{ac}}}{A_{\text{wet}}} \left( \frac{\%D_R}{100} \right) - \frac{P_{\text{comp}}}{\eta_{\text{elect}}} \quad (4.2)$$

where  $\%D_R$  is the percentage frictional drag reduction on the air covered by air,  $f_{FD}$  is the fraction of total drag due to friction,  $A_{\text{ac}}$  area covered by air,  $A_{\text{wet}}$  total wetted hull area,  $P_{\text{comp}}$  is the power required to run the compressor or blower, and  $\eta_{\text{elect}}$  is the efficiency of producing the electricity for the compressor/blower relative to the efficiency of providing power for the shaft. Hence a value of one should be used if the ship's propellers are electrically driven, as is the case for ships with Azipods for example. The percentage of total drag due to friction can be estimated from figure 4.1.

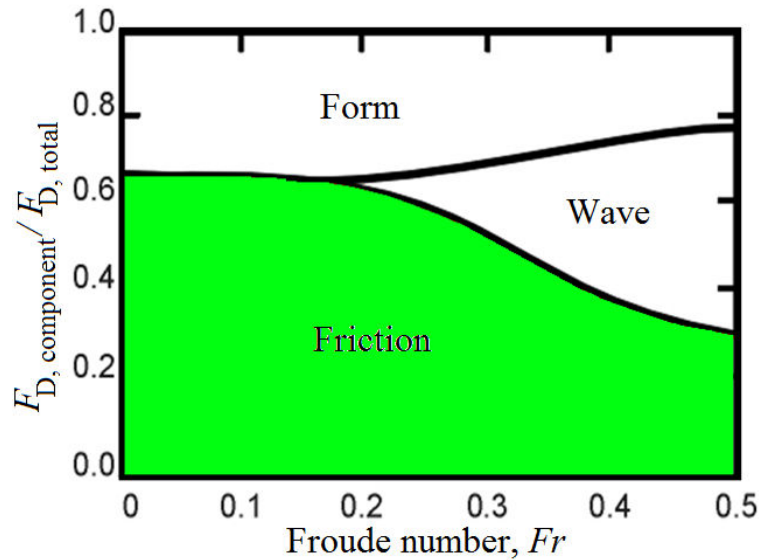


Figure 4.1 – Typical contributions of different components of ship's resistance as a function of Froude number as commonly reported in the literature.

As shown in figure 4.1, of the total drag, frictional drag accounts for approximately 60% for Froude number less than 0.2. Here the Froude number is defined as

$$Fr = U/\sqrt{gL} \quad (4.3)$$

where  $U$  is the ship's speed,  $g$  is the gravitational constant ( $9.81 \text{ m/s}^2$ ), and  $L$  is the overall length of the ship.

The power required to overcome frictional drag,  $P_{FD} = P_D f_{FD}$ , can be estimated from the frictional drag on a flat plate, which according to White (2006) is given by

$$P_{FD} = \frac{1}{2} \rho_w U^3 W L C_D \quad (4.4)$$

where for a turbulent flow over a flat plate with a smooth surface drag coefficient,  $C_D$ , may be taken to be  $0.523/\ln^2[0.06\text{Re}_L]$  (White 2006),  $W$  is the width, and  $L$  is the length of the plate. From basic thermodynamic principles (Sonntag *et al.* 2003) the power needed to compress a given mass flow rate of gas via a polytropic process (*i.e.* process where  $PV^n = \text{constant}$ ) is given by

$$P_{comp} = \frac{\dot{m}_g p_1 n}{\eta_c \rho_{g,1} (n-1)} \left( \left[ \frac{p_2}{p_1} \right]^{(n-1)/n} - 1 \right) \quad (4.5)$$

For an isentropic process the exponent  $n$  (also called index or polytropic index) would be replaced by  $k$ , the ratio of specific heats, which is 1.40 for air.  $\dot{m}_g$  is the mass flow rate of gas,  $p_1$  is the initial pressure, assumed to be 1 atm,  $p_2$  is the pressure to which the gas needs to be compressed, which depends on the pressure beneath the hull determined by

draft and piping losses,  $\rho_{g,1}$  is the density of the gas to be compressed and  $\eta_c$  is the compressor efficiency.

The mass flow rate needed is related to the volume flow rate requirement at pressure below the hull, and assuming that the gas is cooled to 25 °C after compression we can write

$$\dot{m}_g = Q \frac{\rho_{g,1} p_3}{p_1} \quad (4.6)$$

For a slow moving ship the pressure under the hull is assumed to be equal (or slightly less) than the hydrostatic pressure at the draft depth,  $p_3 = \rho_w g D$ , where  $D$  is the ship's draft. Note that  $p_2 = p_3 + \Delta p_{loss}$ . In eqn 4.6,  $Q$  is the volume flux of gas required to achieve ALDR or PCDR at pressure  $p_2$  and it can be estimated by curve fitting the data provided by Elbing *et al.* (2008) and Mäkiharju *et al.* (2010).



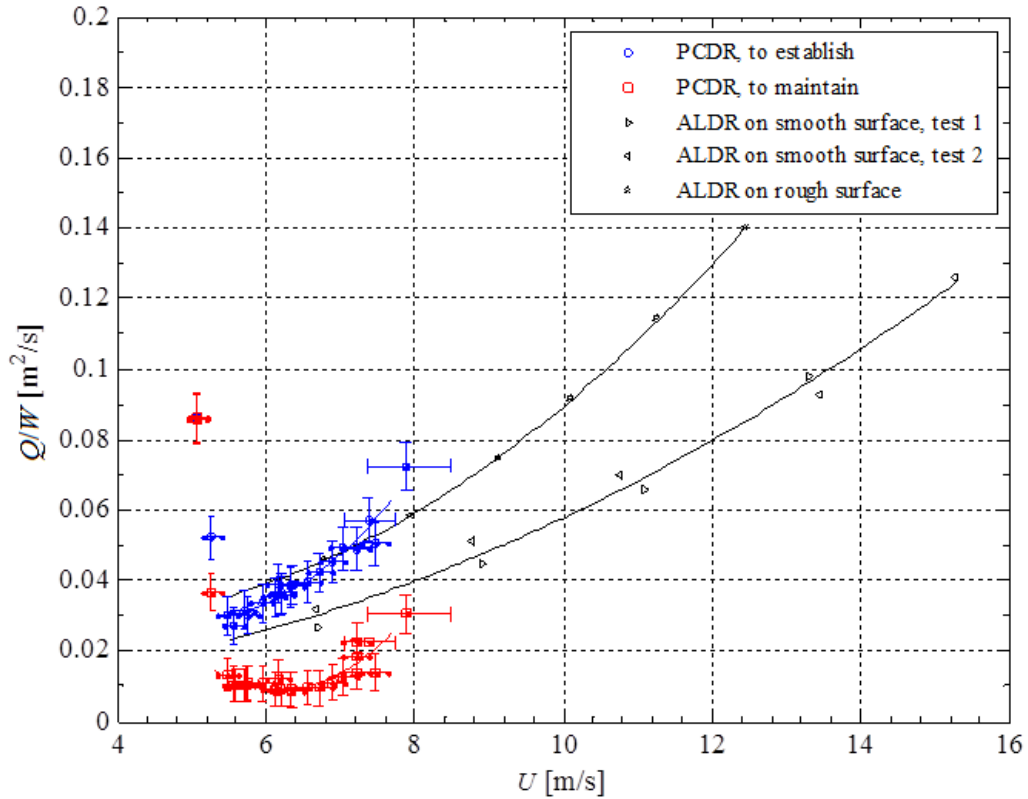


Figure 4.2 – Required volumetric flow rate per unit span to achieve an air layer on a smooth surface ( $\blacktriangleright$  and  $\blacktriangleleft$ ), on a rough surface ( $\star$ ), to establish a partial cavity ( $\circ$ ) and to maintain a partial cavity ( $\square$ ). Solid lines are curve fits given in equations 4.7a-d. The wide error bars at the two highest PCDR test speeds are due to variation of the free stream conditions and uncertainty of the velocity measurement performed using LDV in optically semi-opaque bubbly flow.

The experimental data and simple curve fits are shown in figure 4.2. The curve fits for volumetric air flux per unit span,  $Q/W$ , are given by

$$Q/W = 0.00126U^2 - 0.00755U + 0.0391 \quad (4.7)$$

for ALDR on a rough surface. Original data cover speed range from 6.79 to 12.45 m/s and a quadratic fit is used returning an  $R^2 = 1.00$ . On a smooth surface the original data cover a speed range from 6.67 to 15.26 m/s and a quadratic fit with  $R^2 = 0.99$  is given by

$$Q/W = 0.000501U^2 - 2.98 \cdot 10^{-5}U + 0.00800 \quad (4.8)$$

For PCDR a linear curve fit for the data establishment flux from 5.48 to 7.46 m/s gives a quadratic fit with  $R^2 = 0.95$

$$Q/W = 0.00476U^2 - 0.04796U + 0.150 \quad (4.9)$$

For the maintenance flux in the same range a quadratic fit with  $R^2 = 0.81$  is given by

$$Q/W = 0.00701U^2 - 0.0866U + 0.277 \quad (4.10)$$

#### 4.1 Example calculations

As an example, let's consider a ship like the American Steamship Company's M/V American spirit, shown in figure 4.3.



Figure 4.3 – The M/V American spirit is a cargo ship operating on the U.S. Great Lakes.  $L= 306$  m,  $w= 32$  m and midsummer draft 8.8 m (American Steamship Company).

Assumptions:

- This ship has a very large block coefficient. While the exact hull shape is not available to us, we assume that 7% of the beam has curvature and 15% of the length is bow and stern. This leads to  $A_{ac}/A_{wet} \sim 50\%$ .

- The top speed for this ship is  $\sim 7.5$  m/s, leading to a maximum Froude number of 0.14, hence based on figure 1 we assume that the fraction of frictional drag of total resistance  $f_{FD} = 0.6$ .
- For both air layers and partial cavities we assume that the friction on the area covered is reduced by 80%, which is the lower bound of the frictional drag reduction based on results presented in Lay *et al.* (2010).
- Propulsor efficiency is conservatively assumed to be high (75%), as the higher this value is, the lower the net savings percentage will be.
- Efficiency of the generator providing electricity for the compressor is assumed to be a mere 90%.
- The compressor efficiency was assumed to be 60%. (Based on information given by Continental Blower, the efficiency within +/- 50% of the ideal operating point for the given pressure differential is  $\sim 70\%$ ).
- Pressure drop due to piping losses was assumed to be 101 kPa.
- For ALDR the air layer is assumed to persist indefinitely once formed.
- For PCDR a single multi-wave partial cavity is assumed to span the length of the bottom. (It is assumed that the surface in the recess beneath the hull can have multiple wave crests and troughs along its streamwise length, but that the air entrainment rate would be same as for the shallow water partial cavities discussed in Chapter 2.)

The final expression for the net energy savings is obtained by combining eqn. 4.1 and 4.2, yielding

$$\frac{\%E_{savings}}{100} \approx f_{FD} \frac{A_{AL}}{A_{wet}} \left( \frac{\%D_R}{100} \right) - \frac{P_{comp} \eta_{prop}}{P_D \eta_{elect}} \quad (4.11)$$

The codes used to generate figure 4.4 are given in appendix D.

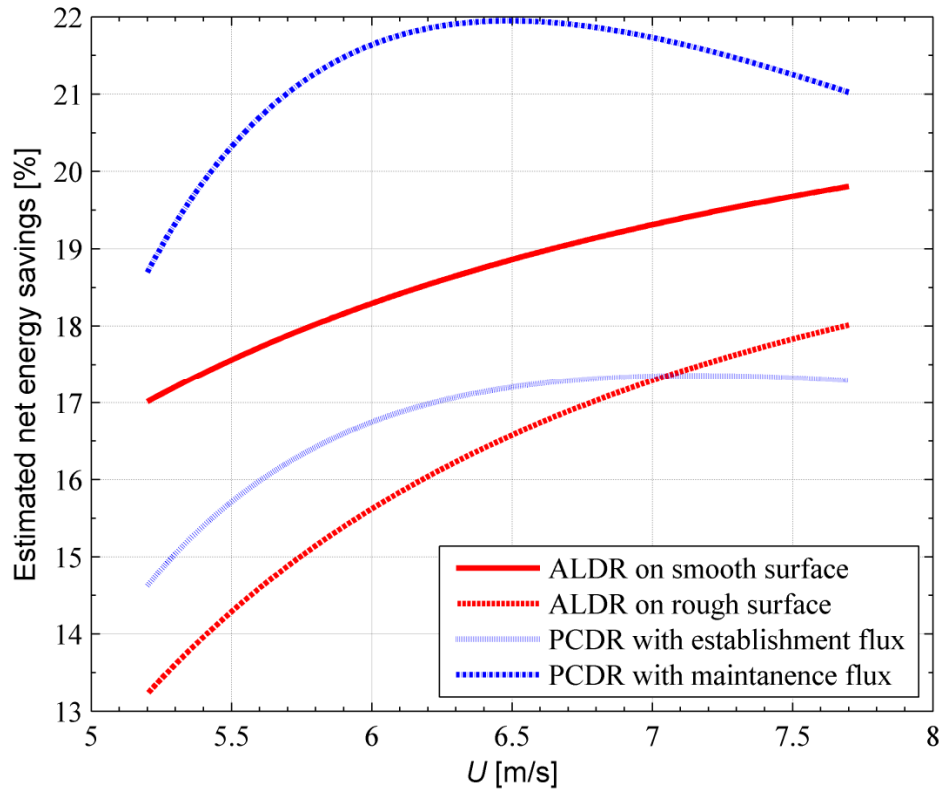


Figure 4.4 – Estimates of the potential net energy savings for a ship similar to the M/V American Spirit.

## 4.2 Discussion

There have been two sea trials where the flow was likely in the BDR-transitional-ALDR region (based on flow regions as defined in Elbing *et al.* 2008). One such sea trial on the Pacific Seagull yielded 5 to 10% net energy savings according to Hoang *et al.* (2009), while a second sea trial by Mitsubishi Heavy Industries achieved 8 to 12% net energy savings (Mizokami *et al.* 2010). As for PCDR, a scale test by MARIN recently showed 15% net energy savings (Foeth, 2011) and for a 1:12<sup>th</sup> scale test by STENA they reported resistance reduction of 20 to 25% (Surveyor 2011). The potential net energy savings predicted for ALDR in figure 4.4 are slightly higher than observed in the sea trials. This is likely explained by a combination of the following: the sea trials may not have had sufficient air flux supplied to achieve a true air layer (as could be assumed from the local frictional drag measurements presented by Hoang *et al.* 2009), presence of flow perturbations in the open ocean or the area fraction of the wetted hull covered for these ships was less than assumed in the current analysis.

For the surface covered by air, the percentage of frictional drag reduction was assumed to be 80% for both ALDR and PCDR to be conservative, and given that other components of drag may in fact increase. It is important to note that any effects of possibly increased form drag and all other details, such as the effect of air entrainment into the propulsor, were omitted. It is not the intent to make a strong quantitative argument, but rather to show qualitatively the trends of the energy economics of air lubrication, and thereby to determine whether the energy savings break-even point could be surpassed.

The energy savings break-even point depends on three principal parameters, ship's draft, length and operating speed. The net energy savings achieved, will likely

deviate from those estimated here as they depend on all the assumptions made in the analysis, and on how the experimental results used would scale to conditions not tested in the experiments. There are certainly boundaries for these techniques that have not been encountered within the limited parameter ranges of the nominally two dimensional experiments on which estimates of required air flux were based.

### 4.3 References for chapter 4

Ceccio, S.L. "Friction Drag Reduction of External Flows with Bubble and Gas Injection," Annual Review of Fluid Mechanics, Vol. 42, pp. 183-203. 2010

Ceccio, S.L., Perlin, M. and Elbing, B.R., "A cost-benefit analysis for air layer drag reduction" Int. Conf. On Ship Drag Reduction, SMOOTH-SHIPS, Istanbul, Turkey. 2010

Elbing, B. R., Winkel, E. S., Lay, K. a, Ceccio, S. L., Dowling, D. R., & Perlin, M. "Bubble-induced skin-friction drag reduction and the abrupt transition to air-layer drag reduction". Journal of Fluid Mechanics, 612, 201-236. doi:10.1017/S0022112008003029, 2008.

Foeth, E.-J. Report, MARIN's news magazine, page 16. August, 2011.

Hoang, C. L., Toda, Y., and Sanada, Y. "Full scale experiment for frictional resistance reduction using air lubrication method," Proc. of the Nineteenth International Offshore and Polar Engineering Conference, 812-817, 2009.

Lay, K.A., Yakushiji, R., Mäkiharju, S., Perlin, M. and Ceccio, S.L. "Partial cavity drag reduction at high Reynolds numbers," Journal of Ship Research, v.54, n.2, pp. 109-119. 2010

Mäkiharju, S., Elbing, B.R., Wiggins, A., Dowling, D.R., Perlin, M. and Ceccio, S.L., "Perturbed Partial Cavity Drag Reduction at High Reynolds Numbers" 28th Symposium on Naval Hydrodynamics, Pasadena, CA, 2010.

Mizokami, S., Kawakita, C., Kodan, Y., Takano, S., Higasa, S., & Shigenaga, R. "Experimental Study of Air Lubrication Method and Verification of Effects on Actual Hull by Means of Sea Trial". Mitsubishi Heavy Industries Technical Review, 47(3), 41-47, 2010.

Surveyor A Quarterly Magazine from AMS, 10-15, 2011.

White, F.M., Viscous Fluid Flow, 3rd ed., McGraw-Hill, New York, 2006.

## CHAPTER 5

### Time Resolved X-Ray Densitometry

Cavitating and other high void fraction gas-liquid flows are encountered in many industrial and naval applications (Brennen 1995 and Terentiev *et al.* 2011). To gain insight into the flow physics and for the development and validation of physical models, knowledge of the spatial and temporal evolution of void fraction is often essential. However, the measurement of local void fraction is challenging, especially in cavitating flows where any intrusive probe could cavitate and perturb the flow considerably. Hence, a non-invasive measurement method is desired. But, optical methods also generally fail, as flows with volume fractions exceeding a few percent are effectively opaque.

In the present work, we describe an x-ray densitometry technique, which is capable of non-intrusively measuring the two dimensional projection of void fraction (along a line of sight) in a small scale cavitation tunnel through 21 cm of water, for up to a 225 cm<sup>2</sup> area at frame rates  $O(1 \text{ kHz})$ . This chapter introduces the technique and brings to the reader's attention some of its challenges and limitations. The tools which can be used to address these challenges are assembled from a myriad of sources.

In the next chapter we also present results from system validation experiments, where non-condensable gas was used to create a partial cavity behind a backward facing



step and the void fraction downstream was measured using x-ray, optical probes and high-speed video.

## 5.1 Introduction

To measure the void fraction in a cavitating or multiphase flow in a non-intrusive manner, electrical resistance and impedance techniques have been used quite successfully (Van Der Welle 1985, Ceccio and George 1996, York 2001, Holder 2005). However, these techniques are based on a soft-field, where the result is dependent on the flow topology and, depending on the flow considered, a priori knowledge of the topology may be required to obtain a solution. Radiation densitometry has the benefit of being a hard-field measurement, meaning the beam path is not dependent on the object being measured. Gamma-radiation based techniques have been used by themselves and also to validate electrical impedance measurements (Ceccio 2007, Tortora *et al.* 2006), but it is difficult for most research laboratories to gain access to a high quality radiation source such as a high energy gamma source or a synchrotron. The next best option is using x-ray techniques. X-ray tubes such as those used in the medical field are readily available, and multiple researchers have used x-ray imaging to investigate both cavitation (Stutz and Legoupil 2003, Coutier-Delgosha *et al.* 2007, Hassan *et al.* 2008 Aeschlimann *et al.* 2011) and bubbling fluidized beds (Hubers *et al.* 2001). Some groups have also developed custom systems based on electron beam scanning, such as Bieberle *et al.* 2011. A recent article by Heindel (2011) gives a comprehensive review of the use of x-ray systems in multiphase flow.

In the present experimental setup, we image gas-liquid flows through a test section that is 21 cm thick, thicker than used in most previously reported multiphase studies.

More significantly, we made large projection area,  $O(200 \text{ cm}^2)$ , time resolved measurements on the order of kilohertz frame rates, since this would be required to resolve the time-evolution of sheet cavitation. To perform these measurements with resources available, we put together a system utilizing a regular image intensifier with fast decaying phosphor and a source capable of high radiation output, albeit with a total exposure limited to only a few seconds at a time. The current system and experiments were briefly discussed in Mäkiharju and Ceccio (2011).

## 5.2 Physical principles of x-ray densitometry

When a beam of high energy photons, such as x-rays or gamma rays, is directed toward an object, a fraction of the photons passes through it without scattering or absorption (*i.e.* without attenuation). The fraction of photons of *any one specific energy*  $V$  that is not attenuated is related to the mass attenuation coefficients, densities and thicknesses of all the materials present along the path of the beam. Based on the Beer-Lambert law, we can write for a domain with  $N$  distinct materials

$$\frac{I}{I_0} = e^{-\sum_{n=1}^N x_n \mu_n / \rho_n} = \prod_{n=1}^N e^{-x_n \mu_n / \rho_n} \quad (5.1)$$

where  $I_0$  is the original intensity of the photon beam,  $I$  is the intensity of the photons transmitted,  $\mu_n / \rho_n$  is the mass attenuation coefficient,  $\rho_n$  is the density,  $x_n$  is the mass thickness ( $x_n = \rho_n t_n$ ), and  $t_n$  is the thickness over the traversed beam path through material  $n$ . The attenuation coefficient is a known property of photon energy and any material in the domain, and is related to the material density and its atomic properties (Hubbell and Seltzer, 2004). Therefore for a single material,  $N = 1$ , a measure of the

change in intensity can be converted into a measure of the average density of the material along the beam path. And, in the case of two phase gas-liquid flows, we can obtain a *quantitative* measure of the void fraction. These facts have been in use in the multiphase flow community for several decades (Stutz and Legoupil 2003, Hubers *et al.* 2005), but some of the nuances such as effects of beam hardening and imaging artifacts, while well known, have not always been discussed and not necessarily included in analysis. The following step-by-step derivation is included for thoroughness, and most importantly to show clearly where and what the assumptions are.

### 5.2.1 Void fraction of a two phase flow

With only water in the test section the x-ray beam passes through the air, *a*, an acrylic window, *g*, the water in the test section, *w*, and all other materials in its path. Thus, the fraction of photons of *any one given energy* that are not attenuated is given the expression

$$\frac{I_w}{I_0} = e^{-x_{air}\mu_{air}/\rho_{air}} e^{-x_{glass}\mu_{glass}/\rho_{glass}} e^{-x_{water}\mu_{water}/\rho_{water}} e^{-x_{glass}\mu_{glass}/\rho_{glass}} \dots \quad (5.2)$$

Substituting an unknown void fraction air-water mixture, *m*, in the test section in place of water, but keeping everything else the same, we can write:

$$\frac{I_m}{I_0} = e^{-x_{air}\mu_{air}/\rho_{air}} e^{-x_{glass}\mu_{glass}/\rho_{glass}} e^{-x_{mix}\mu_{mix}/\rho_{mix}} e^{-x_{glass}\mu_{glass}/\rho_{glass}} \dots \quad (5.3)$$

Dividing eqn. 5.2 by eqn. 5.3

$$\frac{\frac{I_w}{I_0}}{\frac{I_m}{I_0}} = \frac{e^{-x_{air}\mu_{air}/\rho_{air}} e^{-x_{glass}\mu_{glass}/\rho_{glass}} e^{-x_{water}\mu_{water}/\rho_{water}} e^{-x_{glass}\mu_{glass}/\rho_{glass}} \dots}{e^{-x_{air}\mu_{air}/\rho_{air}} e^{-x_{glass}\mu_{glass}/\rho_{glass}} e^{-x_{mix}\mu_{mix}/\rho_{mix}} e^{-x_{glass}\mu_{glass}/\rho_{glass}} \dots} \quad (5.4)$$

The original beam intensities, and effect of materials which remained the same, cancel and we are left with

$$\frac{I_w}{I_m} = \frac{e^{-x_{water}\mu_{water}/\rho_{water}}}{e^{-x_{mix}\mu_{mix}/\rho_{mix}}} = e^{-t_{water}\mu_{water} + t_{mix}\mu_{mix}} \quad (5.5)$$

For the sake of brevity, we switch to using the initial only in the subscripts to identify the material. As the path length (*i.e.* domain thickness),  $t$ , remained unchanged we can simply write the ratio of beam intensities, attenuated by the water and mixture, as

$$\frac{I_w}{I_m} = e^{t(\mu_m - \mu_w)} \quad (5.6)$$

which is equivalent to

$$\ln\left(\frac{I_m}{I_w}\right) = -t(\mu_m - \mu_w) \quad (5.7)$$

The attenuation coefficient of water is known, but the attenuation coefficient of the unknown void fraction mixture must now be written in terms of the void fraction and other known attenuation coefficients for elementary compounds. For the mixture of  $K$  elementary components the mass attenuation coefficient can be written as

$$\frac{\mu_m}{\rho_m} = \sum_{k=1}^K w_k \frac{\mu_k}{\rho_k} \quad (5.8)$$

Here  $w$  is the mass fraction of given elementary compound  $k$ . The density of the air-water mixture is given simply by

$$\rho_m = \alpha\rho_a + (1 - \alpha)\rho_w \quad (5.9)$$

where if  $\alpha$  is volume fraction of air. Now, relating the mass fractions,  $w_k$ , to void fraction we have

$$w_a = \frac{\alpha\rho_a}{\alpha\rho_a + (1 - \alpha)\rho_w} \quad (5.10)$$

for air's mass fraction, and for water's

$$w_w = \frac{(1 - \alpha)\rho_w}{\alpha\rho_a + (1 - \alpha)\rho_w} \quad (5.11)$$

Now for a two phase mixture of only air and water equation 5.8 becomes

$$\frac{\mu_{mix}}{\alpha\rho_a + (1 - \alpha)\rho_w} = \frac{\alpha\rho_a}{\alpha\rho_a + (1 - \alpha)\rho_w} \frac{\mu_a}{\rho_a} + \frac{(1 - \alpha)\rho_w}{\alpha\rho_a + (1 - \alpha)\rho_w} \frac{\mu_w}{\rho_w} \quad (5.12)$$

which in turn yields

$$\mu_{mix} = \alpha\mu_a + (1 - \alpha)\mu_w \quad (5.13)$$

Combining this with eqn. 5.7 we get

$$\ln\left(\frac{I_m}{I_w}\right) = -t(\alpha\mu_a + (1 - \alpha)\mu_w - \mu_w) = -t(\alpha(\mu_a - \mu_w)) \quad (5.14)$$

Similarly, if we start from eqn. 5.2 with all air in the test section, instead of water, we arrive at the following expression

$$\ln\left(\frac{I_m}{I_a}\right) = -t(\alpha\mu_a + (1 - \alpha)\mu_w - \mu_a) = -t(\alpha(\mu_a - \mu_w) - (\mu_a - \mu_w)) \quad (5.15)$$

The void fraction based on eqn. 5.14 is

$$\alpha = \frac{-1}{t(\mu_a - \mu_w)} \ln\left(\frac{I_m}{I_w}\right) \quad (5.16)$$

and the same void fraction based on eqn. 5.15 is

$$\alpha = \frac{-1}{t(\mu_a - \mu_w)} \left[ \ln\left(\frac{I_m}{I_a}\right) - t(\mu_a - \mu_w) \right] = \frac{-1}{t(\mu_a - \mu_w)} \ln\left(\frac{I_m}{I_a}\right) + 1 \quad (5.17)$$

It is not convenient to explicitly have the attenuation coefficients in the expressions, thus we simplify further after equating the right hand sides of the two expressions above to get

$$\frac{1}{t(\mu_a - \mu_w)} \ln\left(\frac{I_m}{I_w}\right) = \frac{1}{t(\mu_a - \mu_w)} \ln\left(\frac{I_m}{I_a}\right) - 1 \quad (5.18)$$

Multiplying through by  $t(\mu_a - \mu_w)$

$$\ln\left(\frac{I_m}{I_w}\right) = \ln\left(\frac{I_m}{I_a}\right) - t(\mu_a - \mu_w) \quad (5.19)$$

and rearranging gives us the attenuation coefficients as function of intensities

$$-t(\mu_a - \mu_w) = \ln\left(\frac{I_m}{I_w}\right) - \ln\left(\frac{I_m}{I_a}\right) = \ln\left(\frac{I_m I_a}{I_w I_m}\right) = \ln\left(\frac{I_a}{I_w}\right) \quad (5.20)$$

Finally, we can combine this with eqn. 5.16 leading to

$$\alpha = \ln\left(\frac{I_m}{I_w}\right) / \ln\left(\frac{I_a}{I_w}\right) \quad (5.21)$$

which provides the void fraction along any given beam path through the test section, as a function of the intensities of photon fluxes after passing through the test section filled with a mixture, all water, and all air (at any one given photon energy,  $V$ ). Note that for a polychromatic beam (*i.e.* a beam containing photons at multiple energies, and hence

wave lengths), the fraction of the beam which makes it through the domain is a function of photon energy  $V$ ,  $I = I(V)$ .

Unless we employ a synchrotron or a gamma source, the photon beam will have a wide continuous spectrum of energies. Also, most detectors, such as those used in the current research, do not discriminate energy (resolving photon energy, *i.e.* wavelength, also would be analogous to recording a color image), but instead only yield an indirect measurement in the form of energy deposited by the combination of photons of all detectable energies (analogous to a black and white image). Given that we have a polychromatic source and a non-energy-discriminating detector, use of equation 5.21 to estimate the void fraction from our “monochrome image” needs to be justified.

### 5.2.2 Beam hardening

Beam hardening is defined as the process of increasing the average energy level of an x-ray beam by preferentially greater attenuation of the lower energy photons, due to the energy dependence of the material’s mass attenuations coefficients, shown for water in figure 5.1. This well-known effect is the cause of a uniform object seeming to have density variation in computer tomography (CT) images (Hsieh *et al.* 2000), and in regular densitometry it can in some cases necessitate calibration using various thicknesses of material with attenuation properties matching those of the test object.

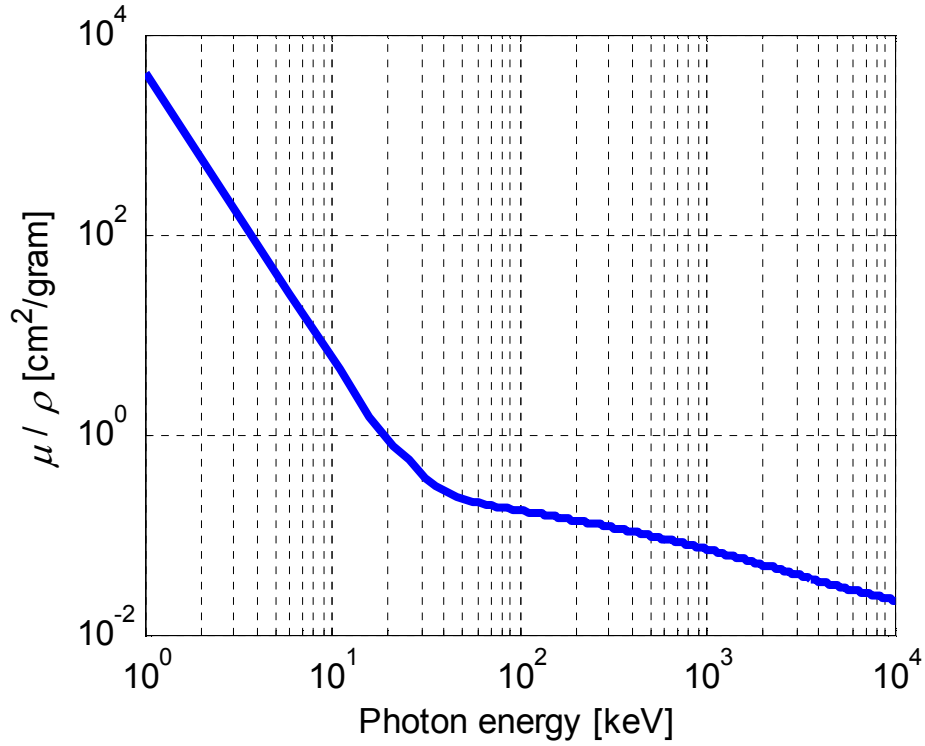


Figure 5.1 – Mass attenuation coefficient,  $\mu/\rho$ , of water as a function of photon energy plotted on a log-log scale. Figure based on data by Hubbell and Seltzer (2004).

The expression corresponding to, or the same as, eqn. 5.21 has been used by numerous researchers (Coutier-Delgosha *et al.* 2007, Aeschlimann *et al.* 2011). However, when using a polychromatic source and non-energy resolving detector, it should be noted that the value actually measured by the detector is not  $I$ , but the light intensity at each pixel of the camera, which is related to intensity  $I$  by

$$E = \int_0^{V_{max}} I(V)Q_{det}(V)VdV \quad (5.22)$$

where  $V$  is the photon energy,  $I(V)$  is related to number of photons hitting a given area of the imager screen and  $Q_{det}(V)$  is the image intensifier's detection efficiency (the efficiency at which x-ray photons are transformed into photoelectrons and then into



photons in the visible range). Figure 5.2, based on Thirlwall (1998), shows a typical shape of a curve for image intensifier conversion efficiency as a function of the photon energy.

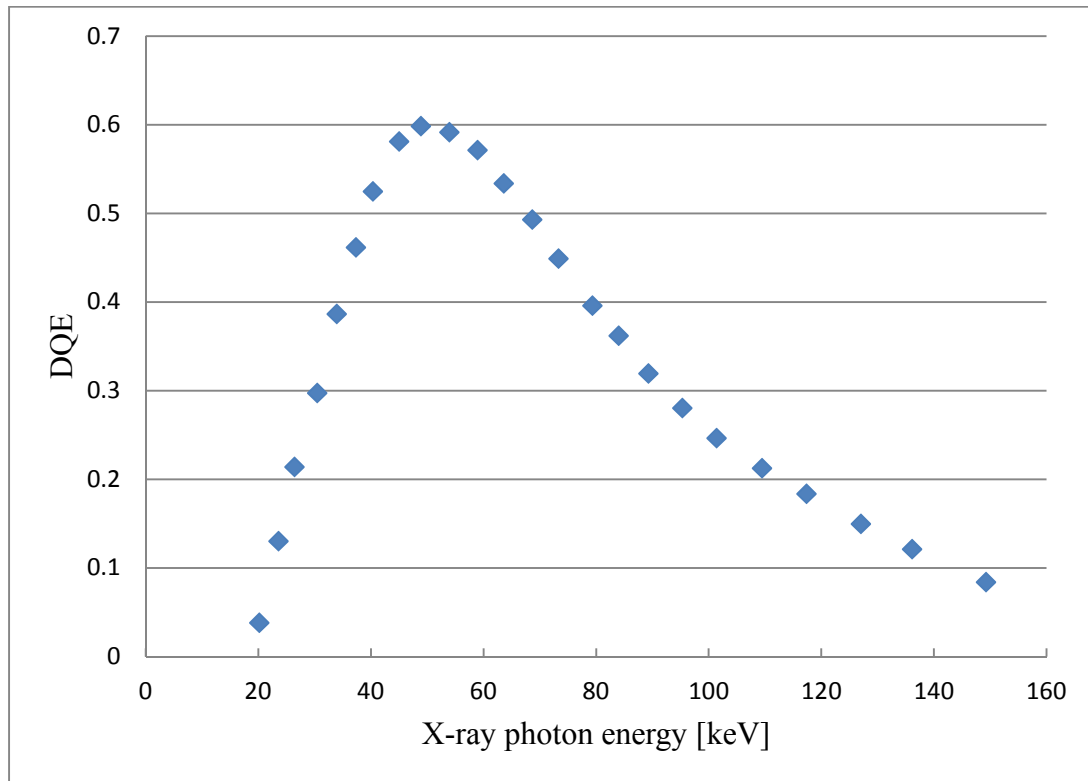


Figure 5.2 – Sketch of the general shape of detective quantum efficiency of x-ray image intensifiers with Cesium Iodine (CsI) input phosphors behind an aluminum/glass vacuum envelope, 0.2 g/cm<sup>2</sup> phosphor. Based on data from Thirlwall (1998).

As both the attenuation and detection efficiency depend on the energy of the x-ray photons,  $V$ ,  $I/I_0$  and  $E/E_0$  are not equivalent. As emphasized previously, the equation for determining the void fraction (5.21)

$$\alpha = \ln \left( \frac{I_m}{I_w} \right) / \ln \left( \frac{I_a}{I_w} \right) \quad (5.21)$$

is valid for intensities of monochromatic photon fluxes. If we were using mono-energetic x-rays or if we measured the full energy spectrum at each location so that we know the intensities as function of photon energy, then beam hardening would not be an issue. However, with the current system the light seen by the camera only gives a measure of the integral of the energy passing through the domain, so by using the grey scale values of the camera's pixels we are actually calculating the void fraction as if  $\alpha \approx \ln\left(\frac{E_m}{E_w}\right)/\ln\left(\frac{E_a}{E_w}\right)$ , where  $E$  is from equation 5.22. And in the experiments discussed,  $V$  is the photon energy ranging from 0 to 150 keV. If the beam is monochromatic or only photons at one specific energy,  $V_s$ , are counted, then we would have

$$\frac{\ln\left(\frac{E_m}{E_w}\right)}{\ln\left(\frac{E_a}{E_w}\right)} = \frac{\ln\left(\frac{\int_0^{V_{max}} \delta(V - V_s) I_m(V) Q_{det}(V) V dV}{\int_0^{V_{max}} \delta(V - V_s) I_w(V) Q_{det}(V) V dV}\right)}{\ln\left(\frac{\int_0^{V_{max}} \delta(V - V_s) I_a(V) Q_{det}(V) V dV}{\int_0^{V_{max}} \delta(V - V_s) I_w(V) Q_{det}(V) V dV}\right)} \quad (5.23)$$

$$= \frac{\ln\left(\frac{I_m(V_s) Q_{det}(V_s) V_s}{I_w(V_s) Q_{det}(V_s) V_s}\right)}{\ln\left(\frac{I_a(V_s) Q_{det}(V_s) V_s}{I_w(V_s) Q_{det}(V_s) V_s}\right)} = \frac{\ln\left(\frac{I_m}{I_w}\right)}{\ln\left(\frac{I_a}{I_w}\right)}$$

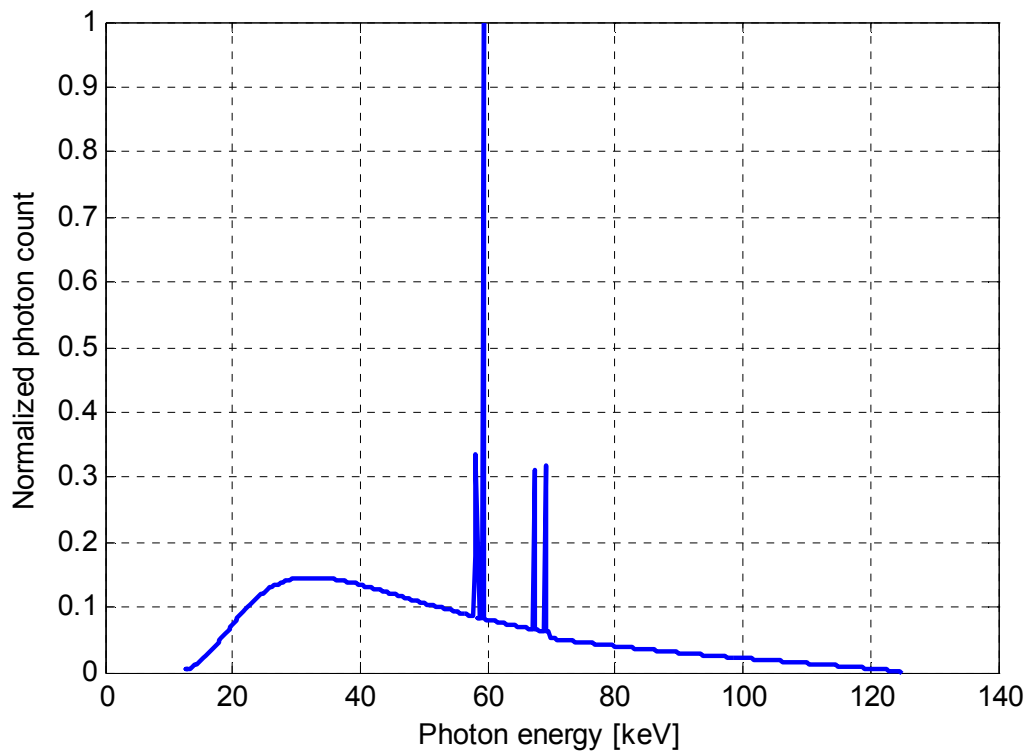
Hence for the specific case of monochromatic radiation, can we actually write

$$\alpha = \ln\left(\frac{E_m}{E_w}\right)/\ln\left(\frac{E_a}{E_w}\right) \quad (5.24)$$

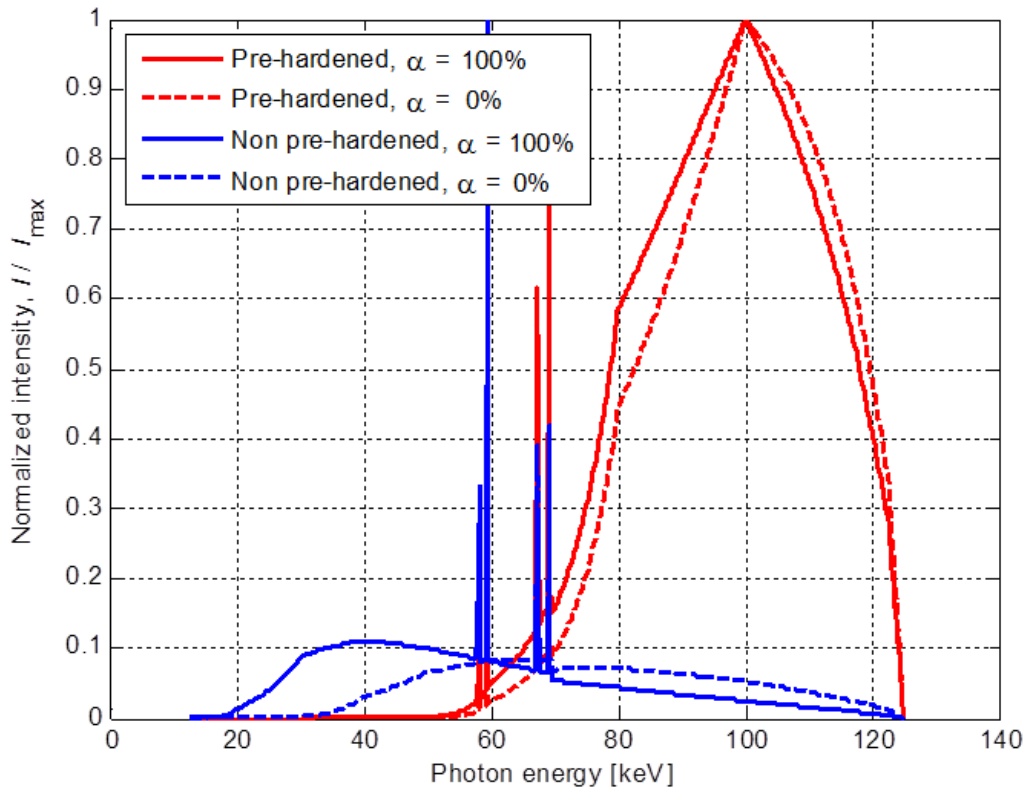
For all other situations, this is not a proper relationship.

To mitigate the impact of beam hardening on the measurements when using a polychromatic x-ray source and non-energy resolving detector(s), the beam can be pre-hardened. Pre-hardening refers to the use of filters to shape the beam's energy spectrum

before it encounters the object to be imaged. Normally the filter is a simple homogeneous metal (*e.g.* aluminum or steel) plate of material with known mass attenuation curve suitable for a given experimental situation. For these experiments, the use of a 0.64 mm thick steel filter pre-hardened the beam and decreased the difference of the lightest and darkest regions by nearly a factor of two. Without the increased attenuation of the lower energy photons everywhere, the difference in the amount of especially lower energy photons passing through the low void fraction region compared to those that were mostly absorbed by the 21 cm of water caused the imager to be saturated at the brightest region though the darkest region had almost no signal.



(a)



(b)

Figure 5.3 – a) X-ray source’s spectrum from a tungsten target simulated using SpecCalc by Poludniowski *et al.* (2009). This is a lightly filtered Bremsstrahlung spectrum, with the characteristic radiation spikes at the atom’s lower shell electron binding energies.

b) The photon energy spectra can be “shaped” by filtering with a highly attenuating material. Green - original spectra, Blue - spectra filtered/hardened with a 0.64 mm thick steel plate. Red – spectra after passing through the test section.

Figure 5.3 shows the simulated normalized photon energy spectra before and after the domain for both a pre-hardened and non-pre-hardened beam. It can be seen clearly that beam hardening modifies the shape of the spectrum of an x-ray beam as it passes through a domain. The lower energy photons in the spectrum are preferentially attenuated compared to the higher energy photons, leading to an increase in the average photon energy of the beam. However, for the pre-hardened beam, the shape of the spectra are much more closer before and after the domain.

To estimate the error resulting from the use of equation 5.21 for a polychromatic beam and non-energy resolving detector, the attenuation and detectable light energy,  $E$ , were simulated, and the void fraction was calculated based on both equation 5.24, and 5.21, which is the proper equation. The mass attenuation coefficients used were from NIST tables, with the detection efficiency estimated based on data shown in figure 5.2 and the x-ray source spectrum calculated using the SpecCalc-software by Poludniowski *et al.* (2009).

Figure 5.4 shows the error caused by using  $\alpha \approx \ln\left(\frac{E_m}{E_w}\right)/\ln\left(\frac{E_a}{E_w}\right)$  for both the unhardened and pre-hardened beams. Here

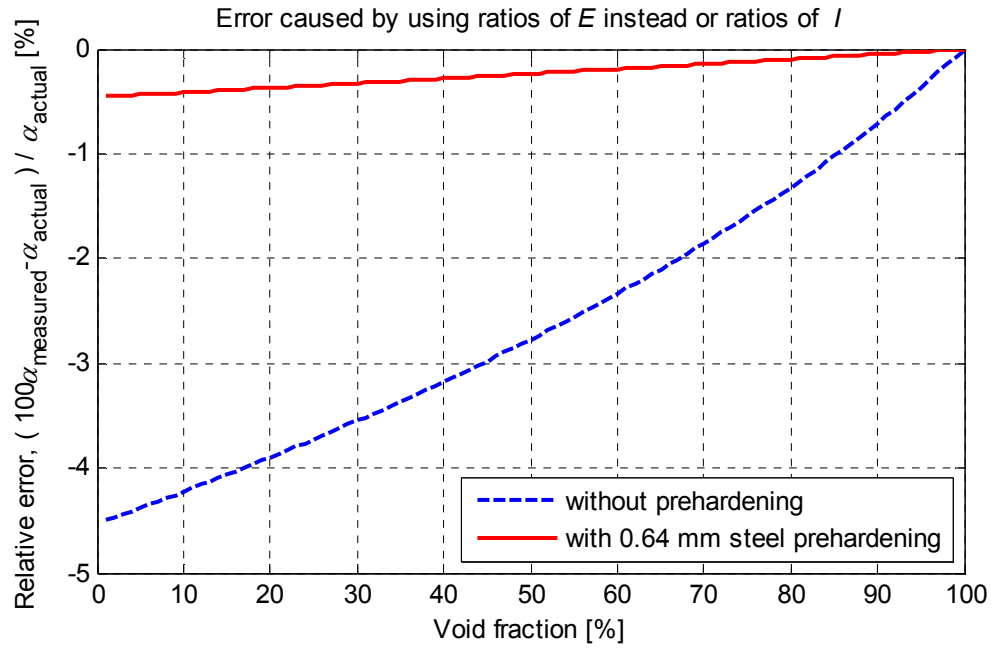
$$E = \int_0^{V_{max}} I(V)Q_{det}(V)VdV \approx \sum_{n=1}^N I_n Q_{det}(V_n) V_n \Delta V \quad (5.25)$$

where the discretized energy levels are  $V_n = (n - 1)\Delta V$  and  $\Delta V = V_{max}/(N - 1)$ , and the intensity at each energy level,  $I_n$ , is given by

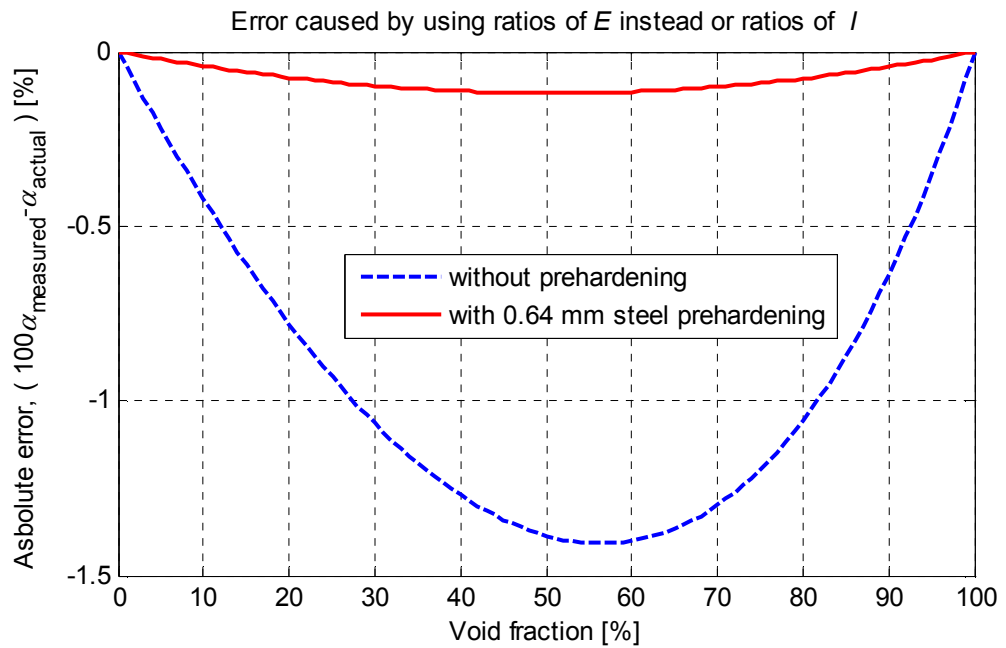
$$I_n = I_{0,n} e^{-(\alpha)t_{mix}\mu_{air,n} \dots} \quad (5.26)$$

$$e^{-(1-\alpha)t_{mix}\mu_{water,n}} e^{-x_{glass}\mu_{glass,n}/\rho_{glass}} e^{-x_{filter}\mu_{filter,n}/\rho_{filter}}$$

Here the x-ray source's spectrum,  $I_{0,n} = I_0(V_n)$ , is calculated using the SpecCalc by Poludniowski *et al.* (2009). There are many other sources of uncertainty in the measurement, but the idealized simulation shows strictly the effect of beam hardening. The error is dependent on the void fraction in the domain, but for all void fractions it can be seen that even a modest pre-hardening can reduce the error by almost an order of magnitude.



(a)



(b)

Figure 5.4 – Illustration of the reduction of error when the void fraction is computed using the ratio of the energy from a polychromatic beam with or without pre-hardening. a) Relative and b) absolute errors in void fraction, as a function of the actual void fraction.

Alles and Mudde (2007) also discuss the effects of beam hardening and introduce “effective attenuation coefficients” to deal with it, and their approach seems promising for tomography. However, as shown in figure 5.4b for the cases discussed in this paper, the maximum bias error for the calculated void fraction can be reduced to less than 0.2% simply by pre-hardening, and this is negligible compared to other sources of error and uncertainty as discussed later. Therefore, pre-hardening alone was used to mitigate the effects of beam hardening in the current set of experiments.

### **5.3 Test facility**

The x-ray system was constructed for use at an existing cavitation tunnel at the University of Michigan, shown in figure 5.5. To facilitate the measurements, a new test section was designed by the author, to allow better optical access and use of thinner windows, enabling also a larger low attenuation x-ray beam access. This test section, shown in figure 5.6, has smooth round-to-square transitions at both ends with maximum angle of 5.8 degrees, and the straight segment is 86.4 cm long with a cross-section that is  $(21.0 \text{ cm})^2$  with 2.9 cm chamfers in the corners. On all four sides 15.2 cm by 86.4 cm windows provide good optical access, and the transparent windows could be made as thin as 1 cm, to reduce the baseline x-ray attenuation. The windows can also be replaced with optically opaque metallic or composite windows possessing lower x-ray attenuation properties than acrylic, while maintaining the strength necessary to not significantly deform or fail during the experiments. The flow in the test section can achieve speeds in excess of 18 m/s, and the pressure can be varied from near vapor pressure to over 200 kPa.



Figure 5.5 – The University of Michigan’s 9” water tunnel before construction of the new platform. A 12 ft x 18 ft test stand capable of accommodating the lead shielding’s weight and size was designed by the author. The white arrow shows the direction of the flow and also points to the test section.

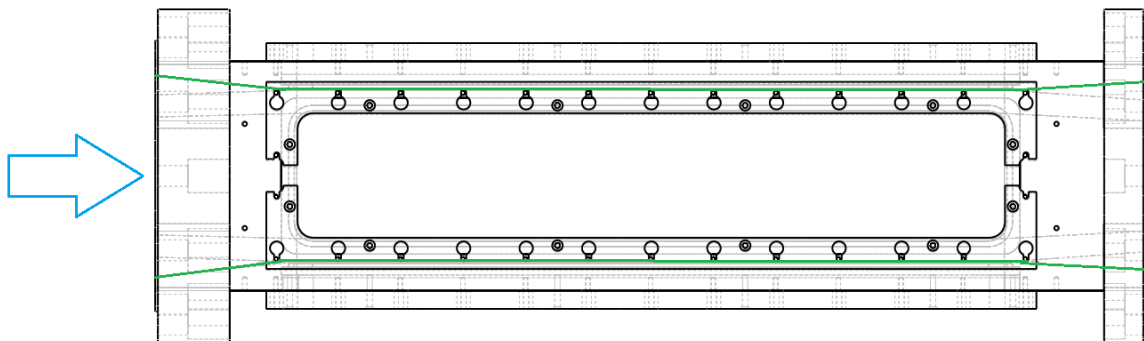


Figure 5.6 – Sketch of the new test section. The green lines indicate the interior contours on the centerline and the blue arrow shows the flow direction.



#### **5.4 X-ray source and imager**

The x-ray source and detector were chosen to provide the necessary photon energy and flux in order to achieve time resolved measurements. The source selected, Varian G-1092, is a 150 kV rotating anode tube designed for radiography, cineradiography and angiography. It can be operated at up to 800 mA (at 81kV) or 150 kV (at 433 mA), when supplied by the selected 65 kW high frequency (100 kHz) generator with a high-speed starter (CMP 200 DR). (The high speed starter was necessary to achieve the fastest anode RPMs and thus enable higher power levels to be used without damaging the source.) The photon flux needed to be sufficiently high both in the number and energy of photons that a sufficient fraction passes through the object, but low enough that enough attenuation takes place over short distances to yield an adequate contrast and signal-to-noise ratio when there are subtle differences in void fraction. The source had a selectable focal spot size of 0.6 or 1.2 mm, allowing less focal spot blur or higher power when using the smaller or larger spot size, respectively. Another benefit of using a medical source only going up to 150 kV is that the photon energies are also suitable to be used with commercial image intensifiers, as shown in figure 5.2.

Figure 5.7 shows a schematic of how the essential system components interact, while figure 5.8 shows conceptually the relative positions of the main components, and figure 5.9 shows photos of the actual system components and gives additional detail.

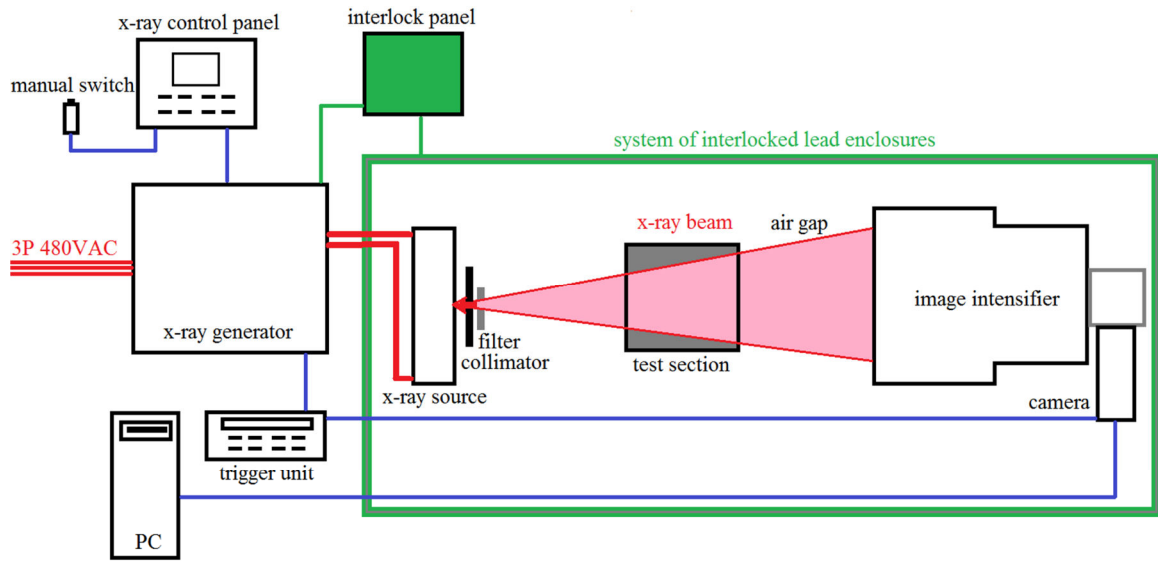
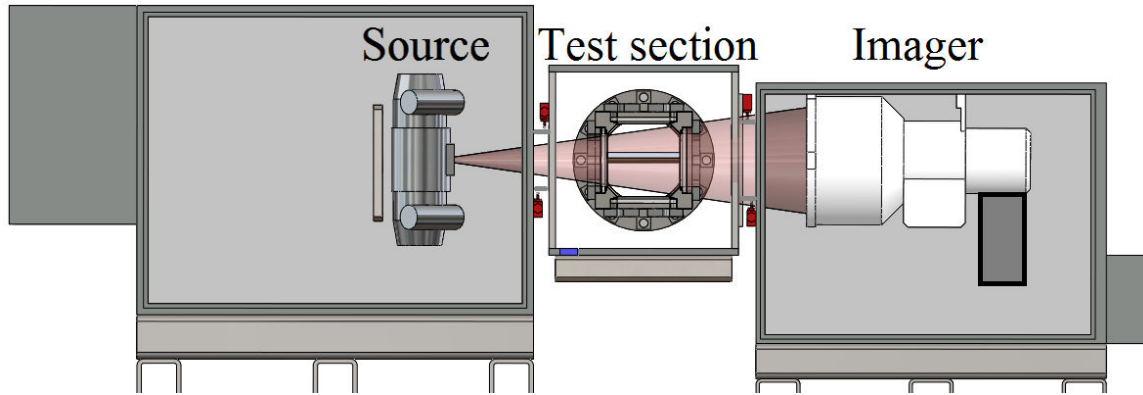
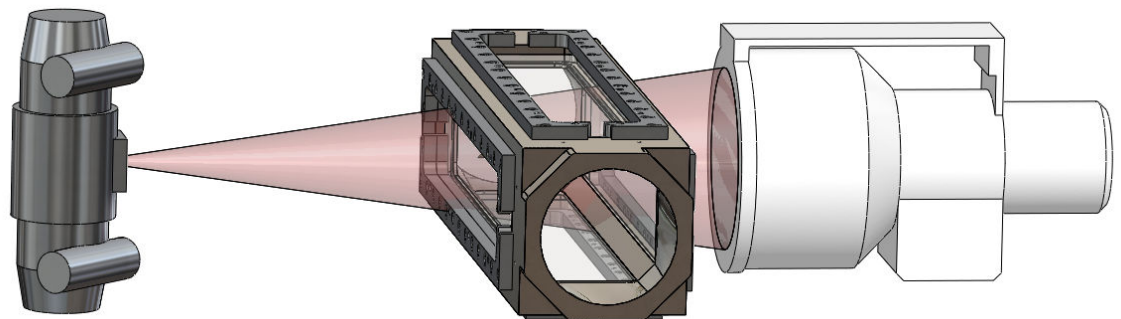


Figure 5.7 – Schematic of the x-ray system’s key components. The control panel is used to set the x-ray tube’s current, voltage and duration of exposure. The II field size is set by a three position toggle-switch (not shown), while software running on the PC is used to set the camera’s exposure settings, which include resolution, frame rate, exposure time, and number of post trigger frames to be captured. A push-button switch is used to trigger the exposure, which can only occur if all the interlocks are engaged. Once an exposure begins, a stepped down AC voltage signal is sent to the trigger unit (Stanford Research Systems model DG535 delay generator), which after a specified delay sends a TTL signal to the high speed camera.

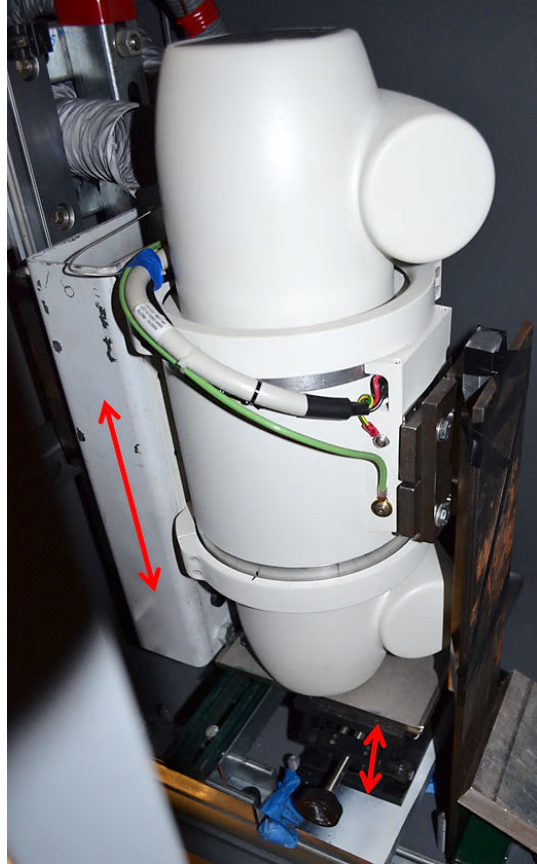


(a)

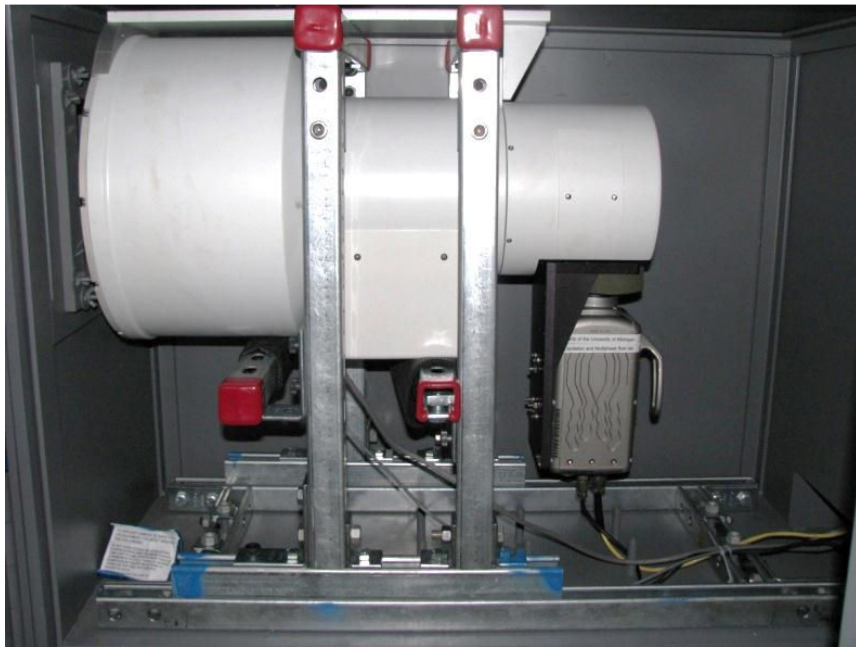


(b)

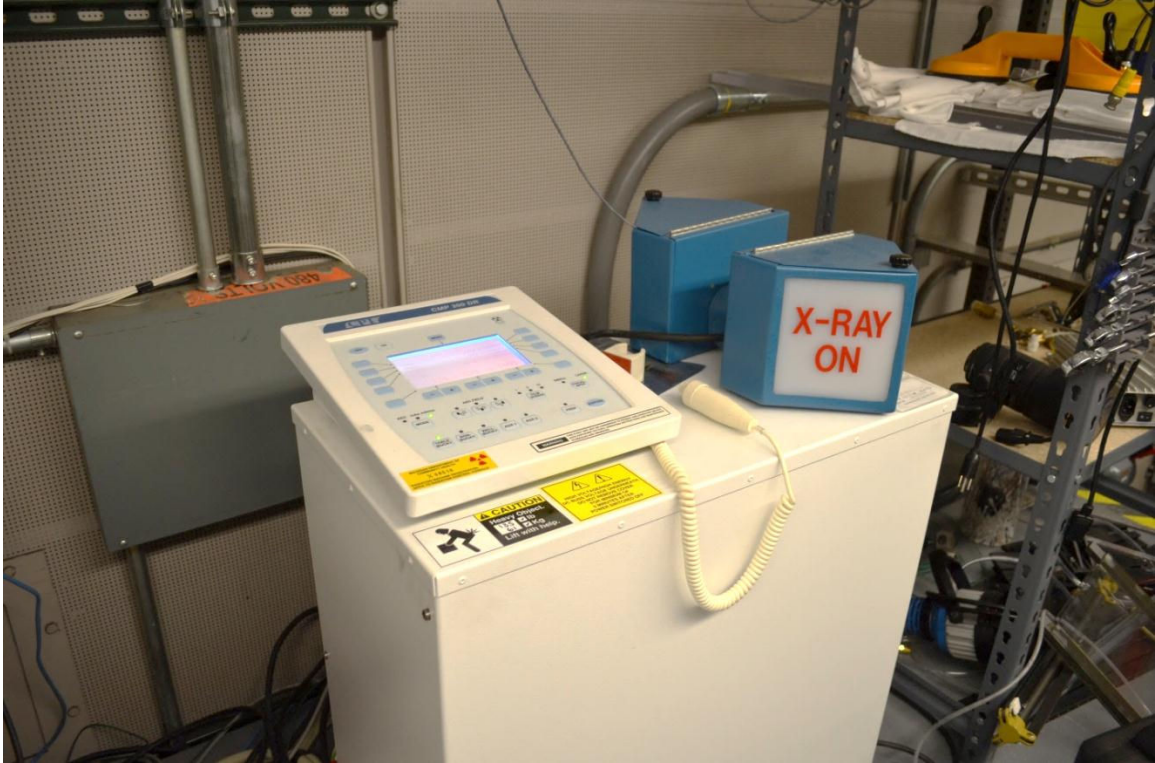
Figure 5.8 – a) Side elevation view of the x-ray densitometry system showing the source enclosure on the right, test section in the middle and imager enclosure on the left. The red cone indicates the x-ray cone beam originating from the source. b) View from an oblique angle. Note the "large" (>70 cm) distance between the test section and the imager. This space provides an "air gap" which reduces the amount of scatter reaching the imager. The source is housed in a separate enclosure and its distance to the test section can be adjusted. The further the source is, the lower the beam intensity, which goes as  $1/(\text{distance})^2$ , but the beam will encounter more of the domain with a shallower angle (see section 5.7.10).



(a)



(b)



(c)

Figure 5.9 – a) The x-ray source is shown in its enclosure. The red arrows indicate the vertical adjustment mechanism, which is connected on a horizontal slide at the bottom of the enclosure. b) The image intensifier with the high speed optical camera. Together these components form the "imager". Both source and imager are housed in the custom lead enclosure designed for easy access to the test section. c) The x-ray control panel, manual switch and warning lights on the high voltage generator.

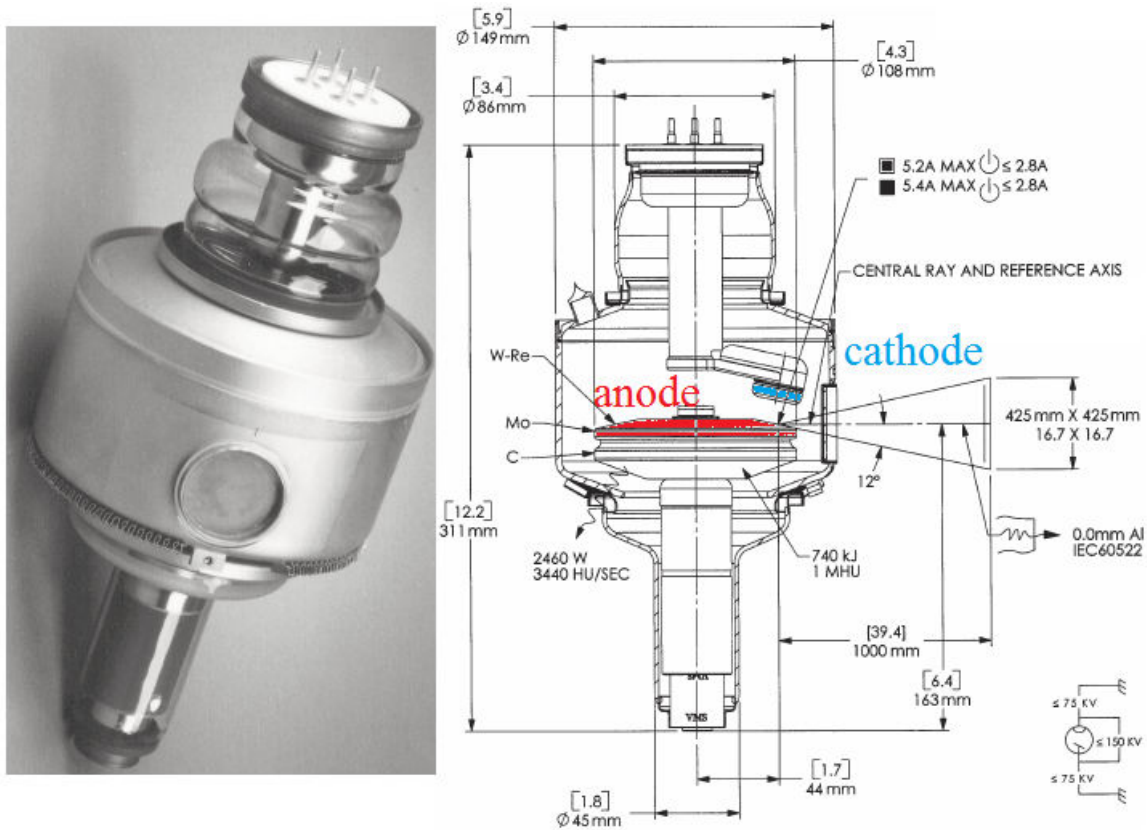


Figure 5.10 – Photo and a diagram of a rotating anode x-ray tube insert, Varian G-1092. Image from the G-1092’s data sheet by Varian. The cathode is colored blue and the anode red, to make it easier to identify them. Both are housed in a vacuum. To generate the x-rays, electrons are freed at the cathode and then accelerated to the focal spot on the anode, by up to a 150 kV electrical potential difference.



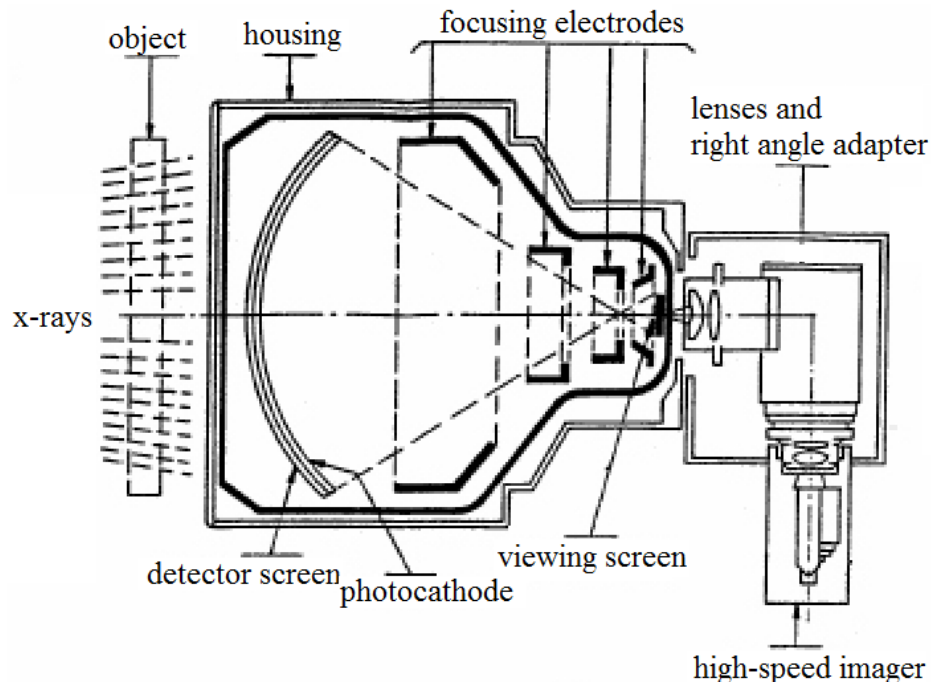


Figure 5.11 – A sketch showing the main components of a generic image intensifier with a right angle adapter and a high-speed imager mounted to it. This sketch is a retouched version of one posted on Alternative Vision Corporation’s web-page ([http://www.alt-vision.com/medical\\_imaging\\_optics.htm](http://www.alt-vision.com/medical_imaging_optics.htm)).

The imager subsystem depicted in the previous figures is comprised of a high-speed camera (Vision Research v9.0) coupled with a high efficiency, high-resolution image intensifier (II). A tri-field (30.5/22.9/15.2 cm) image intensifier was chosen to enable image magnification without changing the physical setup of the experiment. It has a resolution of 48/54/62 line pair per cm, conversion factor of  $320 \text{ cdm}^2/\text{mRs}^{-1}$  and 65% DQE (detection quantum efficiency) at 59 keV. An image intensifier was chosen rather than an array of detectors to have an economical system that is still capable of rapidly acquiring information about the attenuation through multiple beam-paths. Using a two-dimensional detector also enables partial bubble or particle tracking from one projection. (If two orthogonal projections would be measured simultaneously, this would yield the

3D particle location at each instant in time, assuming the seeding density is sufficiently sparse for the particles not to often overlap.)

The incoming x-ray photons enter the enclosure with the II through a viewport, interact with the input phosphor to produce photons in the visible wave lengths, which are then converted into electrons that are subsequently accelerated and hit a second output phosphor. The output phosphor produces photons in the visible wavelengths detectable by an optical high-speed camera. The light collected at each of the camera's 1.92 million pixels (or a subassembly of neighboring pixels) gives a measure of attenuation through one unique beam path.

The Vision Research Phantom v9.0 was controlled using Phantom Camera Control v. 8.06.606.0-C software. The movies were recorded in Vision Research's CIN-format (Vision Research 2007) and converted to a format suitable for post-processing in Matlab. For the conversion, a modified version of code by Hendrix (2010) was used.

#### 5.4.1 Shielding

The enclosures around the source, test section and imager were originally designed for a 320 kV source, and hence provide adequate protection from the 150 kV source. The lead thickness for the primary beam's beamstop is 3.2 cm (thickness of locations where beam is normal to the enclosure wall). Lead thickness for locations where primary beam might graze the wall is 1.9 cm and 1.3 cm where only scatter can be encountered. The shielding was designed by the author, fabricated by Applied Machining / Nuclear Lead at Oak Ridge, TN. The radiation safety survey was done by University of Michigan's Department of Occupational Safety and Environmental Health (Dr. J. Miklos) and by the



State of Michigan OSEH. If biological samples were to be tested, the U.S. FDA informed us that they would also be required to do an inspection.

## **5.5 Void fraction measurement accuracy**

The resulting void fraction measurement is subject to error arising from noise, scatter and other phenomena discussed in sections 5.6 and 5.7, but an upper limit for the void fraction accuracy in a single frame is dependent on the dynamic range of the camera and fraction of this range corresponding to the lowest and highest void fraction of interest. (When averaging multiple frames, one could postulate that with no bias error a true intermediate value of say 23.4 with +/- 0.5 of noise producing values between 22.9 and 23.9 registering as 23 and 24 from time to time and as the number of samples averaged grew, the mean would be expected to approach 23.4.) The camera in the current system, Phantom v9.0, is 8-bit and hence no light corresponds to a grayscale value of zero and the sensor saturates at a value of 255. Ideally we would like to have zero be the value for a void fraction zero, and 255 to be the value for a void fraction of unity. However, to ensure that the sensor is not saturated and that some light is getting through, we aimed to have 10 and 245 for the values with minimum and maximum void fractions, respectively.

### **5.5.1 Void fraction accuracy in theory**

To obtain a reasonable estimate of the accuracy of the void fraction measurement (for a single pixel in a single frame) let us assume the value at each pixel of the 8-bit camera is correct to within +/- $\Delta I$ , where is the  $\Delta I$  uncertainty in the intensity (+/- 0.5 for a perfect camera, and for a real camera something higher than this due to noise). Assuming

statistically independent variables, following Doebelin (1990), the overall error can be estimated from

$$E_{\alpha_{rms}} = \sqrt{\left(\Delta I_m \frac{\partial \alpha}{\partial I_m}\right)^2 + \left(\Delta I_a \frac{\partial \alpha}{\partial I_a}\right)^2 + \left(\Delta I_w \frac{\partial \alpha}{\partial I_w}\right)^2} \quad (5.27)$$

where the void fraction  $\alpha$  is based on equation 5.21 from section 5.2.1. The partial derivatives of the three terms are

$$\frac{\partial \alpha}{\partial I_m} = \frac{-1}{I_m \ln \frac{I_a}{I_w}}$$

$$\frac{\partial \alpha}{\partial I_a} = \frac{\ln \frac{I_m}{I_w}}{I_a \ln^2 \frac{I_a}{I_w}}$$

$$\frac{\partial \alpha}{\partial I_w} = \frac{-1}{I_w \ln \frac{I_a}{I_w}} + \frac{\ln \frac{I_m}{I_w}}{I_w \ln^2 \frac{I_a}{I_w}}$$

Assuming that the uncertainty of intensity when measuring mixture, air or water is the same,  $\Delta I_m = \Delta I_a = \Delta I_w$ , expression 5.27 can be simplified to

$$E_{\alpha_{rms}} = \frac{\Delta I_m}{I_a I_m I_w \ln^2 \frac{I_a}{I_w}} \sqrt{I_a^2 (I_m^2 + I_w^2) \ln^2 \frac{I_a}{I_w} - 2 I_a^2 I_m^2 \ln \frac{I_a}{I_w} \ln \frac{I_m}{I_w} + I_m^2 (I_a^2 + I_w^2) \ln^2 \frac{I_m}{I_w}} \quad (5.28)$$

Assuming  $\Delta I = +/- 0.5$  or  $+/- 1.0$  and intensity with zero void fraction to be  $I_w = 6$  and with void fraction of unity to be  $I_a = 240$ , we get the results presented in figures 5.12 and 5.13. It is immediately obvious that the uncertainty envelope (red lines) grows as one approaches the lower values.

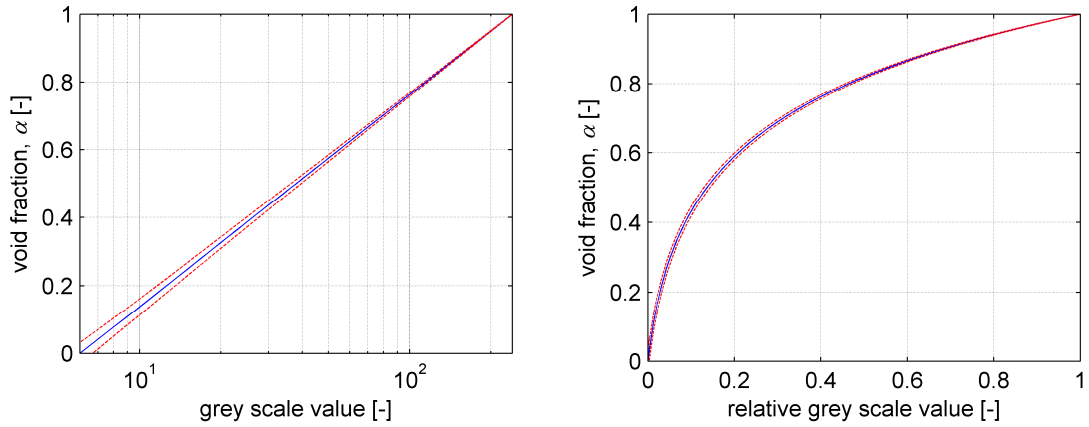


Figure 5.12 – Assuming  $\Delta I = \pm 0.5$ ,  $I_w = 6$  and  $I_a = 240$ . True void fraction (blue curve) and uncertainty envelope (within red lines), as a function of the pixel's grey scale value.

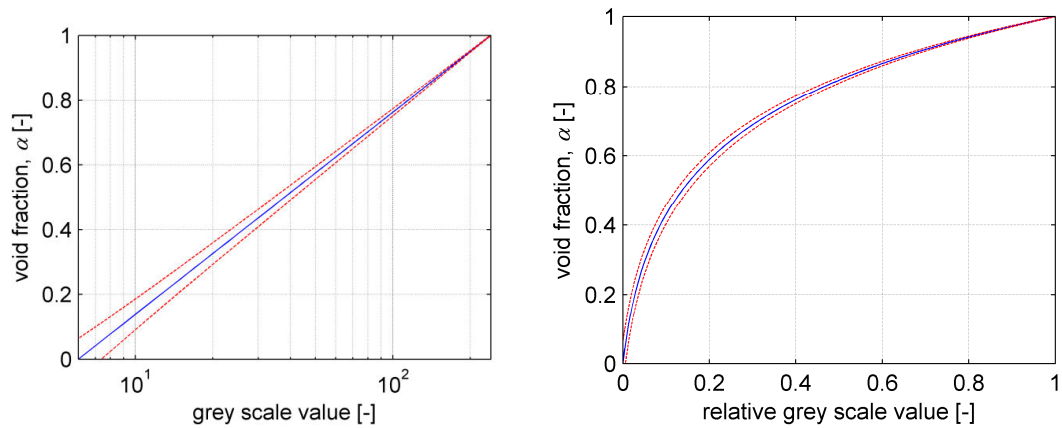


Figure 5.13 – Assuming  $\Delta I = \pm 1$ ,  $I_w = 6$  and  $I_a = 240$ . True void fraction (blue curve) and uncertainty envelope (within red lines), as a function of the pixel's grey scale value.

### 5.5.2 Calibration procedure for the sub-range of the void fractions

If one wishes to investigate a range other than the full range of void fraction from 0 to 1, it is possible to narrow the range by defining as all air and as all water conditions where a container of desired width is placed in front of the test section. Then with the test section full of water, the all air condition is defined as one where the container is empty, and all water condition is one where the container and test section are both full of water. Using thus obtained all air and all water values, the void fraction in the desired range can now be calculated based on the attenuation through a mixture in the test section. The container must be kept full and not be moved, so that the attenuation of the container itself remains the same and cancels its effect as in eqn. 5.5.

### 5.5.3 Experiment for measured versus actual void fraction

Figure 5.14 shows the experimental setup for a straightforward void fraction validation case. Six containers with parallel walls spaced 1.6 mm to 101.6 mm apart were constructed for use as void fraction calibration phantoms. The attenuation due to the test section, which was also in the beam's path, and container material cancels as in eqn. 5.5. These containers had drains so that they could be individually filled and emptied without moving them. The combined path thickness of water could be varied from 0 to 191.3 mm. The cumulative uncertainty of the water path thickness through the six calibration volumes was estimated to be 1-2 mm leading to a 0.5-1.0% uncertainty in the reference void fraction. Figure 5.15 shows the results from 14 different fill combinations with void fraction ranging from 0 to 100%, and figure 5.16 shows the relative error in void fraction.

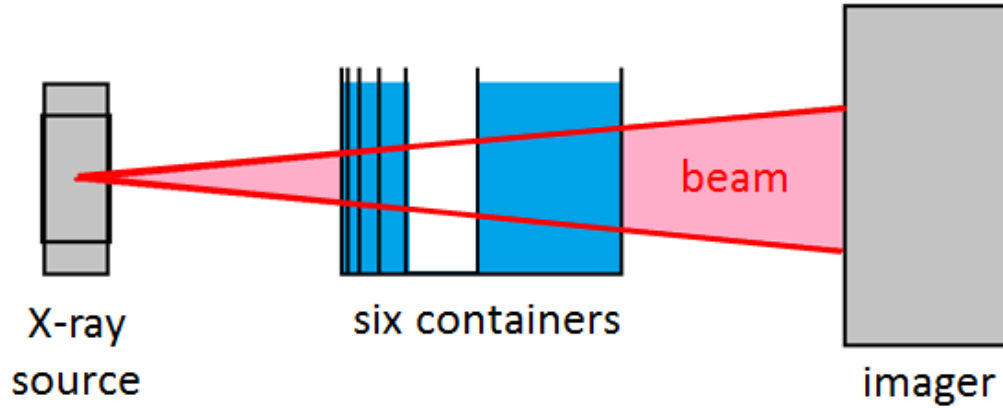


Figure 5.14 – The experimental setup for the void fraction comparison. The containers between were filled and emptied in different combinations, thus providing varying, but known, void fractions within the accuracy of container thickness (*i.e.* uncertainty of water thickness along the beam path).

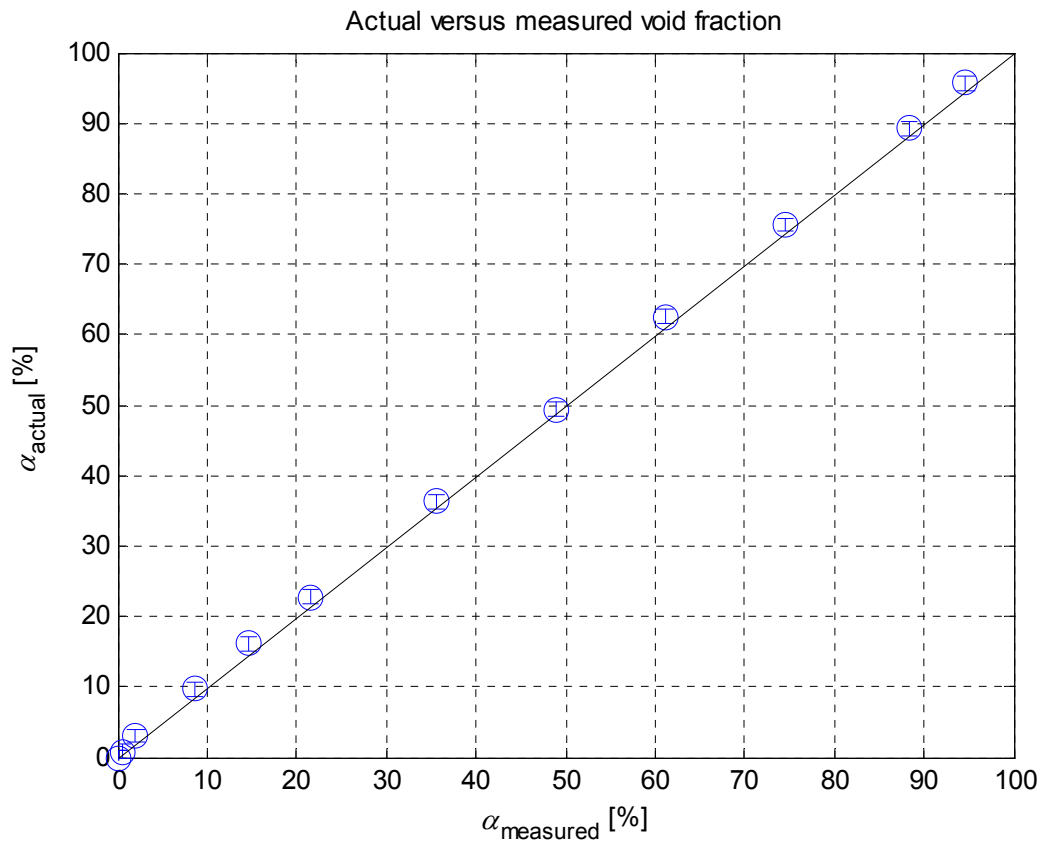


Figure 5.15 – Comparison of void fraction based on container thicknesses versus the measured void fraction. The circles are measurement results and the solid line is the curve these points would ideally be on. From measurement, 200 frames and a 60,000 pixel area averaged to get a single value for the void fraction for comparison.

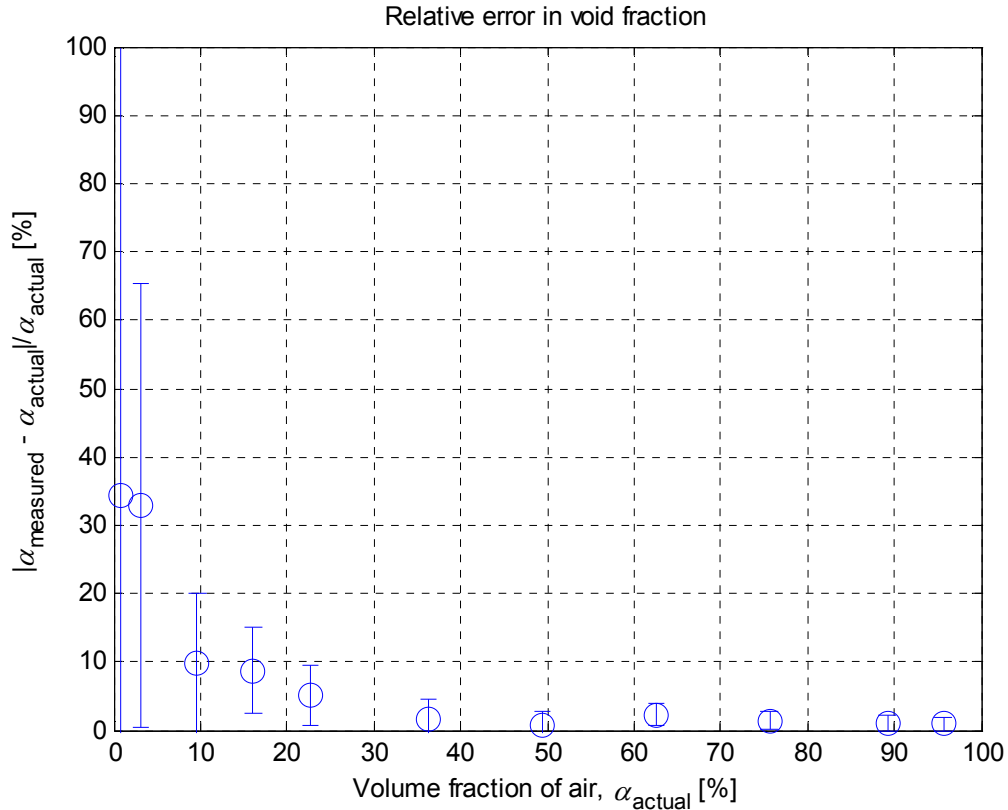


Figure 5.16 – Relative error in void fraction based on container thicknesses versus the measured void fraction. From measurement, 200 frames and a 60,000 pixel area averaged to get a single value for the void fraction for comparison.

The deviation of about -0.74% in figure 5.15, could potentially be attributed to varying error in the thickness of the six reference volumes, which would have easily introduced a bias error. Also random variation of the source strength could cause a minor difference, if  $I_0$  varied for the measurements. A bias error varying smoothly with void fraction could have been expected from the beam hardening and the varying effect of dynamic range as a function of the void fraction. (Note that based on figure 5.4 the actual could be expected to be up to 0.2% higher due to beam hardening alone.)

These results suggest that across a path of 191.3 mm of water and ~8 cm of acrylic the x-ray system can be calibrated to determine the path averaged volume fraction

in the domain within a few percent void fraction over a range of void fraction from 0% to 100%. The precision in void fraction in a narrower range can be improved, if the desired measurement range is reduced and calibration in that range performed (Sect. 5.5.2).

## **5.6 Temporal resolution**

The temporal resolution is limited by both the frame rate of the camera, flux and the decay time of the II's input and output phosphors. Another limitation is the availability of sufficient light, depending on the light sensitivity of the camera, intensity of the x-ray flux reaching the imager, II's conversion efficiency, light gain, etc. Whether the main limitation is the available light or phosphor decay time, depends on the experimental setup.

Assuming the phosphor decay time to be  $O(1\text{ms})$ , one empirical measure of the temporal resolution would be to have an object move rapidly across the beam with a precisely known velocity of at least 10 pix/ms while recording images at  $\sim 5\text{kHz}$ . From the lagging "ghost" of the object the time resolution could be determined. Another option would be to use a very high-speed shutter, or assume the time constant of the source to be an order of magnitude smaller than that of the imager's. In both of these cases, we could use a time trace of the area-averaged image intensity to experimentally determine the time constant.

### **5.6.1 Time constant of the imager system**

The phosphor of the II has a finite rise and decay time, which limits the temporal resolution. (that is if the time constant is 1 ms, little is gained by recording images of the slowly decaying phosphor at frame intervals orders of magnitude larger than the decay

time constant.) The data sheet for the image intensifier (Thales 2006) lists that for a 5 mR/s exposure, the luminescence rises to 50% and 80% of the final value in 1 ms and 10 ms, respectively. The reported decay times are 30% and 10% after 1 ms and 10 ms, respectively. These numbers do not yield a simple time constant,  $\tau$ , fitting the usual  $e^{-t/\tau}$ . However, based on the 10 ms luminosities alone, the rise and decay time constants would be 6.2 ms and 4.3 ms, respectively. A simple test was conducted using a time series of frames, which formed the time averaged image shown in figure 5.17. A time trace and expanded view of the average image intensity is shown in figures 5.18 and 5.19.

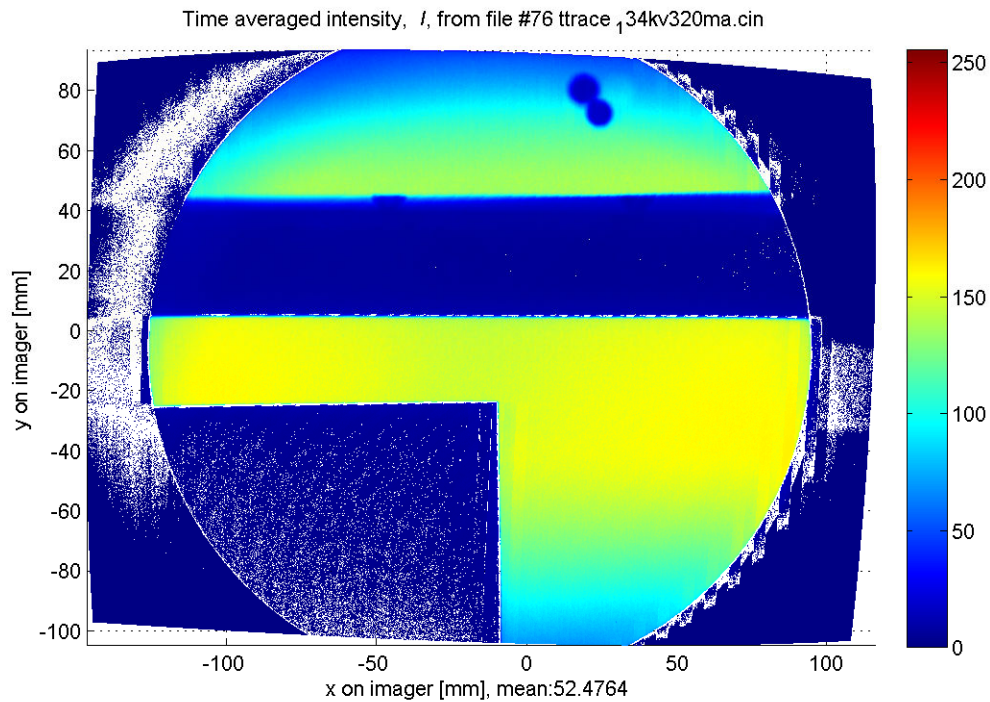


Figure 5.17 – Time averaged image of the case for which the following figures present the area averaged time traces. There were no transient events in the test section; hence for an ideal system the next figure should show a step function.



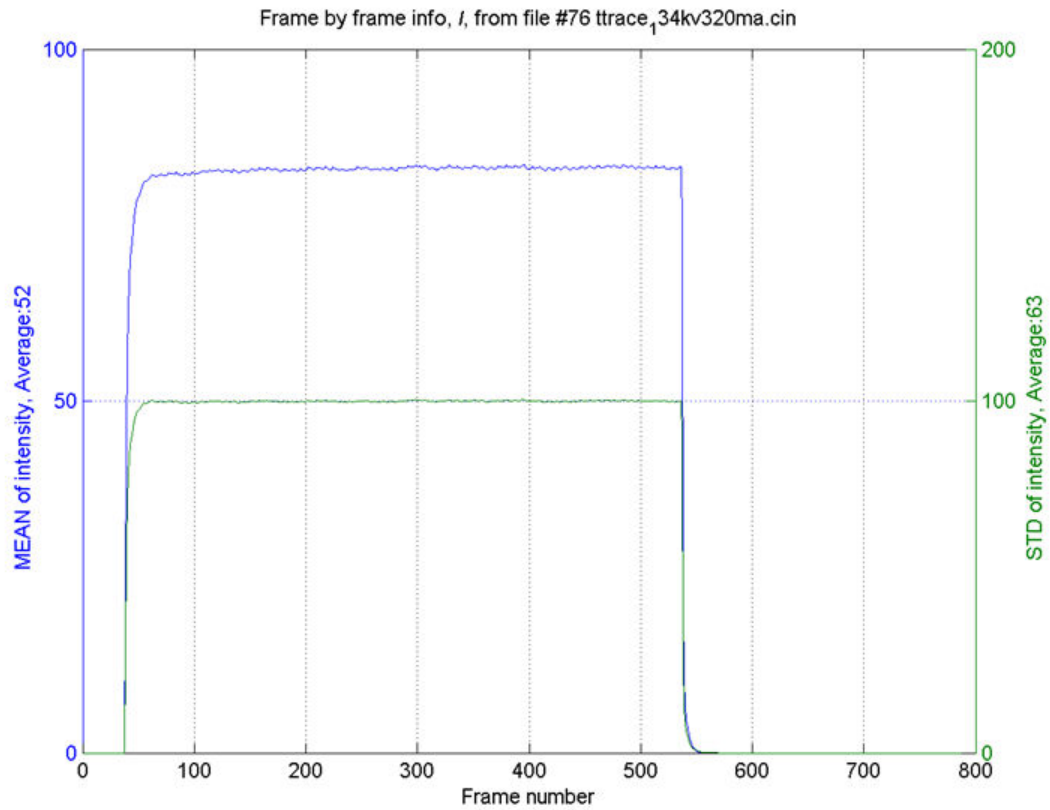


Figure 5.18 – Time traces of spatially averaged mean intensity, and standard deviation of intensity. The vertical units are the pixel's grey scale values, and each frame was recorded 1 ms apart. The ordinate values are averages over the entire exposure of the respective quantity.

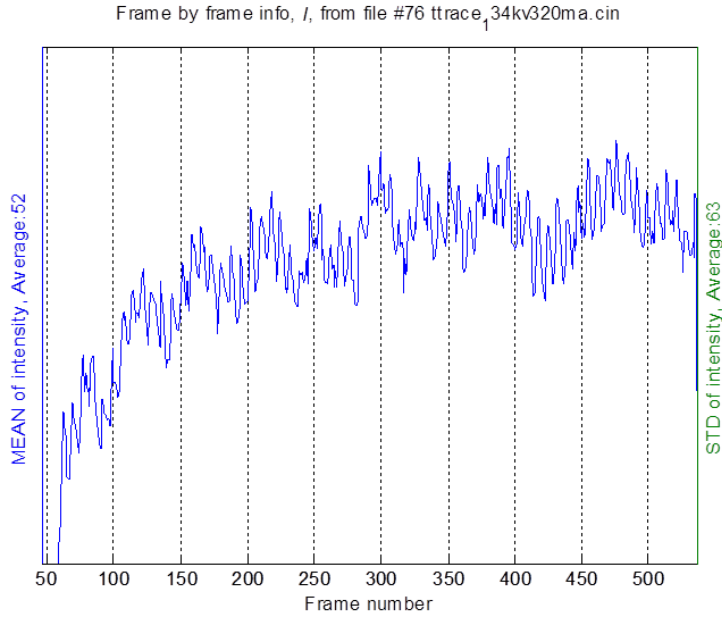


Figure 5.19 – Expanded view of the time traces of the spatially averaged mean intensity shown in figure 5.18. There is a ripple present due to noise, which was not evident in fig. 5.18. The ordinate values are averages over the entire exposure of the respective quantity.

Figures 5.18 and 5.19 showed the time trace of average intensity of the entire image, and in an ideal case we should have seen a true step function. For this particular case, the rise time to 95% of the final value was approximately 12.9 ms. Assuming the source's rise and decay times were orders of magnitude faster and that the lag is due to the phosphor, the imager's time constant would be  $\tau \approx 4.3$  ms.

If the time constant of the imager's phosphor is thus assumed to be  $\sim 4$  ms, to insure that one records independent frames it would be better, for instance, to pulse the source for 1 ms followed by 3 ms of no emissions, and record only a single frame during this 4 ms. While the current system is not capable of this, it will be considered in the future. Also, the imager's time constant will be verified in the future by use of a high speed shutter.

### 5.6.2 Time dependence of the x-ray source

The slow drift in average intensity observed in figure 5.19 over time cannot be attributed necessarily to the imager alone. According to the sources manufacturer (phone communication with Varian), the flux of photons from the x-ray source has some time dependence that can be caused by the generator, filament heating, anode heating, etc. Figures 5.20 and 5.21 show time traces where the ordinate's range has been reduced. Disregarding the first ~50 frames in 5.20, the mean intensity drifts by ~1/2 gray scale values (GSV) and there is a less than 1/4 gray scale value jitter around the mean. For all the void fraction calculations, only the data after the mean reaches ~0.5 GSV from the final value were considered. It's worth noting that based on equation 5.28 in section 5.5.1 the error caused by a 0.5 GSV drift can be estimated and found to be 2.6% and 0.2% at 10% and 90% void fractions respectively.

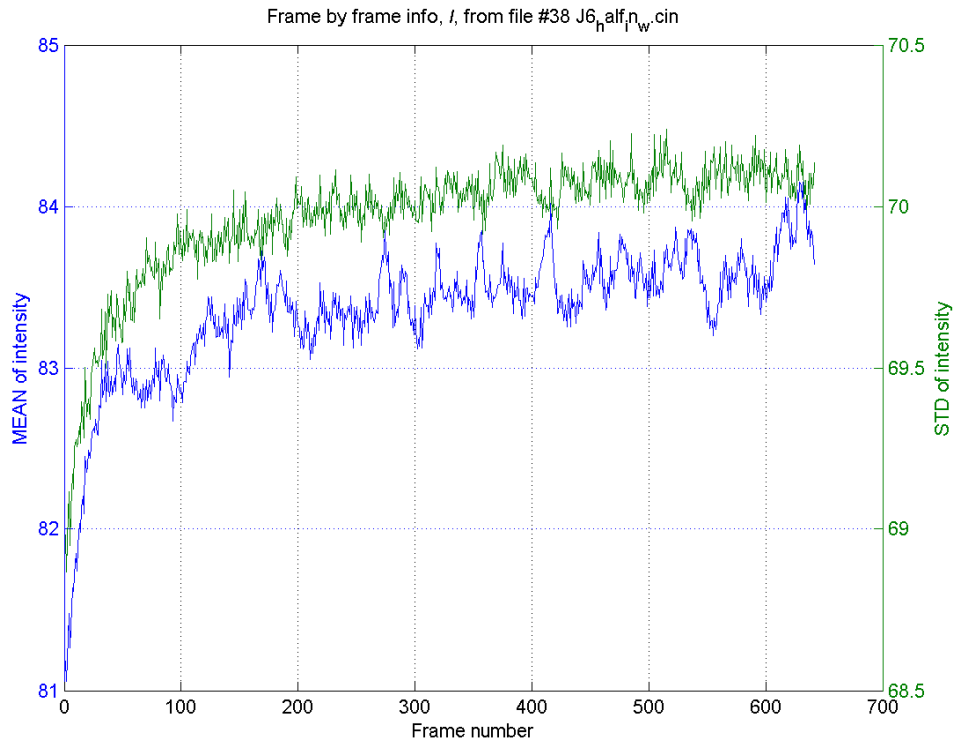


Figure 5.20 – Time trace of average intensity. Note that ~0.5 GSV drift occurred even after the first 100 ms (100 frames). The blue lower line is the spatial mean intensity.

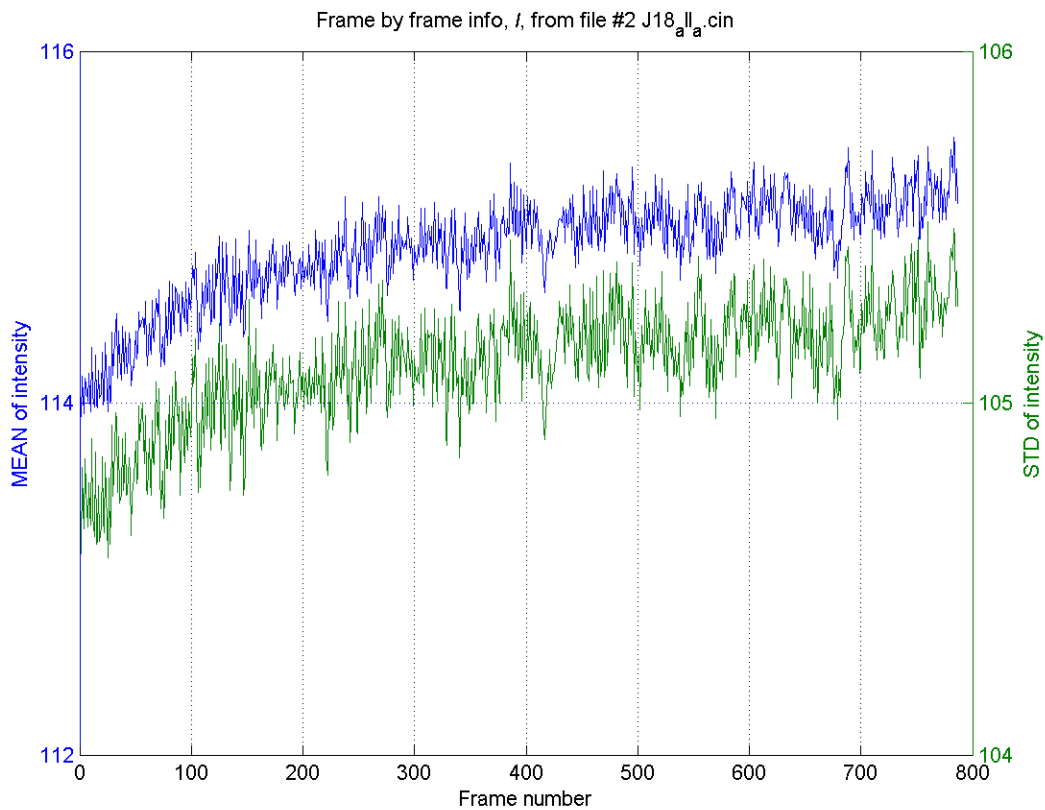


Figure 5.21 – Time trace of average intensity. The recording was started several dozen milliseconds after the start of the exposure, so that a longer time trace of the slow drift would be visible. Note that  $\sim 0.5$  GSV drift occurred even after the first 100 ms (100 frames). The blue upper line is the mean intensity.

## 5.7 Spatial resolution and positional accuracy

The spatial resolution of the image is limited by the performance of the individual components of the imaging system. A commonly used measure of the spatial resolution of a system, or its individual components, is the modular transfer function (MTF). A comprehensive discussion of this topic can be found for instance in Bushberg *et al.* (2001), but the key points are introduced here as they are relevant for the system being discussed. We'll cover the focal spot blur, image noise, camera resolution, effect of scatter, veiling glare, image distortions and non-parallel beam paths.

### 5.7.1 Focal spot blur

The focal spot blur, penumbra, is caused by a finite size of the source of the x-ray photons. One of the limitations for the size of the focal spot is set by heating of the target material, which can be alleviated by using a rotating anode. Another limitation is based on how closely the electrons can be kept as they propagate to the anode. The source intensity sets the number of electrons streaming to the anode. These electrons repel each other causing focal spot “blooming”, which is worse when the current is larger (more electrons) or the kV potential is lower (slower electrons and more time for them to repel each other). Blooming is the enlargement of the focal spot size as the current is increased due to the repulsion of adjacent electrons which is more pronounced at low kV (Huda and Slone 2003).

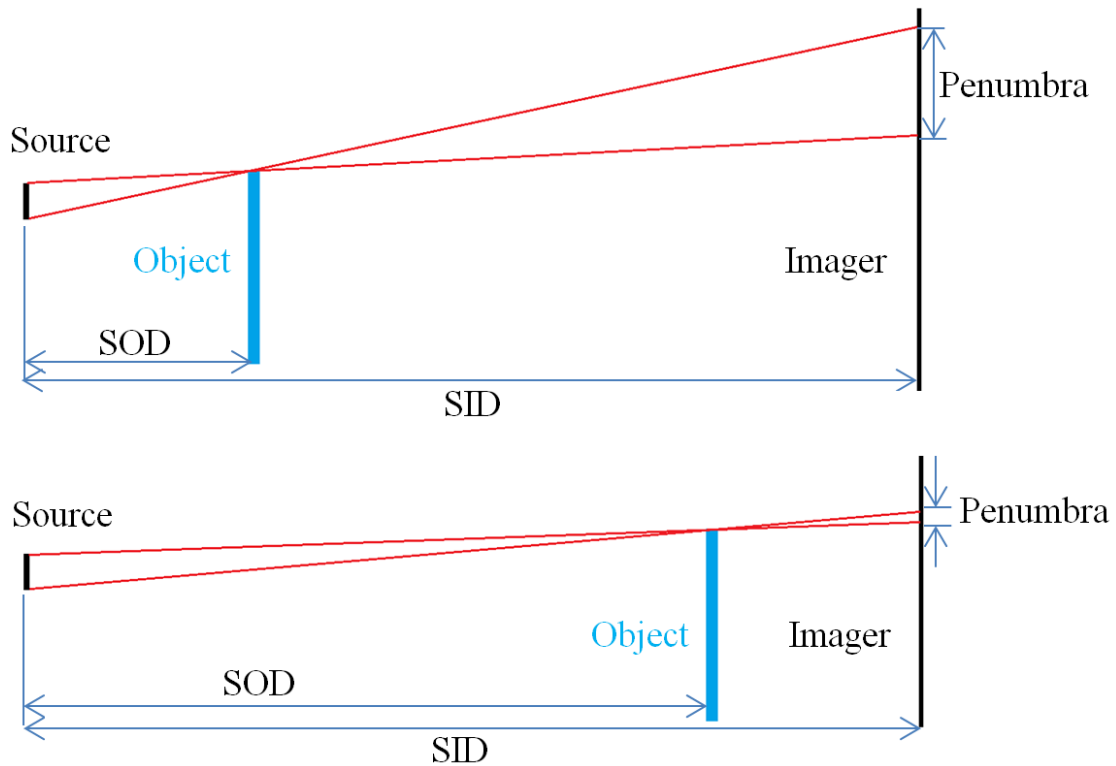


Figure 5.22 – Penumbra with the same source focal spot size, but with different source to object distance (SOD) and source to imager distance (SID) ratios. (The SID/SOD ratio is also called the object’s magnification.)

The effect of the finite focal spot's size is most easily visualized by looking at the image of an edge of a thin object as shown in figure 5.22. The edge blur is determined by the size of the focal spot, profile of the beam emerging from the focal spot (top hat profile would naturally be worse than a triangular or Gaussian with same total width), together with source-to-object (SOD) and source-to-imager (SID) distances.

For what we could control in these experiments: the smaller the focal spot or magnification,  $M = \text{SID}/\text{SOD}$ , the smaller the blur.

### 5.7.2 Noise

The noise of the source, II and camera affects the spatial, temporal and void fraction resolutions. Presumably the noise is Gaussian and has zero bias, and hence given a sufficiently large sample its effect would be removed by averaging. However, with any finite, and especially with our very short sample times, each of the camera's pixels received light generated by a relatively small number of x-ray photons, making the random noise of the source also potentially significant. The source alone has both spatial and temporal noise, both of which would average-out if the integration time per frame was increased. Noise of the source and dynamic range of the detector are also important, but not discussed as we only had one source and one imager available and these parameters could not be varied. However, many textbooks offer additional discussions on noise (for example Bushberg *et al.* 2001).

The signal to noise ratio (SNR) could be defined for each pixel as the ration of the mean value and root mean square deviation  $RMSD$ ,  $RMSD = \sqrt{\frac{1}{N} \sum_{n=1}^N (I_n - \bar{I})^2}$ , where  $N$  is the number of frames and  $I$  is the intensity at the pixel of interest. The SNR defined in this manner would vary depending on the flow condition, exposure and camera settings, but in these experiments for the region of interest it was found to be about 22.3 to 61.8, with a 29.0 mean for an image of the empty test section

In this work, the effect of noise is minimized by utilizing temporal and/or spatial averaging. Only for the time resolved movies did we use filters in post processing. For instance a 10 pixel 2D median filter, was used reduce the random noise in the animations presented.



### 5.7.3 The camera resolution

The resolution of the camera also directly limits the highest spatial frequency detectable. Based on the Nyquist criteria the highest distinguishable spatial cyclic frequency,  $f_{max} = 1/2\Delta$ . In our case,  $\Delta$  is the linear dimension of a square area on the II's input plane, which is mapped onto a single pixel on the camera's CMOS. The Vision Research Phantom V9.0 camera has a 1632 by 1200 pixel CMOS. For the lenses used in the system, the image of the output phosphor is mapped onto a circle of diameter 1360 pixels. For the 305/229/152mm (12/9/6") selectable input sizes  $\Delta = 0.22/0.17/0.11$ mm. This means that the camera alone would limit the highest spatial frequency to approximately 2.2, 3.0, and 4.5  $\text{mm}^{-1}$  for the 30.5, 22.9 and 15.2 cm input fields, respectively. For all the results shown in this dissertation, the 22.9 cm input field was used and hence the camera limited us to below 3.0  $\text{mm}^{-1}$ .

### 5.7.4 Scatter

X-ray photons are scattered from everything in the beam's path, and this can also obscure the details visible in the image. In medical applications, use of anti-scatter grids, and in some cases air gaps, is standard practice to minimize this effect. In this research, an air gap and a collimator were used. The principle is based on minimizing the number of scattered x-rays reaching the imager, and an air gap helps because the scattered photons tend to have large angles, different from those of the primary beam's photons. The photon's scattering angle probability depends on the photon energy as shown in figure 5.23 for Compton scatter. The collimator narrows the cone beam at the source, so that only the part of the beam illuminating the area of interest enters the domain. This reduces

the number of photons that might scatter and end up adversely affecting the image quality.

Scattering can be due to elastic (coherent) Rayleigh scatter, which is more likely off higher atomic number materials and at lower x-ray photon energies, or due to inelastic (incoherent) Compton scatter, which is dominant at higher energies such as those used in these experiments (Seibert and Boone 2005). At over 1.02 MeV, there could also be pair production, but our source limited the photon energies to below 150 keV, hence this will not affect the results of these experiments.

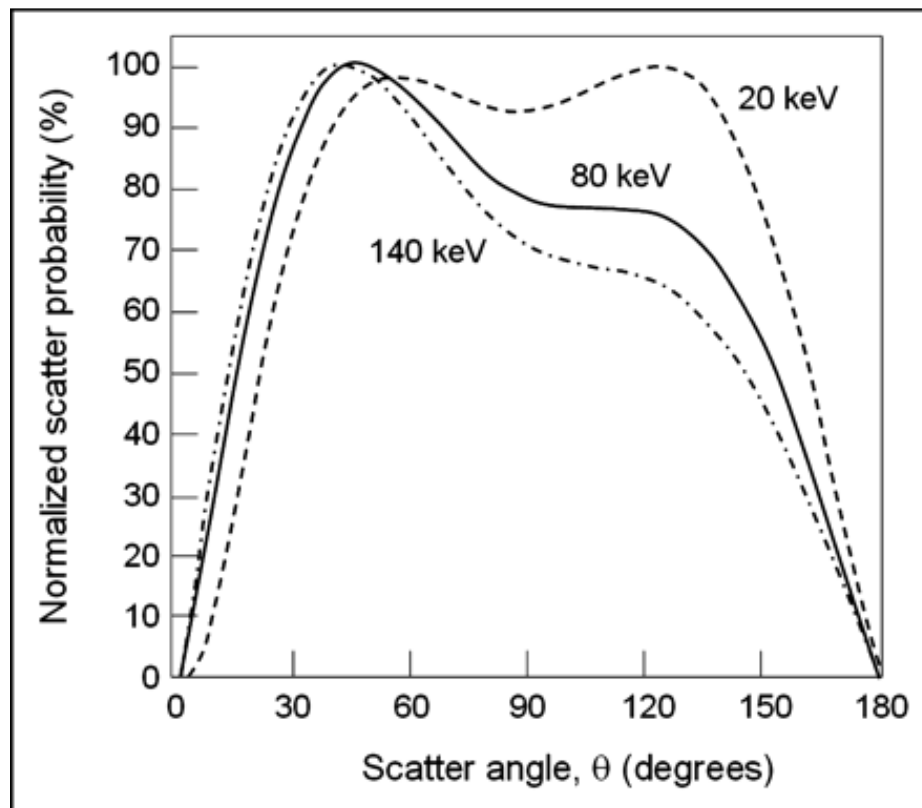


Figure 5.23 – Probable angle of scatter for different photon energies. From Seibert and Boone (2005). Note how at higher energies, forward scatter becomes more probable. (Reprinted with permission.)

### 5.7.5 Imaging – characterizing the spatial frequency response

To characterize the spatial frequency response of the imaging system, we'd need to know the point spread function (PSF) of the system. The PSF is the distribution of light which one would observe if a plate with an infinitely small round hole was placed immediately in front of the image intensifier's input screen to block the light from everywhere except the hole. However, using this direct approach has the limitation that any hole will have a finite size, and secondly the amount of light passing through a small hole would be miniscule, making it more challenging to obtain the PSF in this direct way. However, if we assume the PSF to be axisymmetric, we can determine the PSF from the so called line spread function (LSF), explained in the next paragraph, using the mathematical relationship

$$LSF(x) = \int_{-\infty}^{+\infty} PSF(x, y) dy \quad (5.29)$$

If one places a plate with very thin slit on the image intensifiers input screen, the image resulting from this will be that of a Gaussian distribution of light reaching its maxima at the slit's centerline location. If the slit were infinitely long, the distribution would only vary normal to the slit, and a distribution taken along this normal is called the line spread function (LSF) of the imager. This technique can be used to characterize the spatial frequency response of the entire imager subsystem (II, lenses and camera). One commonly used criteria for the spatial resolution is the full width half max (width of the function at half its maximum value, FWHM) of the line spread function (LSF) shown in figure 5.24c,

$$resolution \approx FWHM(LSF) \quad (5.30)$$

or the modular transfer function (MTF), *i.e.* the spatial frequency response. According to Bushberg *et al.* (2001), the modular transfer function can be determined by  $MTF(f) = F_1\{LSF(x)\}$ , where  $F_1\{A\}$  signifies the one dimensional Fourier transform of any variable A.

Trying to use a very thin (ideally infinitely thin) slit poses obvious challenges, one of which is that very little light will be observed. A much simpler experimentally obtained measure of resolution is the edge spread function (ESF). If an infinitely long plate is placed in front of an infinitely large imager, the resulting distribution will vary only normal to the edge of the plate. An intensity distribution along the normal to the edge is the ESF. The LSF is related to the edge spread function (ESF) by

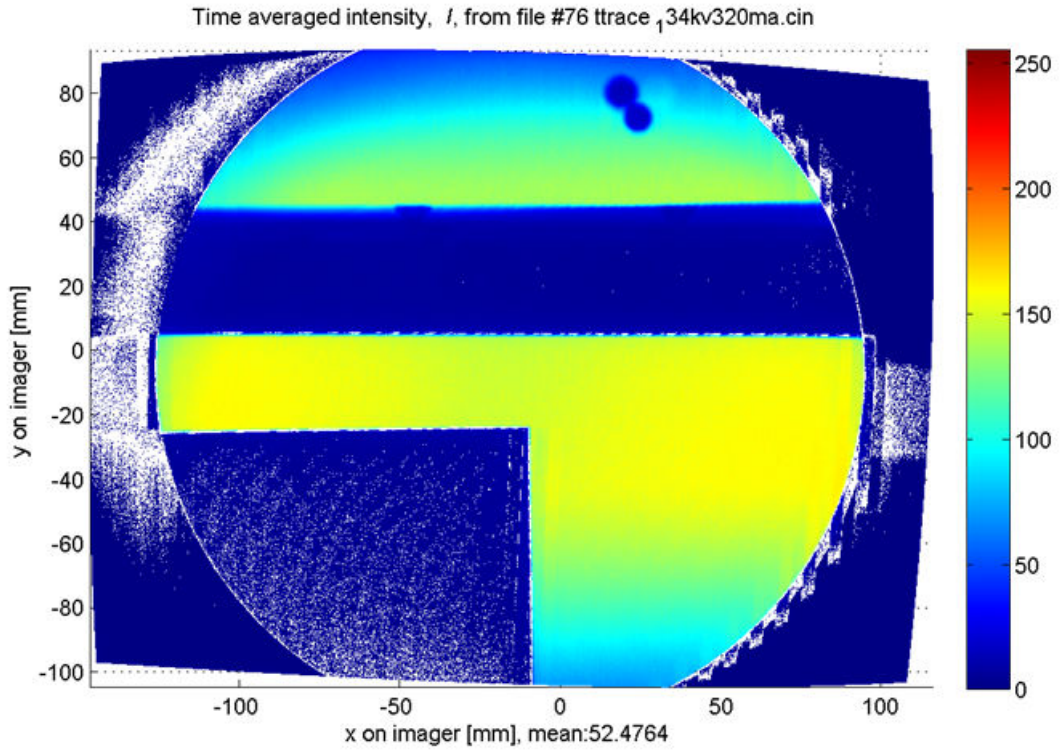
$$LSF(x) = \frac{d}{dx} ESF(x) \quad (5.31)$$

Hence it can be calculated from a discrete image on an edge as

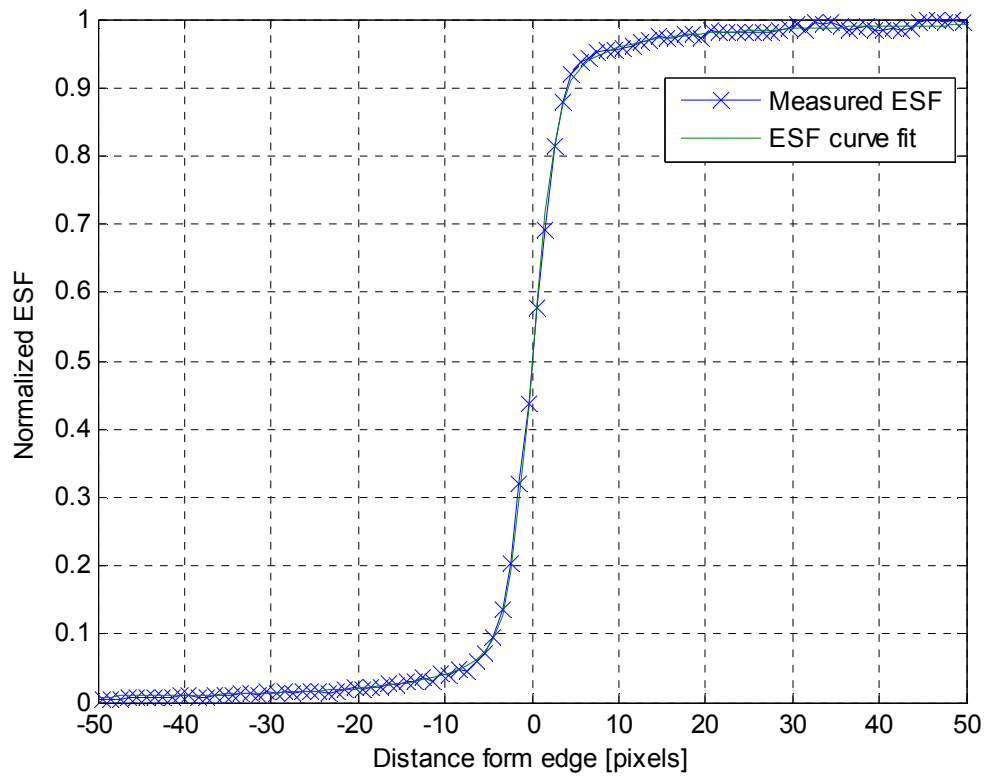
$$LSF(x_i) \approx \frac{ESF(x_{i+1}) - ESF(x_{i-1}))}{(x_{i+1} - x_{i-1})} = \frac{ESF_{i+1} - ESF_{i-1}}{2\Delta x} \quad (5.32)$$

where  $\Delta x$  is the spacing between centers of areas on the II input screen projecting onto neighboring pixels of the camera.

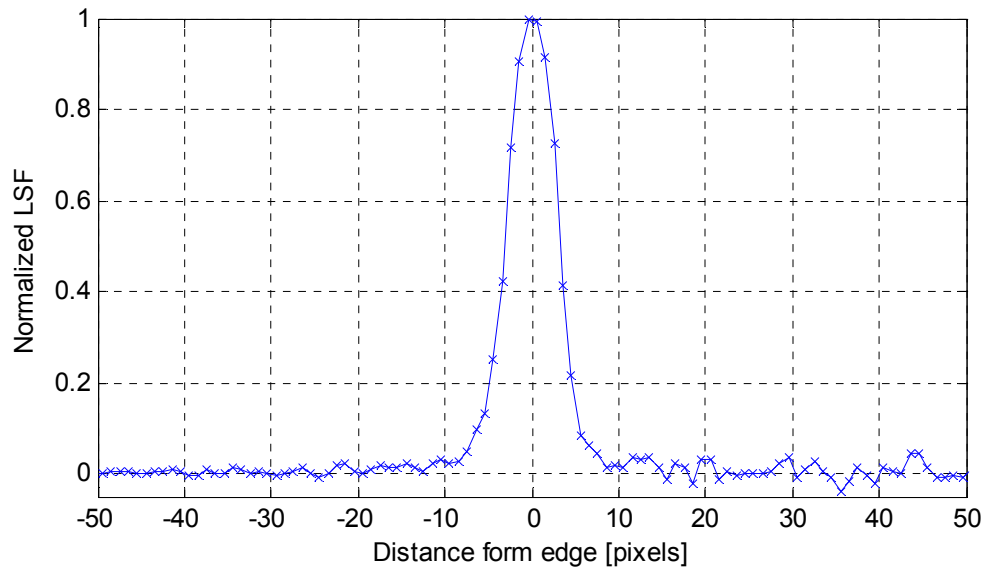
These definitions of PSF, LSF, and ESF are now used in the following sections; figure 5.24 shows the ESF, and LSF for the system used in one particular configuration.



(a)



(b)



(c)

Figure 5.24 – a) Sharp edged 1.6 mm thick lead sheet placed directly onto the II's input screen is visible in the bottom left quadrant of the image. The shadow in the middle is cast by the model used in the experiments described in Chapter 6. To check the relative locations of the source, object and imager, two lead spheres were placed between the source and the object and their shadows appear at the top of the figure. b) The ESF determined by plotting the intensity normal to the lead sheet. c) LSF, calculated using eqn. 5.32, with a 6.46 pixel full width half max.

### 5.7.6 Veiling glare

In general, a glow can be observed around a high void fraction region. In some situations if areas of the image are formed by beams having a large angle relative to the normal, this could be largely due to a non-parallel beam traversing part of the high void fraction region. Scatter from the object can also contribute, and a small glow around any point is also expected from the finite focal spot size or x-ray scatter from the object. However, as shown in figures 5.25 and 5.26 the glow can be wider and stronger than would be expected based on any of these sources. This glow is due to the “veiling glare”.

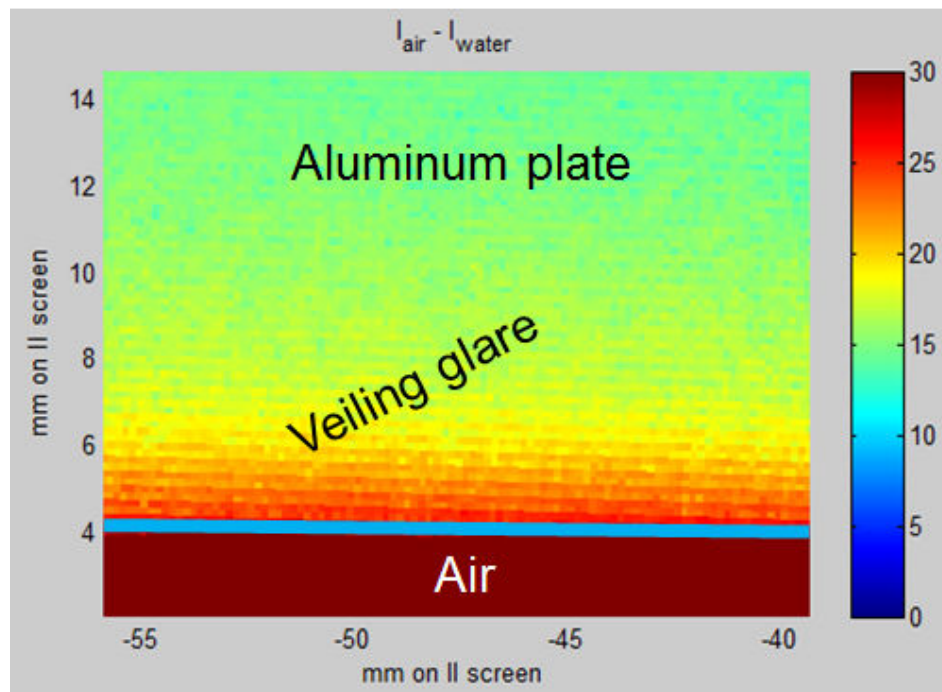


Figure 5.25 – Veiling glare caused by scatter of x-ray and visible photons in the imaging system (II and lenses). A glow over 10 mm wide is clearly seen near the edge of plate, which produced a sharp discontinuity in attenuation. Faint pixel lines caused by the camera are also visible.

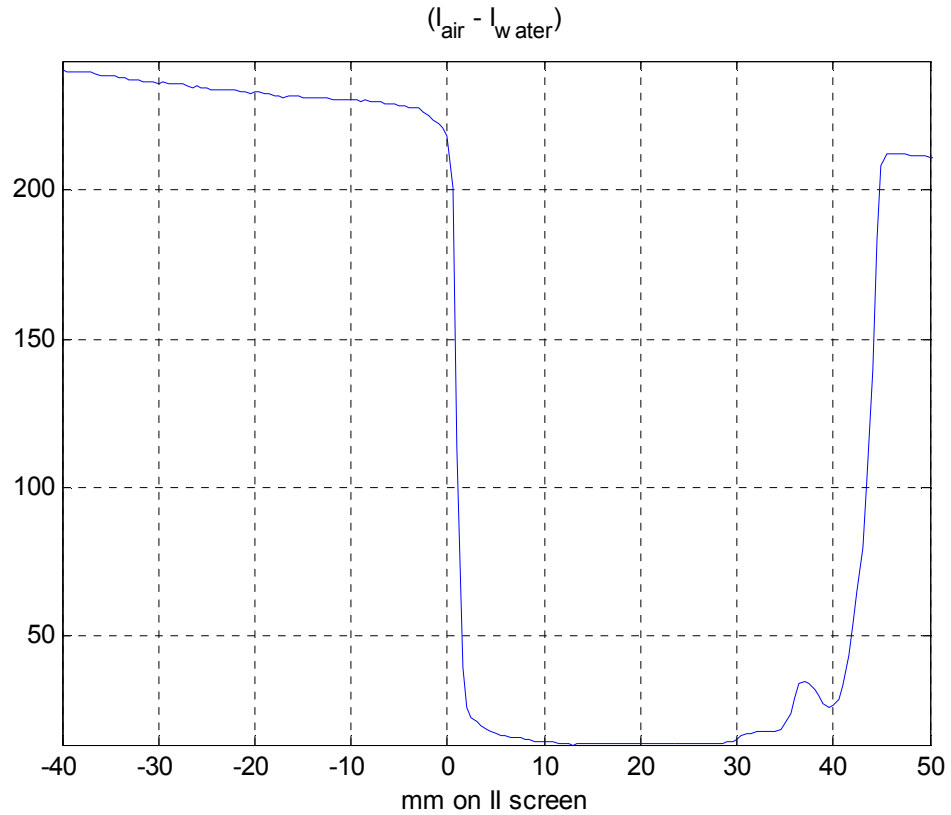


Figure 5.26 – A trace of intensity through all air minus that through all water in the test section, at a random streamwise location of the edge shown in figure 5.25. The edge is at  $\sim 2$  mm, and at that point the GSV on the vertical axis should drop rapidly to zero, and rise to some constant value to the left. The shape of the curve beyond 25 mm is due to geometry of the object in the test section.



The veiling glare is particularly obvious, and detrimental to image quality, when high intensity and low intensity regions are nearby in the image (*i.e.* large attenuation differences over small distances in the object being imaged, such as encountered at interfaces of an air or vapor cavity in two-dimensional flow). The scatter of photons from the output phosphor is believed to be the main culprit for the veiling glare (Seibert *et al.* 1984), although the scattering of photons and electrons in the input screens, and the scattering of visible wavelength photons in the camera's lenses can also contribute.

Another clear definition directly quoted from Medcyclopedia.com:

“Veiling glare, a term used to indicate light which is scattered and reflected within the lens system. In an x-ray/image intensifier system, veiling glare relates to all processes which contribute to the observed image scatter, except the actual x-ray scatter process. In an image intensifier, veiling glare results from optical scatter in the input phosphors, electron scatter within the tube itself, and optical scatter in the output optics. The net effect of veiling glare is to reduce contrast between objects of significantly different x-ray opacities. A highly attenuating object will appear less dense due to the scatter from less attenuating regions in the image.”

#### 5.7.7 Correcting for veiling glare

An image correction with veiling glare can be attempted as a convolution of the original image and the point spread function of the veiling glare. From Seibert *et al.* (1984, 1985 and 1988) we have

$$D = h ** U \quad (5.33)$$

where  $D$  is the detected image,  $h$  is the point spread function (PSF),  $**$  signifies a 2D convolution and  $U$  is the undegraded image we wish to recover. In the frequency domain this can be written as a multiplication

$$F_2[D] = F_2[h]F_2[U] \quad (5.34)$$

where  $F_2[A]$  signifies the 2D Fourier transform of any variable  $A$ . We can solve for  $U$  by dividing through by the Fourier transform of  $h$  and taking the inverse 2D Fourier transform  $F_2^{-1}$ , yielding

$$U = F_2^{-1} \left[ F_2[D] \frac{1}{F_2[h]} \right] = F_2^{-1} [F_2[D] \hat{H}^{-1}] \quad (5.35)$$

Seibert *et al.* (1985) proceed by analytically transforming  $h$  to obtain its Fourier transform's reciprocal,  $\hat{H}^{-1}$ . They cite as the benefit of doing this analytically, rather than numerically starting from  $h$ , as “avoiding singularities and oscillatory behavior, present in digital calculations caused by finite sampling width, truncation errors, and problems associated with noise”. At this point we begin to deviate from Seibert *et al.* (1984)'s derivation, as their PSF was defined as

$$h(r) = (1 - \rho) \frac{\delta(r)}{r} + \frac{\rho}{2kr} e^{-r/k} \quad (5.36)$$

where  $\rho$  is the fraction of light scattered,  $r$  is the radial distance,  $k$  represents mean propagation distance of scattered light, and  $\delta(r)$  is the Dirac delta function of  $r$ . We do not use this PSF, as the edge spread function (ESF) resulting from this PSF does not fit our experimental data shown in figure 5.27.

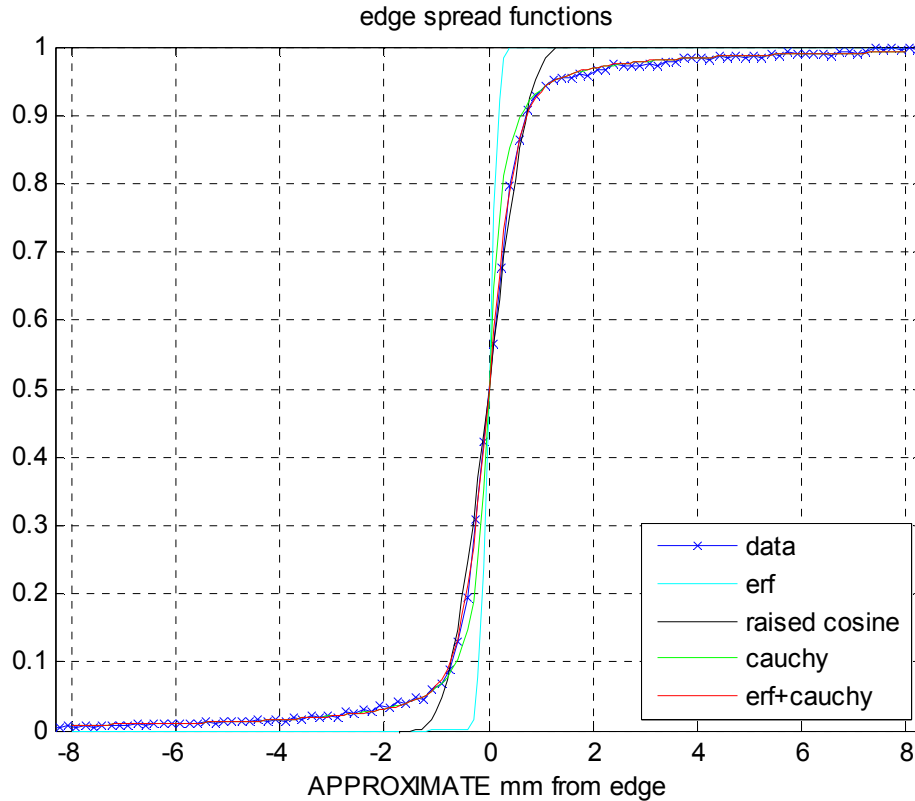


Figure 5.27 – Edge spread function obtained experimentally compared to various curve fits, some of whose forms can have a physical interpretation (Barney Smith 2006).

It could be speculated that at the higher energies used in these experiments there was more significant Compton scatter also from the input screen, and hence the form of eqn. 5.36 does not fit our PSF (but whether the scatter is from input screen optical lens train, etc. cannot be determined in the scope of the current work.)

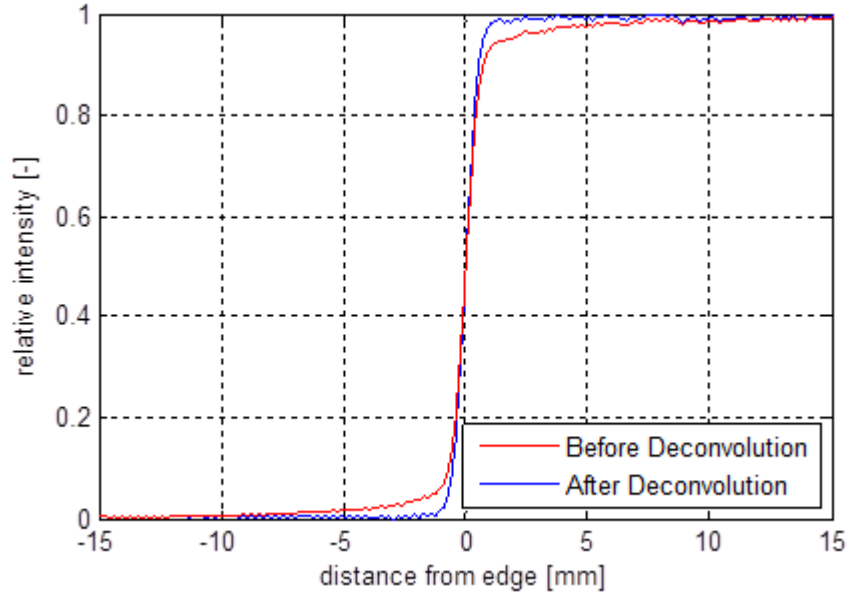
A more suitable ESF was found by combination of error and Cauchy functional forms as given by Smith (2006), whose expression for the Gaussian ESF seem to be missing a multiplier of  $\frac{1}{2}$  in front of the error function. This approach yielded the result shown in figure 5.27 by the red line (erf + cauchy). The ESF used is given by

$$ESF(x) = p_1 \left[ \frac{1}{\pi} \tan^{-1} \left( \frac{x}{\alpha} \right) + \frac{1}{2} \right] + p_2 \left[ \frac{1}{2} \operatorname{erf} \left( \frac{x}{\sigma} \right) + \frac{1}{2} \right] \quad (5.37)$$

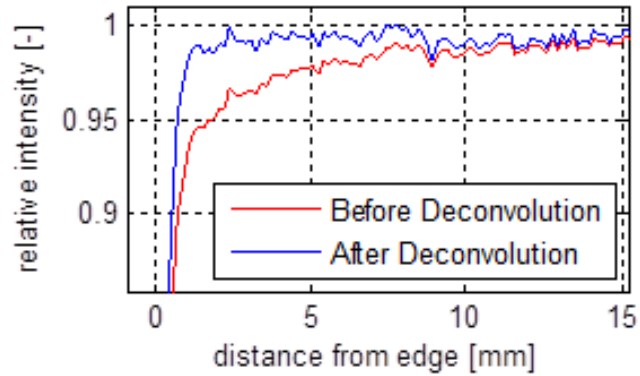
where  $p_1, p_2, \alpha$  and  $\sigma$  are coefficients. Empirically found coefficients  $p_1 = p_2 = 0.5$ ,  $\alpha = 0.4$  and  $\sigma = 0.6$  produced the fit shown in figure 5.28. The PSF corresponding to this ESF is given by

$$h(r) = (1 - p_1 - p_2) \frac{\delta(r)}{r} + p_1 \frac{\alpha/\pi}{r^2 + \alpha^2} + p_2 \frac{1}{\sigma\sqrt{2\pi}} e^{-\frac{1}{2}\left(\frac{r}{\sigma}\right)^2} \quad (5.38)$$

where the coefficients are the same. Employing this PSF, the deconvolution was performed using Matlab's built-in function, `deconvlucy`, which is based on the Lucy-Richardson method. Figure 5.28 shows the result of this approach, and while there is still room for improvement, the sharp edged Heaviside step function we might expect is clearly more fully recovered.



(a)



(b)

Figure 5.28 – a) Relative intensity normal to the edge of the lead sheet (as shown in figure 5.24a) for the original and deconvolved image. Ideally the result should be a Heaviside step function. b) An expanded view clearly showing the improvement. Additionally visible is that the higher frequency ripple was not smeared by the deconvolution. In this case the ripple may have been just noise, but in other situations it could contain information.

Work was also done to find a faster and more complete veiling glare correction. The previous approach was adjusted after encountering the very recently published article by Poludniowski *et al.* (2011). As will be shown, their approach is similar, but the advantage is that it is more-mature published work, and therefore we'll make use of their work in what follows. A modified version of their PSF, where we retain all the terms is given by

$$\begin{aligned}
 h(r) = & (1 - a_1 - a_2 - a_3) \frac{\delta(r)}{2\pi r} + \frac{a_1}{2\pi b_1^2} e^{-\frac{1}{2}(\frac{r}{b_1})^2} + \frac{a_2}{2\pi b_2^2} e^{-r/b_2} \\
 & + \frac{a_3}{2\pi b_3^2} \frac{1}{(1 + r^2/b_3^2)^{3/2}}
 \end{aligned} \tag{5.39}$$

Here the first, second and fourth terms all have a corresponding term in eqn. 5.38. Instead of directly employing the approach by Poludniowski *et al.* (2011), where they ignored the second and third terms due to what they say “deblurring being unstable at high-spatial-frequency region”, we recall Seibert *et al.* (1985)’s comment about the benefit of using the analytical inverse of the Fourier transform of the PSF, and proceed to derive the analytical  $\hat{H}^{-1}$ .

As in Seibert *et al.* (1985) we must analytically transform the above PSF, at which point we can take advantage of the assumed circular symmetry and write the Fourier transform of  $h$  as

$$\hat{H}(f) = 2\pi \int_0^{\infty} h(r) J_0(2\pi r f) r dr \tag{5.40}$$

where  $f$  is the spatial frequency,  $r$  the radial distance and  $J_0()$  the zero order Bessel function of its argument. Integrating term by term gives:

$$\frac{\hat{H}(f)}{2\pi} = \left\{ \begin{array}{l} \int_0^{\infty} \left[ (1 - a_1 - a_2 - a_3) \frac{\delta(r)}{2\pi r} \right] J_0(2\pi r f) r dr + \\ \int_0^{\infty} \left[ \frac{a_1}{2\pi b_1^2} e^{-\frac{1}{2}(\frac{r}{b_1})^2} \right] J_0(2\pi r f) r dr + \\ \int_0^{\infty} \left[ \frac{a_2}{2\pi b_2^2} e^{-r/b_2} \right] J_0(2\pi r f) r dr + \\ \int_0^{\infty} \left[ \frac{a_3}{2\pi b_3^2} \frac{1}{(1 + r^2/b_3^2)^{3/2}} \right] J_0(2\pi r f) r dr \end{array} \right. \quad (5.41)$$

The actual integration was done utilizing Mathematica 7.0 (by Wolfram). The integrals are possible if  $b_2^2 > 0$  and  $\text{Real}(f) > 0$  (or  $\text{Real}(f) = 0$  and  $\text{Imag}(f) > 0$ ) etc. The full set of constraints as well as the syntax is shown in the Mathematica worksheet included in Appendix E. The result is given by

$$\frac{\hat{H}(f)}{2\pi} = \left\{ \begin{array}{l} \frac{1 - a_1 - a_2 - a_3}{4\pi} + \\ \frac{a_1}{2\pi} e^{-2(\pi b_1 f)^2} + \\ \frac{a_2}{2\pi(1 + 4(\pi b_2 f)^2)^{3/2}} + \\ \frac{a_3}{2\pi} e^{-2\pi b_3 f} \end{array} \right. \quad (5.42)$$

which we can rewrite after factoring with  $a$ 's as

$$\hat{H}(f) = \frac{1}{2} \left[ 1 + a_1 (2e^{-2(\pi b_1 f)^2} - 1) + a_2 \left( \frac{2}{(1 + 4(\pi b_2 f)^2)^{3/2}} - 1 \right) + a_3 (2e^{-2\pi b_3 f} - 1) \right] \quad (5.43)$$

The reciprocal is now given by

$$\hat{H}^{-1} = \frac{2}{1 + a_1(2e^{-2(\pi b_1 f)^2} - 1) + a_2\left(\frac{2}{(1 + 4(\pi b_2 f)^2)^{3/2}} - 1\right) + a_3(2e^{-2\pi b_3 f} - 1)} \quad (5.44)$$

Recalling eqn. 5.35, we can now solve for the undegraded image

$$U = F_2^{-1}[F_2[D]\hat{H}^{-1}] \quad (5.45)$$

Note: the matrix multiplication is performed point by point in the frequency domain.

All the three approaches to veiling glare correction were attempted (eqn. 5.38 or 5.39 with the Lucy-Richardson deconvolution, and eqns. 5.44 and 5.45), but none was found to be clearly better than the others. The best veiling glare correction approach for a given experiment could be established by constructing void fraction phantoms approximating the specific flow being investigated, and empirically determining the best approach.

### 5.7.8 Distortion

The x-ray image of any object placed in the beam's path is distorted because *i*) the x-rays are not parallel for all  $x$  and  $y$  in the domain, *ii*) the image intensifier introduces distortion especially near the edges of the image due to its geometry and the imperfections of its electric fields, and *iii*) the optics in front of the camera can additionally distort the image seen on the image intensifier's output phosphor.



### 5.7.9 Image intensifier and lens distortions

Addressing *ii* and *iii* is simpler, and we begin with them. The image intensifier introduces a “pincushion” distortion and possibly “S-distortion” (Bushberg *et al.* 2001), and the optics in front of the camera can additionally distort the captured image. To correct for these distortions, a calibration image is needed and the procedure is quite similar to that used in Particle Imaging Velocimetry, except that the calibration grid is placed on the imager directly and the markers must have different attenuation than the surrounding material. Figure 5.29 shows an aluminum calibration grid that was placed on the II-screen and used to correct for the II’s pincushion and S-distortions. (The rods and features of the model are used to find the central beam path of the x-ray cone produced by the source. These will be used for the non-parallel beam path correction.)

Many researchers have proposed unwarping algorithms to correct for the distortion caused by the II. Cerveri *et al.* (2002) discuss local unwarping polynomials and radial basis function neural networks. We first wrote a dewarping code in Matlab, but then found that the dewarping functions in LaVision’s DaVis 7.2 provided a more robust two dimensional 3<sup>rd</sup> order polynomials for the correction. Hence, DaVis 7.2 was used to find the coefficients of the polynomials, and these coefficients were then imported into our own Matlab code where they were used to dewarp the images. Figure 5.30b shows a dewarped x-ray image of part of the calibration target.

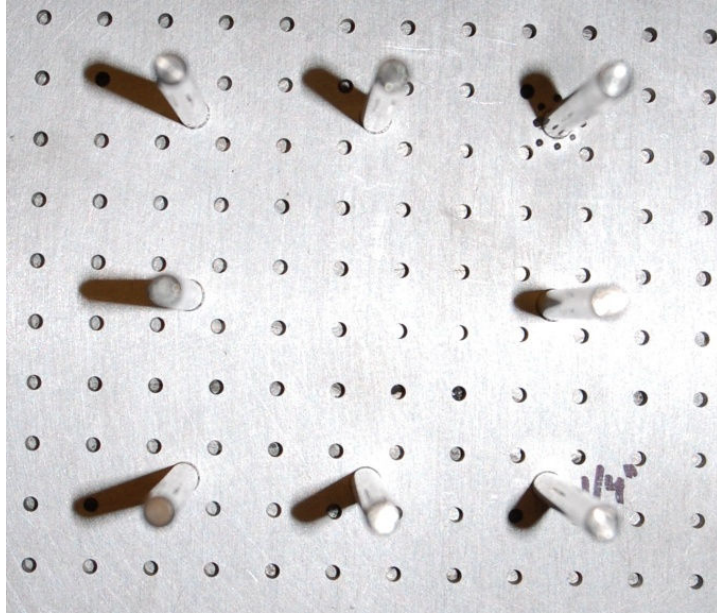
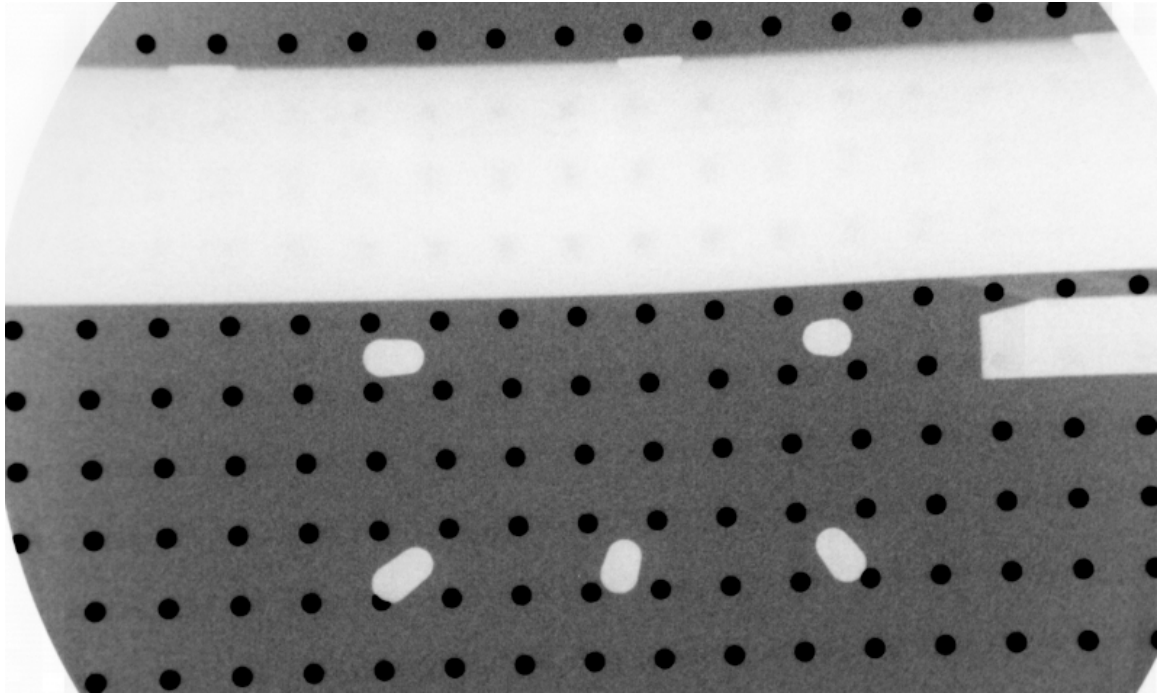
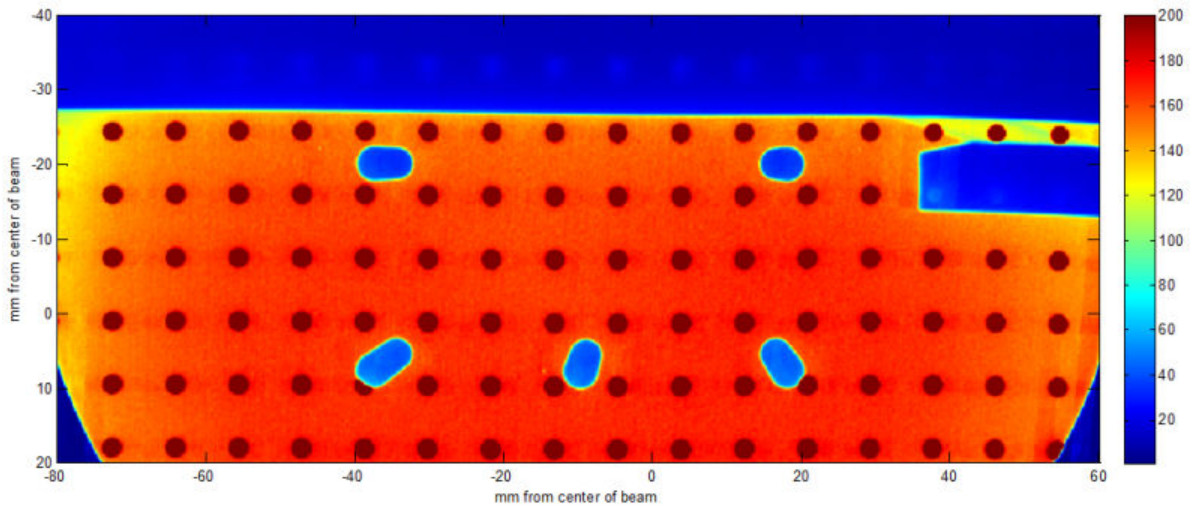


Figure 5.29 – A photograph of the aluminum calibration plate that was machined with 3.3 mm holes regularly spaced 12.7 mm apart. 15 cm long parallel rods were additionally used because, based on geometry their projections could be employed to determine the relative location of the source with respect to the imager.



(a)



(b)

Figure 5.30 – a) X-ray image of the bottom part of the calibration plate shown in figure 5.29 before distortion correction. Colors are inverted so that low attenuation regions appear black. b) Part of the same image after the feature recognition algorithm is applied and the image dewarped. A small amount of distortion remains at the extreme right edge because the model obscured the markers, but this area is not of interest.

#### 5.7.10 Non-parallel beam paths

The distortion due to the non-parallel beams paths of the conical beam is demonstrated in the simplified setup of figure 5.31, where the domain has a perfect two dimensional distribution of void fraction alternating from high to low. (It is noted that no practical x-ray beam reflecting technique to correct the beam angles for a polychromatic source, such as the one we used, exists.) It will be shown that in principle the correction can be performed if the flow is assumed to be perfectly two dimensional. However, it may not always be necessary since the primary beam is centered in the area of interest, the area may be small and the angles shallow. If the dimensions of the area of interest extend +/- 0.64 cm vertically and +/-5.0 cm horizontally, as will often be the case in Chapter 6, and the source is 111 cm from the test section's centerline, then the largest angle of the beam is 2.88 degrees.

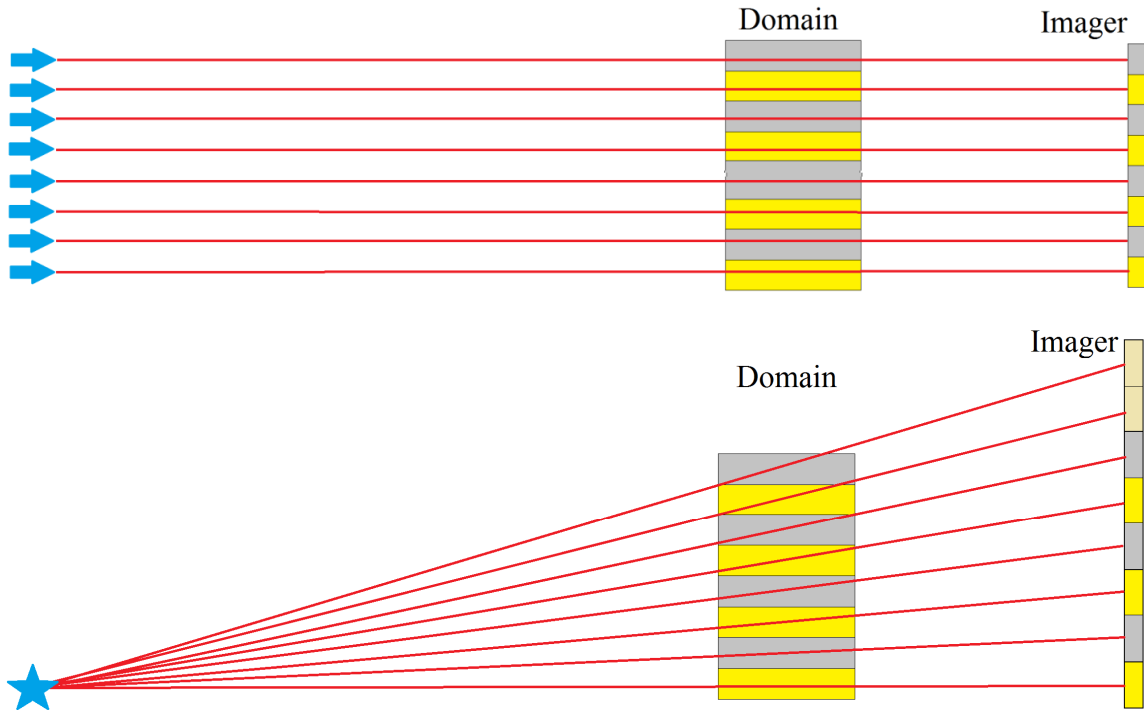


Figure 5.31 – Upper figure shows an ideal case where a perfect 2D void fraction distribution is projected onto the imager by parallel beams. The bottom figure illustrates the actual situation. (Although the beam originates from a finite size focal spot, here it is simplified as a point.) The ‘one’ parallel beam still projects a 'perfect' image onto the imager, but beams with higher angles project an increasingly smeared and stretched projection of the void fraction distribution as is indicated by the slightly stretched rectangles with grey fill.

Also because of the non-parallel beams, the distance traversed through the test section by different beams is a function of the beam angle. The mixture thickness in the path of the beam is given by  $t = \frac{8.25''}{\cos \theta}$ , where  $\theta = \tan^{-1} \frac{\sqrt{\Delta x^2 + \Delta y^2}}{\text{SID}}$ . Here  $\Delta x$  and  $\Delta y$  are distances from the “central beam”, which is the beam travelling normal to the image screen along a horizontal line. SID is the source-to-imager distance and SOD is the source-to-object-distance, as before.

### 5.7.11 Non-parallel beam path correction

When correcting for the non-parallel beam paths, we must first correct for the II's pincushion and S-distortions, as well as for any distortion due to the camera lenses. To do this, we take reference images of the calibration grid with chosen II magnification and average more than a 100 frames from the series of reference images to minimize noise (done in Matlab). Now using the image of the grid we find the equations to correct for the image distortion. This was done either by using DaVis 7.2's calibration functions (3<sup>rd</sup> order polynomials) or in Matlab using own code, which was less robust. Using the polynomials, we undistorted images taken with the same II settings. Once the image is undistorted, we rotate image's  $x,y$ -coordinate system to match with test section's coordinates

$$\begin{pmatrix} x_{k,l} \\ y_{k,l} \end{pmatrix} = \begin{pmatrix} \cos \vartheta & -\sin \vartheta \\ \sin \vartheta & \cos \vartheta \end{pmatrix} \begin{pmatrix} \tilde{x}_{k,l} \\ \tilde{y}_{k,l} \end{pmatrix} \quad (5.46)$$

where  $\vartheta$  is the angle between the test section's horizon and camera's horizon as determined from the shadows of the lead spheres and/or model's shadow. Then we calculate void fraction distribution for each image using eqn. 5.21 and correct for the veiling glare (and scatter).

Now assuming a perfectly two dimensional flow, we can correct for the distortion caused by non-parallel beam paths. First from an average of more than 100 images, we calculate the relative location of the source's focal spot ( $x, y, z$ ) using the images of the lead balls and features of the model. Then we choose physical size on image discretization on the II-screen and bounds of the area of interest. Without going into

mundane detail, a short description of the (non-parallel beam) unwarp code's algorithm is given next.

First, we divide the image into  $(K_t+K_b)*(L_l+L_r)$  mesh interpolating the void fraction from the original mesh, as shown in figure 5.32. Here  $K$  and  $L$  are the vertical and horizontal indices, respectively. Sub-indexes  $t$ ,  $b$ ,  $l$ , and  $r$ , represent top, bottom, left, and right quadrants, respectively. The center beam path does not need to be in the center of the image, or even in the image, as long as its coordinates on the  $\Pi$  screen's plane are known.

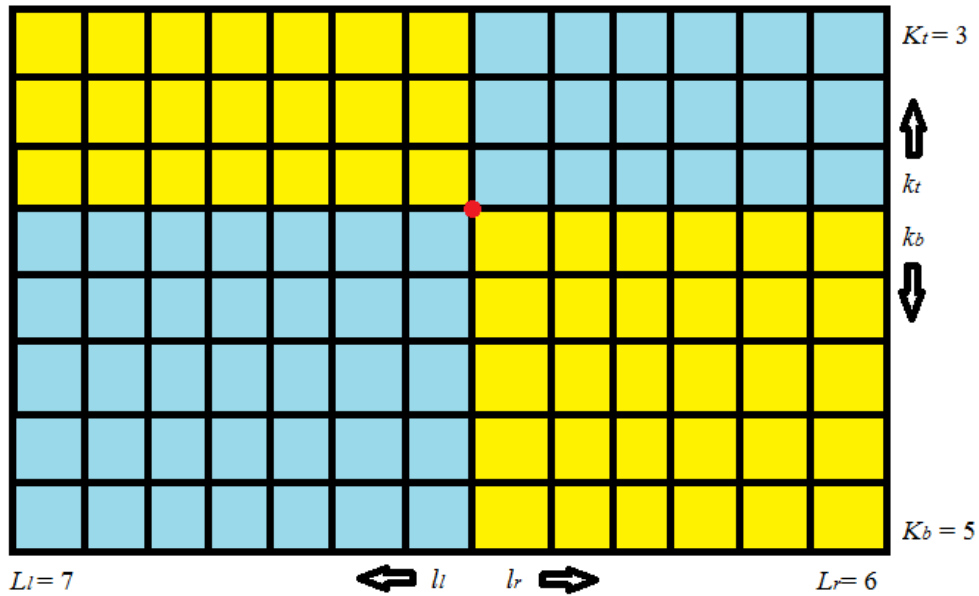


Figure 5.32 – Sketch showing the origin (red dot) and labeling of the grid. The origin is at the  $(x, y)$ - location of the central beam path from the source normal to the model.

Secondly, the beam path to the center of each area  $(k, l)$  is used to approximate the contribution from the given region of the flow domain. Given that the angle of any single ray across the domain is constant, this can be used to greatly simplify the calculations by only considering the lengths of the beam path's projection onto the  $z$ -axis

$$\bar{\alpha} = \frac{1}{z_e - z_s} \int_{z_s}^{z_e} \alpha dz \quad (5.47)$$

where  $\bar{\alpha}$  is the mean void fraction encountered by the beam traversing through the area of interest. The discretized form of the equations can be written as

$$\bar{\alpha}_{k,l} = \sum_{i=0}^k \sum_{j=0}^l f_{i,j,k,l} \alpha_{i,j} \quad (5.48)$$

where for a ray going to area  $(k, l)$  in the II screen,  $f_{i,j,k,l}$  is the fraction of the ray's length spent in voxel  $(i, j)$ . This fraction can be written as

$$f_{i,j,k,l} = \frac{1}{z_s - z_e} \Delta z_{i,j,k,l}$$

where  $\Delta z_{i,j,k,l}$  is the length of the ray going to area  $k, l$  passing through the domain  $i, j$ . However, a large reduction in the number of required operations determining  $\Delta z_{i,j,k,l}$  can be achieved if advantage is taken of the linear path of the rays, by starting at the voxel  $i, j$  where the beam to pixel  $k, l$  enters the domain at  $z = z_s$ , and tracing the beam's path from this point forward, and this was the approach adopted.

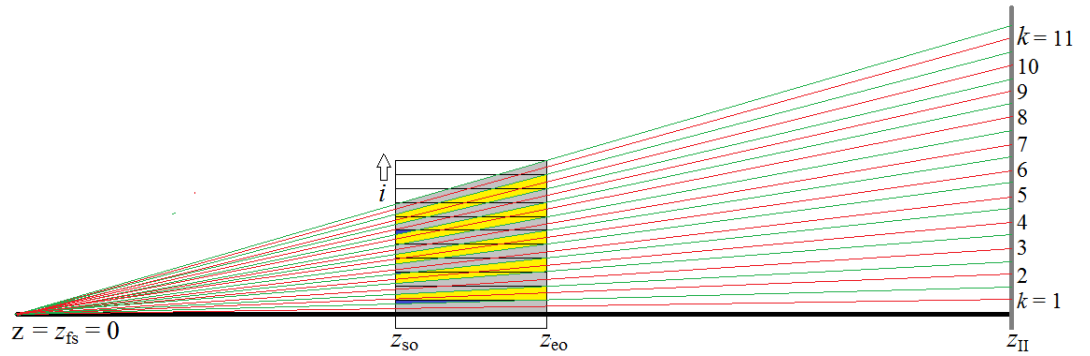


Figure 5.33 – Sketch of the beam paths in the  $(z,y)$  - plane.



If the imager screen is divided into equally spaced regions, with spacing  $\Delta x_{II} = \Delta y_{II}$  then

$$\theta_{i,j,k,l} = \theta_k = \tan^{-1} \frac{y_k}{z_{II}} \quad (5.49)$$

$$\varphi_{i,j,k,l} = \varphi_l = \tan^{-1} \frac{x_l}{z_{II}} \quad (5.50)$$

yield the angles of the beam in the  $(z,y)$ - and  $(z,x)$ -planes, respectively. Here  $y_k$  is the  $y$ -coordinate of the center of the  $k^{\text{th}}$  area on the II screen and given by  $y_k(z_{II}) = (k - 1/2)\Delta y_{II}$ , and similarly  $x_l(z_{II}) = (l - 1/2)\Delta x_{II}$ .

Owing to the uniform size of areas on the II, and knowledge of the  $x$  and  $y$  coordinates where the center beam first encountered the flow domain, the locations of the beams going to other than the center pixel can be calculated from

$$y_{i,j,k,l}(z_{so}) = y_k(z_{so}) = y_k(z_{II}) z_{so}/z_{II}, \text{ and}$$

$$x_{i,j,k,l}(z_{so}) = x_l(z_{so}) = x_l(z_{II}) z_{so}/z_{II}$$

To calculate to which  $i, j$  voxel this corresponds in the fluid domain, we first define the “top” (as shown in figure 5.33) boundaries of the rectangular voxels as  $y_{iB} = k\Delta y_{II} z_{eo}/z_{II}$  and  $x_{jB} = l\Delta x_{II} z_{eo}/z_{II}$ .

Note that we have uniform voxel spacing  $\Delta y_{iB} = \Delta y_{II} z_{eo}/z_{II}$  and  $\Delta x_{jB} = \Delta x_{II} z_{eo}/z_{II}$ .

Therefore the index of the voxel for which we search is given by

$$i_k(z_{so}) = [y_k(z_{so})/\Delta y_{iB}] \quad (5.51)$$

$$j_l(z_{so}) = [x_l(z_{so})/\Delta x_{jB}] \quad (5.52)$$

Here the symbol  $[a]$  means rounding any variable  $a$  to the closest higher integer value.

Then for  $i = i_k(z_{so}) \dots (k - 1)$ , the  $z$ -coordinate at intersection is

$$z_k(y_{iB}) = y_{iB} / \tan \theta_k \quad (5.53)$$

As  $j(z_k(y_{iB})) = \lceil z_k(y_{iB}) \tan \varphi_l / \Delta x_{jB} \rceil$  and for  $j = j_l(z_{so}) \dots (l - 1)$ , the  $z$ -coordinate at intersection is

$$z_l(x_{jB}) = x_{jB} / \tan \varphi_l \quad (5.54)$$

Next with the minimum number of operations (avoiding Dirac delta and Heaviside functions, and minimizing *if*-statements in the code due to the computational cost) we must determine through which voxels the center of the beam passes. Starting from  $[i_k(z_{so}), j_l(z_{so})]$  where by definition  $z = z_{so}$ , we find the next lowest value from sets of  $[z_k(y_{iB}), z_l(x_{jB}), z_{eo}]$  and increase the value of  $i$  or  $j$  depending on from which set the value was chosen. Therefore we generate a list of  $\Delta z_{i,j}$  for each  $k, l$ . Thus equation 5.48 can be re-written as

$$\bar{\alpha}_{k,l} = \frac{1}{z_{eo} - z_{so}} \sum_{list\ for\ k,l} \Delta z_{i,j,k,l} \alpha_{i,j} \quad (5.55)$$

We have a known  $\bar{\alpha}_{k,l}$  and want to recover the void fraction information  $\alpha_{i,j}$  for each rectangular voxel in the flow domain. This can be accomplished by forming a set of matrices or proceeding sequentially from index 1,1 to  $K_u L_r$  etc. in each quadrant of the flow domain.

$$\alpha_{k,l} = \frac{\bar{\alpha}_{k,l}(z_{eo} - z_{so}) - \sum_{list\ for\ k,l}^{except\ k,l} \Delta z_{i,j,k,l} \alpha_{i,j}}{\Delta z_{k,l}} \quad (5.56)$$

A more precise method would be to use the relative voxel volumes through which the unscattered photons reaching area  $k$ ,  $l$  have gone. However, the number of mathematical operations required would be more than one order of magnitude larger.

As stated, the relative location of the source with respect to the flow domain and II, as well as the central beam path location in the plane of the II input screen must be known for the reconstruction. Using a setup shown in figure 5.34 below, the shadows of the eight lead balls can be used to determine the relative location of the focal spot.

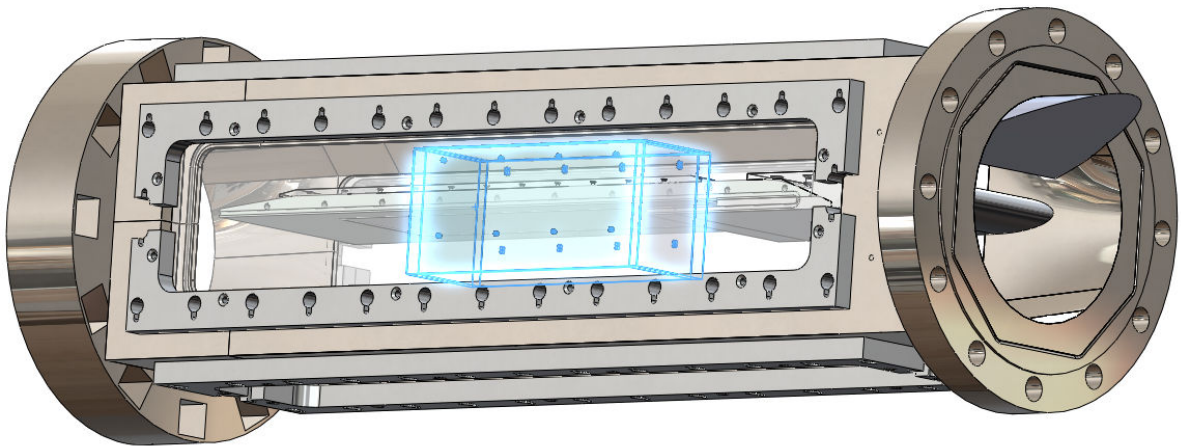


Figure 5.34 – Location calibration target (glowing blue) located on the source's side of the test section. The target has 16 lead spheres in two different z-planes, two different y-planes and four different x-planes. The relative positions of the lead spheres are known precisely, as they are in pockets machined into the plastic frame by a CNC mill. Flow is from right-to-left through the test section.

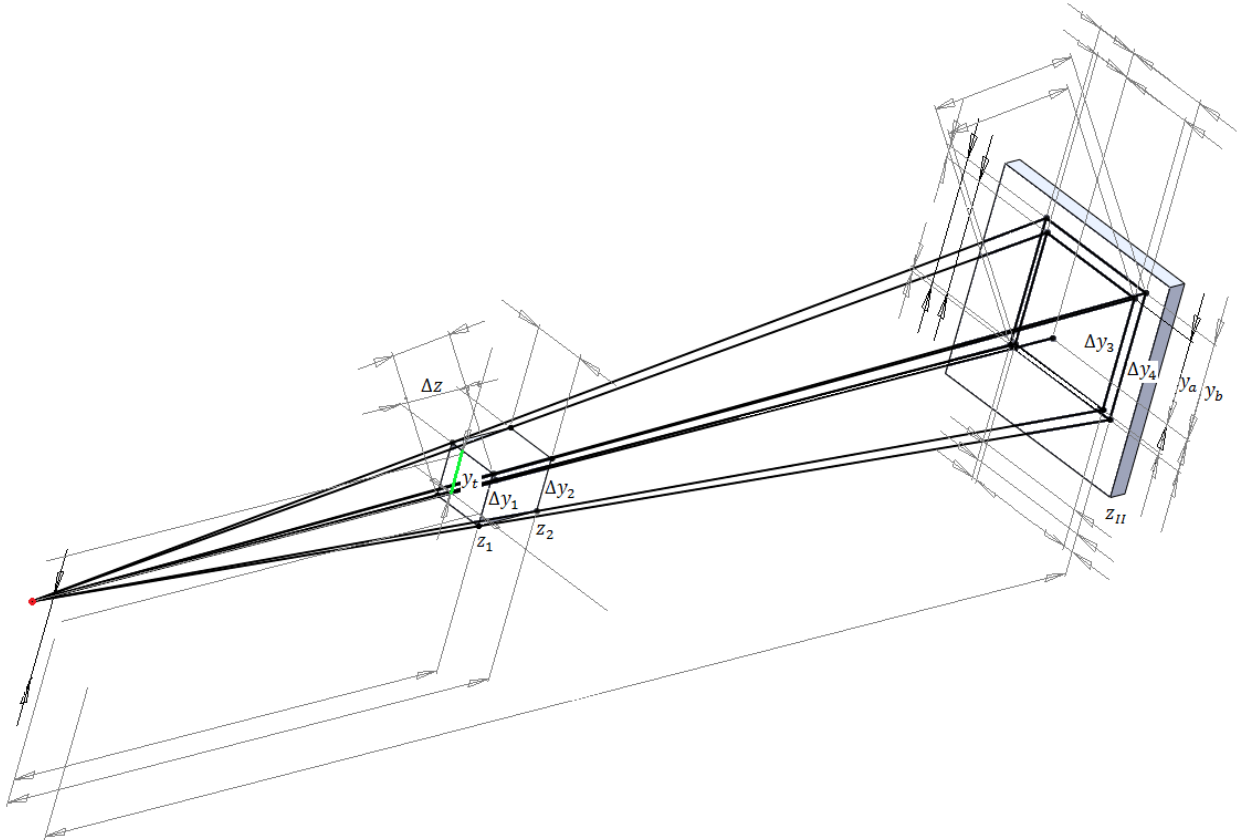


Figure 5.35 – Sketch of the setup to find the relative source location. All the dimensions shown on the right, except  $z_{II}$ ,  $y_a$  and  $y_b$  can be measured directly from the II image, and used to determine the remaining dimensions needed.

It should also be noted that the angle with respect to the horizon of the test section and camera coordinate system may not match, and this needs to be corrected by rotating the acquired images (eqn. 5.46). Referring to the labels on figure 5.35, the following geometric relations can be used to determine the unknown relative source location to better accuracy than achieved by simple measurement of the setup. The shadows yield the same data from four independent pieces of information as

$$\left. \begin{array}{l} \frac{\Delta y_4}{\Delta y_1} = \frac{z_{II}}{z_1} \\ \frac{\Delta y_3}{\Delta y_2} = \frac{z_{II}}{z_2} \\ z_2 - z_1 = \Delta z \end{array} \right\} \Rightarrow \begin{array}{l} z_{II} = \Delta z / \left( \frac{\Delta y_2}{\Delta y_3} - \frac{\Delta y_1}{\Delta y_4} \right) \\ z_1 = z_{II} \frac{\Delta y_1}{\Delta y_4} \\ z_2 = z_{II} \frac{\Delta y_2}{\Delta y_3} \end{array}$$

$$\left. \begin{array}{l} \frac{\Delta x_4}{\Delta x_1} = \frac{z_{II}}{z_1} \\ \frac{\Delta x_3}{\Delta x_2} = \frac{z_{II}}{z_2} \\ z_2 - z_1 = \Delta z \end{array} \right\} \Rightarrow \begin{array}{l} z_{II} = \Delta z / \left( \frac{\Delta x_2}{\Delta x_3} - \frac{\Delta x_1}{\Delta x_4} \right) \\ z_1 = z_{II} \frac{\Delta x_1}{\Delta x_4} \\ z_2 = z_{II} \frac{\Delta x_2}{\Delta x_3} \end{array}$$

The determination of the  $x$  and  $y$ -coordinates does not yield an equally compact expression; hence the solution of  $y_t$  and  $x_t$  is included in the Appendix E.

$$\left. \begin{array}{l} y_B - y_a = \Delta y \\ y_a = z_{II} \sin \theta_1 \\ y_b = z_{II} \sin \theta_2 \\ \theta_1 = \tan^{-1} \frac{y_t}{z_2} \\ \theta_2 = \tan^{-1} \frac{y_t}{z_1} \end{array} \right\} \Rightarrow \begin{array}{l} y_a = \sqrt{\frac{z_{II}^2 y_t^2}{z_2^2 + y_t^2}} \\ y_b = \sqrt{\frac{z_{II}^2 y_t^2}{z_1^2 + y_t^2}} \\ \Delta y = \sqrt{\frac{z_{II}^2 y_t^2}{z_1^2 + y_t^2}} - \sqrt{\frac{z_{II}^2 y_t^2}{z_2^2 + y_t^2}} = \frac{z_{II} y_t [(z_2^2 + y_t^2)^{1/2} - (z_1^2 + y_t^2)^{1/2}]}{[(z_1^2 + y_t^2)(z_2^2 + y_t^2)]^{1/2}} \end{array}$$

$$\left. \begin{array}{l} x_B - x_a = \Delta x \\ x_a = z_{II} \sin \varphi_1 \\ x_b = z_{II} \sin \varphi_2 \\ \varphi_1 = \tan^{-1} \frac{x_t}{z_2} \\ \varphi_2 = \tan^{-1} \frac{x_t}{z_1} \end{array} \right\} \Rightarrow \begin{array}{l} x_a = \sqrt{\frac{z_{II}^2 x_t^2}{z_2^2 + x_t^2}} \\ x_b = \sqrt{\frac{z_{II}^2 x_t^2}{z_1^2 + x_t^2}} \\ \Delta x = \sqrt{\frac{z_{II}^2 x_t^2}{z_1^2 + x_t^2}} - \sqrt{\frac{z_{II}^2 x_t^2}{z_2^2 + x_t^2}} = \frac{z_{II} x_t [(z_2^2 + x_t^2)^{1/2} - (z_1^2 + x_t^2)^{1/2}]}{[(z_1^2 + x_t^2)(z_2^2 + x_t^2)]^{1/2}} \end{array}$$

Based on the above equations, SID, SOD and center beam part may be determined from the shadows of the lead spheres.

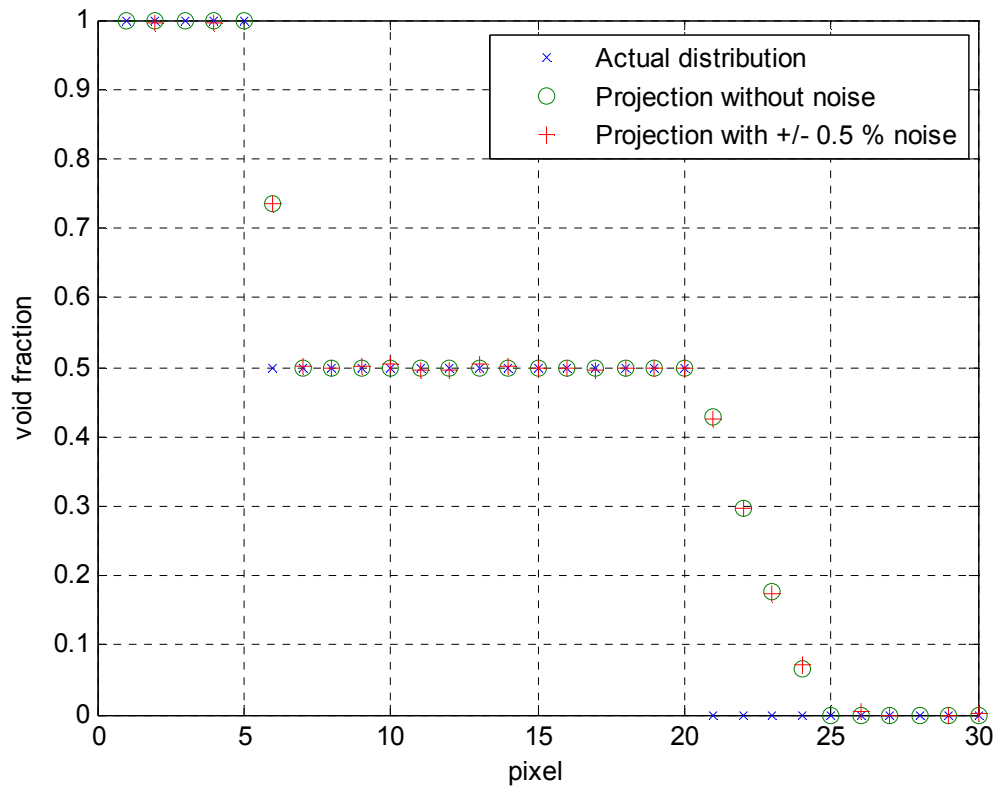


Figure 5.36 – Simulated void fraction distribution (X), and distorted void fraction distributions that would be observed in the imager plane due to non-parallel beam paths. Circles are “perfect” projections, and red plus-signs are projections with +/- 0 to 0.5 % random noise in void fraction measurement, mimicking the type of errors a real image might have.

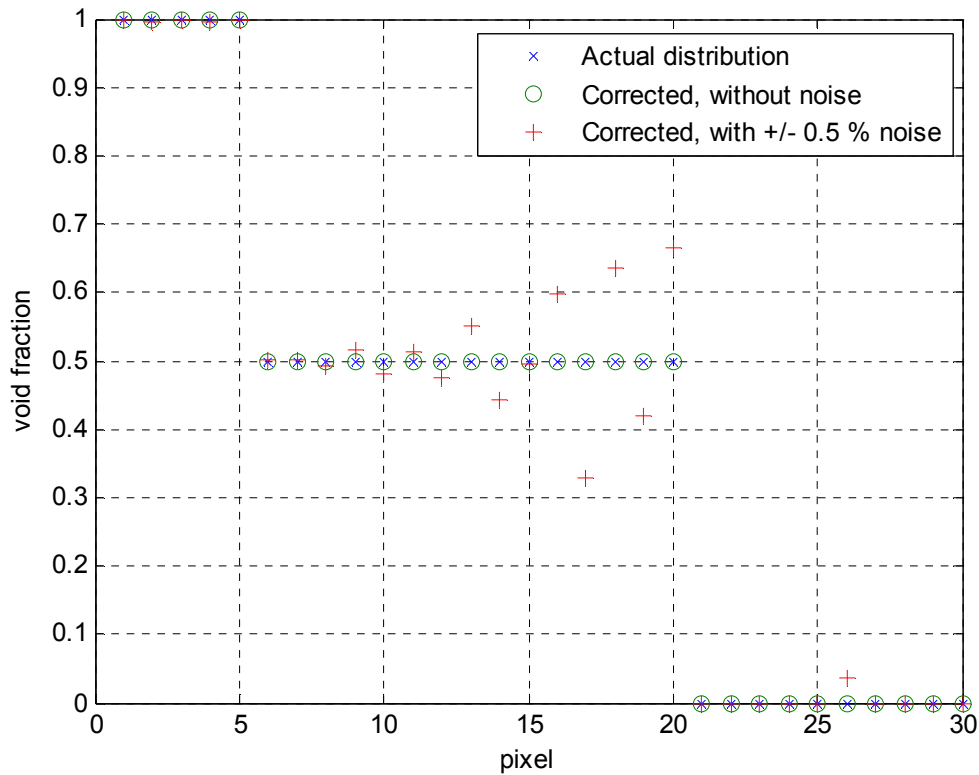


Figure 5.37 – Reconstructed void fraction distribution (x) using eqn. 5.56. In the absence of noise (o) the non-distorted void fraction distribution is recovered within the round off error accumulated during the simulation. However, the data which had noise (+) did not return the actual distribution, but rather the noise produced a large error of increasing magnitude as the reconstruction progressed away from the center beam path.

Figures 5.36 and 5.37 show the simulated projected and corrected one dimensional void fraction distributions. During reconstruction besides using eqn. 5.56, the only limitation placed on void fraction was that it had to be between zero and unity for every point. The reconstruction starts from the center beam path at the origin, and errors are cumulative. This is clearly demonstrated in figure 5.37 where the error grows. It is also evident that when void fraction for one point is calculated to be lower than it should be, the tendency is for the next point to return a higher value, and *vice versa*.

To deal with noise, development of an iterative reconstruction method was initiated. The method attempted to minimize a weighted global error, and could place additional constraints on the distribution, such as monotonically decreasing values in certain areas. Also, it would help if multiple projections, *i.e.* additional data to constrain solution, would be available. A robust algorithm utilizing the information from a single projection and capable of dealing with noise is not yet complete, and this will be part of future work. However, the preceding shows that in principle the correction for non-parallel beam paths is possible. Additionally, if for a given experimental setup the error due to non-parallel beam paths is smaller than that due to other sources, such as might be the case with shallow ray angles, it may not be necessary to attempt the correction.

#### 5.7.12 Empirically determined resolution

Section 5.7 focused on the various factors affecting the spatial resolution, and we concluded it by empirically determining the system resolution. A standard x-ray resolution test tool with 16 to 50 lines/inch (0.63 to 1.97 lines/mm) was used to quantify the system resolution. Besides the camera and phosphor resolution, the image is blurred due to the finite size of the source's focal spot, causing a penumbra. The source could be operated with a 0.6 mm or 1.2 mm focal spot, with the smaller yielding better image sharpness, but limiting the power that could be used without damaging the source. Figure 5.38 is an image of the resolution test tool, illustrating that using the basic system configuration we can resolve up to approximately 1.6 lines/mm.



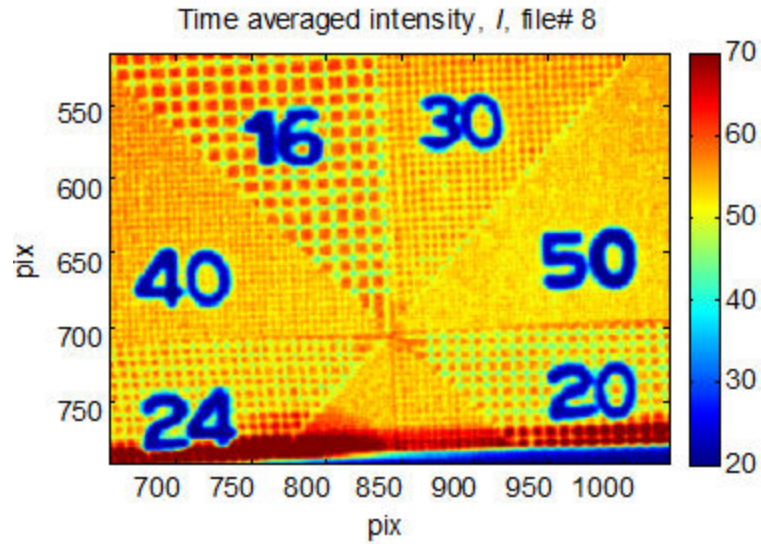


Figure 5.38 – X-ray image of a standard-resolution test tool in the flow domain. The numbers in the image give the grid spacing in units of lines per inch.

## 5.8 Discussion

For evaluation of the entire system's performance the key questions are: how accurately is void fraction measured, what is the spatial and temporal resolution. The former is answered by the actual versus measured void fraction curve presented in figure 5.15 where, in this time averaged case, the results agreed within 1%. In turn the spatial resolution can be estimated from an image of the resolution test tool (figure 5.38), or more properly from a modular transfer function of a line pair target. The temporal resolution could be defined, for instance, as time that needs to elapse in order for the phosphor to decay, in which case it would be  $O(10 \text{ ms})$ , however more rapid changes in the void fraction at times order of magnitude faster can be clearly observed.

Based on the results presented, we estimate that the current system is suitable for the task of quantitatively measuring the time averaged two dimensional projections of 0

to 100% void fraction to within 2%, distinguishing features of  $O(1 \text{ mm})$ , and detecting changes at time scales of the order of 1 ms. However, care must be taken to not overstate the quantitative usefulness of the instantaneous images, where based on simple pixel size the apparent image resolution could be mistaken to be better than 0.2 mm and areas with veiling glare may not be obvious.

In this work, the effect of noise is usually minimized by temporal or spatial averaging. Only for the time resolved movies did we use, for instance, a 10 pixel 2D median filter to reduce the random noise in the animation.

This chapter covered many of the challenges of the technique, and from various sources brought together methods for dealing with them each. The purpose was to have the capability to obtain validation-quality void fraction data, therefor much emphasis was placed on understanding the sources of uncertainty so that they can be quantified.

To investigate the suitability of this system for complex cavitating flows, we still must validate it against a void fraction field measured by other means. For this purpose, Chapter 6 is devoted to discussing the use of this system for a ventilated cavity behind a backward facing step, where the results were compared to those from optical probes and high speed video.

## 5.9 References for Chapter 5

Aeschlimann, V., Barre, S., and Legoupil, S., “X-ray attenuation measurements in a cavitating mixing layer for instantaneous two-dimensional void ratio determination”, *Phys. Fluids*, 23, 055101, 2011

Alles, J., & Mudde, R. F. “Beam hardening: Analytical considerations of the effective attenuation coefficient of x-ray tomography”. *Medical Physics*, 34(7), 2882. doi:10.1118/1.2742501, 2007.

Barney Smith, E. H. “PSF estimation by gradient descent fit to the ESF”. *Proceedings of SPIE*, 6059(January), 60590E-60590E-9. *Spie*. doi:10.1117/12.643071, 2006.

Bieberle, M., Barthel, F., Menz, H.-J., Mayer, H.-J. and Hampel, U., “Ultrafast three-dimensional X-ray computed tomography”, *Appl. Phys. Lett.* 98, 034101, 2011.

Brennen C. E. “Cavitation and Bubble Dynamics”. Oxford University Press, Oxford, UK, 1995.

Bushberg, J.T, Seibert, J.A Leidholdt, Jr, E.M. and Boone, J.M. "The Essential Physics of Medical Imaging, 2<sup>nd</sup> edition", Lippincott Williams & Wilkins, Philadelphia, 2001.

Ceccio, S.L. and George D. L. "A Review of Electrical Impedance Techniques for the Measurement of Multiphase Flows" *Journal of Fluids Engineering*, 118(2), 391-399, 1996.

Ceccio, S. L., “Quantitative Measurements in Multiphase Flows Using Gamma Densitometry Tomography and Electrical Impedance Tomography,” Keynote at Proc. 6th International Conference on Multiphase Flow- ICMF 2007, Leipzig, 2007.

Cerveri, P., Forlani, C., Borghese, N.A., and Ferrigno G., “Distortion correction for x-ray intensifiers: Local unwarpong polynomials and RBF neural networks”, *Am. Assoc. Phys. Med.* 29(8) August, 2002.

Coutier-Delgosha, O., Stutz, B., Vabre, A., & Legoupil, S. “Analysis of cavitating flow structure by experimental and numerical investigations”. *Journal of Fluid Mechanics*, 578, 171. doi:10.1017/S0022112007004934, 2007.

Doebelin, E. O. “Measurement systems application and design, 5<sup>th</sup> edition”, McGraw-Hill , 1990.

Hassan, W., Legoupil, S., Chambellan, D., and Barre, S., “Dynamic Localization of Vapor Fraction in Turbo pump Inducers by X-ray Tomography”, *IEEE Transactions on Nuclear Science*, 55(1), 656-661, 2008.

Heindel, T. J. "A Review of X-Ray Flow Visualization With Applications to Multiphase Flows". *Journal of Fluids Engineering*, 133(7), 074001. doi: 10.1115/1.4004367, 2011.

Hendrik, T., Tysonlab at the University of North Carolina "Matlab tools for digitizing video files and calibrating cameras". <http://www.unc.edu/~thedrick/software1.html>. Software accessed in October 2010.

Holder, D. *Electrical impedance tomography: methods, history, and applications* IOP publishing, 2005.

Hsieh, J., Molthen, R. C., Dawson, C. a, & Johnson, R. H. "An iterative approach to the beam hardening correction in cone beam CT". *Medical physics*, 27(1), 23-9. Retrieved from <http://www.ncbi.nlm.nih.gov/pubmed/10659734>, 2000.

Hubbell JH, Seltzer SM "Tables of X-Ray Mass Attenuation Coefficients and Mass Energy-Absorption Coefficients (version 1.4)". National Institute of Standards and Technology, Gaithersburg, MD. 2004. <http://www.nist.gov/pml/data/xraycoef/index.cfm> Accessed 27 June 2011.

Hubers, J.L., Striegel, A.C., Heindel, T.J., Gray, J.N., Jensen, T.C., "X-ray computed tomography in large bubble columns", *Chem. Eng. Science*, 60, 6124-6133, 2005.

Huda,W and Slone R "Review of Radiologic Physics" Lippincott, Williams and Wilkins, 2003.

Makiharju, S. and Ceccio, S.L. "Time Resolved X-Ray Densitometry System for Cavitating Flows". WIMRC 3rd Int. Cavitation Forum, Warwick, UK, 2011.

Poludniowski, G., Evans, P. M., Kavanagh, a, & Webb, S. "Removal and effects of scatter-glare in cone-beam CT with an amorphous-silicon flat-panel detector". *Physics in medicine and biology*, 56(6), 1837-51. doi:10.1088/0031-9155/56/6/019, 2011

Poludniowski, G., Landry, G., DeBlois, F., Evans, P. M., & Verhaegen, F. "SpekCalc: a program to calculate photon spectra from tungsten anode x-ray tubes". *Physics in medicine and biology*, 54(19), N433-8. doi:10.1088/0031-9155/54/19/N01, 2009.

Seibert, J. A., Nalcioglu, O., & Roeck, W. W. " Characterization of the veiling glare PSF in x-ray image intensified fluoroscopy". *Medical Physics*, 11(2), 172, 1984.

Seibert, J. A., Nalcioglu, O., & Roeck, W. "Removal of image intensifier veiling glare by mathematical deconvolution techniques". *Medical Physics*, 12(3), 281, 1985.

Seibert, J. a, & Boone, J. M., “Scatter removal by deconvolution”. *Medical physics*, 15(4), 567, 1988.

Seibert J A and Boone J M, “X-Ray Imaging Physics for Nuclear Medicine Technologists. Part 2: X-Ray Interactions and Image Formation”, *J. Nucl. Med. Technol.* March 1, vol. 33 no. 1 3-18., 2005

Stutz, B., & Legoupil, S. “X-ray measurements within unsteady cavitation. *Instrumentation*”, 35, 130-138. doi:10.1007/s00348-003-0622-0, 2003.

Terentiev AG, Kirchner IN, Uhlman JS “The hydrodynamics of Cavitating Flows”. Backbone Publishing Company, 2011.

Thales electron devices, “Technical specification: x-ray image intensifier TH 9432 QX H686 VR13”, Moiras, France 2006.

Thirlwall, J. T. “The detective quantum efficiency of medical x-ray image intensifiers”. *Review of Scientific Instruments*, 69(11), 3953. doi:10.1063/1.1149205, 1998.

Tortora, P. R., Ceccio, S. L., O’Hern, T. J., Torczynski, J. R., and Trujillo, S. M. “Quantitative Measurement of Solids Distribution in Gas-Solid Riser Flows Using Electrical Impedance Tomography and Gamma Densitometry Tomography,” *Int. J. of Multiphase Flow*, 32(8), 972-995, 2006.

Van Der Welle, R. “Void fraction, bubble velocity and bubble size in two-phase flow”, *Int. J. of Multiphase Flow*, 11(3), 317-345, 1985.

York, T.J. “Status of electrical tomography in industrial applications”, *Electron. Imaging* 10, 608, 2001.

Vision research Inc, 2007, The CINE File Format, 2007.

## CHAPTER 6

### **A Ventilated Partial Cavity Downstream of a Backward Facing Step**

The x-ray densitometry system described in the previous chapter is intended for the study of cavitating flows in which any in situ probes would greatly perturb the flow, surface mounted sensors would not give void fraction information far from the wall and optical techniques would fail due to the opaque nature of flow with multiple light scattering phase interfaces. To validate the x-ray technique, especially the post-processing algorithms used, we first employed the system to investigate a ventilated cavity. This enabled us not only to know the actual gas flux being ventilated, but also to measure the void fraction using optical probes and high speed video. The first section describes the experimental setup. The second presents results of single phase flow measurements. The third section briefly discusses the optical probes, high speed video, and how their results were processed. The results obtained from these three methods (x-ray, optical probes and high speed video) are then compared, followed by a brief discussion in the last section.

## 6.1 Experimental setup

The experiments were conducted in the water tunnel described in Chapter 5. A ~91 cm long flat plate with a 12.7 mm tall backward facing step and a 2:1 elliptical nose, with a boundary layer trip at the leading edge was placed in the test section. The backward facing step was located ~35 cm downstream of the leading edge. Air was injected from the base of the step through a 4.7 mm tall slot spanning the width of the model. The plate thickness downstream of the step was 19.1 mm. The air was first introduced into a chamber inside the model, and exited the chamber through a porous plate to produce a spanwise uniform flow. The spanwise uniformity of the air injection was qualitatively checked using a hot wire anemometer, and was found to be approximately uniform within the accuracy of the measurement. A gate was used to form a free surface upstream of the model to allow for long periods of air injection, similar to that used for the PCDR experiments described in Chapters 2 and 3. The static pressure over the free surface was kept at 1 atm, by a 5 cm vent which was open to the atmosphere. Figure 6.1 shows cross section of the model and free surface forming gate in the test section. The model and gate span the entire width of the test section (209.6 mm).

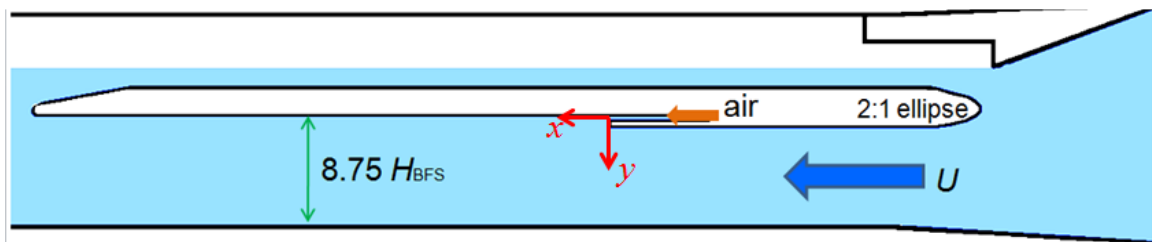
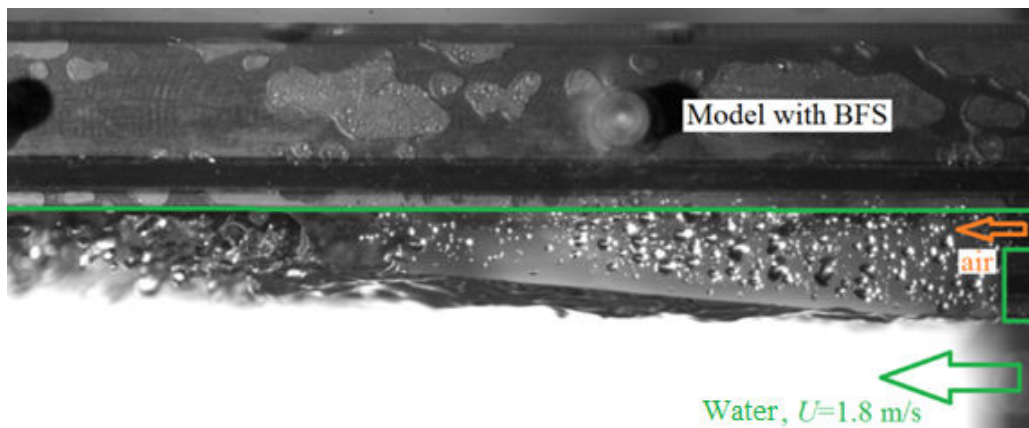
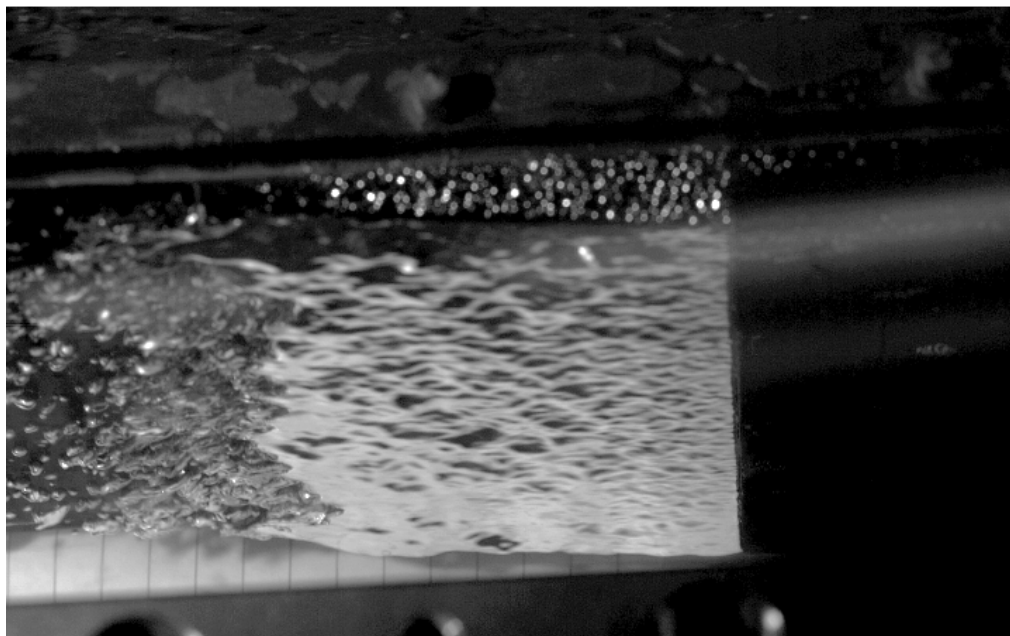


Figure 6.1 – Schematic of the model in the test section. The red arrows indicate the  $x$ - and  $y$ -coordinate axis, and the origin is located at the base of the step. The free surface forming gate was located immediately upstream of the model. Flow is from right to left as indicated by the arrow.

Depending on the ventilation rate (volume flux of air injected) a ventilated partial cavity, in this case only occupying the recirculation zone behind the step, or an air layer persisting for the length of the model was formed. For the x-ray densitometry system's validation study, the focus was on ventilated partial cavities, such as shown in figure 6.2.



(a)



(b)

Figure 6.2 – Cavity viewed from the side (a) and from below at an oblique angle (b). The photos have a different downstream field of view as can be seen by the different location of the step.



The measurement locations are shown in figure 6.3. The x-ray system was used to obtain 2D void fraction distributions at two locations: view #1, which included the entire recirculation region behind the step, and view #2, which was centered ~23 cm downstream of the backward facing step. Optical probes were used at two streamwise locations on the centerline of the water tunnel to obtain vertical profiles of void fraction, bubble size distribution and interfacial velocity distribution. Position #1 was located ~6.3 cm downstream of the step, still inside, but near the end of the typical recirculation region. Position #2 was 26.7 cm downstream of the step.

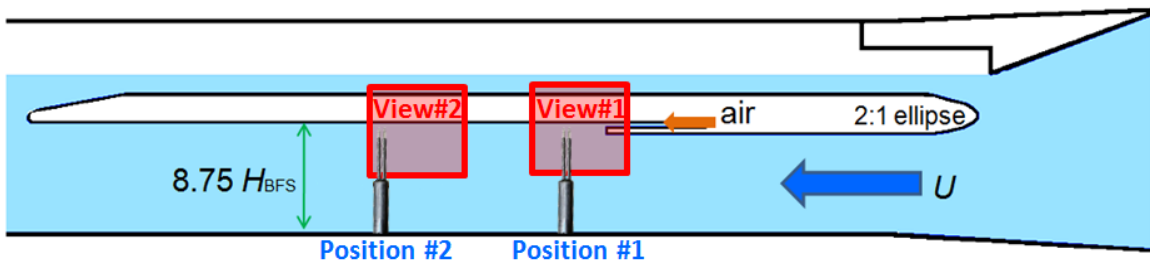


Figure 6.3 – Instrument locations. The coordinate axis are as shown in figure 6.1, and the origin is located at the base of the step.

A static pitot tube was used to measure the free stream speed. It was located approximately 15 cm upstream of the step, and ~4 cm below the step surface. The pitot was connected to an Omega PX2300-5DI, 0 to 5 psid transducer. The flow speed was then calculated using the following equation

$$U = \sqrt{\frac{2(p_{stagnation} - p_{static})}{\rho_w}} \quad (6.1)$$

where  $\rho_w$  is the density of water and the stagnation and static pressures are sensed by the pitot's pressure ports. The static pressure in the tunnel was measured from a pressure tap on the bottom of the tunnel approximately at the streamwise location of the step using a second Omega PX2300-5DI, 0 to 5 psid transducer. Additionally, the pressure differential between the static pressure tap and inside of the cavity, in the slot  $\sim 2$  cm upstream of the step, was measured using an Omega PX76 0 to 6 in H<sub>2</sub>O differential pressure transducer. All the transducers were connected to a National Instruments DAQ NI USB-6259, and signal processing and recording performed using Labview 2009 Virtual Instruments.

## 6.2 Description of the single phase flow

The turbulent boundary layer at the backward facing step was measured using time averaged, 2D, two-component particle image velocimetry (PIV). At the flow speed of 1.8 m/s the boundary layer thickness was  $\delta \sim 7$  mm and momentum thickness was  $\theta = 0.8$  mm, giving  $Re_\theta \sim 1400$ . Figure 6.4 shows the measured boundary layer (BL) profiles just upstream of the step. The momentum thickness was determined from

$$\theta = \int_0^\delta \frac{U(y)}{U_\infty} \left(1 - \frac{U(y)}{U_\infty}\right) dy \approx \sum_{n=1}^N \frac{U(y_n)}{U_\infty} \left(1 - \frac{U(y_n)}{U_\infty}\right) (y_n - y_{n-1})$$

where boundary layer thickness  $\delta$  was found by interpolating the  $y$ -coordinate of the location where velocity reached 99% of free stream speed outside the TBL.

Figure 6.5 shows the time averaged 2D velocity vector field in the recirculation zone behind the step, and figure 6.6 shows the velocity profile obtained 61 mm downstream of the step. Figure 6.8 shows the velocity profile at approximately the streamwise position of probe 2.

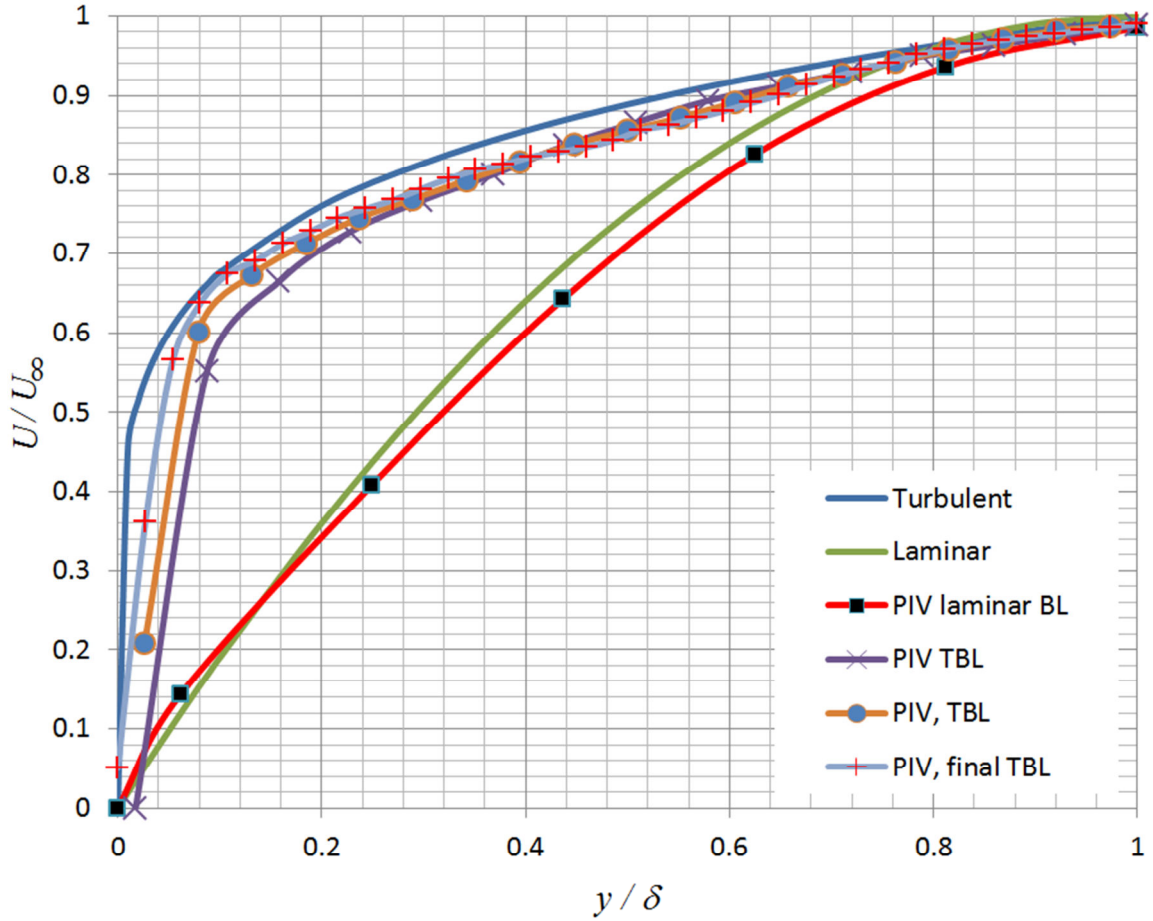


Figure 6.4 – Time averaged PIV velocity profiles immediately upstream of the step. The solid blue and green curves show the theoretical turbulent and laminar velocity profiles. The red curve shows a laminar BL measured without a trip. The crosses and circles show the boundary layers obtained with various trips, and finally the + - signs show the TBL with the trip which was used for these experiments.

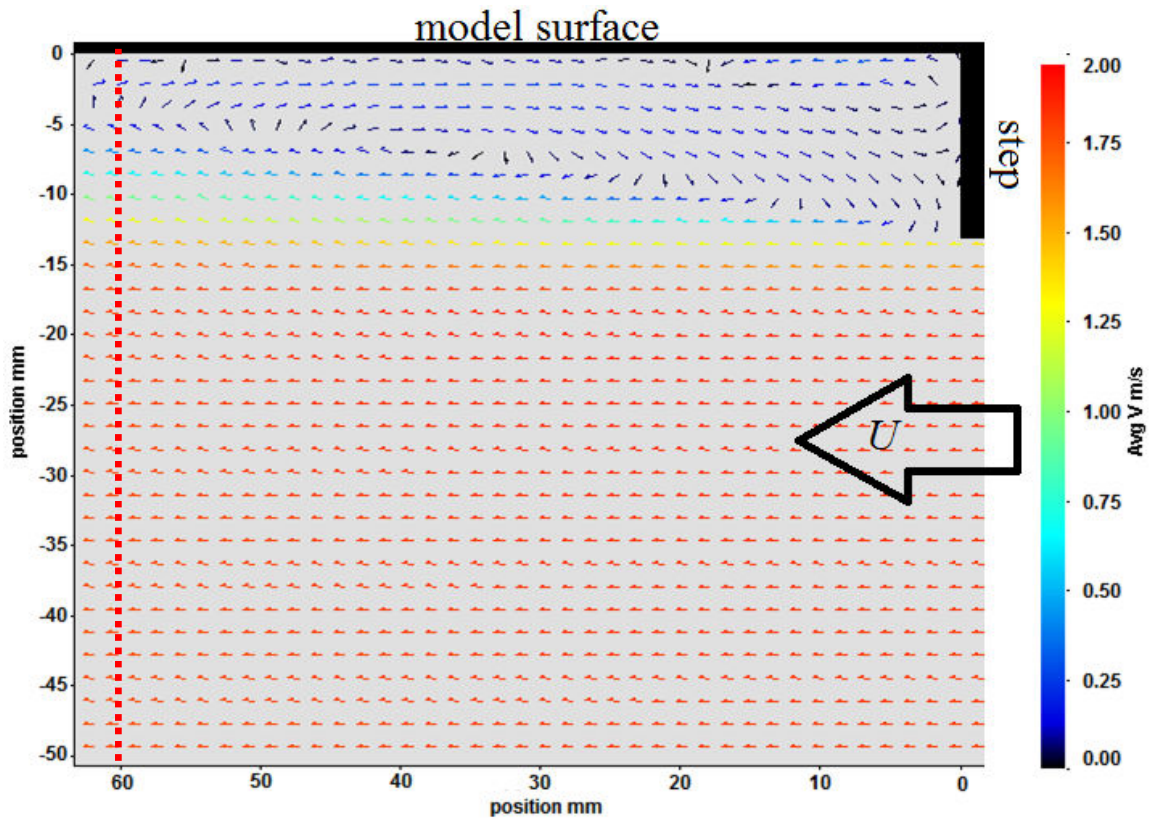


Figure 6.5 – Time averaged PIV velocity field immediately after the backward facing step. The black lines on the top are sketched to indicate location of the step and model test surface at  $y = 0$  mm. The red dashed line indicates the location from which the velocity profile shown in the next figure is taken from.

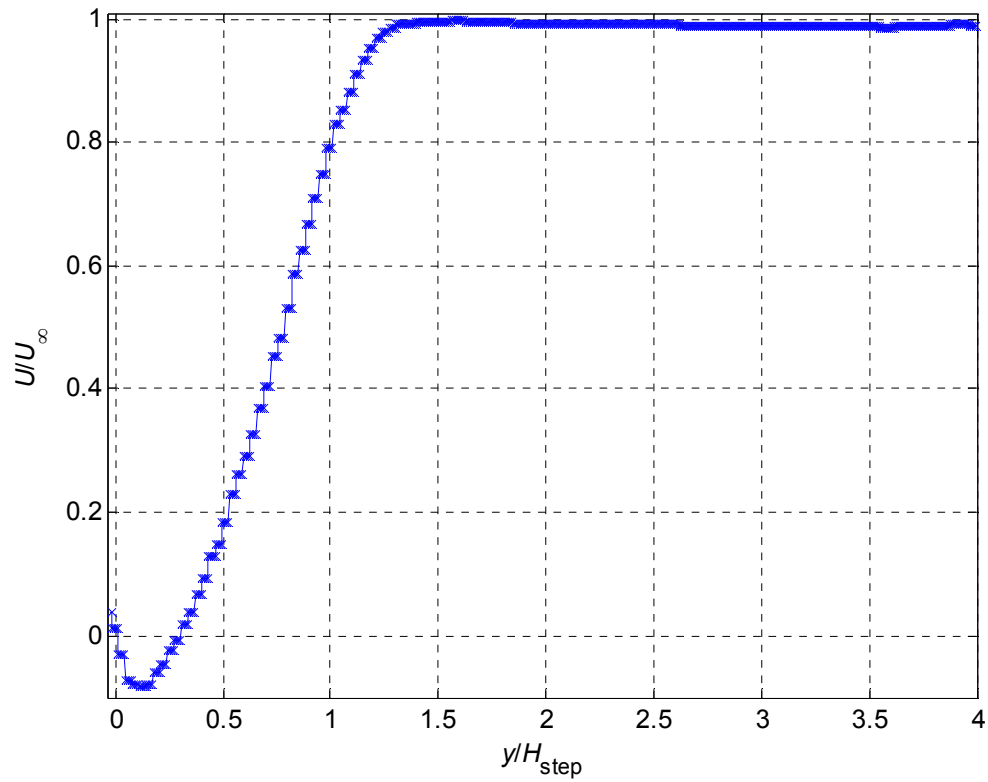


Figure 6.6 – Time averaged streamwise velocity component 61 mm downstream of the step. The measured velocity near the wall may be incorrect due to reflection of laser light and particle images from the wall. Here position 0.0 mm is measured from the model’s test surface downstream of the step.

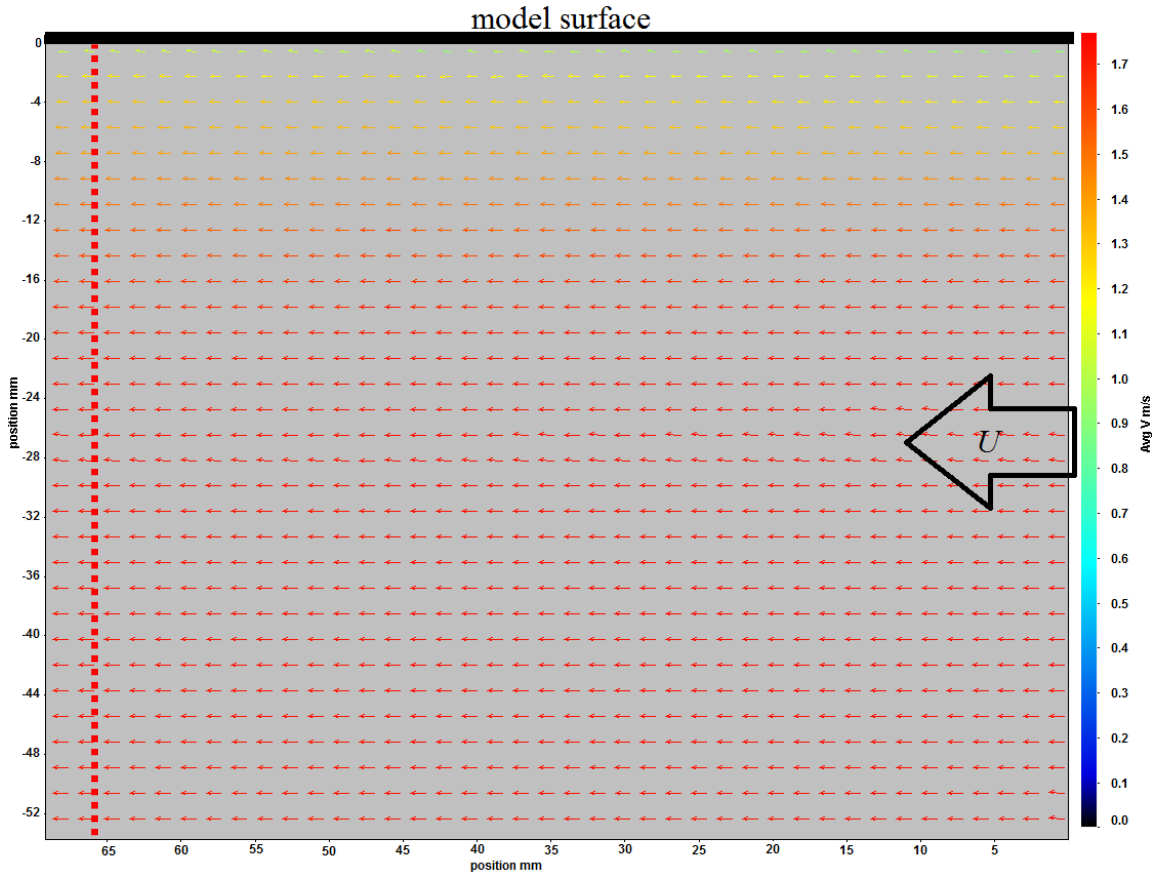


Figure 6.7 – Time averaged PIV velocity field in vicinity of probe position #2 after the backward facing step. The black line on the top indicates the location of the model test surface at  $y = 0$  mm. The red dashed line indicates the location from which the velocity profile shown in the next figure is taken from.

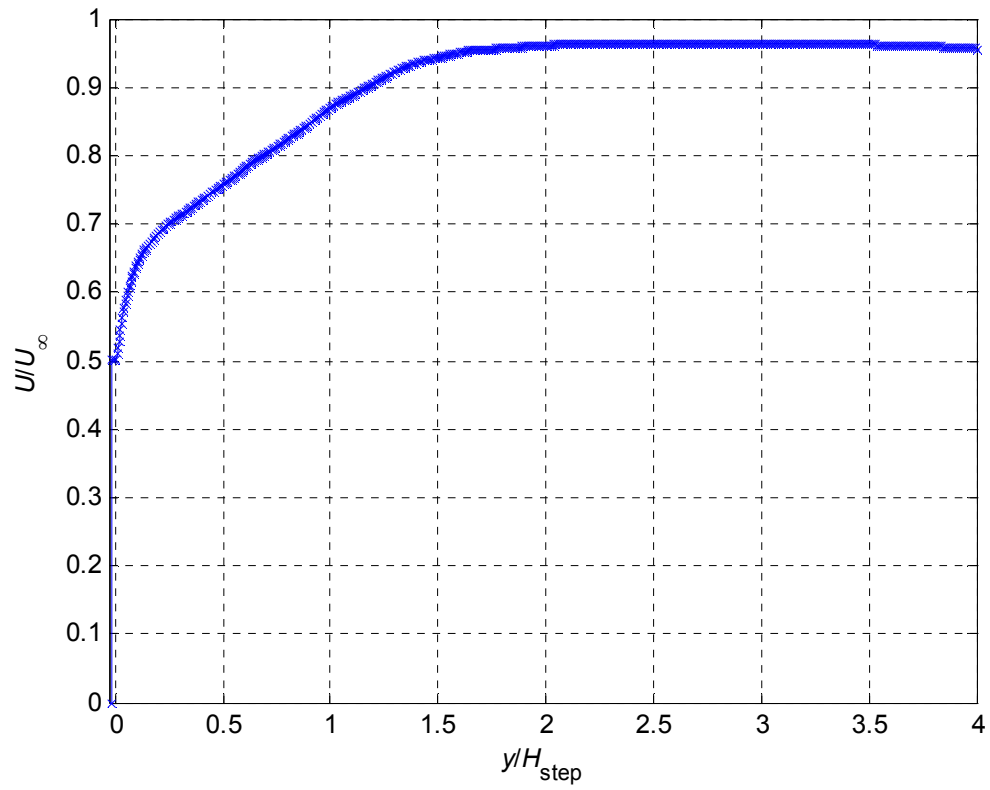


Figure 6.8 – Time averaged PIV velocity field at approximately the second optical probe position. Velocity is normalized by the free stream speed at the backward facing step.

### 6.3 Optical probes and high speed video

Two different optical probes made by RBI Instrumentation were used to measure the void fraction. First a double probe, shown in figure 6.9, with 10 micron tips was used. The main limitation of this probe was that it is not suitable to be used in the recirculating region behind the backward facing step, as in reverse flow the probe tips will be in the wake of the support. The second optical probe was ideally suited for bi-directional flow, as it was symmetrical around the middle axis of the support. The optical probes by RBI were on loan from Dr. Celine Gabillet of Ecole Navale. She generously loaned the probes and participated in the processing of data. Besides the simplest determination of void fraction based on the time the probe tip was in air versus water, the data processing was accomplished as explained in Gabillet *et al.* (2002) using Prof. Gabillet's codes.

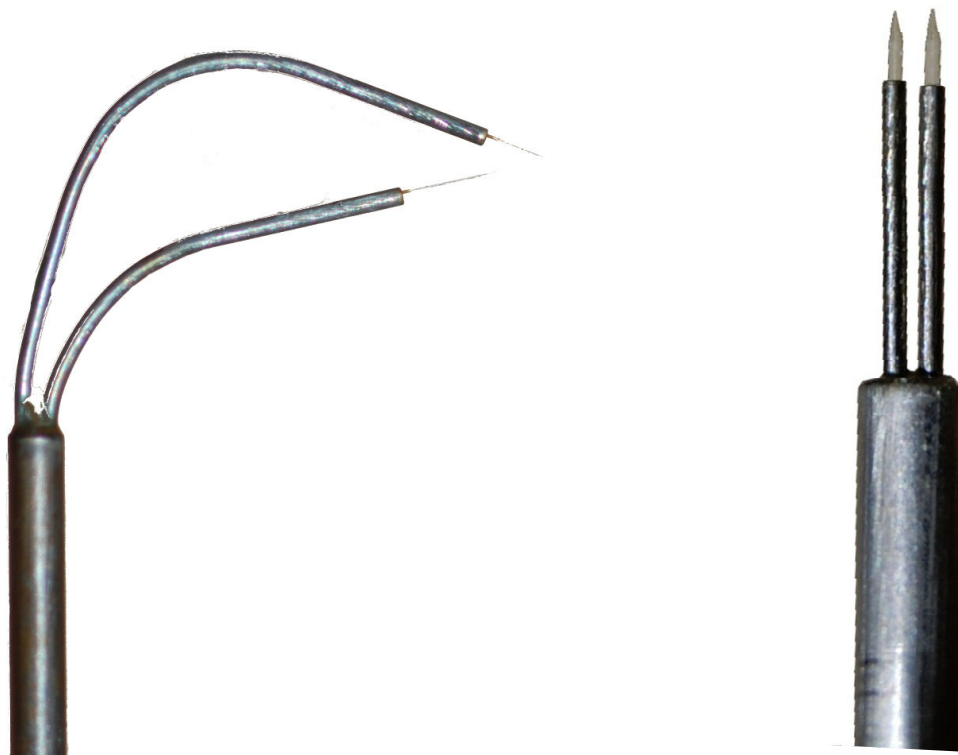


Figure 6.9 – Left: a dual fiber optical probe with 10 micron tips. Right: a dual fiber optical probe with 30 micron tips suited for use in bi-directional multiphase flow.



The probes were attached to a traverse mechanism designed by the author (originally used as the traverses described in Chapter 2 and Appendix C). The mechanism is shown in figure C.8. It enabled the probes to be positioned with accuracy of 0.2 mm or better. However, the position relative to the plate was only accurate to within +/- 0.7mm, as the tips could not be allowed to touch the model surface and it was not possible to access the inside of the water tunnel with both the model and probes installed.

The simple void fraction plots presented in the figures 6.10-21 are based on the fraction of time the probe tip was in water versus air, based on data processed by the author; however the bubble histograms and all advanced processing of the probe data were performed by Dr. Gabillet. She also recalculated the void fraction distributions. First we present the data from optical probe position 1 for the two different flow speeds and three ventilation rates, followed by the corresponding data for position 2.

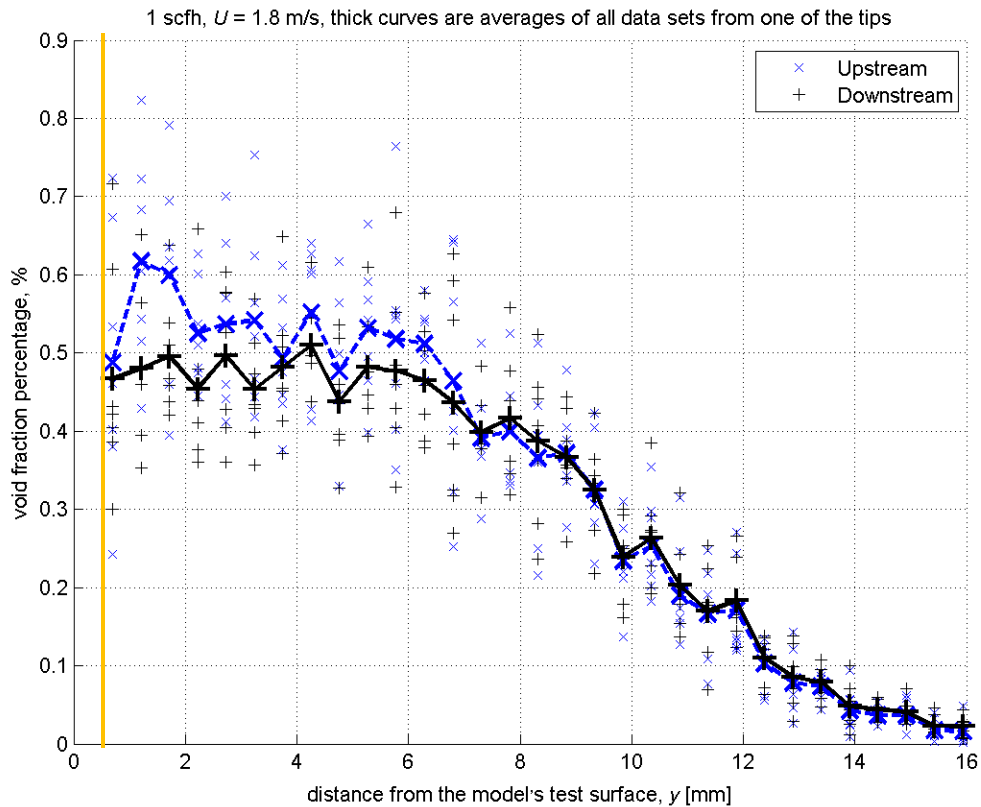


Figure 6.10 – Void fraction distributions from optical probe at position #1. Flow speed was 1.8 m/s and ventilation rate  $7.87 \times 10^{-6} \text{ m}^3/\text{s}$ . The blue and black points are based on data provided by the upstream and downstream tips, respectively. The small scattered markers were based on data averaged over 30 seconds, and the thicker markers connected by lines are the combined averages, representing averaging over  $\sim 3$  minutes and 30 seconds. Number of bubbles detected varied from 24 at  $y = 15.9$  mm to 309 at  $y = 7.8$  mm, and decreasing to 90 at  $y = 1.7$  mm. The orange line indicates the location beyond which optical probe data was not recorded to avoid risking the probe tips touch the model surface.

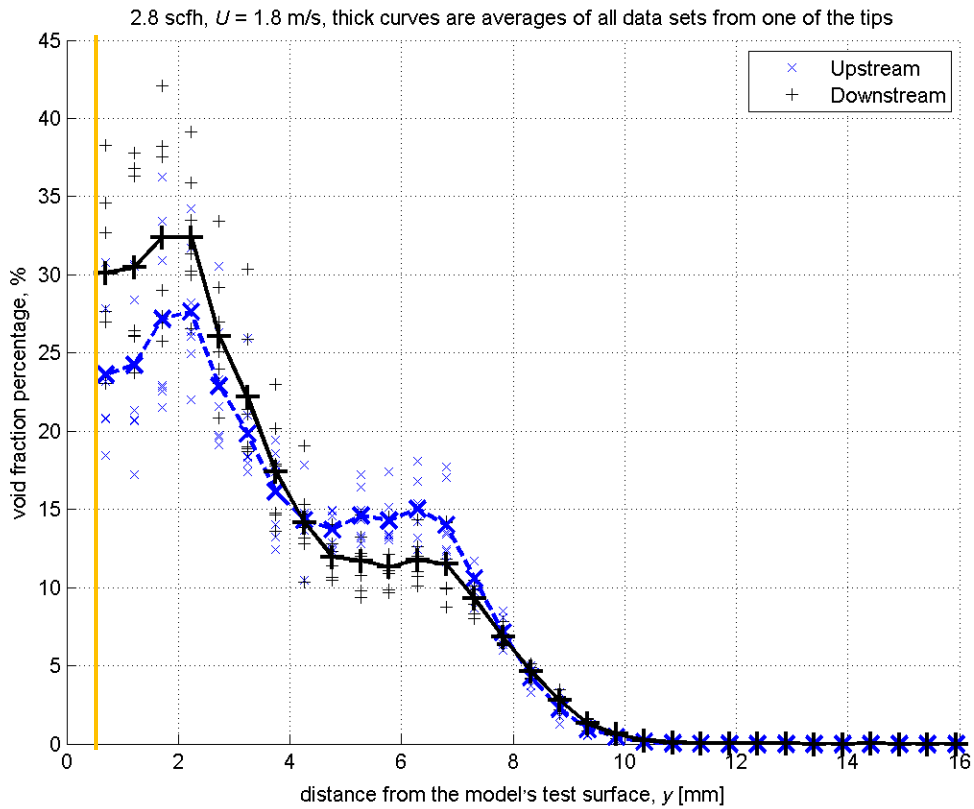


Figure 6.11 – Void fraction distributions from optical probe at position #1. Flow speed was 1.8 m/s and ventilation rate  $2.2 \times 10^{-5} \text{ m}^3/\text{s}$ . The blue and black points are based on data provided by the upstream and downstream tips, respectively. The small scattered markers were based on data averaged over 30 seconds, and the thicker markers connected by lines are the combined averages, representing averaging over  $\sim 3$  minutes and 30 seconds. The orange line indicates the location beyond which optical probe data was not recorded to avoid risking the probe tips touch the model surface.

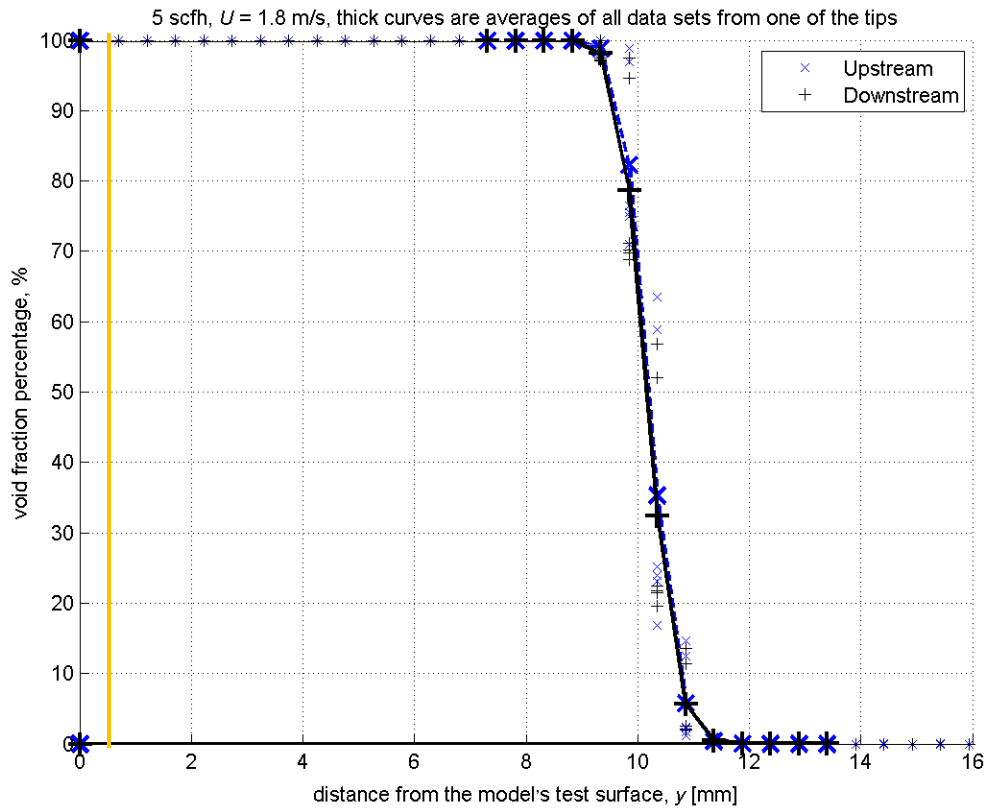


Figure 6.12 – Void fraction distributions from optical probe at position #1. Flow speed was 1.8 m/s and ventilation rate  $3.93 \times 10^{-5} \text{ m}^3/\text{s}$ . The blue and black points are based on data provided by the upstream and downstream tips, respectively. The small scattered markers were based on data averaged over 30 seconds, and the thicker markers connected by lines are the combined averages, representing averaging over  $\sim 3$  minutes and 30 seconds. The orange line indicates the location beyond which optical probe data was not recorded to avoid risking the probe tips touch the model surface.

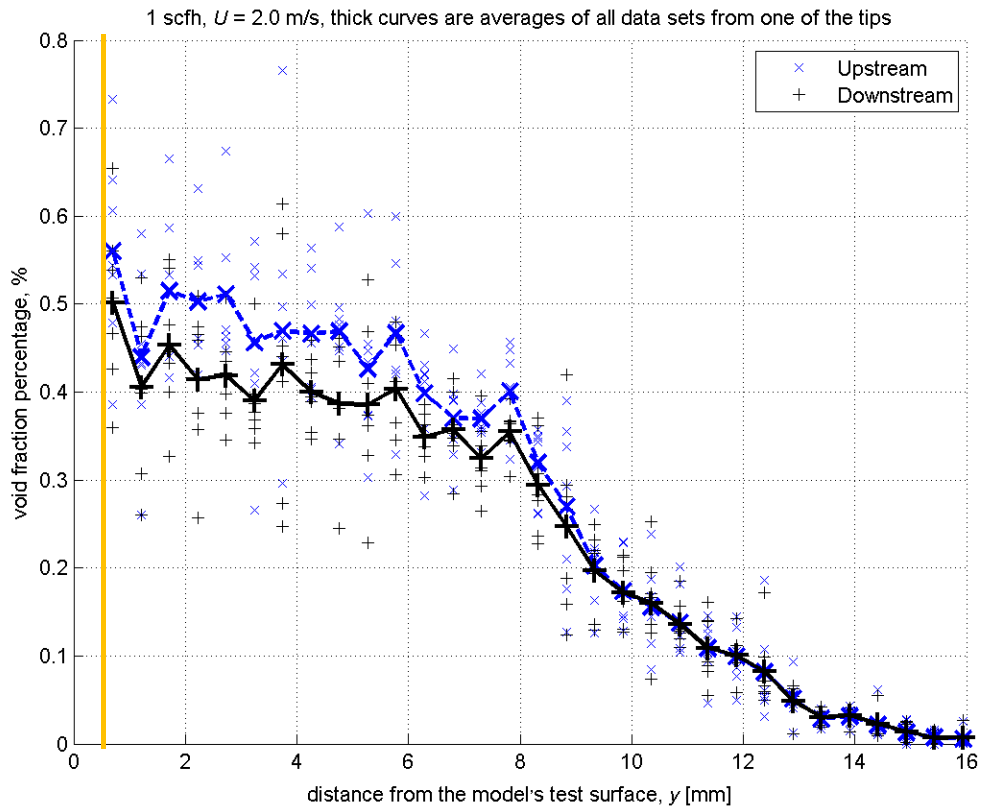


Figure 6.13 – Void fraction distributions from optical probe at position #1. Flow speed was 2.0 m/s and ventilation rate  $7.87 \times 10^{-6} \text{ m}^3/\text{s}$ . The blue and black points are based on data provided by the upstream and downstream tips, respectively. The small scattered markers were based on data averaged over 30 seconds, and the thicker markers connected by lines are the combined averages, representing averaging over  $\sim 3$  minutes and 30 seconds. The orange line indicates the location beyond which optical probe data was not recorded to avoid risking the probe tips touch the model surface.

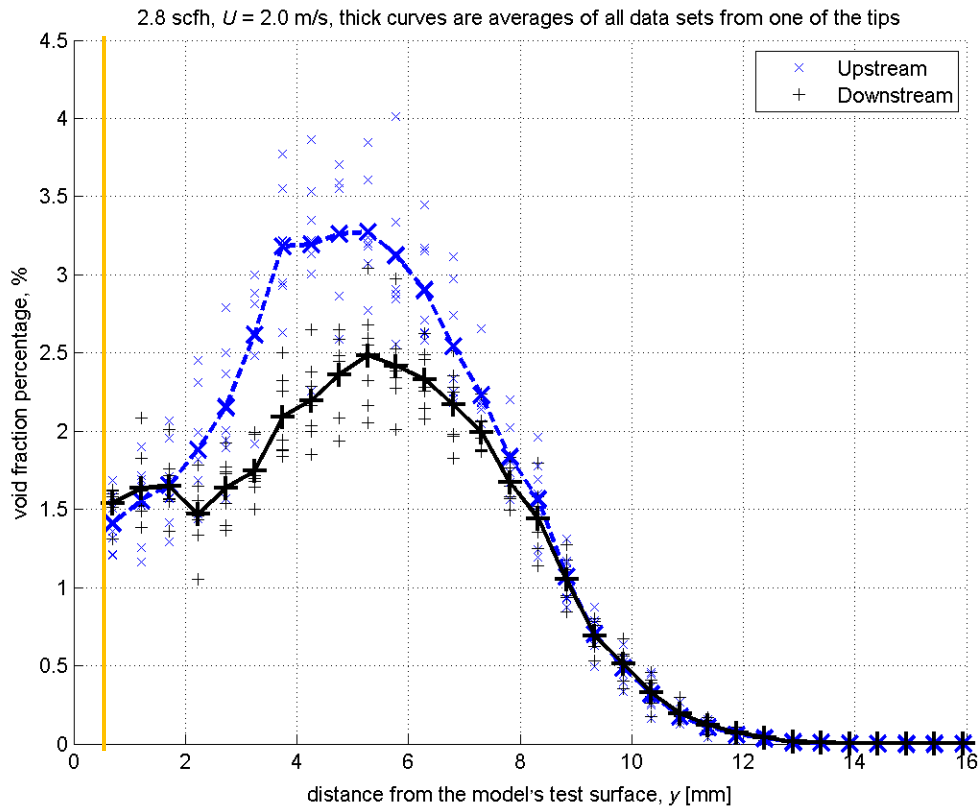


Figure 6.14 – Void fraction distributions from optical probe at position #1. Flow speed was 2.0 m/s and ventilation rate  $2.2 \times 10^{-5} \text{ m}^3/\text{s}$ . The blue and black points are based on data provided by the upstream and downstream tips, respectively. The small scattered markers were based on data averaged over 30 seconds, and the thicker markers connected by lines are the combined averages, representing averaging over  $\sim 3$  minutes and 30 seconds. The orange line indicates the location beyond which optical probe data was not recorded to avoid risking the probe tips touch the model surface.

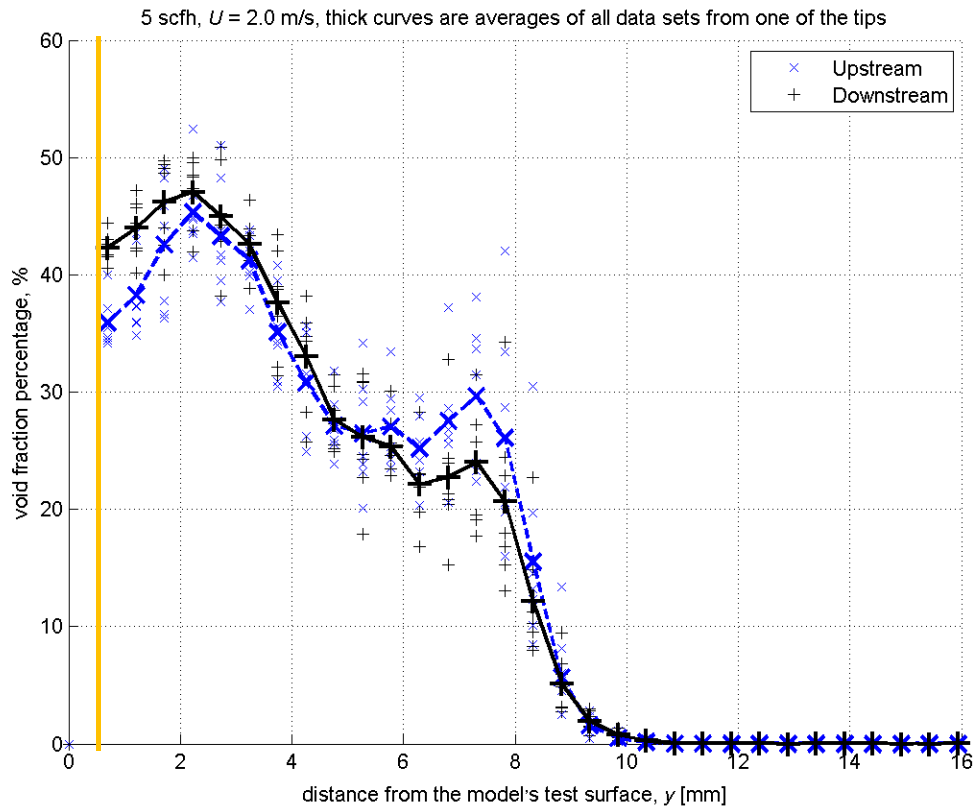


Figure 6.15 – Void fraction distributions from optical probe at position #1. Flow speed was 2.0 m/s and ventilation rate  $3.93 \times 10^{-5} \text{ m}^3/\text{s}$ . The blue and black points are based on data provided by the upstream and downstream tips, respectively. The small scattered markers were based on data averaged over 30 seconds, and the thicker markers connected by lines are the combined averages, representing averaging over  $\sim 3$  minutes and 30 seconds. The orange line indicates the location beyond which optical probe data was not recorded to avoid risking the probe tips touch the model surface.

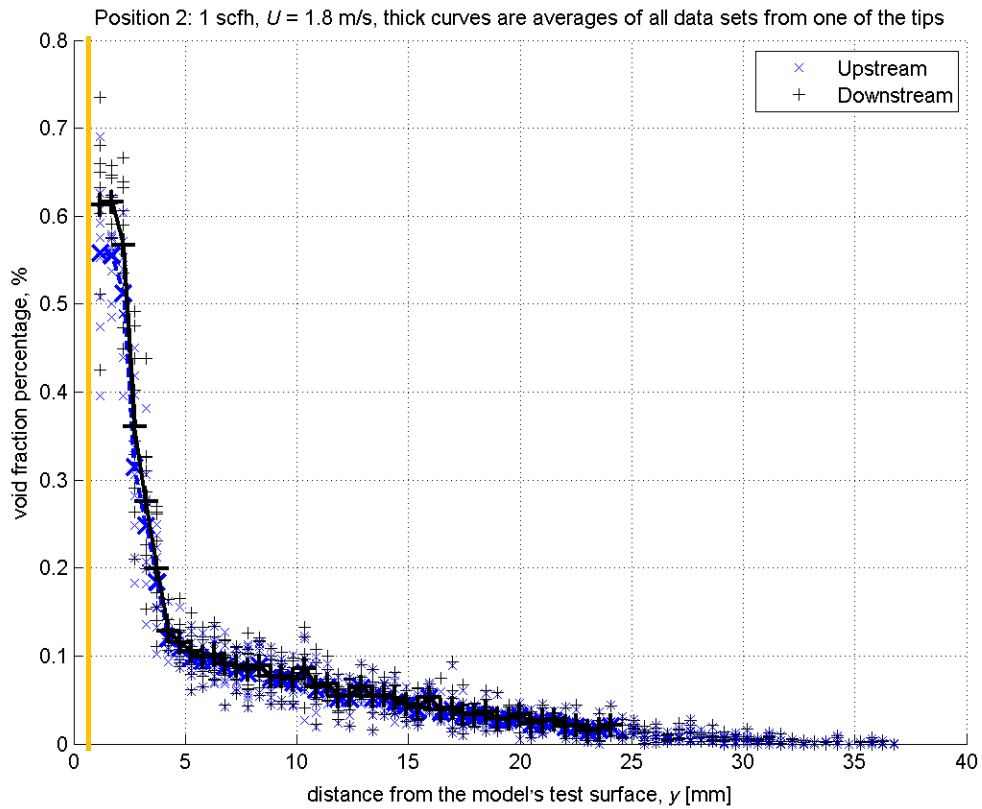


Figure 6.16 – Void fraction distributions from optical probe at position #2. Flow speed was 1.8 m/s and ventilation rate  $7.87 \times 10^{-6} \text{ m}^3/\text{s}$ . The blue and black points are based on data provided by the upstream and downstream tips, respectively. The small scattered markers were based on data averaged over 30 seconds, and the thicker markers connected by lines are the combined averages, representing averaging over  $\sim 3$  minutes and 30 seconds. Number of detected bubbles varied from over 900 at the peak and decaying towards zero far from the plate. The orange line indicates the location beyond which optical probe data was not recorded to avoid risking the probe tips touch the model surface.



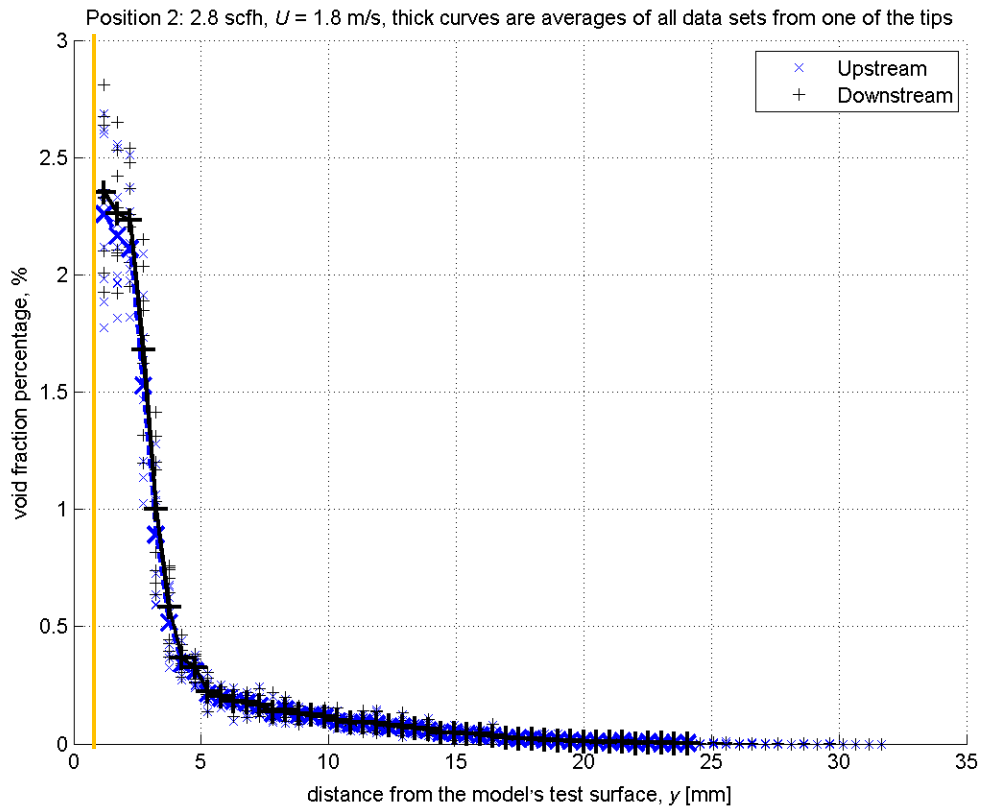


Figure 6.17 – Void fraction distributions from optical probe at position #2. Flow speed was 1.8 m/s and ventilation rate  $2.2 \times 10^{-5}$  m<sup>3</sup>/s. The blue and black points are based on data provided by the upstream and downstream tips, respectively. The small scattered markers were based on data averaged over 30 seconds, and the thicker markers connected by lines are the combined averages, representing averaging over  $\sim 3$  minutes and 30 seconds. The orange line indicates the location beyond which optical probe data was not recorded to avoid risking the probe tips touch the model surface.

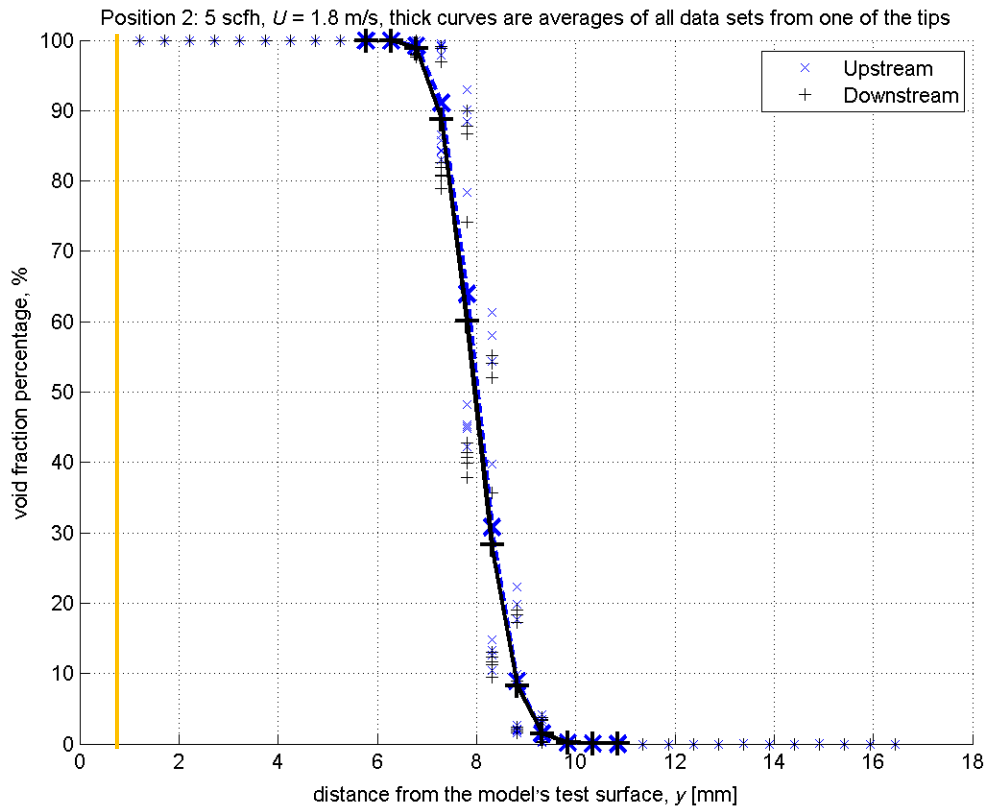


Figure 6.18 – Void fraction distributions from optical probe at position #2. Flow speed was 1.8 m/s and ventilation rate  $3.93 \times 10^{-5}$  m<sup>3</sup>/s. The blue and black points are based on data provided by the upstream and downstream tips, respectively. The small scattered markers were based on data averaged over 30 seconds, and the thicker markers connected by lines are the combined averages, representing averaging over ~3 minutes and 30 seconds. The orange line indicates the location beyond which optical probe data was not recorded to avoid risking the probe tips touch the model surface.

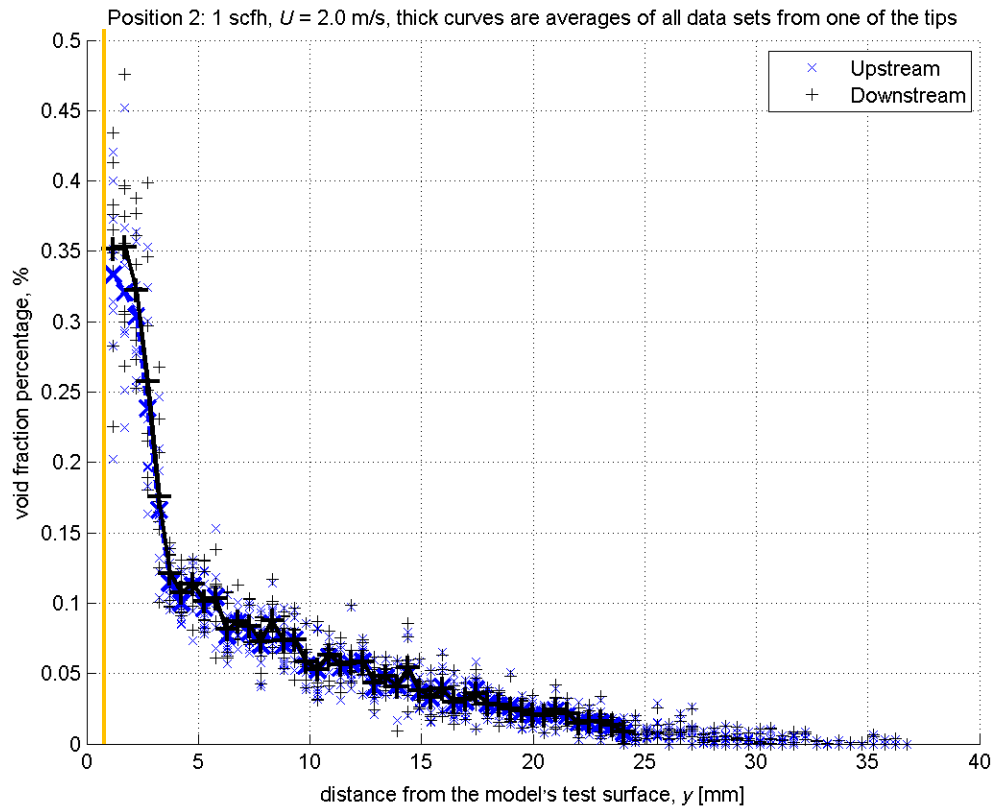


Figure 6.19 – Void fraction distributions from optical probe at position #2. Flow speed was 2.0 m/s and ventilation rate  $7.87 \times 10^{-6}$  m<sup>3</sup>/s. The blue and black points are based on data provided by the upstream and downstream tips, respectively. The small scattered markers were based on data averaged over 30 seconds, and the thicker markers connected by lines are the combined averages, representing averaging over ~3 minutes and 30 seconds. The orange line indicates the location beyond which optical probe data was not recorded to avoid risking the probe tips touch the model surface.

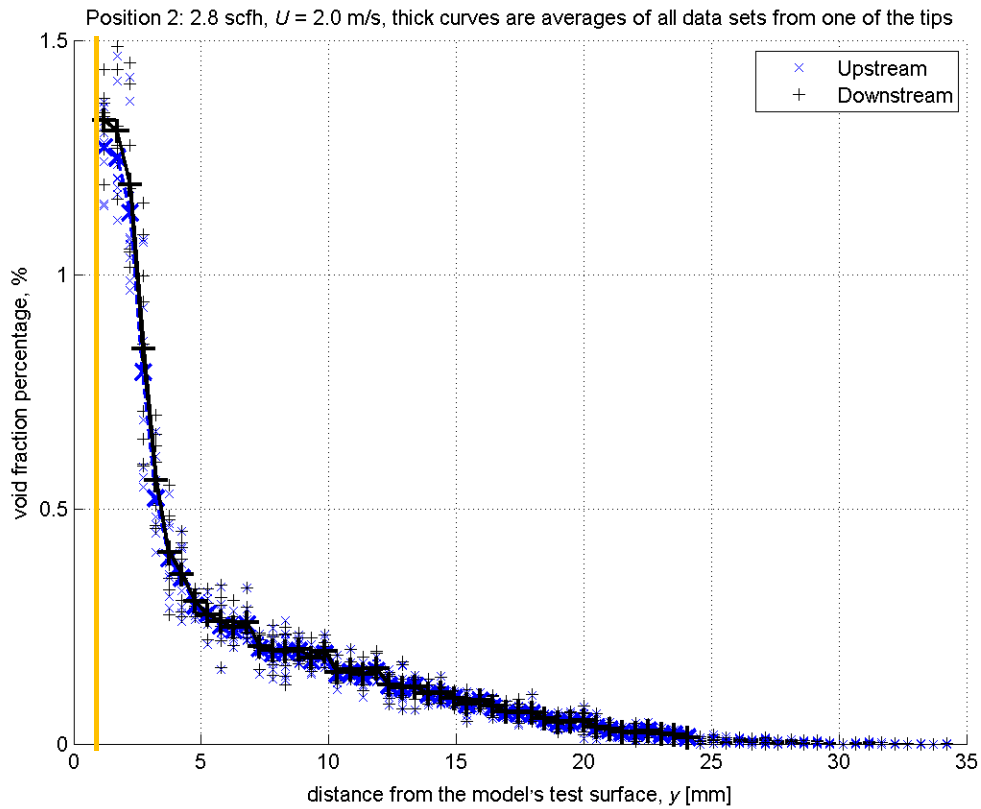


Figure 6.20 – Void fraction distributions from optical probe at position #2. Flow speed was 2.0 m/s and ventilation rate  $2.2 \times 10^{-5}$  m<sup>3</sup>/s. The blue and black points are based on data provided by the upstream and downstream tips, respectively. The small scattered markers were based on data averaged over 30 seconds, and the thicker markers connected by lines are the combined averages, representing averaging over ~3 minutes and 30 seconds. The orange line indicates the location beyond which optical probe data was not recorded to avoid risking the probe tips touch the model surface.

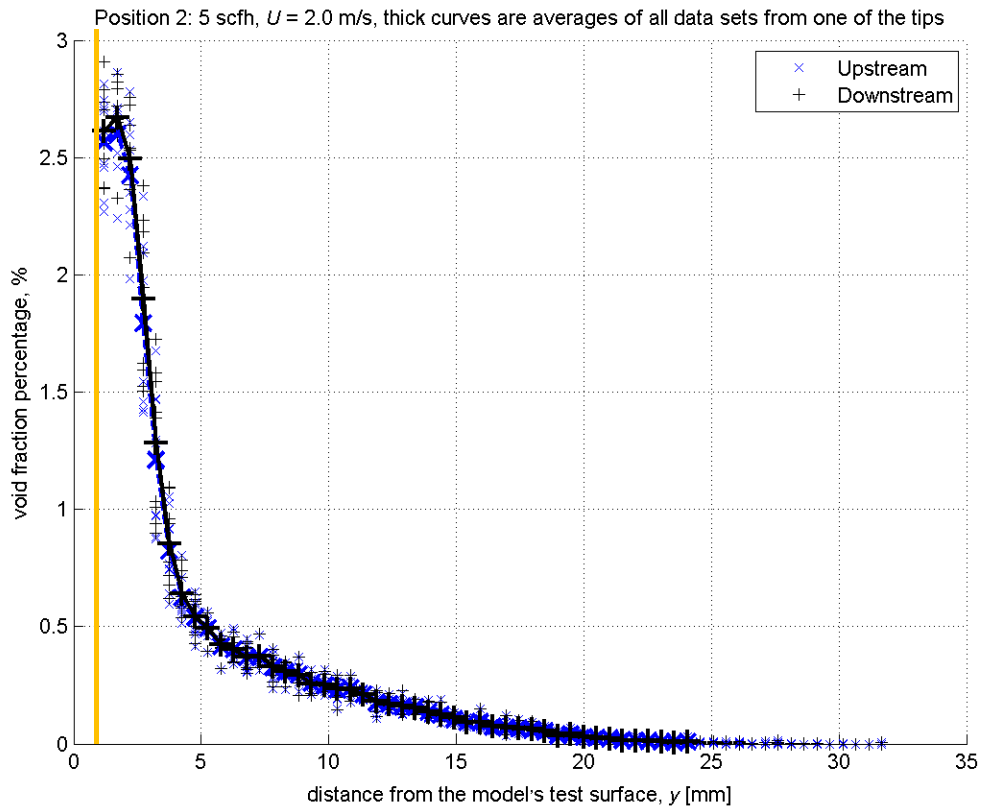


Figure 6.21 – Void fraction distributions from optical probe at position #2. Flow speed was 2.0 m/s and ventilation rate  $3.93 \times 10^{-5} \text{ m}^3/\text{s}$ . The blue and black points are based on data provided by the upstream and downstream tips, respectively. The small scattered markers were based on data averaged over 30 seconds, and the thicker markers connected by lines are the combined averages, representing averaging over  $\sim 3$  minutes and 30 seconds. The orange line indicates the location beyond which optical probe data was not recorded to avoid risking the probe tips touch the model surface.

#### 6.4 High speed video

High speed video was recorded at multiple flow conditions using a Vision Research Phantom v710 camera. However, only at the lower air fluxes were the individual bubbles distinguishable (i.e. minimal overlap when viewed from below). Figure 6.22 shows the setup used, 6.23 shows a still photo of the bottom view and 6.24 a still of the side view. All results presented in this section are for flow of 1.8 m/s and ventilation rate  $7.87 \times 10^{-6} \text{ m}^3/\text{s}$ .

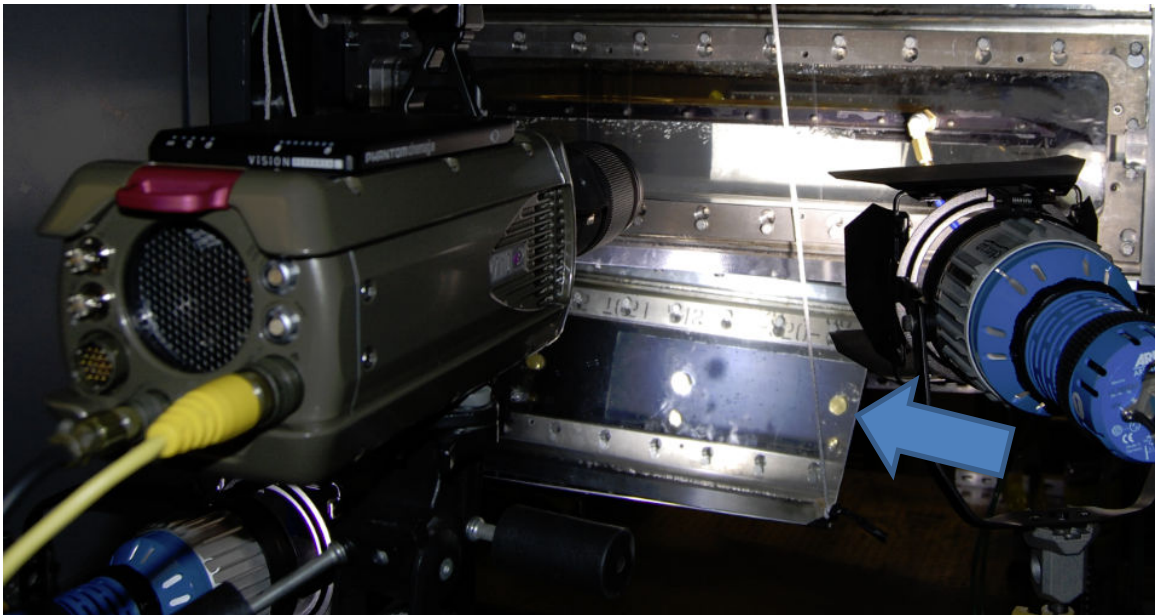


Figure 6.22 – The high speed camera setup, where side view was measured. The mirror seen in the figure, as indicated by the arrow, was used to record the bottom view as well as to reflect light sometimes when a second high power Arri-studio light was used.



Figure 6.23 – Still photograph from a 1000 fps movie showing the bubbles near probe position #2 as viewed from below. The dashed lines are spaced on average 2.54 cm apart.

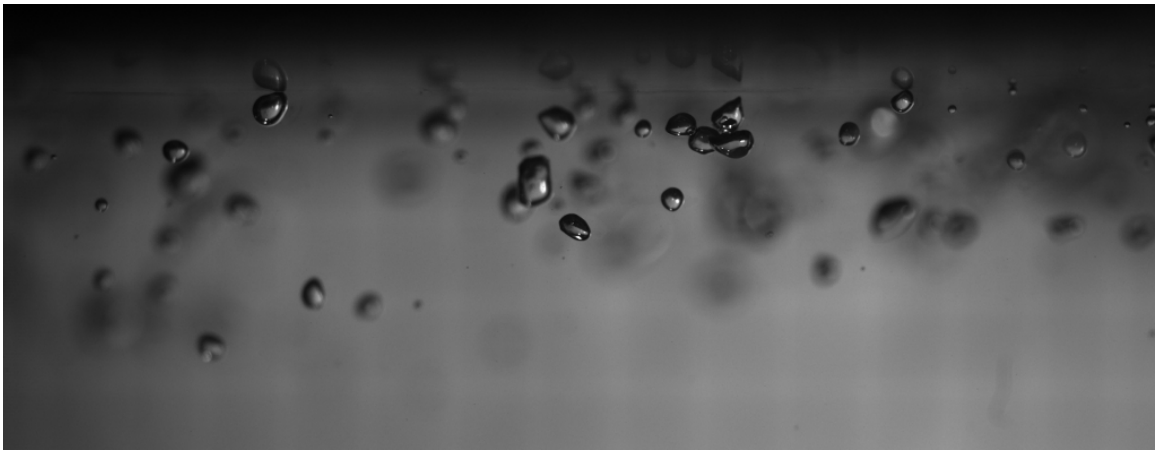


Figure 6.24 – Image showing the bubbles as viewed from the side in the vicinity of probe position #2.

The video was processed in collaboration with Mr. Christopher Haddad, who manually viewed the frames and sized the bubbles, and with Dr. Bu-Geun Paik who also manually processed some of the frames, and who together with the author helped guide Mr. Haddad's work. For every bubble the dimensions specified in figure 6.25 were measured.

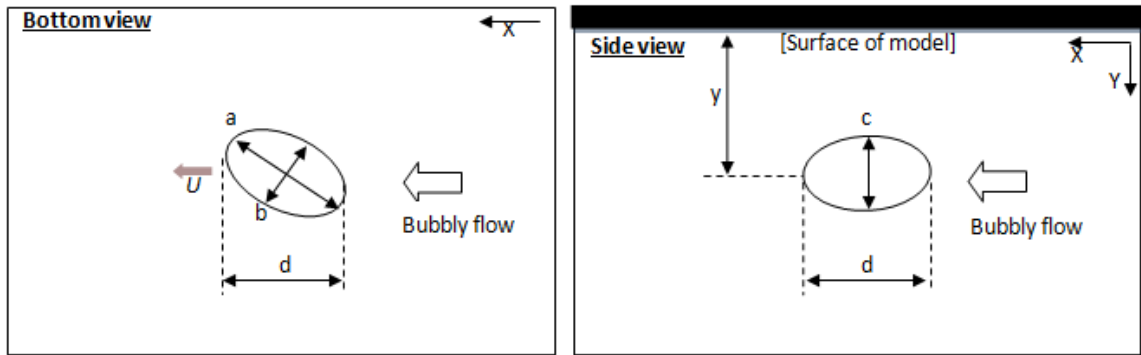


Figure 6.25 – Dimensions of the bubbles which were determined for the bottom and side views.

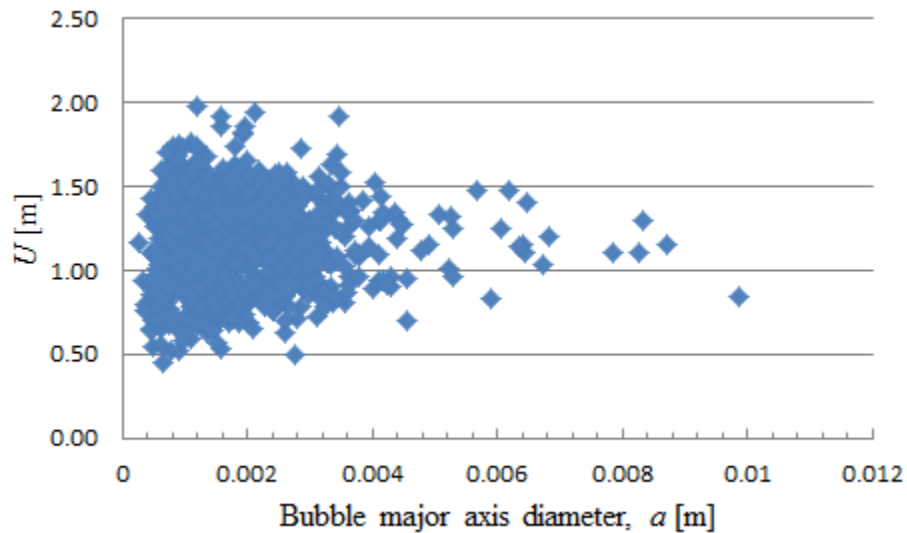


Figure 6.26 – Scatter plot of the bubble speed versus major axis diameter.



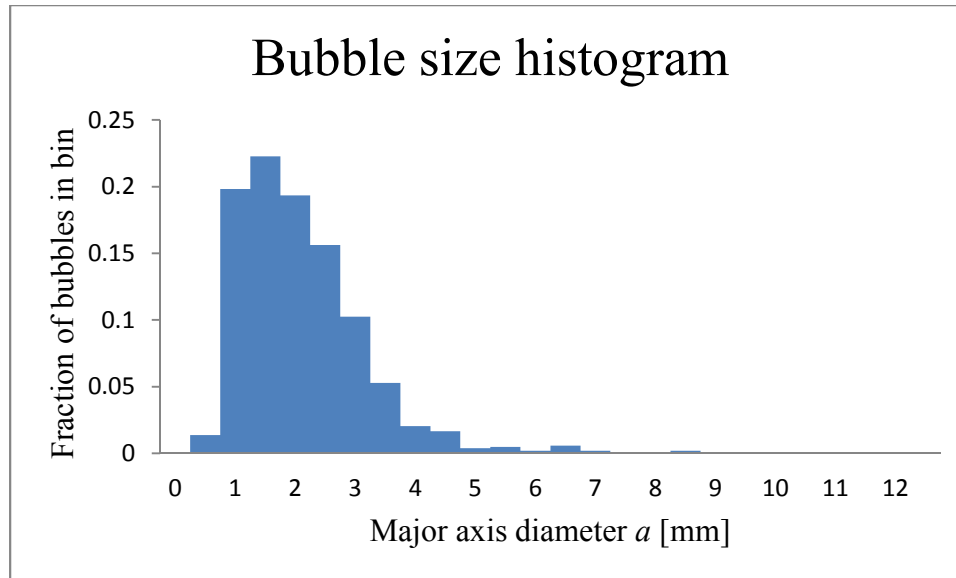


Figure 6.27 – Bubble size histogram.

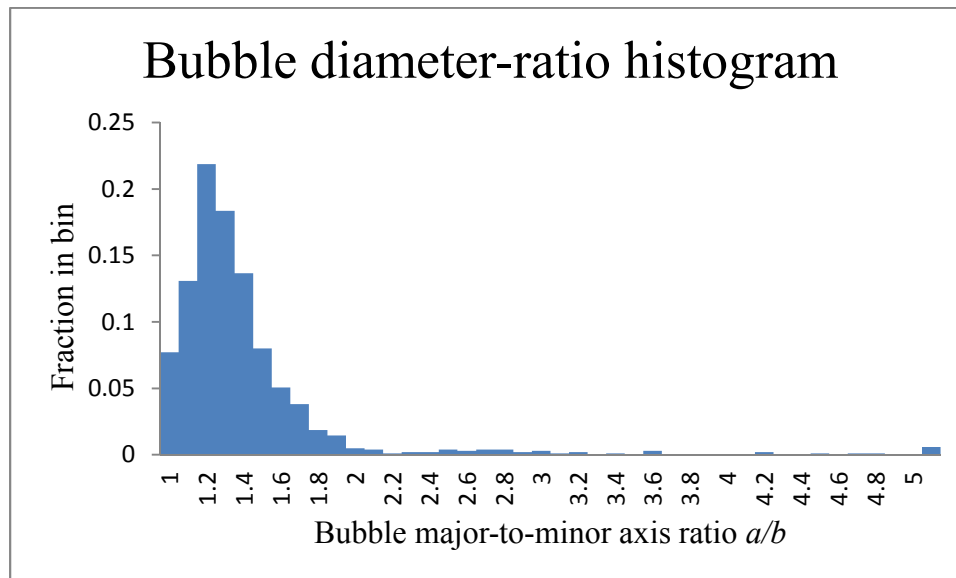


Figure 6.28 – Bubble axis diameter ratio histogram, showing that most bubbles were slightly elliptical.

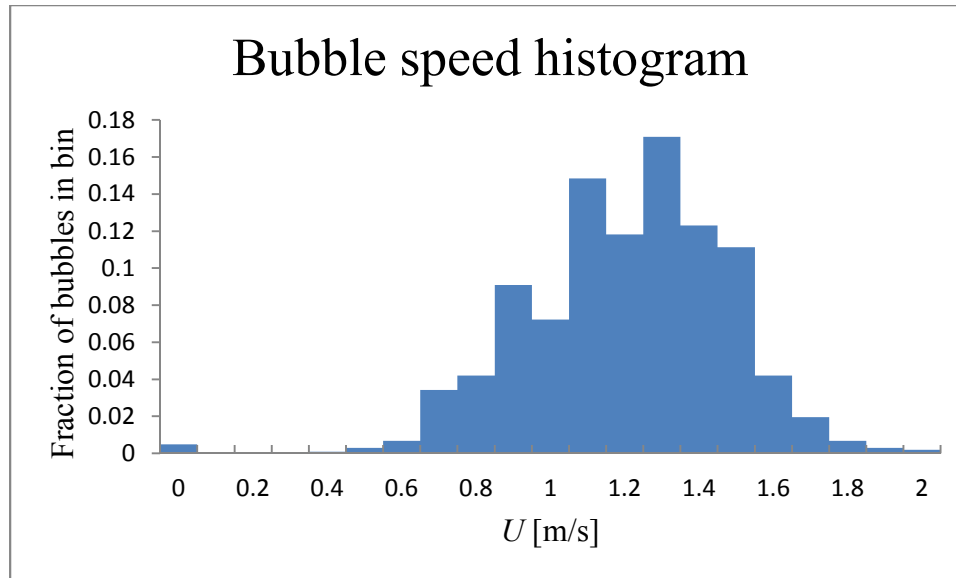


Figure 6.29 – Bubble speed histogram.

The weber number,  $\rho_w U^2 a / \sigma$ , based on the nominal free stream speed of 1.8 m/s would be  $O(100)$ , for a typical 2 mm diameter bubble.

## 6.5 X-ray measurements

An example of the raw images provided by the x-ray is given in figure 6.30, where we see a cavity behind a backward facing step. Some of the inner structure of the model is also visible.



Figure 6.30 – Image showing the instantaneous beam intensity distribution behind the backward facing step.

Typical x-ray exposure settings during a medical examination range from as low as 120 kV at 1.3 mAs (with 2.6 mm aluminum filter) to 79 kV at 354 mAs (with 2.5 mm aluminum filter) as reported by Muhogora *et al.* (1999). For these multiphase flow experiments the dose rate was not a concern and the exposure settings that were used went up to 125 kV and 500 mAs (with 6.4 mm steel and 19.1 mm aluminum filters).

However, 81 kV at 800 mA for 1000 ms, and 134 kV at 320 mA for 1100 ms were some of the most typical settings used.

Figure 6.31 shows a single frame from a void fraction movie. Here no distortion correction or glare correction was applied, and it is apparent that significant distortion can be seen in the shape of the plate surface, and below the cavity there is a strong glow. Also somewhat visible is random noise everywhere in the image. Figures 6.32 to 6.34 show distortion corrected average images of the same flow conditions.

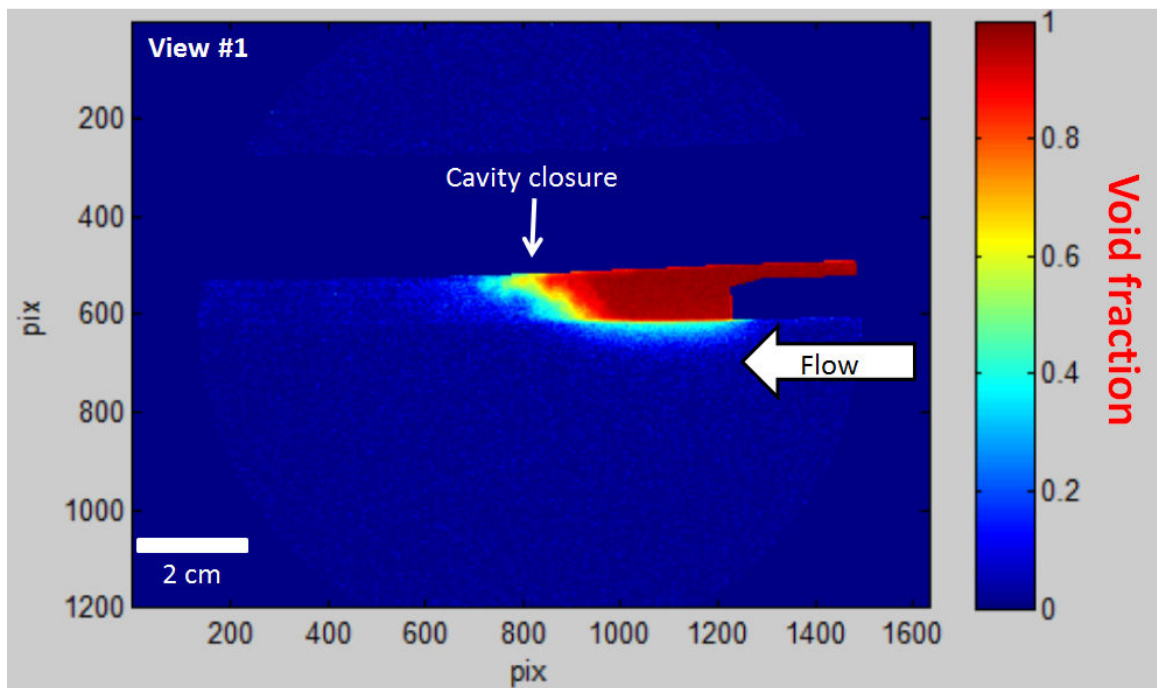


Figure 6.31 – False color image of the instantaneous void fraction calculated without any distortion or glare correction.

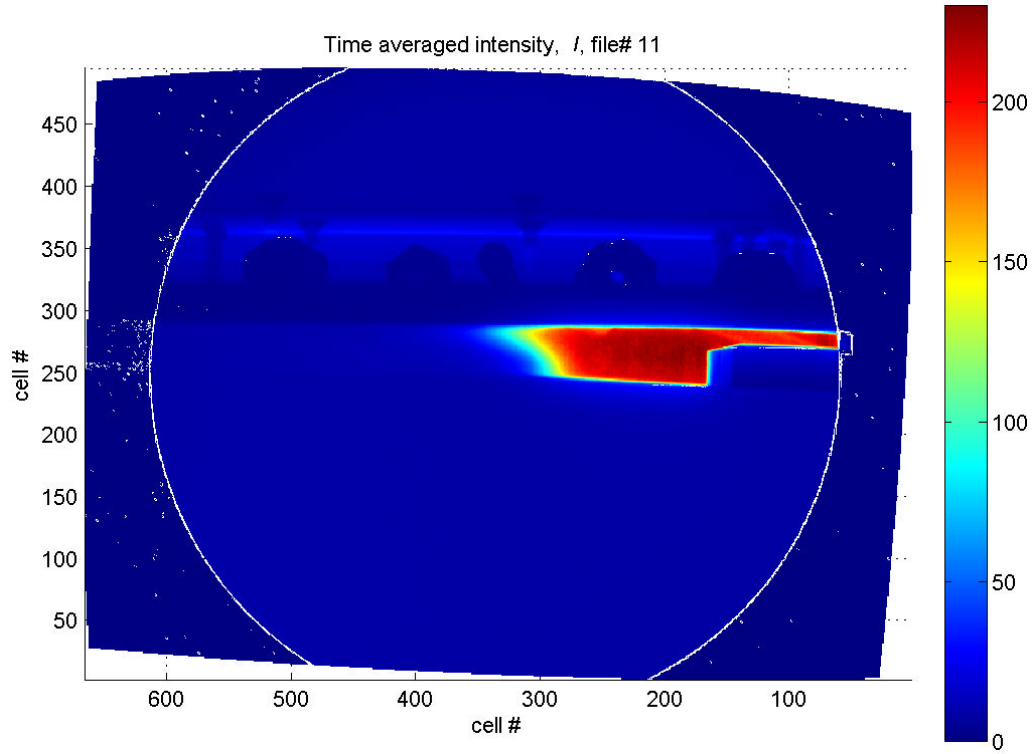


Figure 6.32 – Time averaged light intensity field.

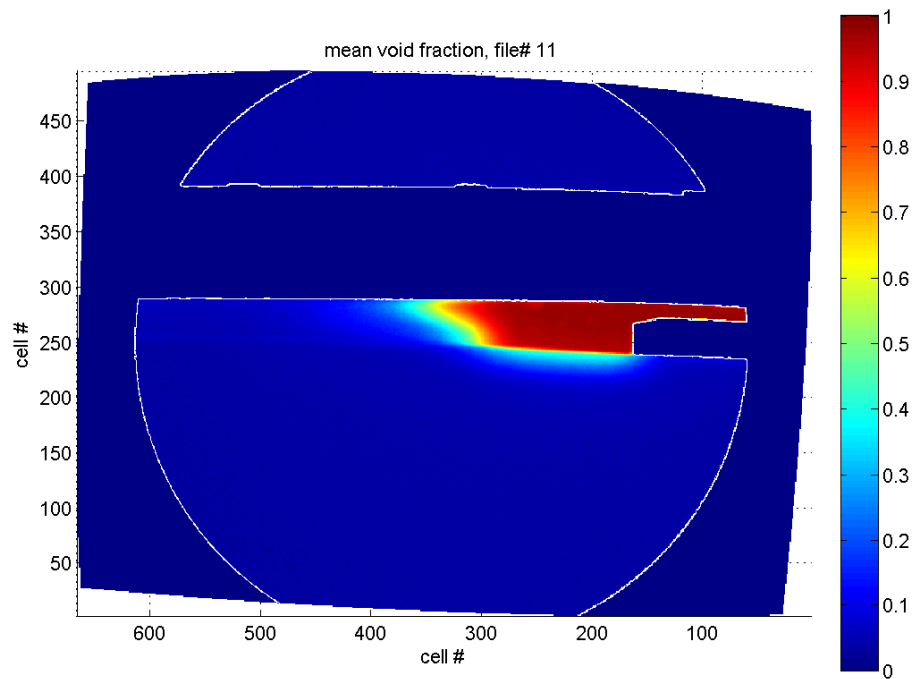


Figure 6.33 – Time averaged void fraction calculated from the data presented in image 6.32, and from the reference images taken with void fractions zero and one.

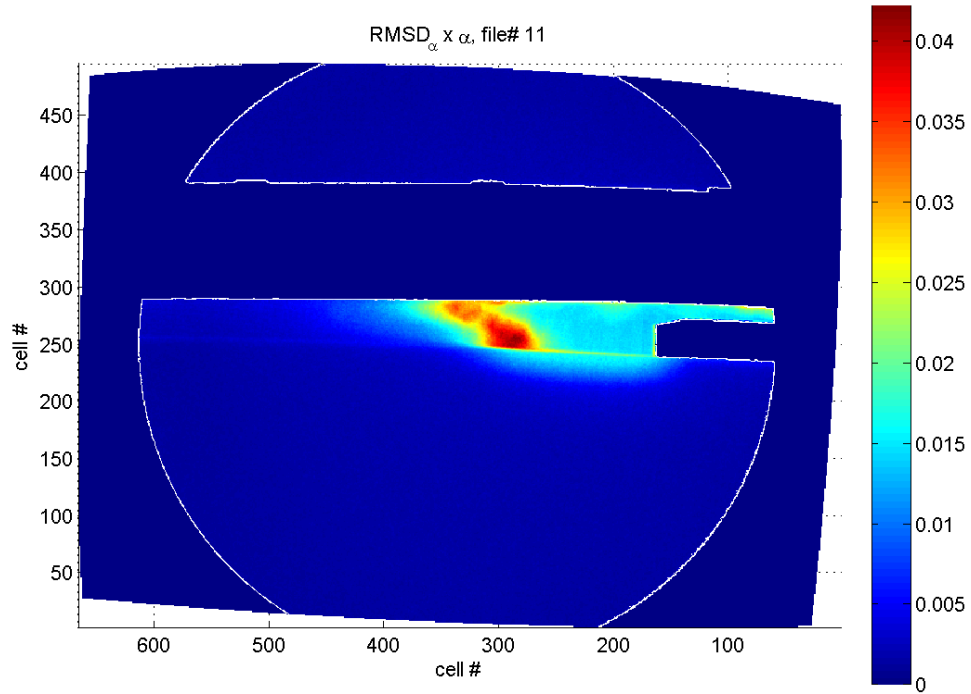


Figure 6.34 – The root mean square deviation of the void fraction weighted by the mean void fraction to highlight the area of large fluctuation with significant void fractions. This result is valuable as it clearly shows the size of the area where the cavity is oscillating, and enables a quantitative definition of the mean oscillations.

The previous figures showed the distortion corrected void fraction distribution before any correction for veiling glare was implemented. The glare and some noise are observed easily. To correct for the veiling glare, many different point spread functions could be used, as explained in Chapter 5. The author has not found any one PSF that works for all situations, as the exposure and camera settings also likely affect the correct PSF shape. Additionally, the coefficients of the PSF are empirically determined using imperfect data, hence the selection of the PSF used is subjective, unless one performs a systematic test using various void fraction phantoms of the proper thickness and void fraction range.

For the data presented in what follows, the point spread function was presumed to be sufficiently represented by

$$h(r) = p_1 \frac{\alpha/\pi}{r^2 + \alpha^2} + p_2 \frac{1}{\sigma\sqrt{2\pi}} e^{-\frac{1}{2}\left(\frac{r}{\sigma}\right)^2} \quad (6.2)$$

which is the second PSF discussed in Chapter 5. The coefficients were found by taking an image of a sharp lead edge placed on the II screen, plotting the ESF and the LSF normal to the edge and then curve fitting. The optimized curve fit was found using a built-in Matlab function `fminsearch`, which is a derivative free minimization function. The quantity to minimize was weighted and defined as

$$E = \sum_{n=0}^N x_n^M (ESF_{measured,n} - ESF_{fit,n})^2 \quad (6.3)$$

where  $x$  is the distance from the edge and the exponent  $M$  is 0, 1, or 2 depending on the weighting desired. Also, if any of the coefficients exceeded limits set by the physical meaning of the terms in eqn. 6.2, the error was artificially amplified by a factor of  $10^2$  to  $10^5$ , which helped bound the solution. We found coefficients  $p_1 = 0.3557$ ,  $p_2 = 1 - p_1$ ,  $\alpha = 3.084$  pixels and  $\sigma = 1.3023$  pixels produced a satisfactory fit. Now the PSF of eqn. 6.2 was used in the deconvolution performed using Matlab's built-in function, `deconvlucy`, which is based on the Lucy-Richardson method.

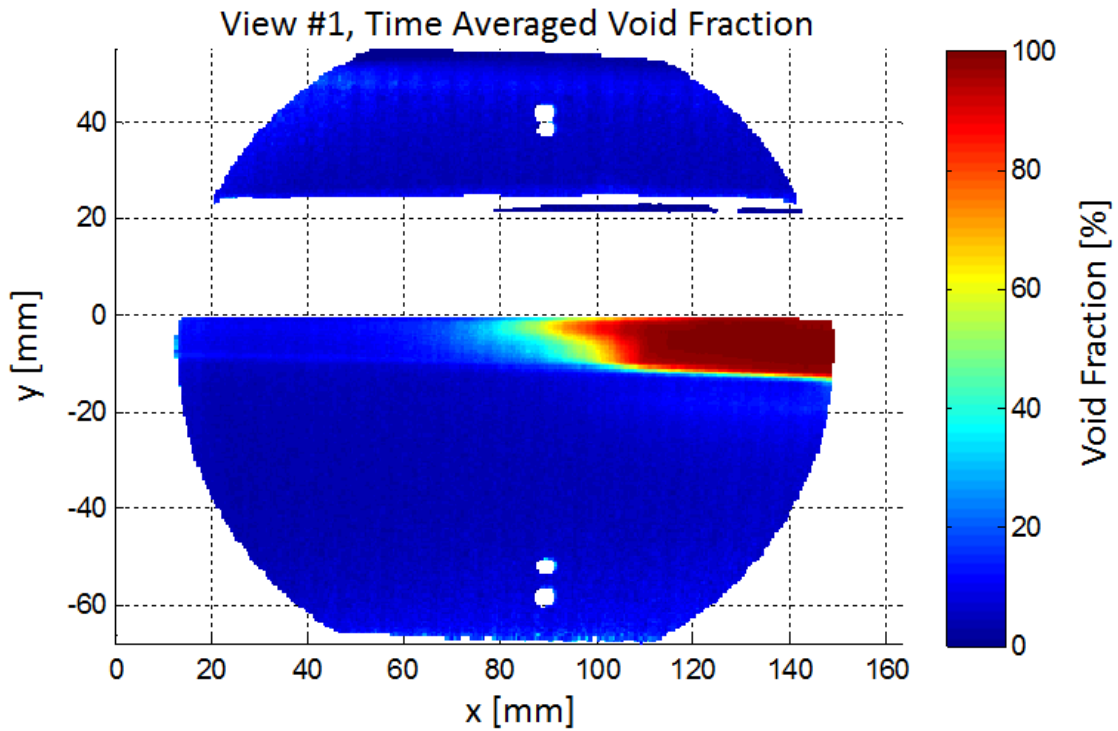


Figure 6.35 – Void fraction distribution corrected for some of the veiling glare and geometric distortion

Before proceeding with a comparison of the results, figure 6.36 shows an uncorrected void fraction distribution obtained at view #2, where even some individual bubbles can be observed clearly.



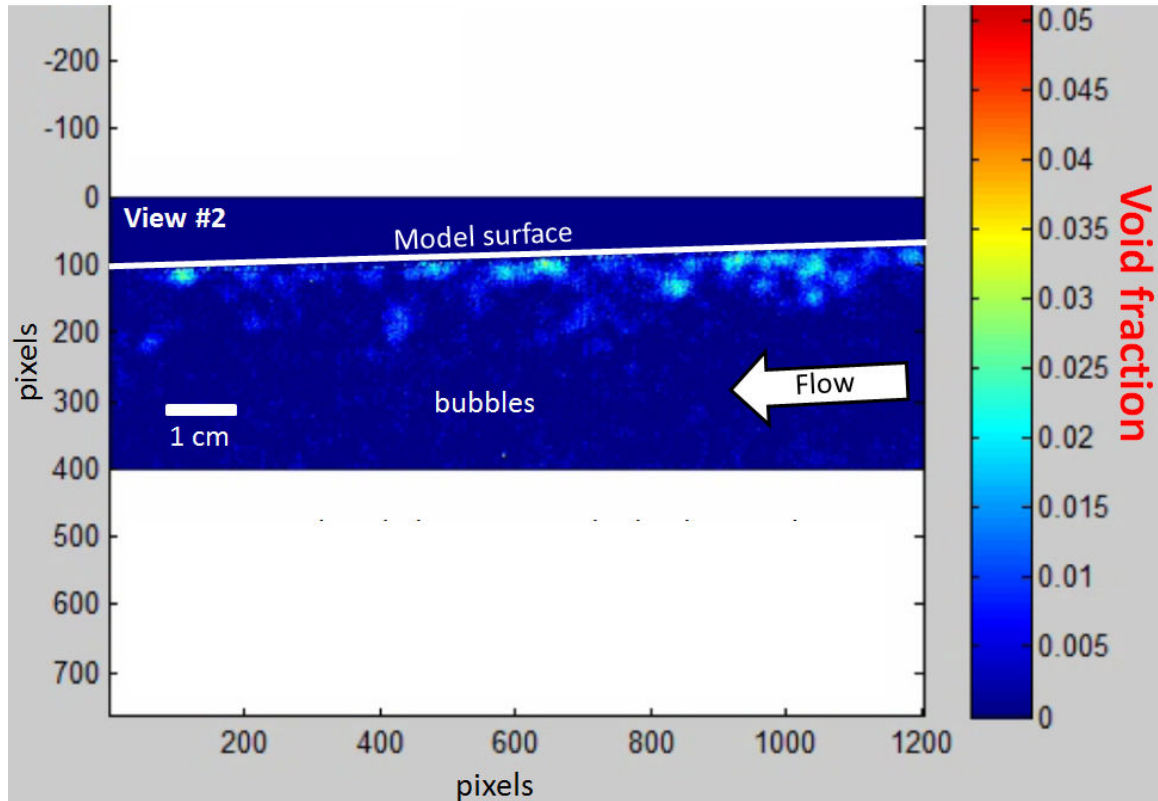


Figure 6.36 – One frame of a movie where each frame represented a mere 1 ms.  $Q_{inj} = 2.2 \times 10^{-5} \text{ m}^3/\text{s}$ ,  $U = 1.8 \text{ m/s}$ . Some random light spots on the background are noise 10 pixels wide. A 2D median filter was applied to reduce noise in the animation. The void fraction through a single 5 mm bubble should be 2.4%. We can see that the size of the bubbles visible and the void fraction through the center are as expected.

## 6.6 Comparison of the results

The injected air flux was measured using an Omega FL-2000 series of rotameter, which depending on the model had 2 to 5 % full scale accuracy. Of the five rotameters, the two with the lowest flow ranges were used in the experiments discussed in this thesis. For flow rates to  $7.97 \times 10^{-6} \text{ m}^3/\text{s}$  the flow meter used was the Omega Engineering FL-2001 with manufactures specified accuracy of  $\pm 0.39 \times 10^{-6} \text{ m}^3/\text{s}$ . For flow rates above  $7.97 \times 10^{-6}$  to  $3.93 \times 10^{-5} \text{ m}^3/\text{s}$  the flow meter used was Omega Engineering FL-2003 with manufactures specified accuracy of  $\pm 0.20 \times 10^{-5} \text{ m}^3/\text{s}$ .

The air fluxes obtained at optical probe's position 2, and x-ray view 2 are compared in table 6.1. (Note that the upstream position, position 1, was inside the recirculation region of the probe and hence a similar comparison was not attempted from that position.)

Table 6.1 – Volume flow rates of air based on the flow meter, optical probe, video and x-ray measurements. For the x-ray measurements the void fraction was integrated from  $y = 0$  to 25 mm. Additional measurement and data processing is needed for x-ray at view #2 for  $U = 2.0$  m/s, hence those data are not available in present table.

Flow speed [m/s]	Injection rate $Q_{inj}$ [m <sup>3</sup> /s]	Optical probes $Q_{OP}/Q_{inj}$	Video $Q_{video}/Q_{inj}$	X-ray [0 to 25mm] $Q_{x-ray}/Q_{inj}$
1.8	$7.87 \times 10^{-6}$	1.114	1.052	2.768 w/ $U_{piv}$
1.8	$2.20 \times 10^{-5}$	1.030	N/A	1.327 w/ $U_{piv}$ 1.267 w/ $U_{op}$
1.8	$3.93 \times 10^{-5}$	air layer	N/A	air layer
2.0	$7.87 \times 10^{-6}$	0.937	N/A	N/A
2.0	$2.20 \times 10^{-5}$	0.906	N/A	N/A
2.0	$3.93 \times 10^{-5}$	0.919	N/A	N/A

Using the optical probe data the volume flow rates were calculated from

$$Q_{OP} = \sum_{n=1}^N \Delta y U(y_n) \alpha(y_n) W \quad (6.4)$$

and similarly for the void fraction based on x-ray densitometry. Here  $W$  is the span of the model, 209.55 mm. While the scalar field of the void fraction obtained by x-ray may contain the velocity information, in the current research no thorough attempt was made to recover it. Hence, the velocity profile's based on single phase PIV at the same location and velocity distributions based on the dual fiber optical probe were used in calculation of the results shown in table 6.1. Note that the volume flow rate was overestimated in both reported cases. The reason for this overestimate can be readily understood by

looking at the void fraction distributions shown in figures 6.37 and 6.38. In figure 6.37 and 6.38 we can see that the value of void fraction is overestimated at values below 0.4%. Besides the possible effect of short averaging times and veiling glare of the x-ray images, at these low void fractions the calculated value is extremely sensitive to the smallest error in any of the light energies recorded passing through air,  $E_a$ , water,  $E_w$  and mixture,  $E_m$  as can be understood based on analysis presented in Chapter 5. For the x-ray measurements, the larger uncertainty at the lowest void fractions can be exemplified by considering the form of eqn. 5.21. From this, it follows that in a flow with void fractions from 0 to 100%, if  $I_a = 250$  and  $I_w = 5$ , at 90% actual void fraction 1 GSV difference causes a 0.5% change in the calculated void fraction, while at 10% actual void fraction 1 GSV difference causes a 3.7 % change.

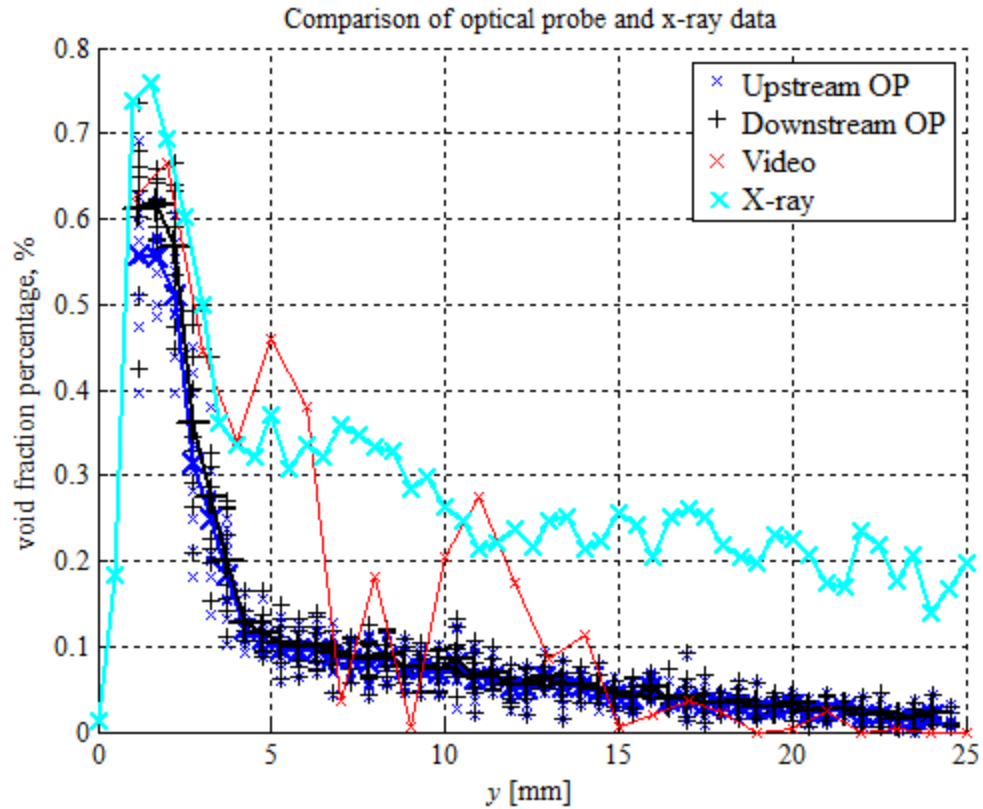


Figure 6.37 – Comparison at flow speed of 1.8 m/s and ventilation rate of  $7.87 \times 10^{-6} \text{ m}^3/\text{s}$ . Void fraction distribution approximately 267 mm downstream of the step. The blue and black optical probe data points are averaged over 30 seconds. Thick lines are averages over 3min 30sec. Cyan crosses are uncorrected x-ray void fraction results averaged over ~1 second. Red crosses are points based on video.

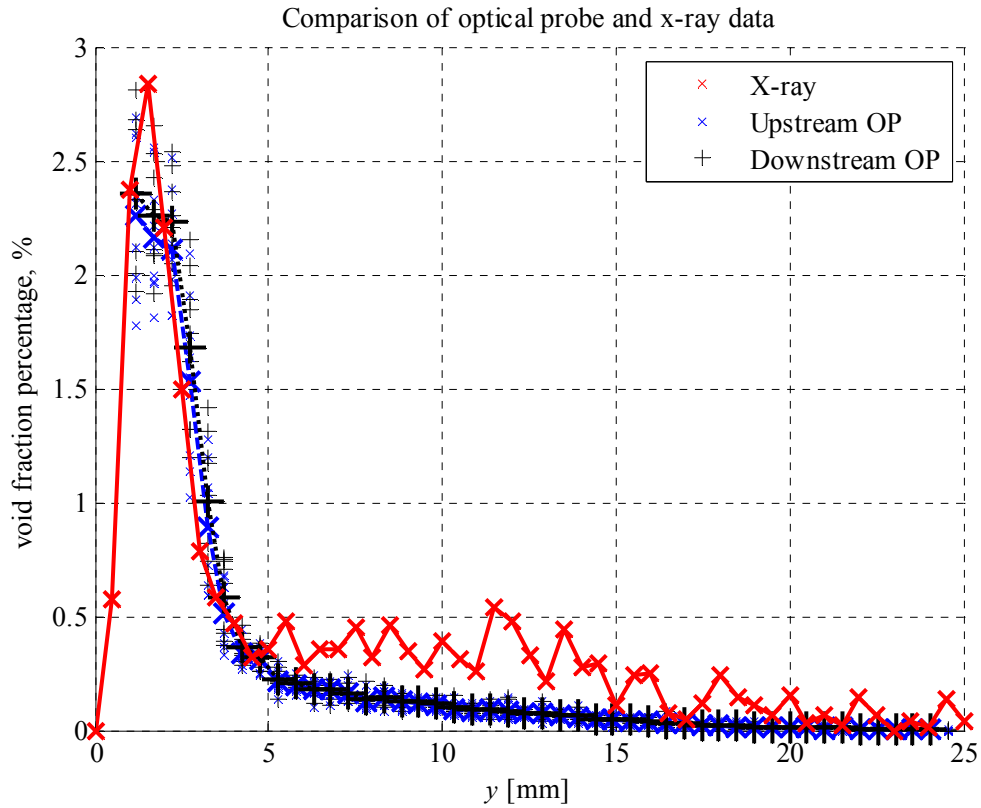


Figure 6.38 – Comparison at flow speed of 1.8 m/s and ventilation rate of  $2.2 \times 10^{-5} \text{ m}^3/\text{s}$ . Void fraction distribution approximately 267 mm downstream of the step. The blue and black optical probe data points are averaged over 30 seconds. Thick lines are averages over 3min 30sec. Red crosses are veiling glare corrected x-ray void fraction results averaged over  $\sim 1$  second.

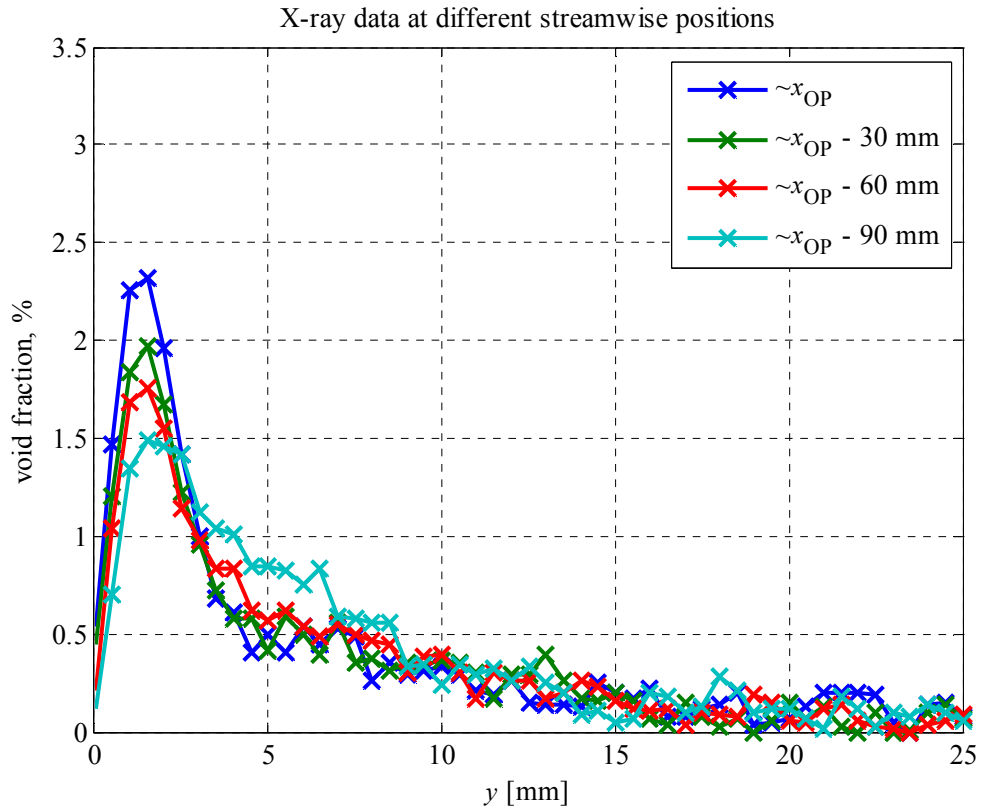


Figure 6.39 – At flow speed of 1.8 m/s and ventilation rate of  $2.2 \times 10^{-5} \text{ m}^3/\text{s}$ . Void fraction distributions at multiple streamwise locations showing the streamwise evolution of the void fraction distribution. Where  $x_{OP}$  was approximately 267 mm downstream of the step. X-ray averaged over  $\sim 1$  second. (From x-ray recording #53)

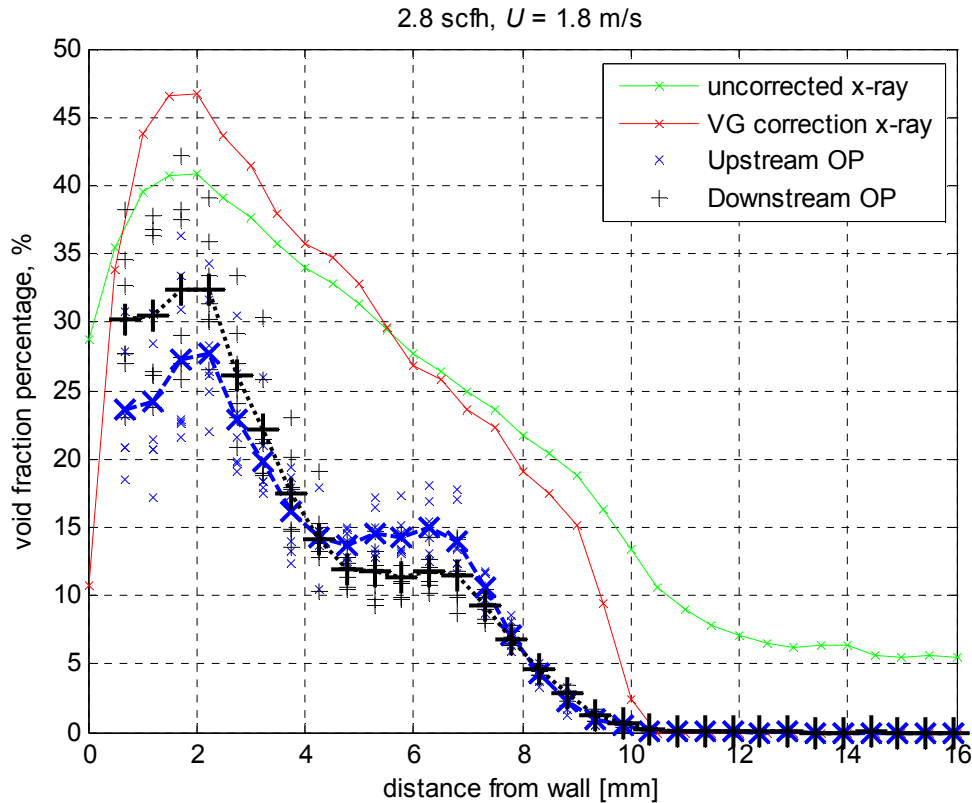


Figure 6.40 – Comparison at flow speed of 1.8 m/s and ventilation rate of  $2.2 \times 10^{-5} \text{ m}^3/\text{s}$ . Void fraction distribution approximately 64 mm downstream of the step. The blue and black optical probe data points are averaged over 30 seconds. Thick lines are averages over 3min 30sec. Green and red crosses are veiling glare uncorrected and corrected x-ray void fraction results, respectively. X-ray averaged over  $\sim 1$  second. Distance specified is  $y$  as measured from the test surface.

In Figures 6.40-42 we also see some disagreement between the void fractions measured using the x-ray and optical probes. This data is obtained in the recirculation region downstream of the step, so the presence of the probe may have also perturbed the flow, but additionally the imperfect correction for veiling glare, different averaging times, positional uncertainty and non-parallel beam paths all play a part in why the data differ.

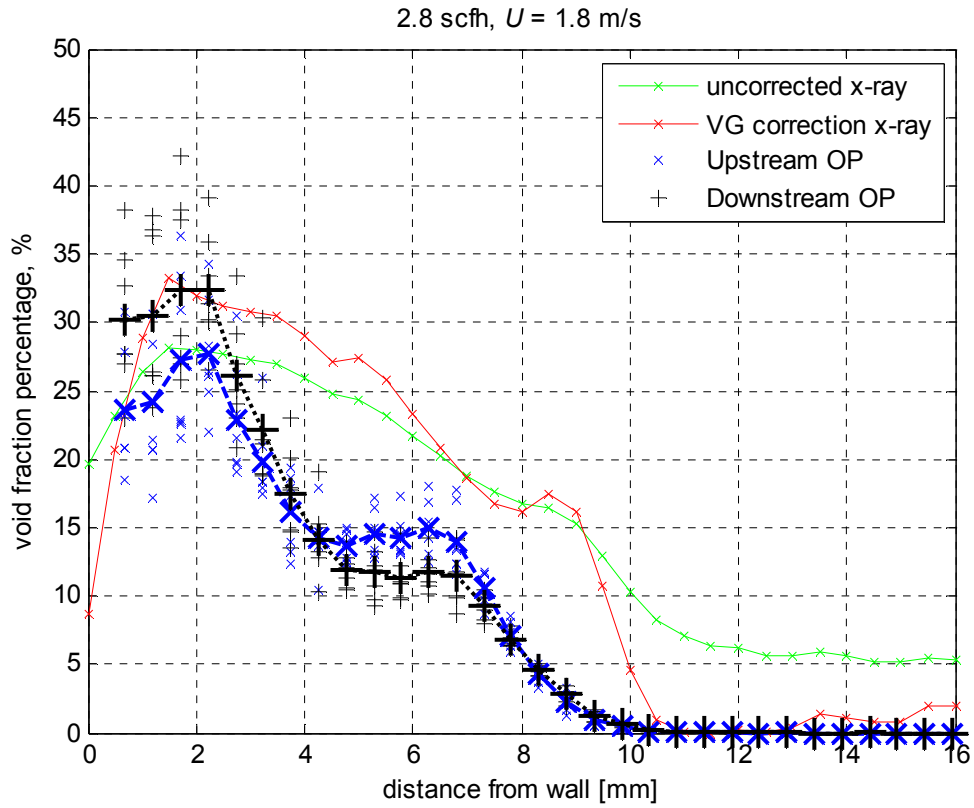


Figure 6.41 – Comparison of cavity at step, for  $U = 1.8$  m/s and  $Q_{inj} = 2.2 \times 10^{-5}$  m<sup>3</sup>/s. Void 6 mm downstream of presumed probe location. Distance specified is  $y$  as measured from the test surface.



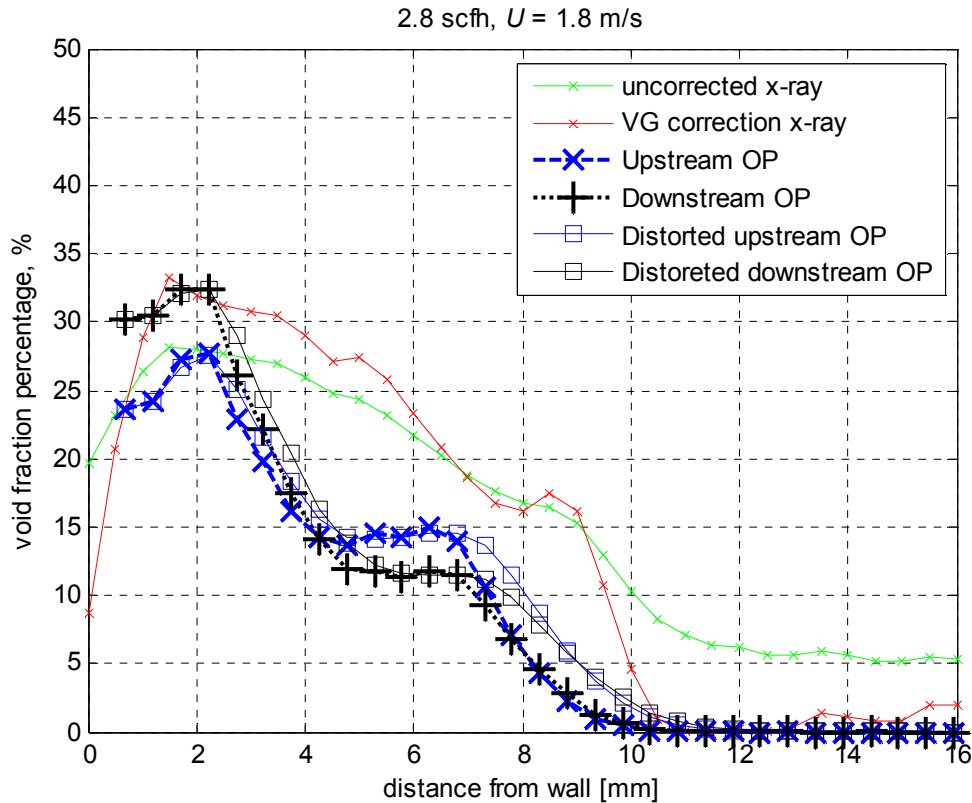


Figure 6.42 – Comparison of cavity at step, for  $U = 1.8 \text{ m/s}$  and  $Q_{inj} = 2.2 \times 10^{-5} \text{ m}^3/\text{s}$ . Void 6 mm downstream of presumed probe location. Distance specified is  $y$  as measured from the test surface. Same as figure 6.41, except the squares show an approximation of the void fraction which would be measured by the x-ray due to the distortion caused by non-parallel beam paths, if the center beam was to be located at  $y = 0 \text{ mm}$  and at the streamwise location,  $x$ , of the optical probe.

If the optical probe data is used to simulate a void fraction distribution distorted due to non-parallel beam paths, the results are as shown by the squares in figure 6.42. It is evident that the agreement is improved. However, the results still differ, as would be expected due to imperfect veiling glare correction, limited averaging times, repeatability of the flow conditions, x-ray scatter, perturbation of the recirculating flow due to the presence of the optical probe, positional uncertainty of the probe and x-ray beam paths, and finite void fraction measurement accuracies of both techniques.

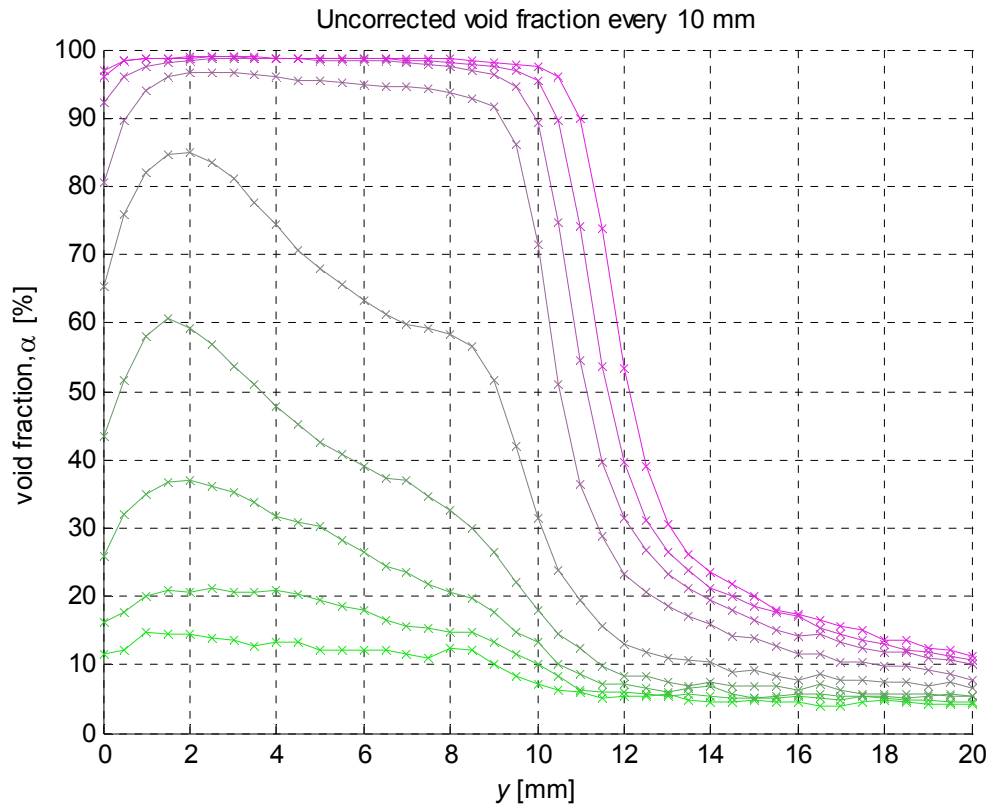


Figure 6.43 – Void fraction profiles downstream of the step for  $U = 1.8 \text{ m/s}$  and  $Q_{inj} = 2.2 \times 10^{-5} \text{ m}^3/\text{s}$ . No veiling glare correction has been employed. Streamwise evolution of void fraction is observed easily, as the peak void fraction monotonically decreases with distance from the step. First profile is taken approximately 10 mm from the step. Each curve represents the profile 10 mm apart.

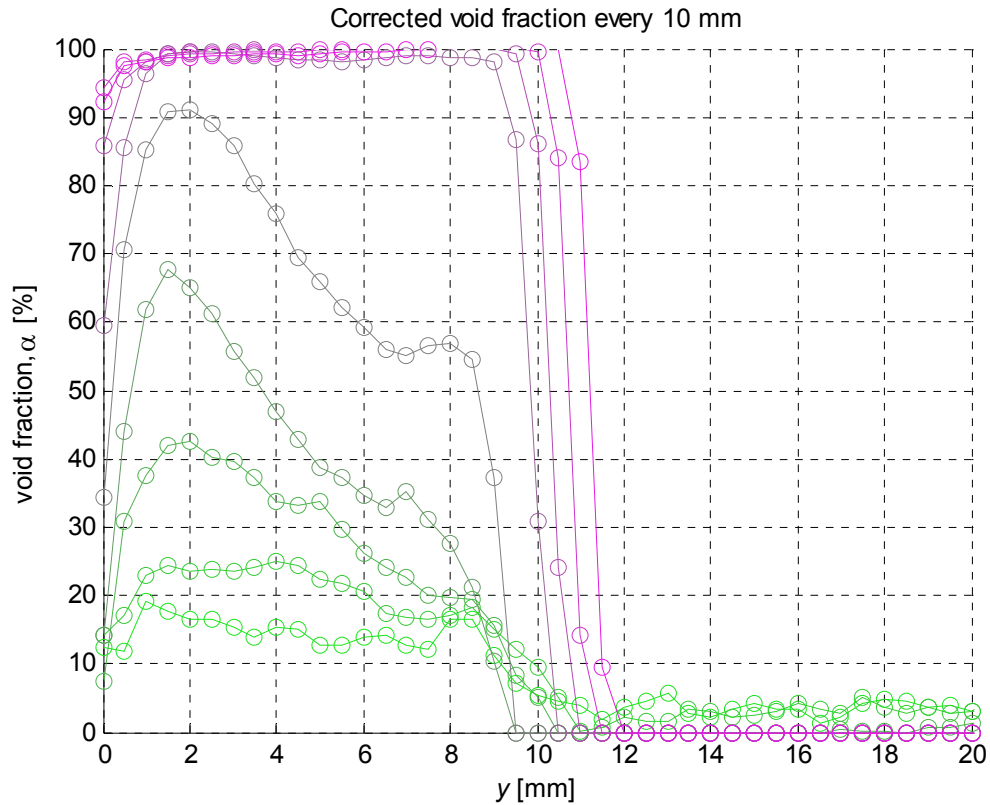


Figure 6.44 – Void fraction profiles downstream of the step for  $U = 1.8$  m/s and  $Q_{inj} =$  of  $2.2 \times 10^{-5}$  m<sup>3</sup>/s, with veiling glare correction employed. Streamwise evolution of void fraction is observed easily, as the peak void fraction monotonically decreases with distance from the step. First profile is taken approximately 10 mm from the step. Each curve represents the profile 10 mm apart. The veiling glare correction could cause the calculated void fraction to “undershoot” returning negative values, which given the physical constraints were converted into zero.

Looking at figures 6.43 and 6.44 it can be seen that the veiling glare (VG) correction sharpened the profiles. Figure 6.45 shows in more detail the effect of the veiling glare correction on the measured void fraction distribution. A more advanced VG correction scheme such as suggested by Janetta (2005) might offer improved results. Also, correction for non-parallel beam paths might improve the accuracy of the distributions if noise is minimized, or if the algorithm can address the noise issue better than the one presented in Chapter 5. While the x-ray and optical probe data agree fairly well, they can deviate due to different averaging times, non-parallel beam paths, imperfect veiling glare correction, x-ray scatter, influence of the intrusive probe on the flow, and positional uncertainty.

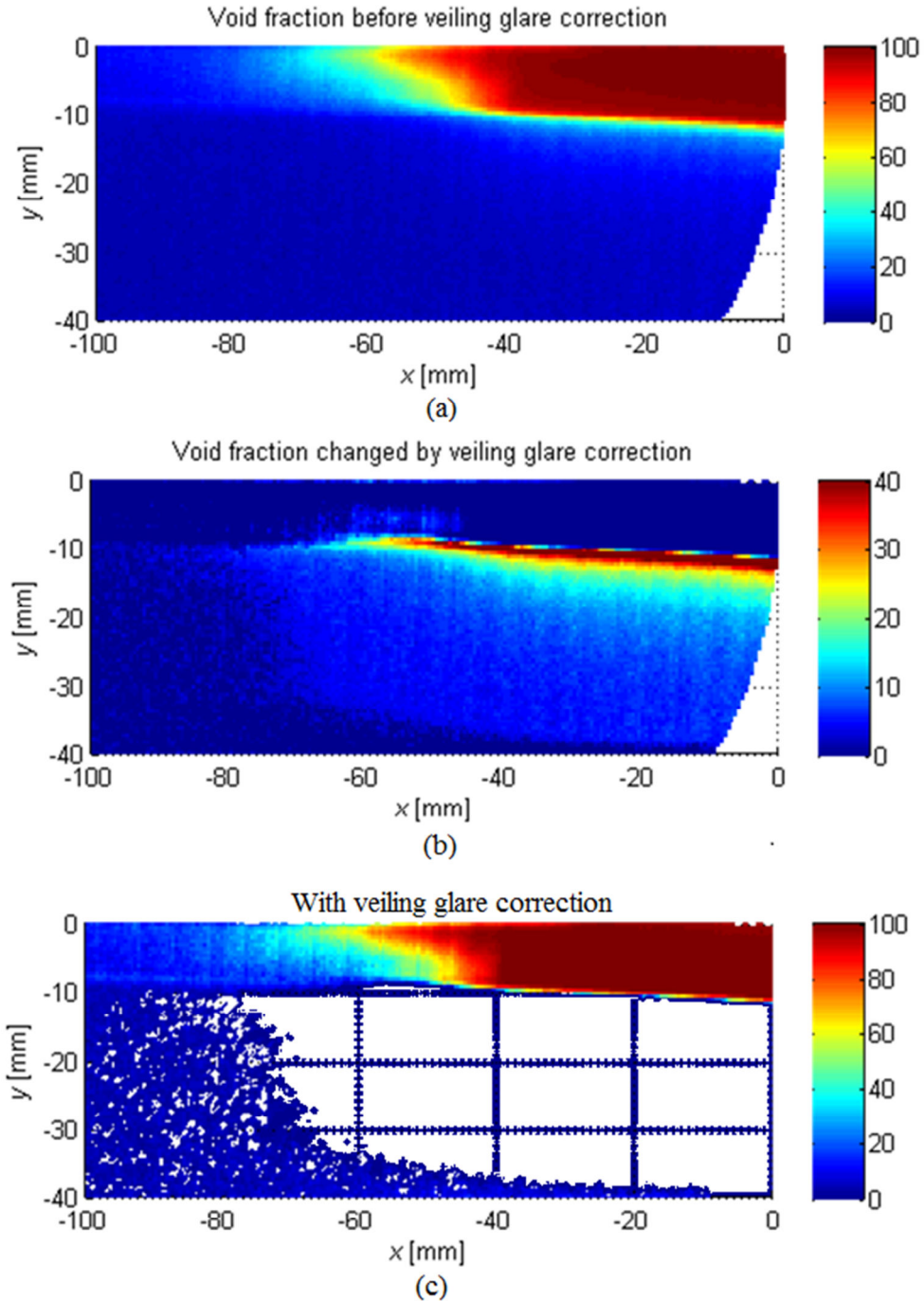


Figure 6.45 – Cavity at step, for  $U = 1.8$  m/s and  $Q_{inj}$  = of  $2.2 \times 10^{-5}$  m<sup>3</sup>/s. a) Void fraction calculated based on uncorrected images. b) Void fraction change due to the correction.

Note that the color bar now spans only 0 to 40%. c) Void fraction distribution after deconvolution using veiling glare PSF from eqn. 6.2. Note: due to a plotting error in the software, what should be a solid blue region was left empty. (Inspection of the void fraction distribution showed the void fraction to be zero in this region.)

## 6.7 Discussion

A cinemagraphic x-ray densitometry system was developed for high Reynolds number multiphase flows. The system is capable of measurements not offered by other techniques without perturbing the flow. Its utility was demonstrated on a ventilated cavity at a backward facing step, and the author compared results to optical probe and high speed video void fraction measurements.

In unidirectional flow, where the optical probe will perturb the flow it is measuring less, and at void fractions above 0.5%, where appreciable attenuation was achieved, the void fraction profiles measured using the x-ray system showed good agreement with those obtained with the optical probes (figure 6.38).

The x-ray also acquired the data quite rapidly in comparison to the point probes. Using the optical probes acquiring the void fraction profiles shown in figures 6.10 through 6.21 took two hours for each condition. The x-ray data took a few seconds per condition and also provided information on the streamwise evolution of the void fraction. (Assuming that the x-ray had  $\sim 1$  mm spatial resolution, using the optical probe would take over eight days without pause to acquire the spatial distribution, while spending 3 minutes per point covering an area  $30\text{ m} \times 140\text{ m}$ , with points every 1 mm.)

With the potential of x-ray densitometry illustrated, and while recalling the limitations and imaging artifacts, the system can be used for cavitating flow where no other void fraction information is available (*i.e.* far away from the surfaces). For instance, non-intrusive surface flush-mounted electrical impedance void sensors can offer a good check for the local void fraction, but only near the surface.

For future experiments, the flow domain should be made narrower, as this would decrease the attenuation, enabling imaging with lower exposure settings (and in some

cases also without image intensification) and effects of non-parallel beam paths would be reduced. It would also be advantageous if the attenuation differences in the domain were less dramatic, *i.e.* not a 0 to 100% void fraction range. This will be the case in a many cavitating flows, for which the system will be used in the future.

## 6.8 References for Chapter 6

Gabillet, C., Colin, C., & Fabre, J., “Experimental study of bubble injection in a turbulent boundary layer”. *International Journal of Multiphase Flow*, 28(4), 553-578. doi:10.1016/S0301-9322(01)00075-1, 2002.

Jannetta, A. L. PhD Thesis. “Advanced deconvolution techniques and medical radiography”. October. University of Northumbria at Newcastle, 2005.

Mäkiharju, S., & Ceccio, S. L., “Time Resolved X-Ray Densitometry System for Cavitating Flows”. 3rd Int. Cavitation Forum (pp. 1-7). Warwick, UK, 2011.

Muhogora, W. E., Nyanda, A. M., Lema, U. S., & Ngaile, J. E. “Typical radiation doses to patients from some common x-ray examinations in Tanzania”. *Radiation Protection Dosimetry*, 82(4), 301-305, 1999.



## **CHAPTER 7**

### **Conclusions**

This dissertation discussed partial cavity drag reduction and x-ray densitometry, which can be a valuable tool for research of partial cavities. The reader was provided with literature reviews of both partial cavities in Chapter 2 and of x-ray densitometry in Chapter 5.

#### **7.1 Achievements and contributions**

##### **7.1.1 Partial cavity drag reduction**

Comprehensively documented partial cavity drag reduction experiments were conducted at Reynolds numbers approaching those encountered in real world applications of this proposed technique. The sensitivity of the partial cavity to its closure region geometry and to global perturbations, mimicking the effect of ambient waves, was examined. We found that small changes in the closure geometry brought about small changes in the required ventilation gas fluxes, but for a given cavity a near optimum could likely be found. The cavity was found also to be able to tolerate perturbations, if a moderate excess gas flux was supplied. In our experiments, the required excess flux was still less than that required to establish the cavity in calm conditions, and thus an air supply system capable of establishing the cavity could also cope with moderate global

perturbations. As part of these large scale experiments, the author also designed, Froude scale tested, and oversaw the construction and installation of a free surface forming actuated gate, which now remains as an optional feature of the world's largest cavitation channel, the LCC.

Experiments were also conducted with a geometrically similar experimental setup, but at Reynolds numbers order and a half apart in magnitude. The comparison of the results from the two different size scales suggest a scaling where the cavity's Froude number is always relevant, but perhaps the properly normalized gas flux becomes insensitive to Reynolds number beyond  $Re$  of a few million. At the lowest Weber numbers the cavity was found also to be sensitive to surface tension; however, this sensitivity was observed to be diminished as the Weber number was increased.

The energy economics of partial cavities were analyzed step-by-step, and making the assumptions made during the course of the analysis clear. Within the limitations of the assumptions, the results showed that partial cavity drag reduction could provide a net fuel savings as high as 20%. This indicated that the technique would be a major economic and environmental success, if these savings can be realized on full scale ships operating on the open oceans, or Great Lakes, and implemented widely.

### 7.1.2 X-ray densitometry

An x-ray densitometry system for quantitative measurements of multiphase flow was developed. While similar systems have been used by previous researchers (Stutz and Legoupil 2003), the current system has some notable advantages. Namely, the entire 2D projection of the flow was obtained simultaneously at frame rates of the order of a kilohertz. Also, the experiments, while conducted at laboratory scale, were still at  $Re$  of

the order of a million, while some of the more exotic and exciting x-ray densitometry experiments utilizing particle tracking velocimetry (Lee and Kim 2003, Dubsy *et al.* 2012) were performed with exceptionally small models and offer a view of an area with size scales only of the order of 1 mm. The current system was also designed and constructed to work with an existing cavitation tunnel, enabling it to be used for a myriad of experiments investigating any multiphase flow that can be generated in the 21 cm x 21 cm test section, such as ventilated and natural partial cavities, cavitating wedges and hydrofoils, vortex cavitation, etc.

The systems limitations and imaging artifacts were also extensively considered. Methods of dealing with the artifacts, such as veiling glare, were adapted from the literature for the system in question. Also, the possibility of reconstructing a 2D distribution, that has been distorted by non-parallel beam paths, was discussed, and for noise-free simulated data, this was shown to provide satisfactory results. Suggestions for how to deal with noise on this reconstruction were discussed also.

The x-ray densitometry system was validated against other void fraction measurement techniques. The author investigated a ventilated partial cavity behind a backward facing step, the far downstream void fraction distribution and its spatial evolution. For void fractions ranging from 100% to near zero ( $\sim 0.5\%$ ), reasonable agreement was found between the measurements using x-ray and optical probes. When acknowledging and addressing the x-ray techniques limitations, the system was shown to provide a fast and non-intrusive quantitative void fraction measurement. If for example, we need to obtain a two dimensional void fraction distribution ranging from zero to 5% for a 10 cm x 10 cm area with 1 mm resolution, in cavitating flow an intrusive probe

might be a non-starter, but even if it weren't, with a point probe the experiments would last over twenty days to measure ten thousand points, while waiting 3 minutes at each location. In comparison, the x-ray densitometry system can provide the two dimensional projection of the void fraction distribution in a few seconds, and averaging over longer times, at most in a half hour.

## **7.2 Future work**

### **7.2.1 Partial cavity drag reduction**

To advance partial cavity drag reduction research, experiments, and possibly numerical modeling, revealing in greater detail the cavity closure dynamics over a wide range of flow and geometrical parameters, would be useful. A series of cavity closure control experiments, where the beach profile would be modified, could also offer invaluable data to progress the technique.

To move expeditiously towards the wider implementation of PCDR, a series of mid- to full-scale sea-trials conducted jointly by with industry and academia, and where all the results would be fully published in peer-reviewed journals, would be the ideal next step. It would be best if the next sea-trials would also benefit from active collaboration, or at least open information sharing, with the current sea-trials by Marin (Foeth 2011), DK-Group (DK Group, 2011) and Stena (Surveyor 2011).

An intermediate step to advance the PCDR research would be to perform the experiments discussed in Chapter 2 and 3 in the mid range or Reynolds number of the order of 10 million, with a geometrically similar model. This could enable more comprehensive scaling arguments to be made for PCDR.

### 7.2.2 X-ray densitometry

For advancement of x-ray densitometry methods for multiphase flow research the author would suggest numerous improvements to the current x-ray system. The smallest suggested changes are: narrowing of the flow domain to reduce attenuation and embedding in the model a regular pattern of attenuation markers located in 3D to ease the registering of the image coordinate system.

The current camera was limited to recording only a thousand full resolution frames, while the source could be operated for up to 6.3 seconds continuously. There would be an immediate benefit if the camera were to be upgraded. Also, it would be helpful to replace the current 8-bit camera with one that has a wider dynamic range, as for some experiments this might enable observing more minute attenuation differences.

For better veiling glare correction, a set of precision machined phantoms, made of plastic with attenuation close to that of water's, representing a series of void fraction differences in close proximity, would be beneficial for finding the PSF's coefficients and for validating the veiling glare correction utilized. The phantoms should match closely the actual water path thickness and be placed in the location of the flow of interest, as the source and II may produce some spatial uniformities not explicitly noted in the current work. The author would start with a set of 100% to 0%, 20% and 40% phantoms, if the void fractions of the planned experiments span this range.

To remove the II distortions, remove much of the veiling glare, reduce image noise, and in some sense to simplify and make the system more compact. A more major improvement would be to replace the II with a flat panel detector. However, the flat panel, unlike those used in the medical field today operating at  $O(30\text{Hz})$ , should be

constructed such that it offers the required kilohertz frame rate, while still providing the simultaneous area view with satisfactory resolution.

The simultaneous use of multiple x-ray systems, or a source such as one utilizing a scanning electron beam similar to Bieberle *et al.* (2011), would offer the benefit of multiple projections acquired near simultaneously. This would not only provide redundant data for imaging artifact correction, but more tantalizingly, could enable time resolved 3D reconstructing of the flow field.

### 7.3 References for Chapter 7

Bieberle, M., Barthel, F., Menz, H.-J., Mayer, H.-G., & Hampel, U. "Ultrafast three-dimensional x-ray computed tomography". *Applied Physics Letters*, 98(3), 034101. doi:10.1063/1.3534806, 2011.

DK Group, web page, <http://www.dkgroup.eu>, last accessed on 12/13/2011.

Dubsky, S., Jamison, A., Irvine, S. C., Siu, K. K. W., Hourigan, K., & Fouras, A. "Computed tomographic x-ray velocimetry". *Applied Physics Letters*, 96(2), 023702. doi:10.1063/1.3285173, 2010.

Foeth, E.-J., "Projects prove that air cavities reduce ship resistance". report, MARIN's news magazine, 16. August, 2011.

Lee, S.-J., & Kim, G.-B. "X-ray particle image velocimetry for measuring quantitative flow information inside opaque objects". *Journal of Applied Physics*, 94(5), 3620. doi:10.1063/1.1599981, 2003.

Surveyor. "Airship of the Sea". *Surveyor, A Quarterly Magazine from AMS*, 10-15. 2011.

Stutz, B., & Legoupil, S. "X-ray measurements within unsteady cavitation". *Instrumentation*, 35, 130-138. doi:10.1007/s00348-003-0622-0, 2003.

## APPENDIX A

### Gate Design and Testing

The need to add a free surface forming gate to the LCC had become apparent during the previous test campaign reported in Lay *et al.* 2010, when as a consequence of air injection the duration of experiments per condition was severely limited by the pressure oscillations and accumulated air in the free stream. For PCDR the time scales involved in cavity growth, collapse and stabilization can be of the order of minutes, unlike for BDR and ALDR which develop and disappear based on the convective time scale of the flow (requiring few multiples of the time it takes for the flow to go from the injector to the tail, to achieve their final state). After the operators of the LCC approved the concept of adding a gate, the design process was started in the fall of 2007. One of the major constraints was that the gate had to be mounted using existing window penetrations, had to be able to withstand the largest forces with good factor of safety (3.5 to yield was self-imposed), and it had to be easily mountable and removable in approximately a day.



### A.1 Initial design and development

The MLCC, the LCC's 1:14<sup>th</sup> scale model, is located at the University of Michigan, and after initial design of the potential gate shapes, extensive Froude scale testing was performed at the MLCC. Three types of gates were tested; a) one with a vertical front shown in figure A.1, which was not suitable due to the strong corner vortices it induced, b) wedge shaped gate with a flap as long as the fixed part and c) a gate with a flap that was approximately 1/3 of the gate's length.

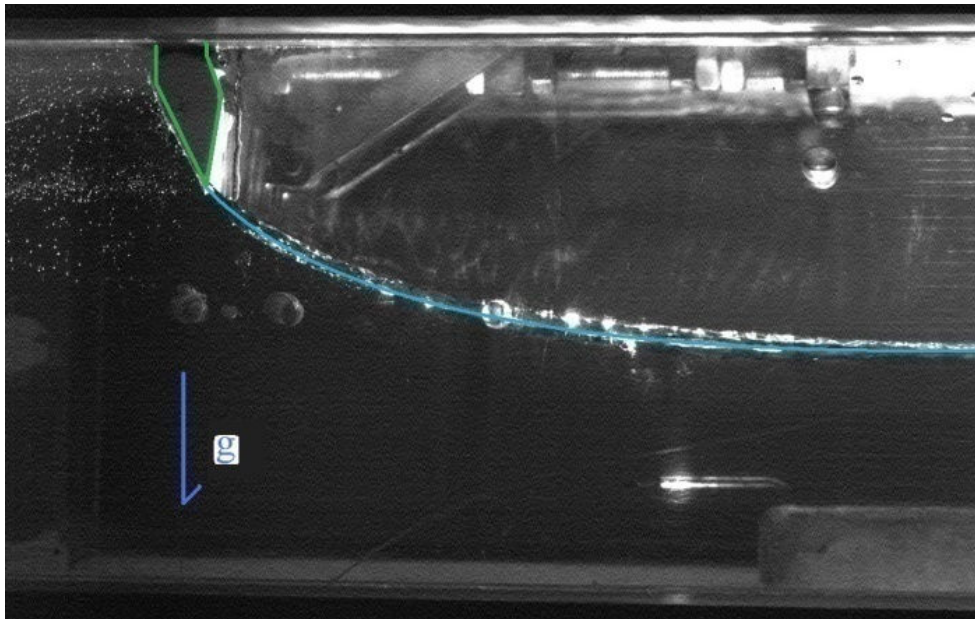


Figure A.1 – Flow is from left to right.  $U = 1$  m/s,  $Fr = 1.1$ . Old version of the gate with the flap at a 22.5 degree angle.

Typical free surface behind the gate was as shown in A.1 and A.2. The surface itself was often quite stable and glassy, until air accumulated upstream of the gate and subsequently ‘burped’ out from under the gate.

At faster speeds the oscillations of the surface became increasingly violent, but still it seemed that most of these oscillations and surface waves were caused by air looping around the MLCC. It was speculated that these problems with air would be mitigated by longer loop times in the LCC, and that improved air scavenging could also be employed.



Figure A.2 – Oblique view of the gate and free surface.  $U = 2.5$  m/s,  $Fr = 2.7$  ( $Fr$ -scaled for LCC: 9.4 m/s), old version of the gate in fully vertical position. The pitot used to measure the flow speed and its foil shaped support can be seen in the middle of the image. The frothy region near the aft of the test section is due to water draining down from hoses that connected the volume in front of the gate to the end of the test section, allowing air accumulating in front of the gate to be removed.

The following figures schematically show some of the flow conditions observed at the MLCC during model gate testing.

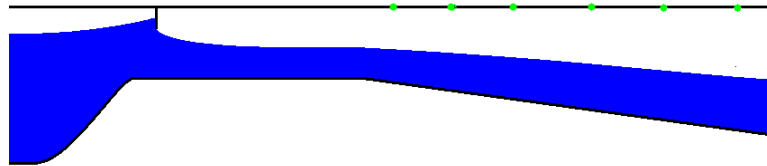


Figure A.3 – At low speed and moderate fill levels a condition was observed where there was a free surface upstream as well as downstream. The green dots on the top of the diffuser correspond to electrical impedance probes used to observe water level and detected splashing.

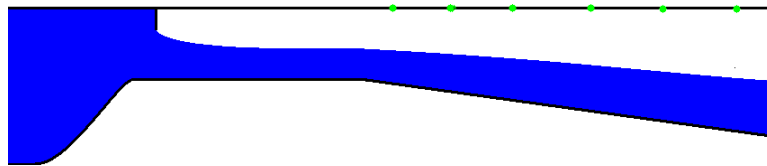


Figure A.4 – At slightly higher speeds up to around 1.5 m/s no free surface was observed upstream and no constant splashing of water was detected at the electrodes. The free surface in the diffuser probably wasn't as smooth as in the sketch, but at least no large splashes hitting the top of the diffuser occurred.

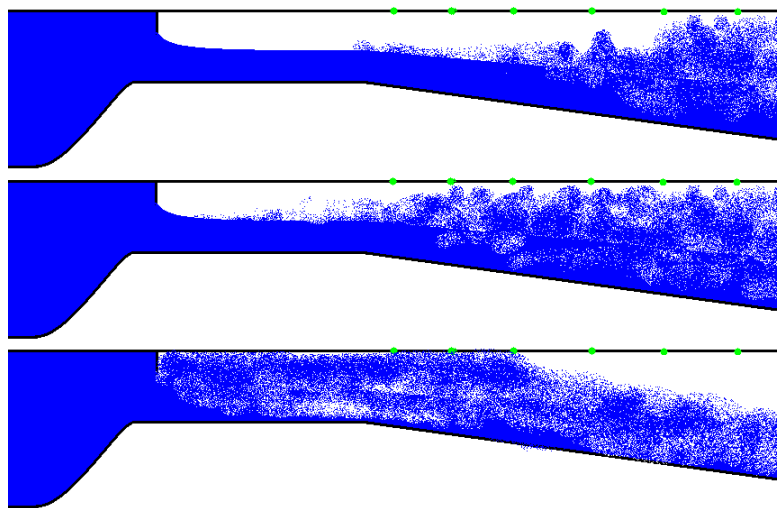


Figure A.5 – Three steps of loss of free surface: At 1.5-2.4m/s rapid splashing was detected at the back two and three electrodes. As speed was increased closer to 3 m/s splashing was indicated at almost all electrodes. Once at this condition, it seems that any significant increase of speed leads to a loss of free surface. Once the free surface was lost the back 2-3 electrodes curiously enough indicated no water and often no splashing. This would indicate that a topology of the type shown in the last sketch may be occurring.



Figure A.6 – The old version of the gate in the MLCC and a loss of cavity.

The loss of free surface shown above is a highly undesirable test condition. However, there always seems to be a warning, in the form of increasing and upstream moving splashing hitting electrodes at the top of the diffuser, before loss of surface. If this also occurs at the LCC, detecting this could enable avoiding the undesirable flow condition where the free surface is lost.

After the initial testing in the MLCC was complete and the mounting location along with the gate's shape were agreed upon, it was necessary to measure the relative locations of the window penetrations and walls more accurately than specified in the LCC's as build drawings. A Leica TCR405 survey station was rented and used by the author to survey the upstream part of the LCC's test section.



Figure A.7 – Looking upstream inside the LCC's test section. Leica measurement station seen in the middle of the image.

Figure A.7 shows the survey station near the contraction, and some of the markers on the wall are visible. A three dimensional point cloud with ~600 points was created and later superimposed onto the SolidWorks model made of the LCC's test section. One of the many useful findings was that on one side the top diagonals were ~1/8" lower than its counterpart. It was decided that the gate should allow for adjustment about all its axis when it is installed the first time. This was achieved via use of sliding diagonal connectors that were welded in place during the first installation, and use of large load blocks that would be machined to final shape only during the first installation.



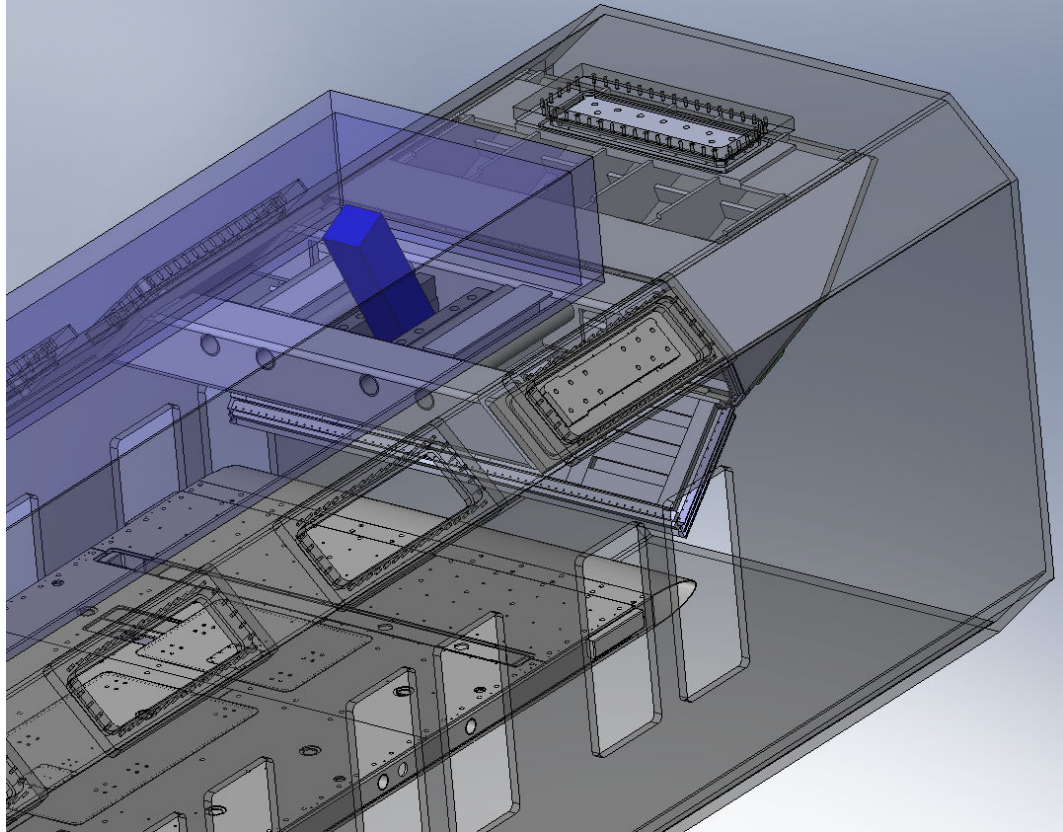


Figure A.8 – Location of the gate. We can see that the gate has three mounting points using the existing front most diagonal windows on both port and starboard sides, and a third window opening in the ceiling of the tunnel.

## A.2 FEA of gate structure

As a structural failure of the gate would be catastrophic, a finite element analysis expert, Dr. Aimin Wang, was employed to analyze the structure. Dr. Wang's model included 25,000 elements, and the static stress analysis was performed using NASTRAN. Some of the key results are shown in the following figures.

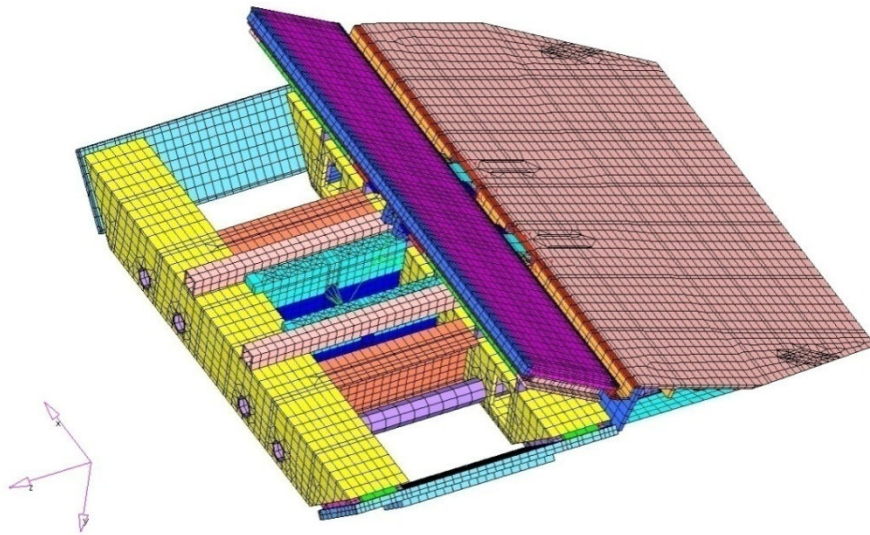


Figure A.9 – FEA model of the gate viewed from below. Figure by Dr. Wang.

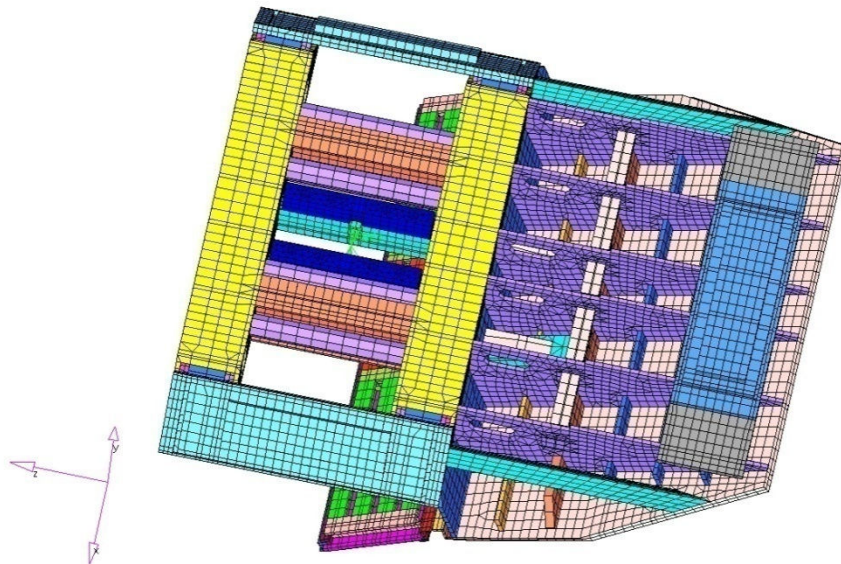


Figure A.10 – FEA model of the gate viewed from above. Figure by Dr. Wang.

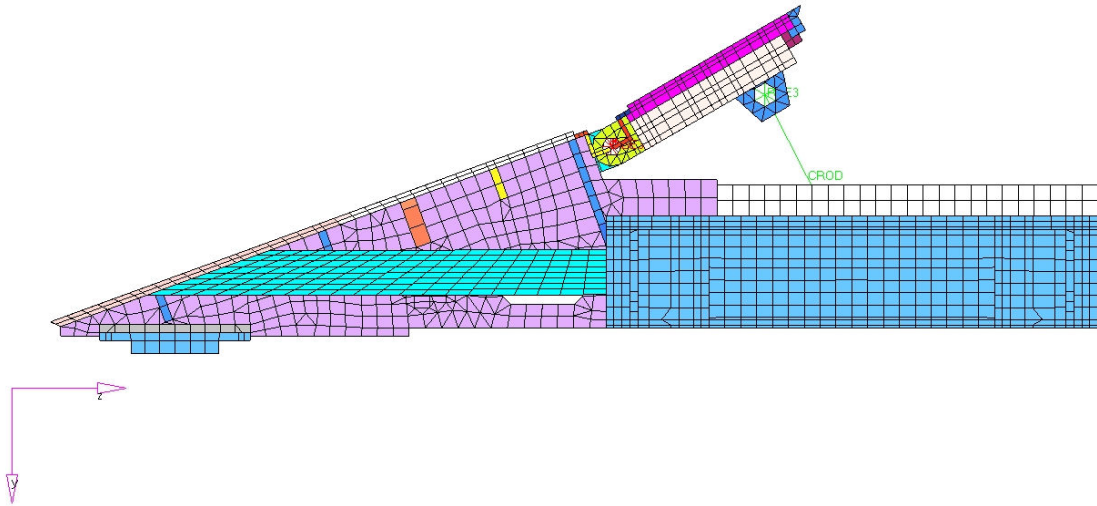


Figure A.11 – FEA model of the gate viewed from the side with the flap at 25 degrees with respect to the flow. Figure by Dr. Wang.

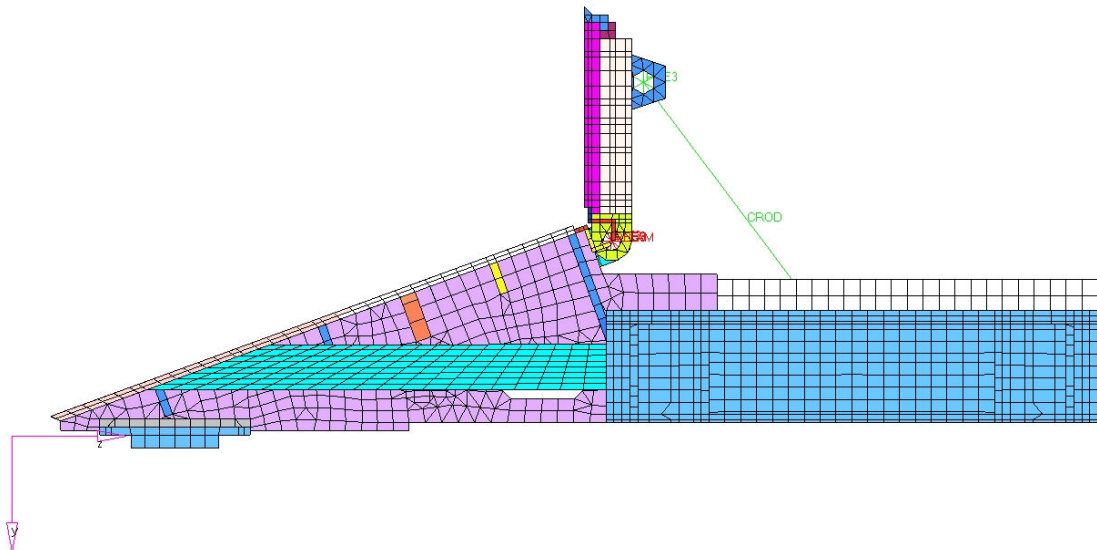


Figure A.12 – FEA model of the gate viewed from the side with the flap at 90 degrees with respect to the flow. Figure by Dr. Wang.



The FEA analysis indicated that at the maximum loading imaginable, with a two-hinge flap at 90 degrees as shown above and incoming flow at 12 m/s, the maximum deflection would be up to 3.5 mm. Consequently, the hinge design was altered to one where a continuous series of hinge blocks span the entire 118” span of the gate.

In addition to the model testing and FEA, the CFD code Fluent was also employed to envision the expected void fraction and pressure distributions when both the gate and HiPlate were installed, and figure A.8 shows some of the result.

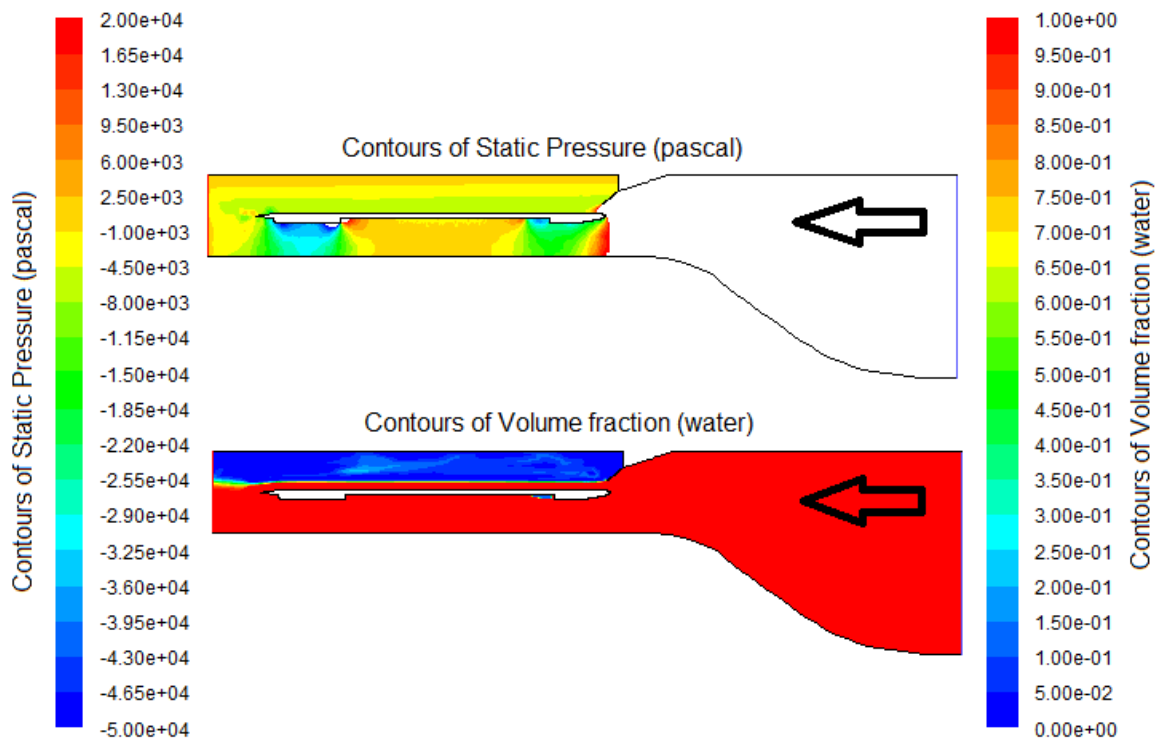


Figure A.13 – Pressure and void fraction contours from CFD.

### A.3 Final gate design and gate's position

The gate's fixed part is at 20 degrees with respect to the horizon. The flap can be actuated from 0 to 90 degrees. The picture below shows the gate at an arbitrary angle. Note that the top of the gate is already in the LCC's contraction and the bottom section of the tunnel in this area is not straight as shown below.

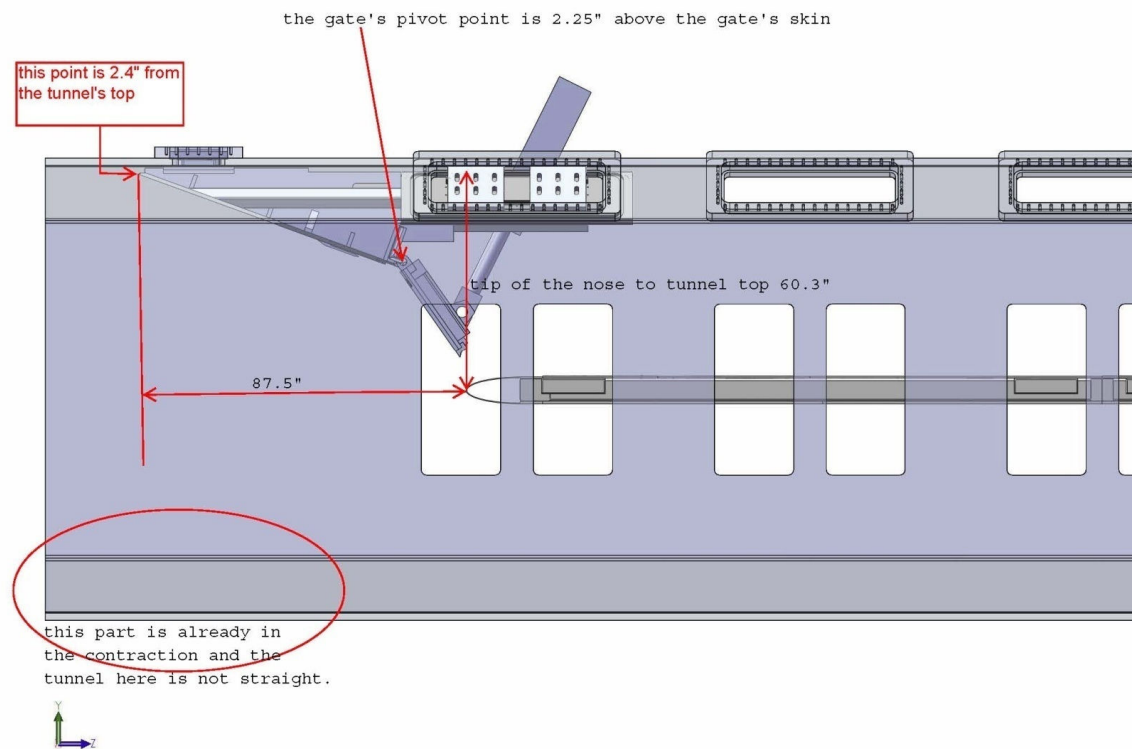


Figure A.14 – The location of the gate and HiPlate.

Details of gate position in relation to the Hiplate are shown in A.14. The top of the HIPLATE is 56.7" from the top of the LCC test section. The LCC test section is 10' by 10' and the HIPLATE spans the whole width of the tunnel.

#### A.4 First test of the gate in the LCC

The following figures show the gate being installed, images and data taken during the gate test.



Figure A.15 – To get the gate into the test section it had to be tilted by over 45 degrees. Once in the test section, it was lowered onto a cart and the crane disconnected so that the chains could be repositioned for the final lift into position, during which the chains upstream went through the window on the LCC’s ceiling upstream of the test section.



Figure A.16 – Gate in the test section with the flap at 0 degrees with respect to the horizon. The gate's hinge was covered by a flexible spring steel sheet which slid in and out of the slot upstream, always providing a smooth flow surface and minimizing water leakage through the hinge.

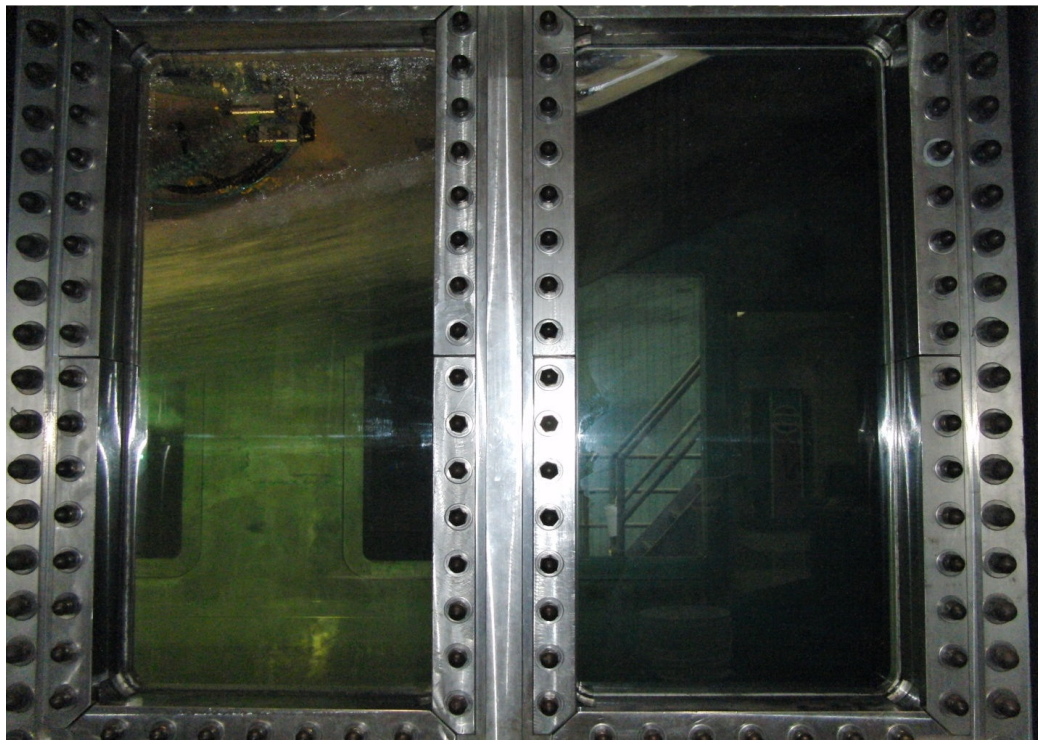


Figure A.17 – The flap can be seen through the right window and the displaced water surface through the left.



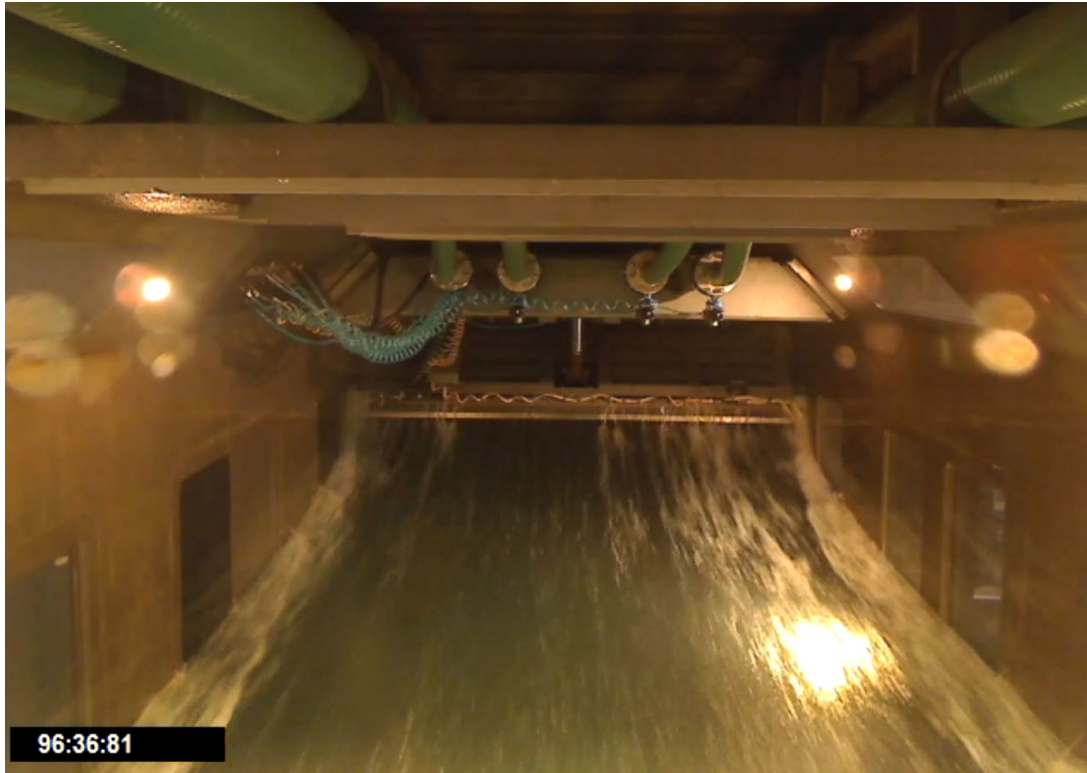


Figure A.18 – Looking upstream towards the gate. The gate’s flap and piston are clearly visible. The green hoses seen in the image are 4” drain lines with pneumatic valves used to divert the air water mixture skimmed from in front of the gate to the back of the test section where the mixture could be discarded without disturbing the flow in the test section, but without loss of water from the flow loop.



Figure A.19 – Looking downstream the free surface can be seen to have become flat and free of major perturbations, providing a suitable surface for free surface testing. The hydraulic jump which terminated the free surface in this case was just after the test section and can partially be seen.

Figure A.20 shows both the horizontal and vertical velocity profiles measured several meters downstream of the gate. The velocity is seen to be quite uniform.

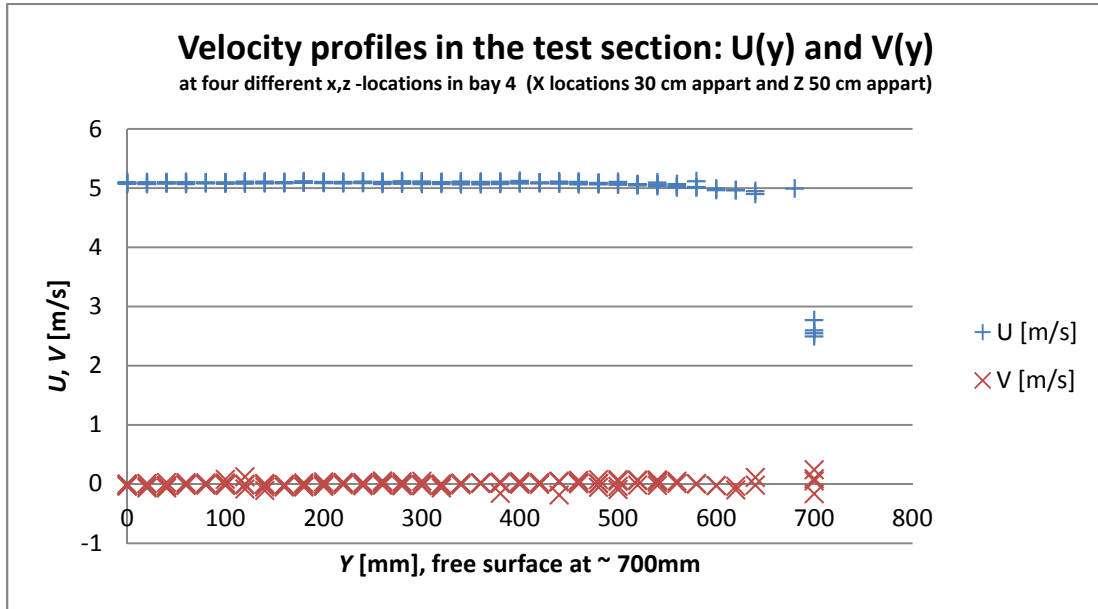


Figure A.20 – The streamwise velocity,  $U$ , was fairly uniform and vertical velocity,  $V$ , was practically zero as it should. (The data from all four profiles overlaps.) The highest point are on the free surface and it is possible that they are erroneous.

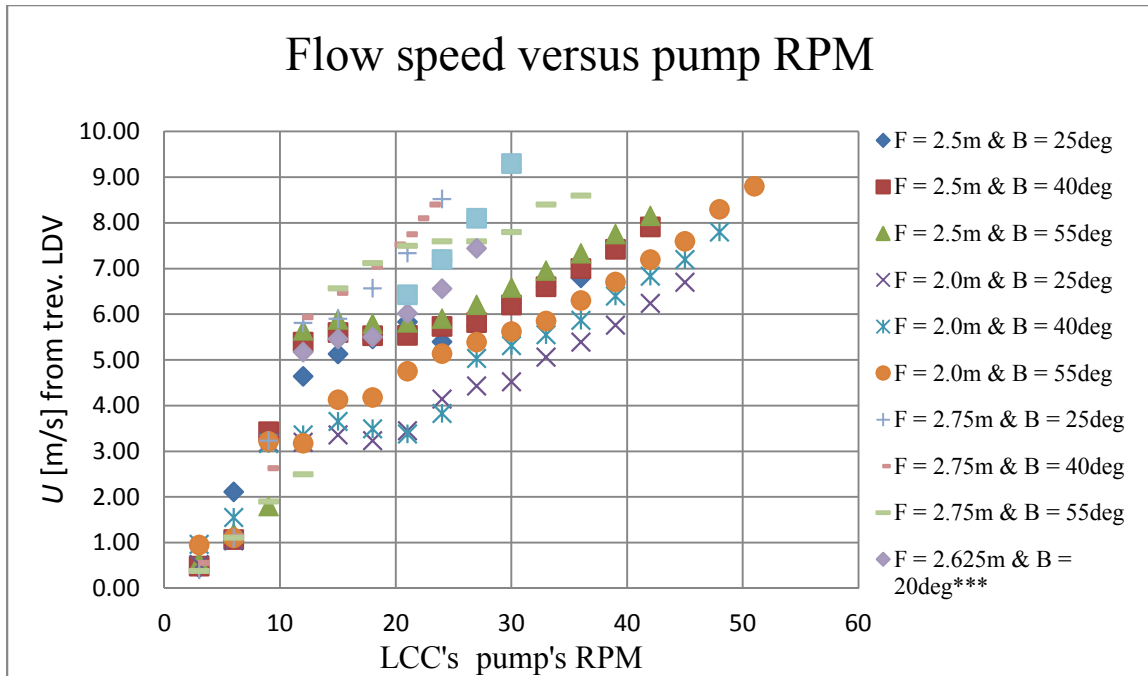


Figure A.21 – Flow speed vs. RPM at various initial fill levels and gate angles, with a free surface and without the HiPlate. Note the bends and dips which occur when the flow topology changed in the test section or diffuser.

Before we could run the test with the gate and model, we had to establish approximately  $U(H_{\text{fill}}, \beta_G, \text{rpm})$  and determine the achievable flow speeds which still allow maintaining tolerable flow conditions. Figures A.21 and A.22 show some of the key results.



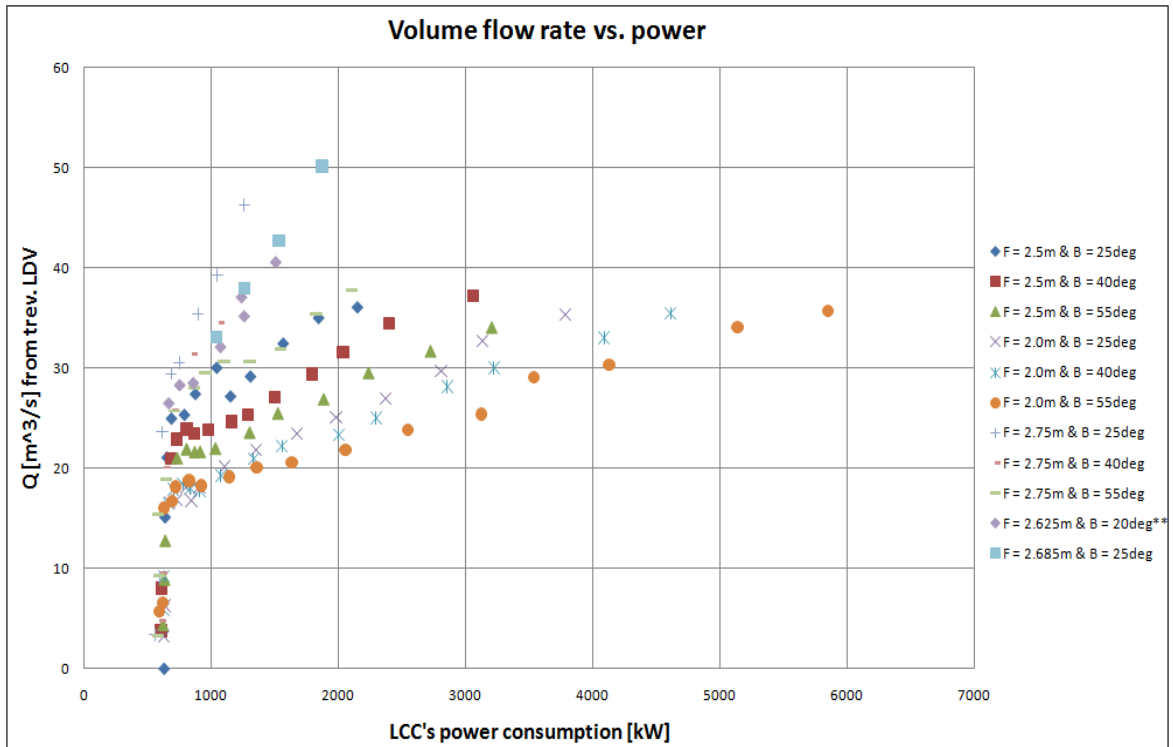


Figure A.22 –The required pump power versus flow rate for different flap angles and initial fill levels. The approximate power measurement was provided by the LCC’s control system.

## A.5 LCC with the gate and HiPlate

Because of the significance of flow topology and volume of air entrained by the flow, the pump rpm alone does not set the flow speed. And, at the highest flow speed the flow had more bubbles, making it fairly opaque and complicating the LDV measurement. The following show measured data points at one initial fill level, and we can observe notable scatter in the data. For these reasons the error bars at the highest test speeds discussed in Chapter 2 are so wide.

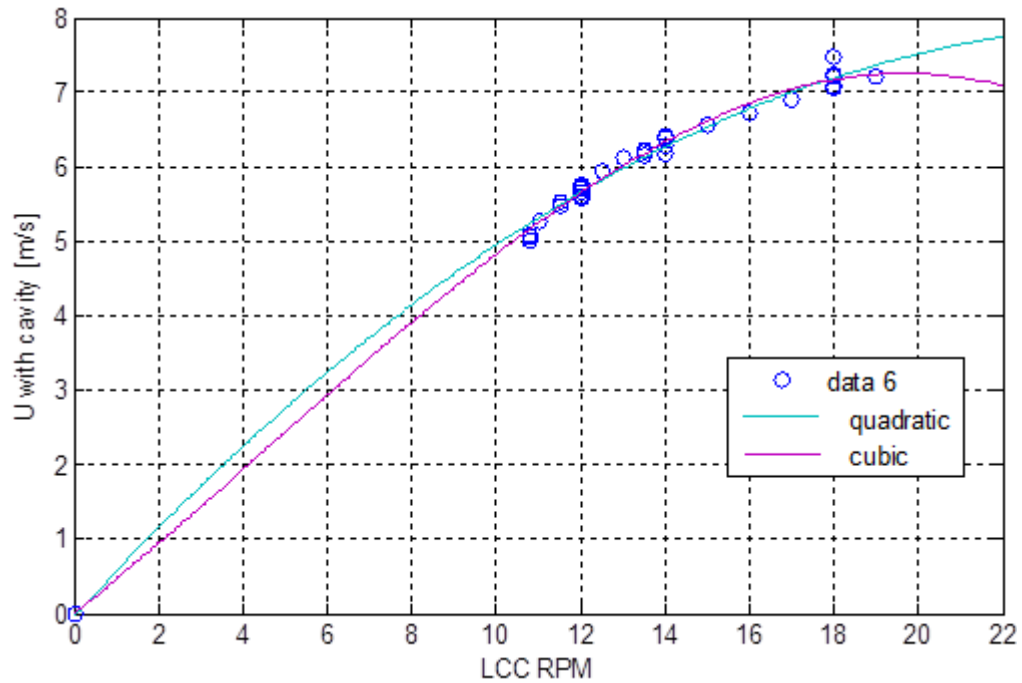


Figure A.23 – The blue circles in the figure below show all the velocities actually measured with the LDV (with the PCDR HiPlate and beach in base position). Depending on the curve fit chosen, two shown for example, the velocity expected at the highest pump PRM had large variation.

## A.6 The variables considered in the testing

For both with and without the HiPlate, the following lists the key variables considered in the experiments. Also listed are the dimensionless groups considered and how they were defined in these experiments.

### The Independent variables:

Free-stream speed,	$U_{\infty}$	[m/s]
Free-surface pressure in the LCC test section,	$p_{\infty}$	[Pa]
No-flow test section liquid fill height,	$H_F$	[m]
Mean gate angle,	$\bar{\beta}_G$	[degrees]
Gate oscillation amplitude,	$\Delta\beta_G$	[degrees]
Gate frequency of sinusoidal oscillation,	$f_G$	[Hz]
Mass flow-rate of injected air,	$Q_A$	[kg/s]
Beach maximum height,	$H_B$	[m]
Beach angle,	$\beta_B$	[degrees]

### Constants:

Density of water,	$\rho_w$	[kg/m <sup>3</sup> ]
Gravity,	$g$	[m/s <sup>2</sup> ]
Test section height,	$H$	[m]
Model span,	$w$	[m]
LCC's loop frequency,	$\omega_n$	[Hz]
Step height,	$H_S$	[m]
Length of recess on model,	$L_c$	[m]

### Dependent variables:

Flow depth after the gate,	$h_d$	[m]
Cavity pressure,	$p_{cav}$	[Pa]
Frequency of surface waves,	$\omega_{w,top}$	[Hz]

Relevant dimensionless groups (without HiPlate):

Froude number downstream,

$$Fr = \frac{U}{\sqrt{gh_d}}$$

Reynolds number downstream,

$$Re_d = \frac{(\text{hydr. diam.})U}{\nu} = \frac{4Hh_d}{H + 2h_d} \frac{U}{\nu}$$

Contraction coefficient,

$$C_c = \frac{h_d}{H - (a + b \cos \theta)}$$

Cavitation number,

$$\sigma = \frac{2(p - p_{vap})}{\rho_w U^2}$$

Strouhal number for waves behind the gate,  $St = \frac{\omega h_d}{U}$

Relevant dimensionless groups (with HiPlate):

Froude number,

$$Fr = \frac{U}{\sqrt{gh_d}}$$

Reynolds number on HiPlate,

$$Re_x = \frac{xU_\infty}{\nu}$$

Cavitation number in cavity,

$$\sigma = \frac{p_{cav} - p_{vap}}{\frac{1}{2}\rho_w U_\infty^2}$$

Strouhal number for cavity oscillations

$$St_{cav} = \frac{\omega_{cav} L_{cav}}{U_\infty}$$

Strouhal number for cavity and air layer ripples

$$St_{AL,ripple} = \frac{\omega_{ripple} h_{AL}}{U_\infty}, \quad St_{PC,ripple} = \frac{\omega_{ripple} h_{cav}}{U_\infty}$$

Strouhal number for cavity closure cloud shedding

$$St_{shedding} = \frac{\omega_{shed} L_{cloud}}{U_\infty}$$

Strouhal number for waves on top of the HiPlate

$$St_{w,top} = \frac{\omega_{w,top} H_{top}}{U_\infty}$$

## APPENDIX B

### The PCDR Model

The PCDR model used in these experiments was a modified version of the "HiPlate" designed by Sanders (2004). The major modifications to the HiPlate were, addition of a 7" backward facing step, reinforcement of the front most mounting blocks and addition of an adjustable composite surface called the "beach" near the trailing edge. The PCDR model is shown in figure B.1.

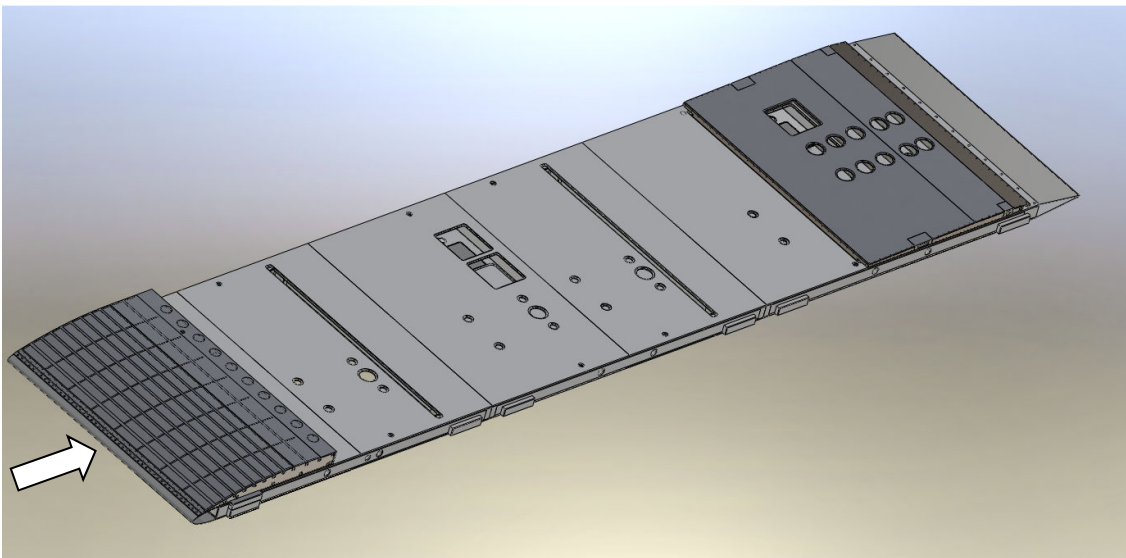


Figure B.1 – The PCDR model, with flow direction indicated by the arrow. The HiPlate model was outfitted with a 7" tall nose at the leading edge and an adjustable beach at the aft.

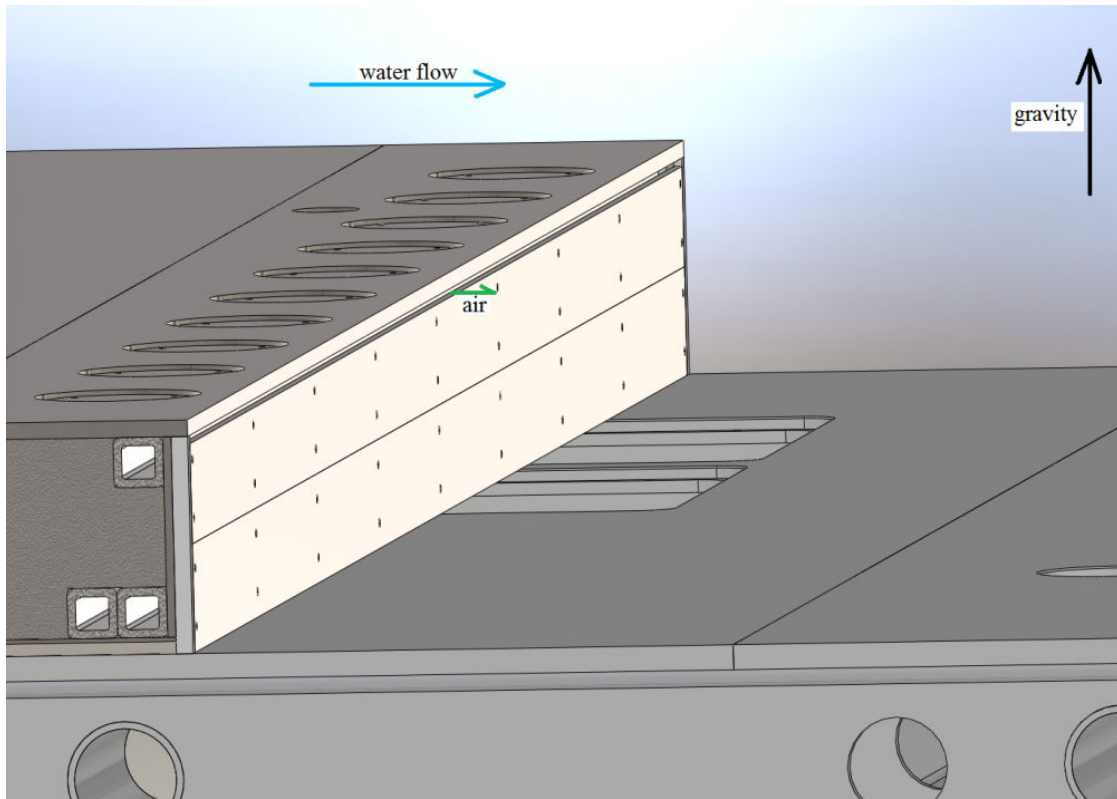


Figure B.2 – View of the 7" step with slot d in use. In these experiments, the slot at the base of the step, a, was always used.

Figure B.2 shows a close up of the back face of the 7" step. The two plates seen at the back of the step could be adjusted so that the air would be ejected out either from the top, middle or base of the step. The air exits a  $\frac{1}{4}$ " tall and  $1\frac{1}{4}$ " wide slot, and depending on the positioning of the plates there were four possible locations of the slot:

- a) 0.00" to 0.25" as measured from the surface of the plate.
- b) 3.00" to 3.25" as measured from the surface of the plate.
- c) 3.25" to 3.50" as measured from the surface of the plate.
- d) 6.25" to 6.50" as measured from the surface of the plate.

The front most load blocks of the model were reinforced because due to the gate the flow encountered the leading edge at an angle of attack, and also the non-symmetrical nose lead to a non-symmetrical pressure distribution. Both of these factors can cause significant vertical loads on the model, which necessitated the reinforcement of the load block. Figure B.3 shows some of the key locations of the model, and the front most load blocks can also be seen near the leading edge.

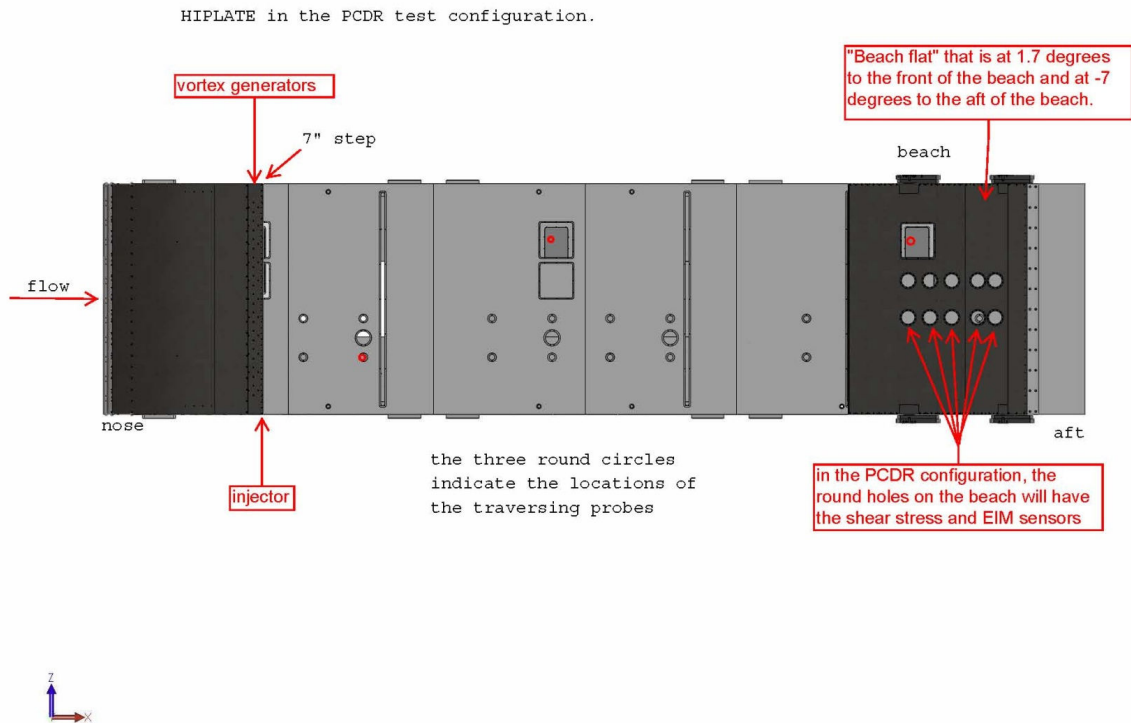


Figure B.3 – PCDR model with some of the instrumentation locations indicated.

## B.1 The beach design

The beach is the surface on which the partial cavity closes. One of the objectives of these experiments was to investigate the sensitivity of the required air fluxes to the closure geometry. For this reason, the beach had three degrees of freedom: height, spanwise and streamwise angle. Figure B.4 shows a side view of the beach and model in the LCC's test section.

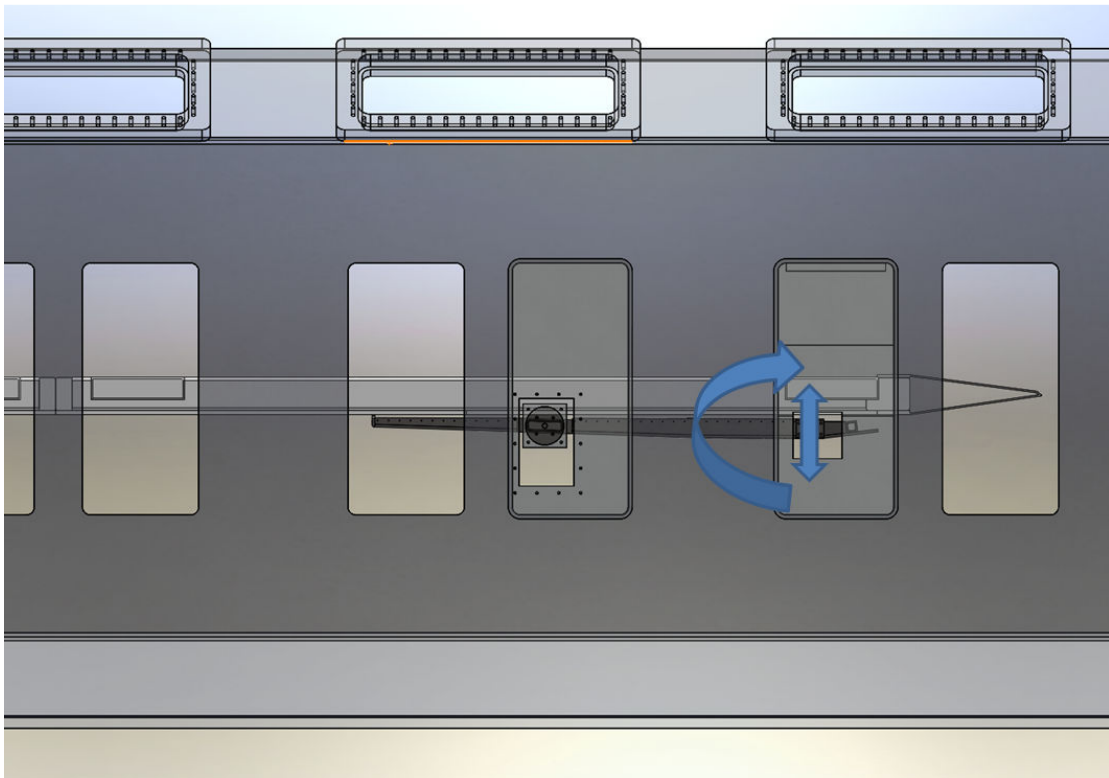


Figure B.4 – The height and angle of the beach could be adjusted by varying the location of the load blocks, which held the beach using the LCC's aluminum windows. To adjust the beach, sealing plates covering the opening were removed from the outside, chain hoists used to suspend the beach and varying the thickness of load blocks under the beach's load-pins in the windows.



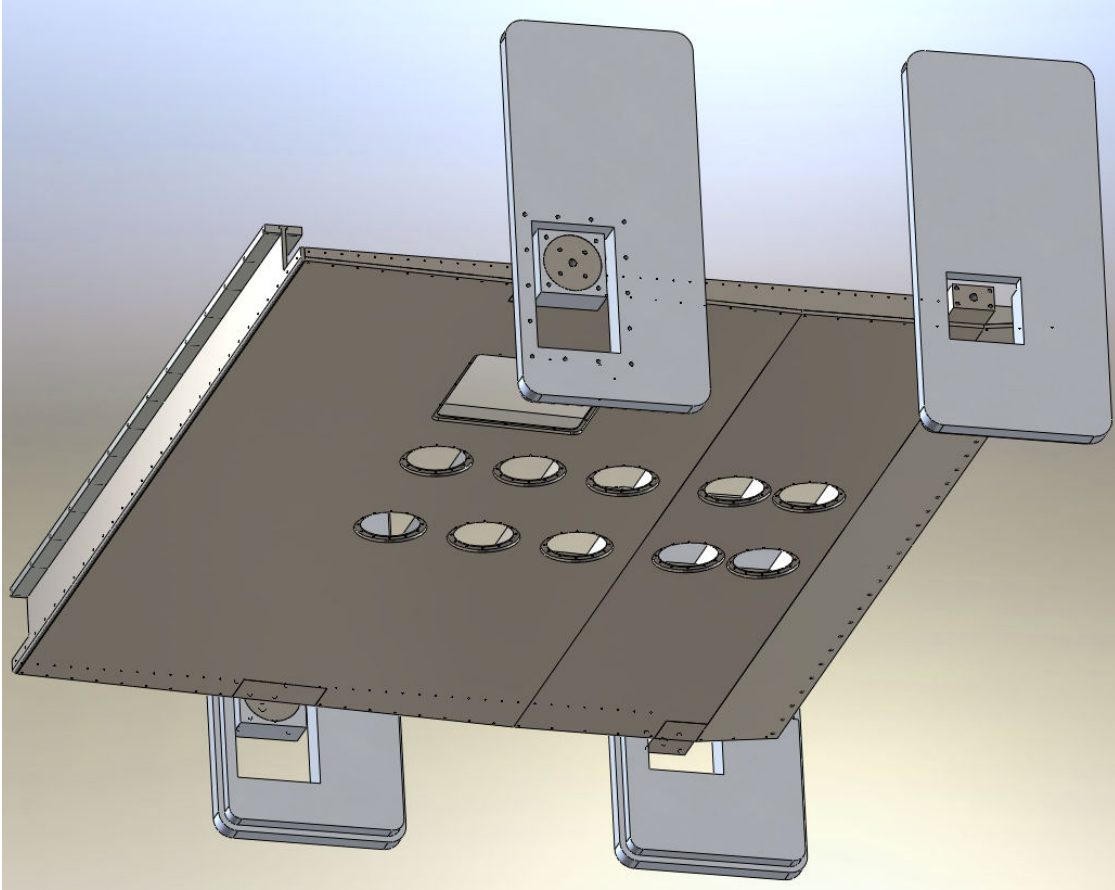


Figure B.5 – Sketch of the beach showing clearly how it mounts into the holes in the LCC's windows.

As shown in figures B.6 and B.7, the beach-structure starts 385” from the tip of the HiPlate’s nose. It is rigid structure that can be described as follows: a flat section that is at 90 degrees with respect to the beach-flat, this section is covered by a flexible seal that can generally be assumed to be flat against the steel. A flat 60” long front section that is at 1.7 degrees with respect to the beach flat. A flat 22” long beach-flat section, followed by a flat 10” long rear section that is at -7 degrees with respect to the beach-flat

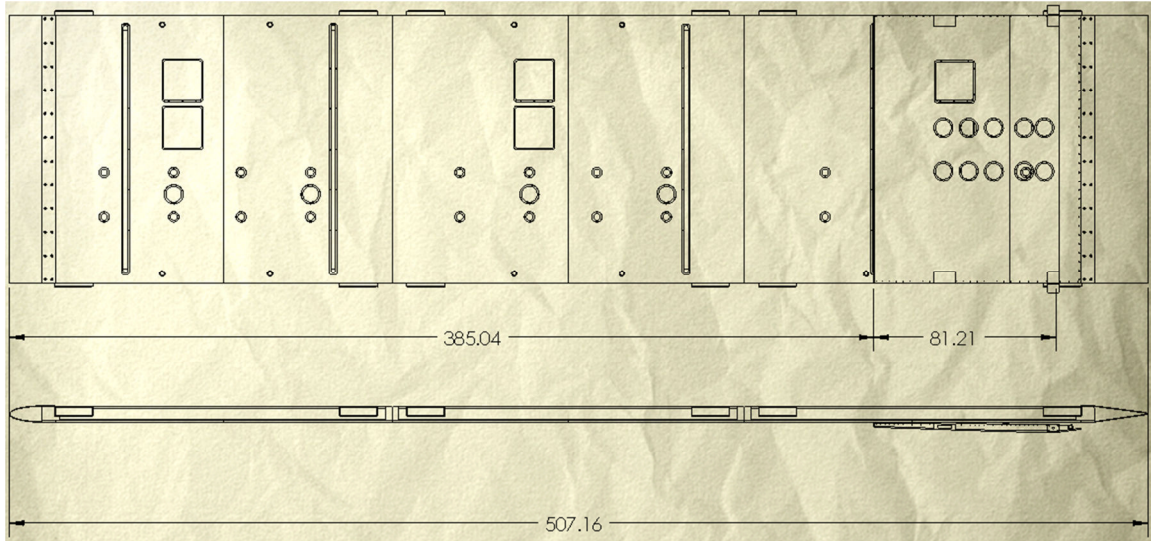


Figure B.6 – Drawing of the HiPlate with the beach.

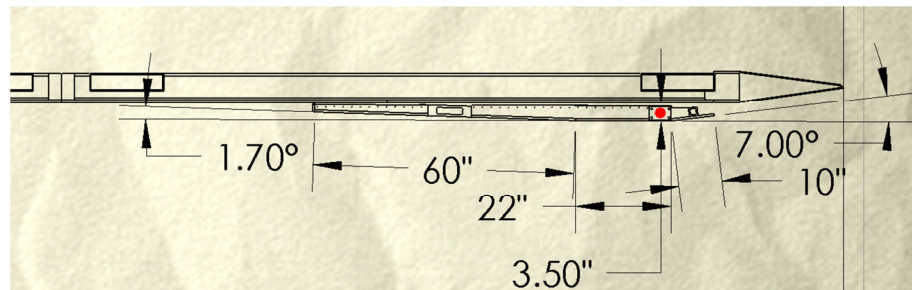


Figure B.7 – Drawing showing the dimensions of the beach, and its location in the "base" configuration when beach flat is at zero degrees and 3.5" below the HiPlate surface.

Range of motion of the beach was as follows. Height of the back edge of beach flat can be 3.5" to 7.5" as measured from the HiPlate skin. Angle of the beach flat can be varied from -1.7 to +3 degrees with respect to HiPlate. Figure B.7 above shows the beach at 3.5" and 0 degrees.

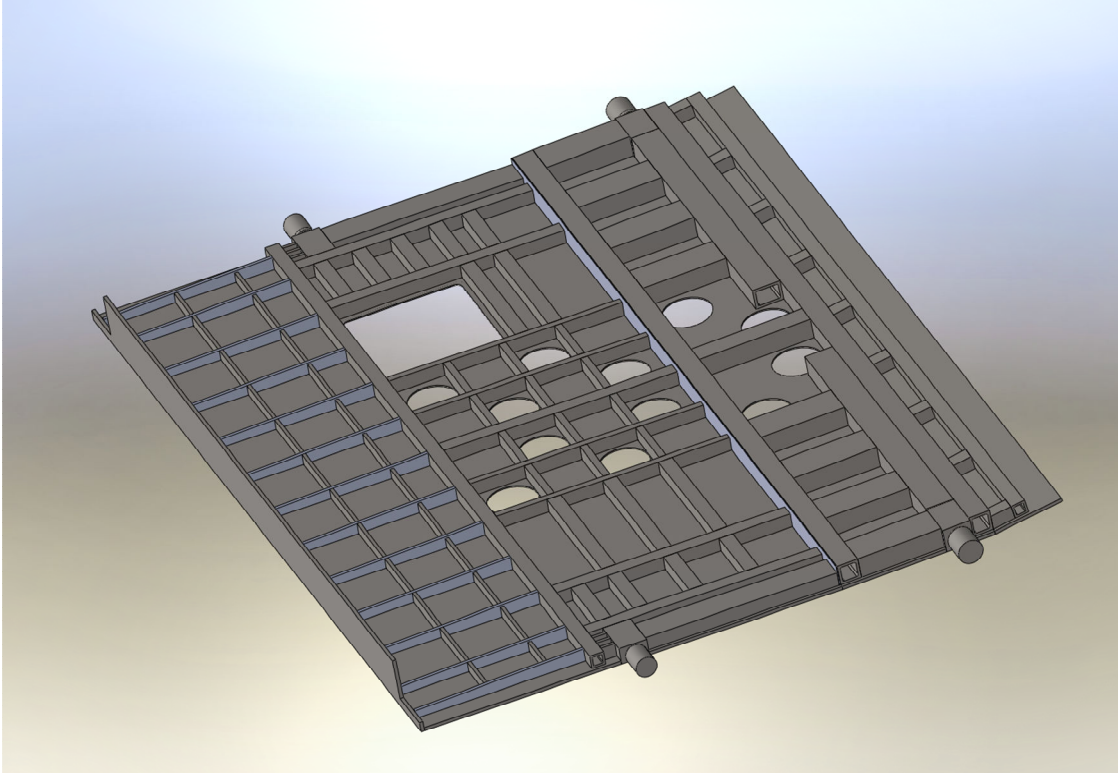


Figure B.8 – View of the structure beneath the beach, for the first design analyzed. In this initial design the round instrument locations were not in two rows and the load pins were found to be too weak as shown in the following.

The finite element analysis (FEA) functionality of Solidworks 2008 was used to investigate the behavior of the beach under load. As the beach was ~82" long and 120" wide, and a pressure difference could exist across it, it was vital to check that the beach would not bend or fail under even the highest imaginable load. Analysis showed that without the structural tubing welded onto the bottom of the beach, the beach would have bent notably, and possibly fail under some flow conditions.

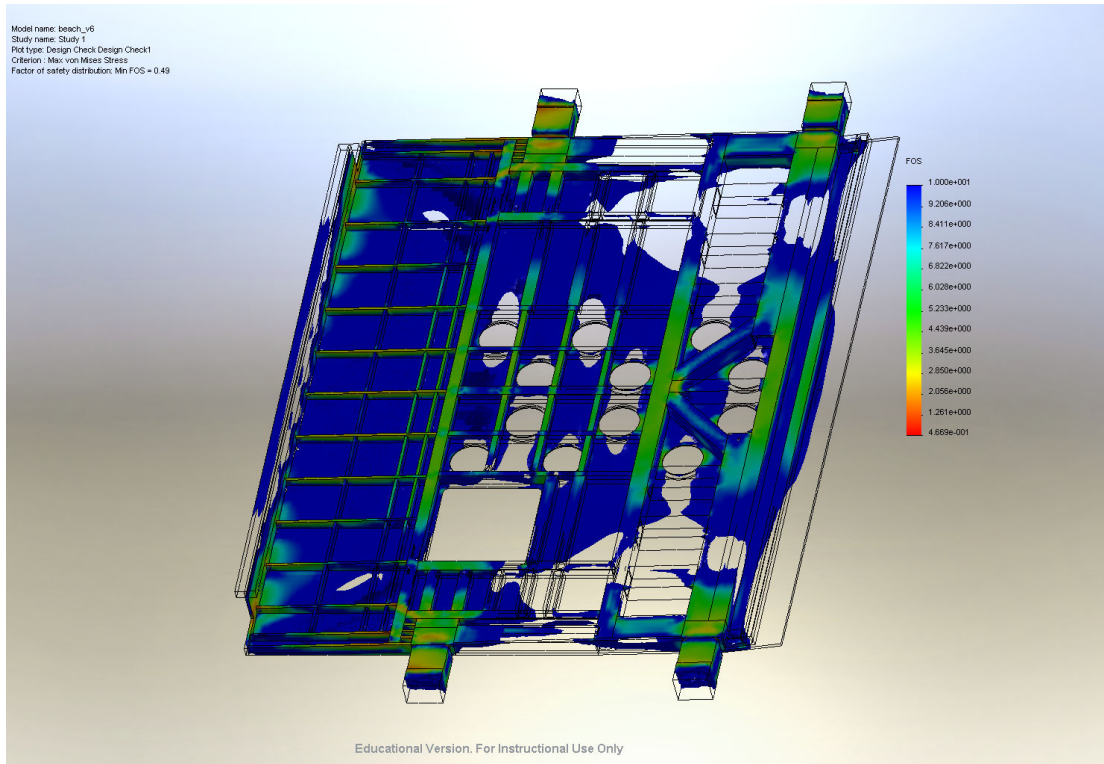


Figure B.9 – Plot of the beach's structural factor of safety to yield.

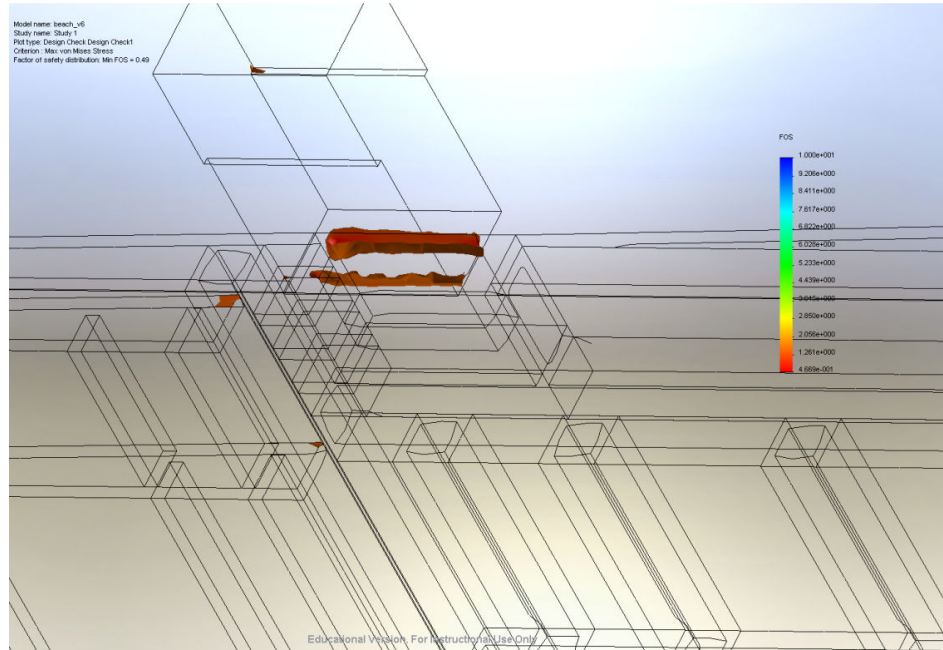
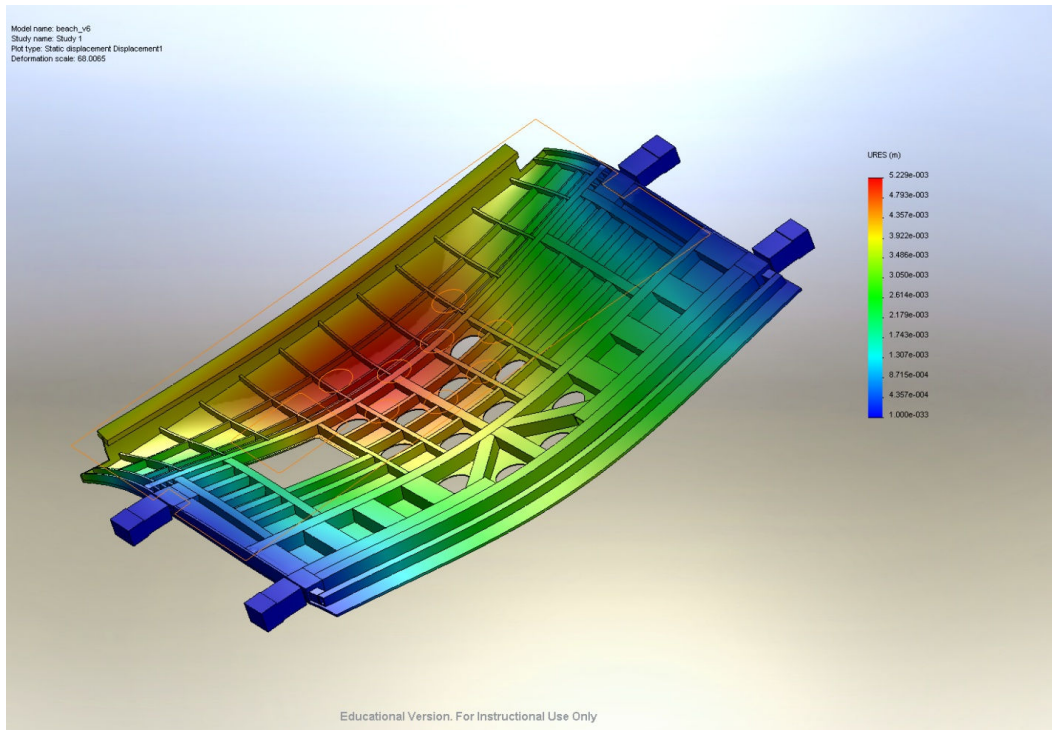
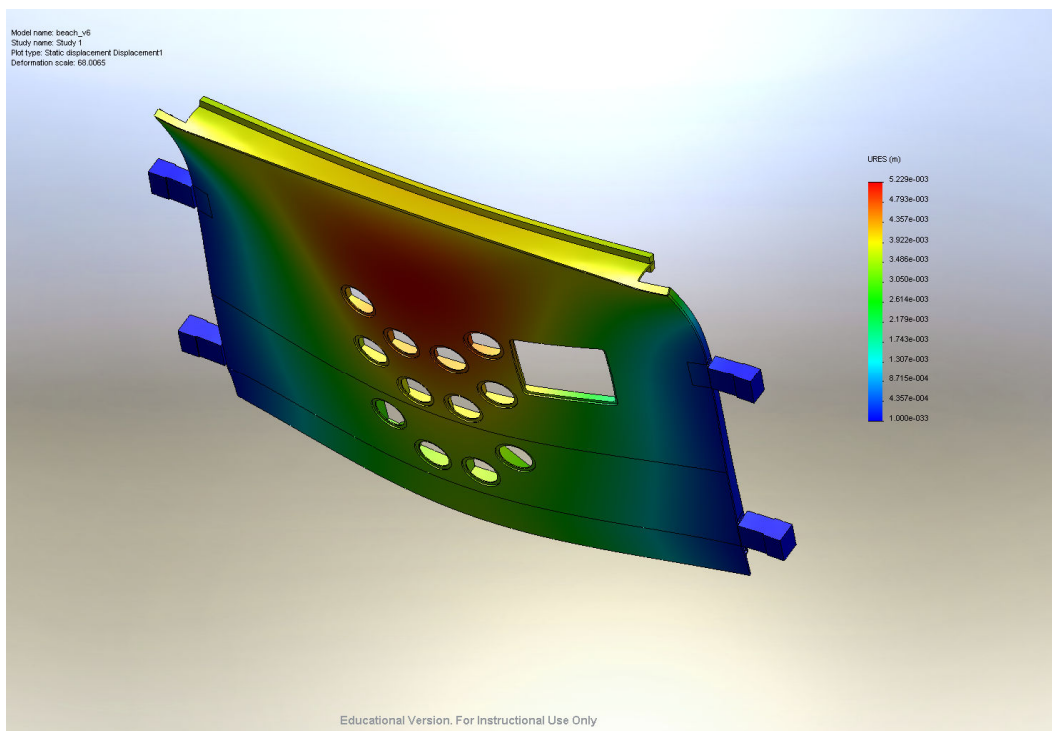


Figure B.10 – The lowest factor of safety was found to be at the base of the load-pins, which were subsequently thickened and a chamfer was added to the base of the pins.





(a)



(b)

Figure B.11 – The excruciated deflection of the beach. Under the highest loads envisioned, the beach could have deflected as much as 5 mm.

## **B.2 References for Appendix B**

Sanders, W. C., "Bubble Drag Reduction in a Flat Plate Boundary Layer at High Reynolds Numbers and Large Scales," PhD dissertation, University of Michigan, 2004.

## APPENDIX C

### Traversing Probes

#### C.1 The traverse mechanism

Figure C.1 shows the motor's watertight anodized aluminum enclosure and stainless steel gear mechanism for one of the traverses. The foil rode up and down on a  $\frac{1}{2}$ "-10 ACME precision stainless steel rod. The enclosures were slightly pressurized and instrumented to detect leaks. The probe positions were verified periodically with direct measurements.

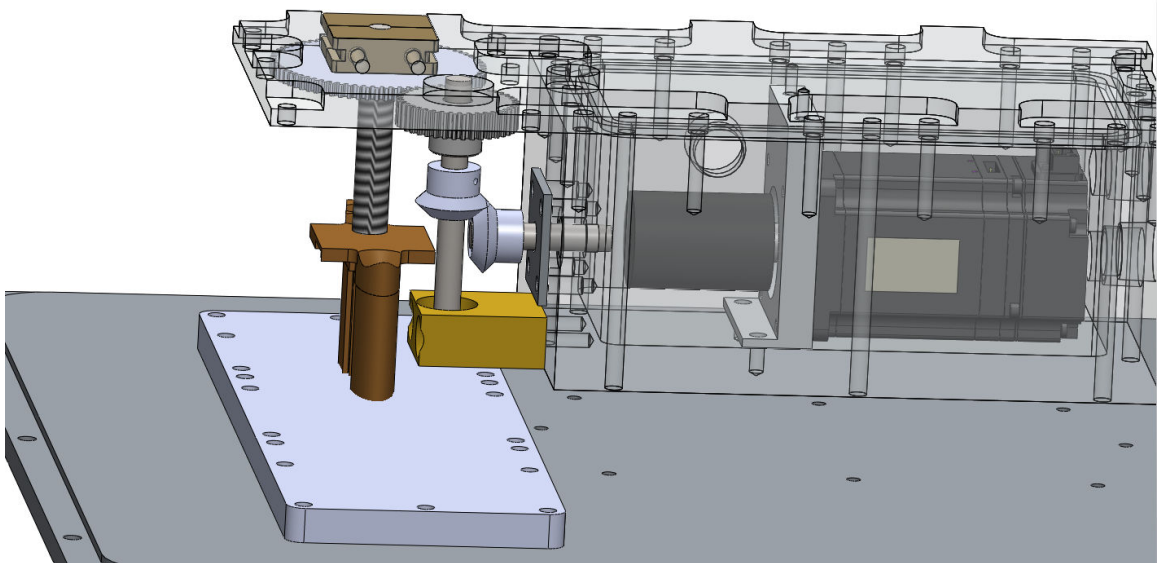


Figure C.1 – The traverse mechanism shown in detail. Note the flexible shaft coupling inside the enclosure and the shaft exiting the enclosure through three seals, which are not shown in this drawing.

Motion was achieved via a gear mechanism connected to a Yaskawa Sigma 5 SGMAV-04A3A61 motor with a 20 bit per revolution absolute encoder. The motors were controlled by SGDV-2R8F11A Yaskawa drives, with position prescribed by a Labview program (via Yaskawa Mechatrolink II JAPMC-NT110 PCI-card).

During testing at UM before and after the experiments, the position of the motor was found to hold, without detectable dither. (Another motor tested previously had a tendency to rotate back and forth by a few degrees constantly while trying to maintain position.)

## C.2 The electrical impedance sensors

Figure C.2 shows the top of the traversing foil, which had a Pitot-tube, point electrode shown in figure C.3 and a time of flight probe.

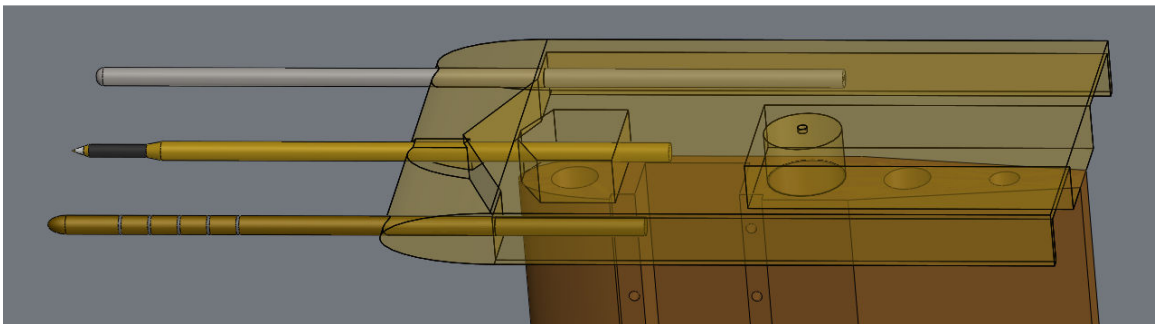


Figure C.2 – A drawing where the top of the traverse is made transparent to reveal detail.





Figure C.3 – A close up of the point electrode. The thicker support is 1/8" in diameter, the excitation was provided by the electrode at the very tip and the sensing was done via the middle conducting copper color ring seen between the black and white insulating material.

Figures C.4 and C.5 show time traces from probe shown in figure C.3, as bubbles pass by it. It can be seen that there is a finite rise and decay time of the signal as the bubble enters and exits the volume of influence of the probe.

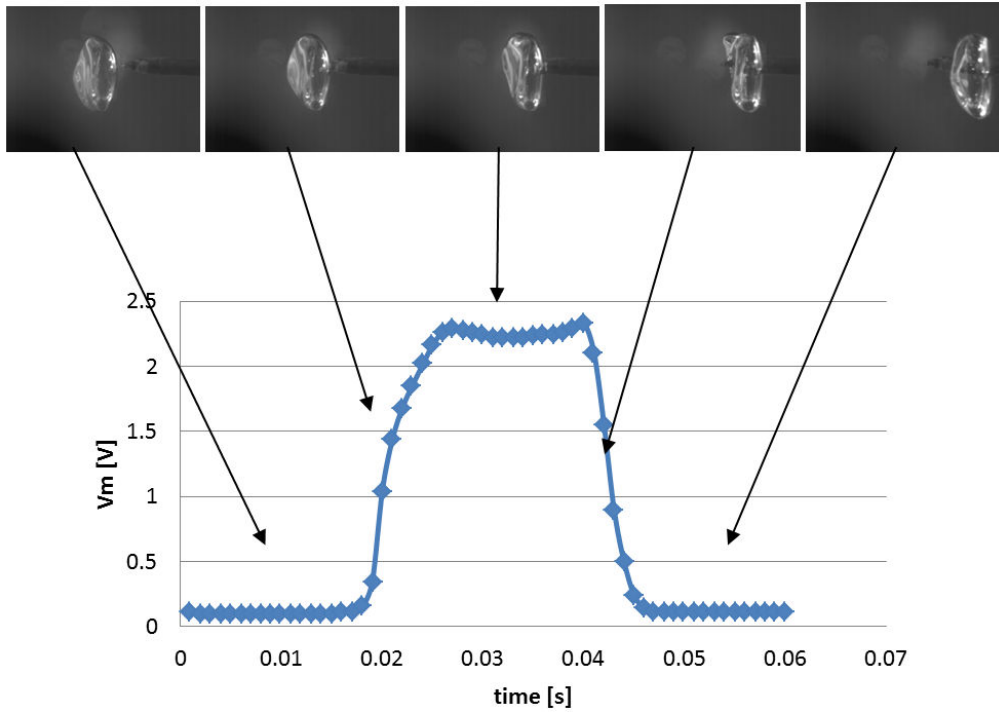


Figure C.4 – Time trace of the point electrode signal as a single bubble passes by. (Figure by Desrippes Eloi and Barazer Aymric)

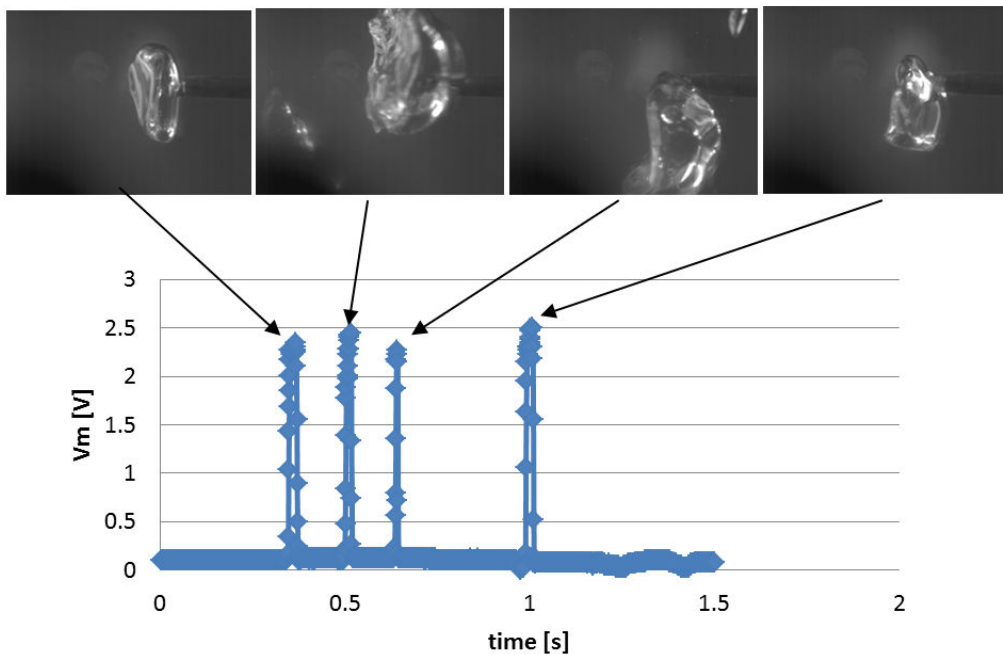


Figure C.5 – Time trace of the point electrode signal multiple bubbles passe by. (Figure by Desrippes Eloi and Barazer Aymric)

The void fraction from these electrodes could be calculated based on the circuit shown in figure C.6 and in the following equations.

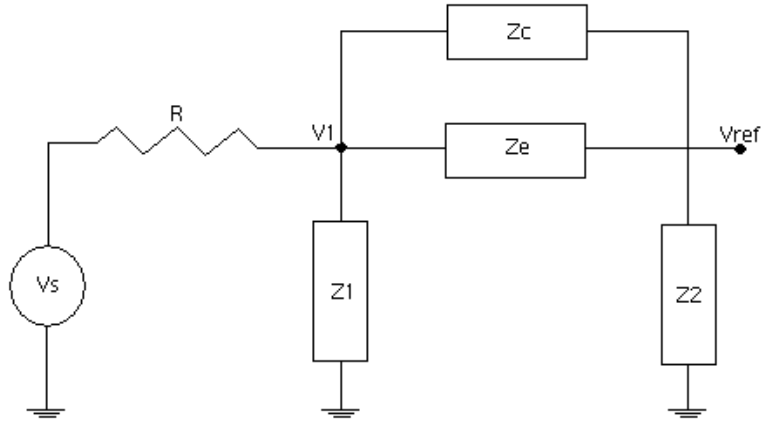


Figure C.6 – Circuit diagram of the EIM setup.  $V_{ref}$  is what is connected to the  $V_a$  input on the lock in amplifiers front panel.

We can now write the equations relating the measured voltages to the impedances as:

$$-\frac{V_{ref}}{Z_2} + (V_1 - V_{ref}) \left( \frac{1}{Z_c} + \frac{1}{Z_e} \right) = 0$$

Therefore we have for the measured impedance is given by

$$Z_e = 1 / \left( \frac{V_{ref}}{Z_2(V_1 - V_{ref})} - \frac{1}{Z_c} \right)$$

So that when we have only water in the domain so that  $V_{ref} = V_w$  we can write

$$Z_w = 1 / (V_w / (Z_2 * V_1 - Z_2 * V_w) - 1 / Z_c)$$

and when we have the unknown mixture in the domain we can write

$$Z_m = 1 / (V_m / (Z_2 * V_1 - Z_2 * V_m) - 1 / Z_c)$$

Based on Maxwell's model, the void fraction of a mixture is related to the impedance of the mixture and water.

$$\alpha = \frac{2(Z_m - Z_w)}{2Z_m + Z_w}$$

The equations were now combined and solved in Mathematica as follows:

$\alpha =$

$$\frac{2V_1(V_m - V_w)Z_c}{3V_1^2Z_2 + 3V_mV_w(Z_2 + Z_c) - V_1(3V_mZ_2 + 3V_wZ_2 + V_mZ_c + 2V_wZ_c)}$$

$$\frac{2V_1(V_m - V_w)Z_c}{3V_1^2Z_2 - V_1 * 3V_mZ_2 - V_1 * 3V_wZ_2 - V_1V_mZ_c - V_1 * 2V_wZ_c + 3V_mV_w(Z_2 + Z_c)}$$

$$\frac{2V_1(V_m - V_w)Z_c}{3V_1^2Z_2 - 3V_1Z_2(V_m + V_w) - V_1(V_m + 2V_w)Z_c + 3V_mV_w(Z_2 + Z_c)}$$

Divide through by  $V_1$  and  $Z_c$  and call  $Z_2/Z_c = A$

$$\frac{2(V_m - V_w)Z_c}{3V_1Z_2 - 3Z_2(V_m + V_w) - (V_m + 2V_w)Z_c + 3\frac{V_mV_w}{V_1}(Z_2 + Z_c)}$$

$$\frac{2(V_m - V_w)}{3V_1A - 3A(V_m + V_w) - V_m - 2V_w + 3\frac{V_mV_w}{V_1}(A + 1)}$$

$$\frac{2(V_m - V_w)}{3A(V_1 - V_m - V_w + \frac{V_mV_w}{V_1}) - V_m - 2V_w + 3\frac{V_mV_w}{V_1}}$$

We also recorded the voltage when there was only air in the domain, so that  $V_{ref} = V_a$ . For  $\alpha = 1$  we solve by:

$$\text{Solve}[2(V_a - V_w) == -V_a - 2V_w + \frac{3V_aV_w}{V_1} + 3A(V_1 - V_a - V_w + \frac{V_aV_w}{V_1}), A]$$

$$\{\{A \rightarrow \frac{V_a}{V_1 - V_a}\}\}$$

Leading to

$$\alpha = 2(V_m - V_w)$$

$$/ \left( 3 * \frac{V_a}{V_1 - V_a} * (V_1 - V_m - V_w + V_m * V_w / V_1) - V_m - 2 * V_w + 3 * V_m * V_w / V_1 \right)$$

Which can be simplified to

$$\alpha = \frac{2(V_1 - V_a)(V_m - V_w)}{V_1(3V_a - V_m - 2V_w) + 3V_mV_w - V_a(2V_m + V_w)}$$

This expression contains the voltage  $V_1$ , not  $V_s$  which is the known source voltage. Through simultaneous measurements of  $V_1$  and  $V_{ref}$  performed after the experiments,  $V_1$  was found to be normally within 10% of  $V_s$ . When calculating the void fraction the assumption was made that  $V_1 \sim V_s$ . Error caused by this assumption is shown in figure C.6, and in post-experiment tests was found to be below 0.1%.

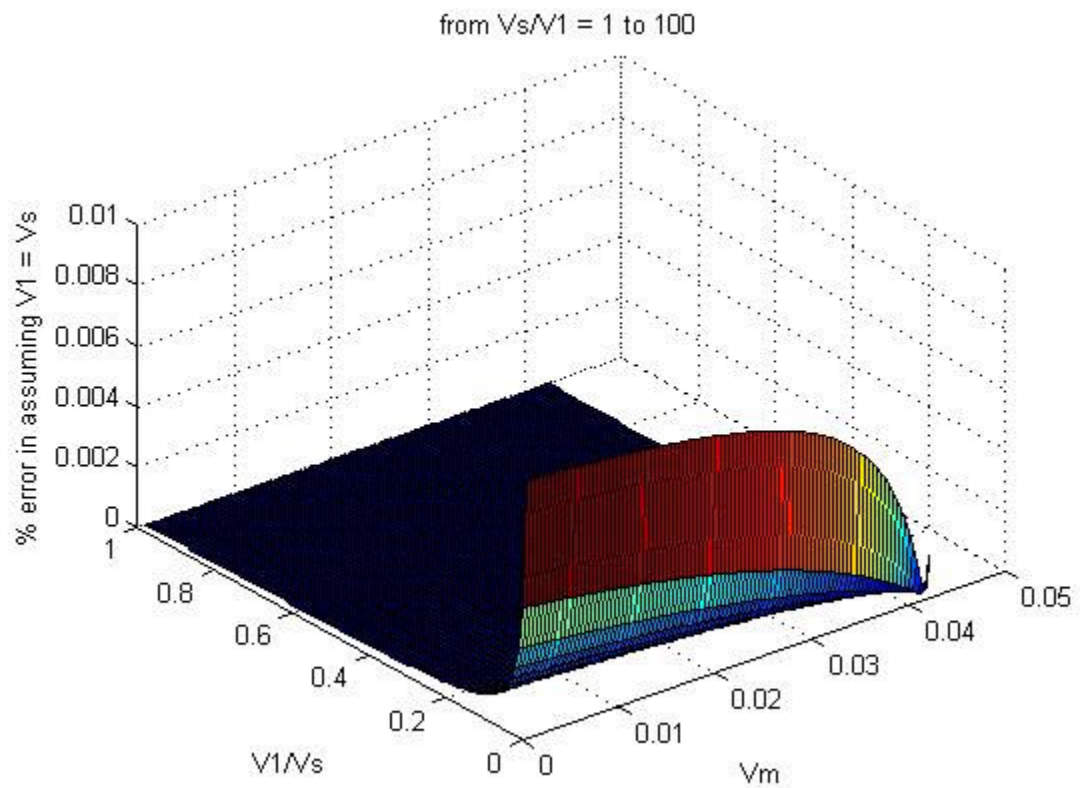


Figure C.7 – The error caused by assumption that  $V_1 = V_s$ .

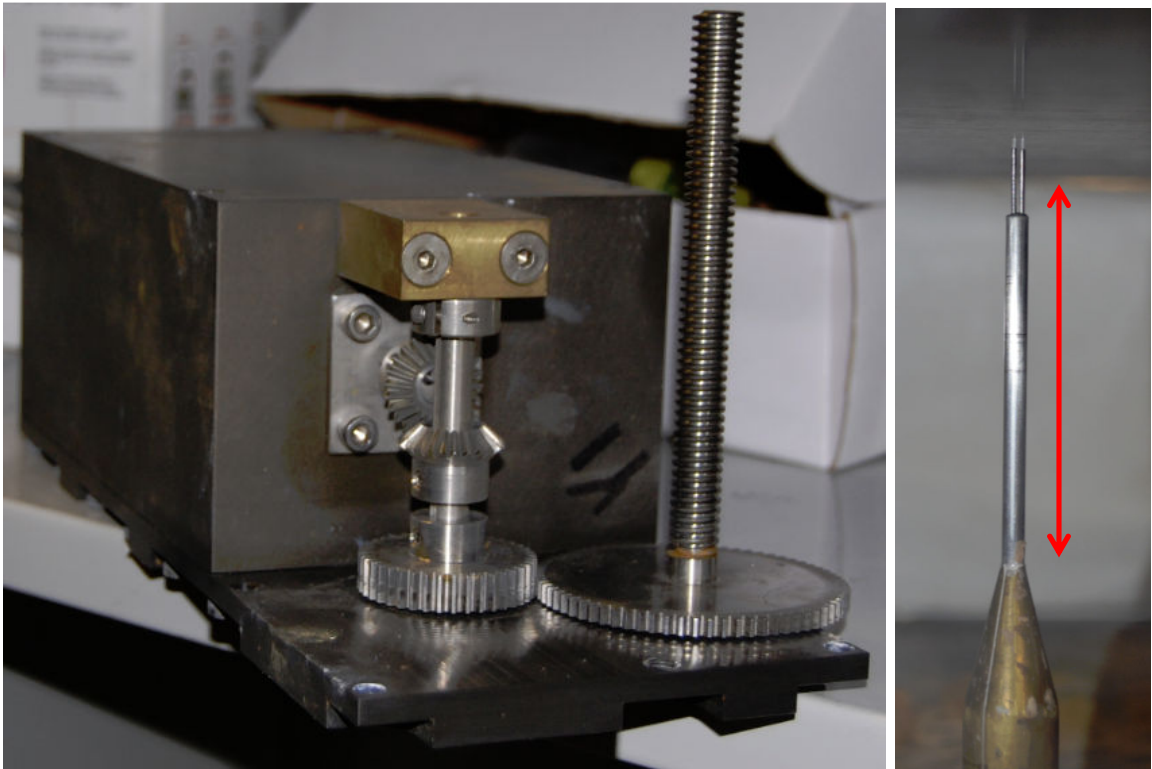


Figure C.8 – Left: The traverse mechanism. Right: optical probe (used to obtain results shown in Chapter 6) below the test surface mounted on its brass support. The probe's reflection can be seen in the test surface.

## APPENDIX D

### Codes used in Chapter 4

This appendix presents the codes used to generate figures shown in Chapter 4.  
(Energy benefit calculations).

```
clc, clear all
```

```
%% Inputs
```

```
Length = 1004*0.3048;           % [m]  
Beam = 105*0.3048;             % [m]  
Draft = 28*0.3048 + 10.75*0.0254; % [m]
```

```
A_bow = Draft*pi*Beam/2;  
A_stern = A_bow;  
A_side = Draft*(Length-Beam);  
A_bot = (Length-Beam)*Beam + pi*(Beam/2)^2;
```

```
% Assuming of the bottom 1.8...12.5% is curved for sides  
% say 93% of beam is ~flat and 84% of length is flat enough for AL
```

```
FracOfBottomFlat = 0.93*0.85;  
AreaWet = A_bow + A_stern + 2*A_side + A_bot; % approximate and assuming bow  
and stern are half cylinders  
FracOfWettedBottom = A_bot/AreaWet;  
FracOfWettedAL = FracOfWettedBottom * FracOfBottomFlat;  
ALDragReduction = 80; % Assuming FDR on surface with AL reduced by this many  
FD_Reduction = FracOfWettedAL*(ALDragReduction/100);  
FracResistanceFD = 0.6; %Fraction of resistance that is from frictional drag  
TotalResistanceReduction = FD_Reduction * FracResistanceFD;
```

```
rho = 998;
```

```

b = 6;           %Beam;
L = 12;         %Length;
U = 6;          % m/s
w = 3.05;

Re = L*U/(10^-6);
Cd = 0.031*Re^(-1/7);
F = 0.5*Cd*rho*U^2*L*b
P = F*U          %power to overcome drag [W]

b*w*U^2

%%
W = 29.76;
eta_comp = 0.7;
rho_w = 998;
d = 8.8;
g = 9.81;
L = 241.74;
dp_piping = 101325;

%for given U and qp_AL
U = linspace(5.2, 7.7,400);
for j = 1:400
    temp =
    3.5*W*(rho_w*d*g+101325)/eta_comp*(((rho_w*g*d+101325+dp_piping)/101325)^.2
    86-1);
    Pc_ALsmooth(j) = qp_ALsmooth(U(j))*temp;
    Pc_ALrough(j) = qp_ALrough(U(j)) *temp;
    Pc_PCest(j) = qp_PCest(U(j)) *temp;
    Pc_PCmain(j) = qp_PCmain(U(j)) *temp;

    Re = L*U(j)/(10^-6);
    Cd = 0.031*Re^(-1/7);
    F = 0.5*Cd*rho*U(j)^2*L*W
    Pp(j) = F*U(j) %power to overcome drag [W]

    Ptot(j) = Pp(j)/(0.6*0.49); %without AL
    Psaved(j) = Pp(j)*0.8;      %saved with AL

% ALsmooth(j) = 100*(Psaved(j)-Pc_ALsmooth(j))/Ptot(j);
% ALrough(j) = 100*(Psaved(j)-Pc_ALrough(j))/Ptot(j);
% PCest(j) = 100*(Psaved(j)-Pc_PCest(j))/Ptot(j);
% PCmain(j) = 100*(Psaved(j)-Pc_PCmain(j))/Ptot(j);
ALsmooth(j) = 100*(0.6*0.49*0.8-Pc_ALsmooth(j)*0.75/(Ptot(j)*0.9));
ALrough(j) = 100*(0.6*0.49*0.8-Pc_ALrough(j)*0.75/(Ptot(j)*0.9));

```



```

PCest(j) = 100*(0.6*0.49*0.8-Pc_PCest(j)*0.75/(Ptot(j)*0.9));
PCmain(j) = 100*(0.6*0.49*0.8-Pc_PCmain(j)*0.75/(Ptot(j)*0.9));
end
% figure(1), clf
% plot(U,Pc_ALsmooth,U,Pc_ALrough,U,Pc_PCest,U,Pc_PCmain,U,Pp)
% legend('ALsmooth','ALrough','PCest','PCmain','Propulsive power')

figure(2), clf
plot(U,ALsmooth,'r-',U,ALrough,'r--',U,PCest,'b:',U,PCmain,'b-','LineWidth',1.0)
legend('ALDR on smooth surface','ALDR on rough surface',...
'PCDR with establishment flux','PCDR with maintenance flux','Location','SouthEast')
grid on
xlabel('itU\rm [m/s]'),ylabel('Estimated NET power savings [%]')
%P_comp =
3.5*qp_AL.*U*W*(rho_w*d*g+101325)/eta_comp*(((rho_w*g*d+101325)/101325)^.2
86-1);

set(gca,'GridLineStyle',':'),grid on
set(gca,'MinorGridLineStyle',':')
set(gca,'XMinorTick','on'),set(gca,'YMinorTick','on')
set(get(gcf,'CurrentAxes'),'FontName','Times New Roman','FontSize',10)
journalfig2('netsavings',1.5*3.5,1.5*2.75,600)
%%
%for given U and qp_AL
U = linspace(4.4, 16,100);
for j = 1:100
    qp_ALrough_vect(j) = qp_ALrough(U(j));
    qp_ALsmooth_vect(j) = qp_ALsmooth(U(j));
    qp_PCest_vect(j) = qp_PCest(U(j));
    qp_PCmain_vect(j) = qp_PCmain(U(j));
end
figure(1), clf
plot(U,qp_ALsmooth_vect,U,qp_ALrough_vect,U,qp_PCest_vect,U,qp_PCmain_vect)
legend('ALsmooth','ALrough','PCest','PCmain')

%

da
=[NaN,1,605,600,5.070000000000000,2112,9552,2700,8700,3200,8000;402,1,600,600,5.
070000000000000,2188,9195,3100,8500,NaN,NaN;403,1,NaN,600,5.070000000000000,N
aN,NaN,NaN,NaN,3100,8200;406,1,210,70,5.600000000000000,NaN,NaN,NaN,NaN,479
2,5543;410,1,NaN,72,5.740000000000000,NaN,NaN,NaN,NaN,4394,6015;418,1,216,69,5
.690000000000000,3338,7456,4778,6030,5081,5428;421,1,265,NaN,6.160000000000000,4
067,7066,6272,4835,NaN,NaN;NaN,1,260,82,6.160000000000000,NaN,NaN,NaN,NaN,6
779,3709;424,1,330,NaN,7.040000000000000,5033,6941,8022,3933,NaN,NaN;425,1,324,

```

83,7.04000000000000,NaN,NaN,NaN,NaN,9500,2100;NaN,1,330,120,7.22000000000000  
0,5331,7075,8500,4000,9700,2100;429,1,500,200,NaN,7300,7000,10000,7000,13500,15  
00;502,1,364,NaN,5.27000000000000,2762,8690,3236,8236,NaN,NaN;503,1,NaN,254,5  
.27000000000000,NaN,NaN,NaN,NaN,3564,7701;505,1,206,NaN,5.48000000000000,33  
79,7711,4179,6949,NaN,NaN;NaN,1,NaN,91,5.48000000000000,NaN,NaN,NaN,NaN,4  
291,6659;508,1,209,NaN,5.75000000000000,3293,7729,4127,6932,NaN,NaN;NaN,1,Na  
N,73,5.75000000000000,NaN,NaN,NaN,NaN,6846,4028;512,1,222,NaN,5.940000000000  
000,6044,4953,8201,2816,NaN,NaN;513,1,224,72,5.94000000000000,NaN,NaN,NaN,N  
aN,5287,5361;515,1,240,NaN,6.11000000000000,3700,7400,5553,5479,NaN,NaN;516,1  
,240,61,6.11000000000000,NaN,NaN,NaN,NaN,5820,4750;518,1,247,NaN,6.210000000  
00000,3700,7450,5830,5292,NaN,NaN;519,1,247,60,6.21000000000000,NaN,NaN,NaN,  
NaN,6048,4521;521,1,263,NaN,6.35000000000000,3980,7300,5880,5318,NaN,NaN;522  
,1,NaN,59,6.35000000000000,NaN,NaN,NaN,NaN,6203,4435;524,1,269,NaN,6.560000  
0000000,4102,7293,6124,5248,NaN,NaN;525,1,273,65,6.56000000000000,NaN,NaN,  
NaN,NaN,6622,4159;527,1,286,NaN,6.72000000000000,4338,7329,6512,5083,NaN,Na  
N;528,1,NaN,63,6.72000000000000,NaN,NaN,NaN,NaN,7161,3812;530,1,306,NaN,6.8  
90000000000000,4572,7299,7018,4792,NaN,NaN;531,1,NaN,73,6.89000000000000,NaN  
,NaN,NaN,NaN,7760,3389;533,1,330,NaN,7.22000000000000,4947,7206,7837,4368,Na  
N,NaN;534,1,331,93,7.22000000000000,NaN,NaN,NaN,NaN,9165,2639;536,1,385,NaN  
,NaN,5639,7115,9125,4052,NaN,NaN;537,1,387,148,7.22000000000000,NaN,NaN,NaN  
,NaN,10297,2097;539,1,243,62,6.20000000000000,3883,7282,5609,5458,5950,4577;617  
,1,259,62,6.34000000000000,4000,7300,6000,5314,6531,4210;640,1,340,91,7.46000000  
000000,5100,7300,8100,4300,9400,2500;664,1,187,72,5.55000000000000,3100,8000,44  
00,6800,4600,6300;NaN,NaN,NaN,NaN,NaN,NaN,NaN,NaN,NaN,NaN,NaN,NaN;437,2,292,  
159,6,3600,8500,5400,6700,5700,6000;441,2,326,NaN,6.38000000000000,3950,8771,60  
00,13000,NaN,NaN;442,2,326,165,6.38000000000000,NaN,NaN,NaN,NaN,6500,12720;  
444,2,362,NaN,6.80000000000000,4456,16351,7076,13644,NaN,NaN;445,2,362,194,6.8  
000000000000,NaN,NaN,NaN,NaN,7900,12800;447,2,751,NaN,6.96000000000000,54  
00,17400,7800,8800,NaN,NaN;448,2,751,590,6.96000000000000,NaN,NaN,NaN,NaN,7  
800,8700;450,2,825,NaN,5.45000000000000,NaN,NaN,NaN,NaN,NaN,NaN;NaN,2,Na  
N,168,5.45000000000000,2750,9775,3900,8300,NaN,NaN;NaN,2,731,NaN,5.67000000  
000000,2700,9400,3600,8600,4300,7300;NaN,NaN,NaN,NaN,NaN,NaN,NaN,NaN,NaN,NaN  
,NaN,NaN;467,3,263,NaN,5.66000000000000,3100,8785,4550,7300,NaN,NaN;468,3,Na  
N,126,5.66000000000000,NaN,NaN,NaN,NaN,4850,6760;470,3,283,NaN,6.1500000000  
0000,3800,8170,5800,6100,NaN,NaN;471,3,286,116,6.15000000000000,NaN,NaN,NaN,  
NaN,6400,4880;473,3,314,NaN,6.55000000000000,4255,8163,6800,5600,NaN,NaN;474  
,3,314,122,6.55000000000000,NaN,NaN,NaN,NaN,7400,4200;476,3,352,NaN,7.100000  
0000000,4760,8200,7700,5300,NaN,NaN;477,3,352,142,7.10000000000000,NaN,NaN,  
NaN,NaN,9100,3500;479,3,497,NaN,7.24000000000000,5900,8500,8900,7300,NaN,Na  
N;480,3,497,183,7.24000000000000,NaN,NaN,NaN,NaN,10000,6400;NaN,NaN,NaN,Na  
aN,NaN,NaN,NaN,NaN,NaN,NaN,NaN;544,5,481,NaN,5.20000000000000,2550,9060,3  
800,7800,NaN,NaN;545,5,NaN,230,5.20000000000000,NaN,NaN,NaN,NaN,3870,7450;  
547,5,247,NaN,5.98000000000000,3624,7500,5430,5586,NaN,NaN;548,5,248,62,5.9800  
0000000000,NaN,NaN,NaN,NaN,5940,4574;550,5,291,NaN,6.61000000000000,4085,74  
54,6418,5072,NaN,NaN;551,5,NaN,70,6.61000000000000,NaN,NaN,NaN,NaN,7045,38  
37;553,5,334,NaN,6.99000000000000,4622,7458,7290,4742,NaN,NaN;554,5,NaN,87,6.

```

99000000000000,NaN,NaN,NaN,NaN,8376,3048;557,5,456,NaN,7.37000000000000,56
22,7544,9470,4351,NaN,NaN;558,5,424,127,7.37000000000000,NaN,NaN,NaN,NaN,11
000,1800;563,5,223,NaN,5.75000000000000,3419,7736,4919,6220,NaN,NaN;564,5,Na
N,70,5.75000000000000,NaN,NaN,NaN,NaN,5270,5537;566,5,210,NaN,5.51000000000
000,3106,8214,4312,6984,NaN,NaN;567,5,NaN,71,5.51000000000000,NaN,NaN,NaN,
NaN,4531,6473;569,5,265,NaN,6.32000000000000,3976,7386,5949,5295,NaN,NaN;570
,5,NaN,63,6.32000000000000,NaN,NaN,NaN,NaN,6337,4224;NaN,NaN,NaN,NaN,NaN
,NaN,NaN,NaN,NaN,NaN,NaN;598,7,297,NaN,6.37000000000000,4450,7380,6800,480
0,NaN,NaN;599,7,NaN,107,6.37000000000000,NaN,NaN,NaN,NaN,7200,3700;601,7,3
20,NaN,6.88000000000000,4750,7398,7421,4600,NaN,NaN;602,7,NaN,118,6.88000000
000000,NaN,NaN,NaN,NaN,8100,3200;604,7,258,NaN,6.25000000000000,3862,7400,5
740,5457,NaN,NaN;605,7,NaN,101,6.25000000000000,NaN,NaN,NaN,NaN,6153,4544;
607,7,246,NaN,6.12000000000000,3663,7500,5340,5760,NaN,NaN;608,7,NaN,97,6.120
00000000000,NaN,NaN,NaN,NaN,5750,4850;610,7,225,NaN,5.68000000000000,3050,7
900,4200,6500,NaN,NaN;611,7,NaN,102,5.68000000000000,NaN,NaN,NaN,NaN,4550,
6130;613,7,325,NaN,5.28000000000000,2464,9001,3525,7850,NaN,NaN;614,7,NaN,19
1,5.28000000000000,NaN,NaN,NaN,NaN,3560,7610;];

```

### % Calculations

```
p_a = 101325; % 1 atm[Pa] W = 3.05; % model width [m]
```

```
Q_SI_est = da(:,3)*p_a./(p_a+da(:,9))*0.000472; % [m^3/s] at p_cav
```

```
Q_SI_main = da(:,4)*p_a./(p_a+da(:,11))*0.000472; % [m^3/s] at p_cav
```

```
q_est = Q_SI_est/3.05; % [m^2/s]
```

```
q_main = Q_SI_main/3.05; % [m^2/s]
```

```
q_est_errorbars = (10+0.01*da(:,3))*p_a./(p_a+da(:,9))*0.000472; % [m^3/s] at p_cav
```

```
q_main_errorbars = (10+0.01*da(:,4))*p_a./(p_a+da(:,11))*0.000472; % [m^3/s] at
p_cav
```

```
qp_est = q_est; % ./da(:,5); % [m]
```

```
qp_main = q_main; % ./da(:,5); % [m]
```

```
A = 1; B = 40; %first and last row to plot
```

```
figure(1),hold on, plot(da(A:B,5),qp_est(A:B),'xb',da(A:B,5),qp_main(A:B),'or')
```

```
ylabel('\itq\rm^+ [m]'),xlabel('\itU\rm [m/s]')%,legend(['est'],['main'])
```

```
grid on
```

```
% q [m^2/s]
```

```
PhaseIV_ALDR =
```

```
[6.70000000000000,0.0267140060000000;8.90000000000000,0.0445233440000000;11.
10000000000000,0.0658945490000000;13.30000000000000,0.0979513560000000];
```

```
PhaseV_ALDR_rough =
```

```
[6.79000000000000,0.0460816610000000;7.95000000000000,0.0581771690000000;9.1
```

```

200000000000,0.0747398530000000;10.110000000000,0.0913841630000000;11.270
0000000000,0.1143359470000000;12.450000000000,0.1398032990000000;];
PhaseV_ALDR_smooth =
[6.67000000000000,0.0320568070000000;8.78000000000000,0.0514244620000000;10.
760000000000,0.0699016500000000;13.440000000000,0.0926085550000000;15.260
0000000000,0.1262300600000000;];
% qp [m]
PhaseIV_ALDR_N = [PhaseIV_ALDR(:,1)
PhaseIV_ALDR(:,2)];%./PhaseIV_ALDR(:,1)];
PhaseV_ALDR_rough_N = [PhaseV_ALDR_rough(:,1)
PhaseV_ALDR_rough(:,2)];%./PhaseV_ALDR_rough(:,1)];
PhaseV_ALDR_smooth_N = [PhaseV_ALDR_smooth(:,1)
PhaseV_ALDR_smooth(:,2)];%./PhaseV_ALDR_smooth(:,1)];

plot(PhaseIV_ALDR(:,1),PhaseIV_ALDR_N(:,2),'>k',...
PhaseV_ALDR_smooth(:,1),PhaseV_ALDR_smooth_N(:,2),'<k',...
PhaseV_ALDR_rough(:,1),PhaseV_ALDR_rough_N(:,2),'pk')
axis([4 16 0 0.25]),grid on

```

```

function qp_required = qp_ALrough(U)
% Linear model Poly2:
%   f(x) = p1*x^2 + p2*x + p3
% Coefficients (with 95% confidence bounds):
%   p1 =  0.001258 (0.001075, 0.001442)
%   p2 = -0.007548 (-0.01109, -0.004002)
%   p3 =  0.03906 (0.02246, 0.05565)
%
% Goodness of fit:
%   SSE: 6.27e-007
%   R-square: 0.9999
%   Adjusted R-square: 0.9998
%   RMSE: 0.0004572
%
% NO excluded points
% range of original data: 6.79 ... 12.45 m/s

qp_required = 0.001258*U.^2 + -0.007548*U + 0.03906;

```

```

function qp_required = qp_ALsmooth(U)
% Linear model Poly2:
%   f(x) = p1*x^2 + p2*x + p3
% Coefficients (with 95% confidence bounds):
%   p1 =  0.0005006 (-3.336e-006, 0.001004)
%   p2 = -2.982e-005 (-0.0109, 0.01084)
%   p3 =  0.008001 (-0.04742, 0.06342)
%
% Goodness of fit:
%   SSE: 0.0001179
%   R-square: 0.9865
%   Adjusted R-square: 0.982
%   RMSE: 0.004433
%
% NO excluded points
% Original data range 6.67...15.26 m/s (HP7 point also ~in line at 6.5 m/s)

qp_required = 0.0005006*U.^2 + -2.982/100000*U + 0.008001;

```

```

function qp_required = qp_PCest(U)
% Linear model Poly2:
%   f(x) = p1*x^2 + p2*x + p3
% Coefficients (with 95% confidence bounds):
%   p1 = 0.00476 (0.001966, 0.007554)
%   p2 = -0.04796 (-0.08492, -0.01101)
%   p3 = 0.1499 (0.02866, 0.271)
%
% Goodness of fit:
% SSE: 0.0001191
% R-square: 0.9466
% Adjusted R-square: 0.9403
% RMSE: 0.002647
%
% From fit, excluded data points for U < 5.3 as this is where the flow
% was in deffierent region
% Original data range (5.07) 5.48...~7.5 (8.5?) m/s

qp_required = 0.00476*U.^2 + -0.04796*U + 0.1499;

```

```

function qp_required = qp_PCmain(U)
% Linear model Poly2:
%   f(x) = p1*x^2 + p2*x + p3
% Coefficients (with 95% confidence bounds):
%   p1 = 0.007005 (0.00448, 0.009531)
%   p2 = -0.08663 (-0.1199, -0.05341)
%   p3 = 0.2769 (0.1686, 0.3851)
%
% Goodness of fit:
% SSE: 0.0001262
% R-square: 0.8089
% Adjusted R-square: 0.7898
% RMSE: 0.002512
%
% From fit, excluded data points for U < 5.3 as this is where the flow
% was in deffierent region
% Original data range (5.07) 5.48...~7.5 (8.5?) m/s

qp_required = 0.007005*U.^2 + -0.08663*U + 0.2769;

```

## APPENDIX E

### Point Spread Functions and Solutions to Equations in Chapter 5

The more involved derivation of equations was done using Mathematica 7 (by Wolfram). The step by step derivation is shown below:

```

In[88]:= Integrate[(1 - rho) * BesselJ[0, 2 f pi r] * DiracDelta[r] / r * r, {r, 0, Infinity}]

$$\frac{1 - \rho}{2}$$

In[93]:= term0 := (1 - rho) * DiracDelta[r] / r
In[96]:= Integrate[term0 * BesselJ[0, 2 f pi r] * r, {r, 0, Infinity}]
Out[96]=  $\frac{1 - \rho}{2}$ 
In[97]:= Term1 := (1 - a1 - a2 - a3) * DiracDelta[r] / (2 * Pi * r)
In[103]:= Integrate[Term1 * BesselJ[0, 2 f pi r] * r, {r, 0, Infinity}]
Out[103]=  $-\frac{-1 + a1 + a2 + a3}{4 \pi}$ 
In[108]:= Term2 := a1 / (2 * Pi * b1^2) * Exp[-((r / b1)^2) / 2]
In[111]:= Integrate[Term2 * BesselJ[0, 2 f pi r] * r, {r, 0, Infinity}]
Out[111]=  $\frac{1}{2 b1^2 \pi} a1 \text{ If}[\text{Re}[b1^2] > 0 \ \&\& \ (\text{Re}[f] > 0 \ || \ (\text{Re}[f] = 0 \ \&\& \ \text{Im}[f] > 0)), b1^2 e^{-2 b1^2 f^2 \pi^2},$ 

$$\text{Integrate}\left[e^{-\frac{r^2}{2 b1^2}} r \text{ BesselJ}[0, 2 f \pi r], \{r, 0, \infty\}, \text{Assumptions} \rightarrow \text{Re}[f] < 0 \ || \ (\text{Re}[f] \leq 0 \ \&\& \ \text{Im}[f] \leq 0) \ || \ \text{Re}[b1^2] \leq 0\right]$$

In[109]=  $\frac{1}{2 b1^2 \pi} a1 * b1^2 e^{-2 b1^2 f^2 \pi^2}$ 
Out[109]=  $\frac{a1 e^{-2 b1^2 f^2 \pi^2}}{2 \pi}$ 
In[114]:= Integrate[Exp[-((r / b1)^2) / 2] * BesselJ[0, 2 f pi r] * r, {r, 0, Infinity}]
Out[114]=  $\text{If}[\text{Re}[b1^2] > 0 \ \&\& \ (\text{Re}[f] > 0 \ || \ (\text{Re}[f] = 0 \ \&\& \ \text{Im}[f] > 0)), b1^2 e^{-2 b1^2 f^2 \pi^2},$ 

$$\text{Integrate}\left[e^{-\frac{r^2}{2 b1^2}} r \text{ BesselJ}[0, 2 f \pi r], \{r, 0, \infty\}, \text{Assumptions} \rightarrow \text{Re}[f] < 0 \ || \ (\text{Re}[f] \leq 0 \ \&\& \ \text{Im}[f] \leq 0) \ || \ \text{Re}[b1^2] \leq 0\right]$$

In[120]:= Term3 := a2 / (2 * Pi * b2^2) * Exp[-r / b2]
In[121]:= Integrate[Term3 * BesselJ[0, 2 f pi r] * r, {r, 0, Infinity}]
Out[121]=  $\frac{1}{2 b2^2 \pi} a2 \text{ If}[\text{Re}[b2] > 0 \ \&\& \ 2 \pi \text{ Abs}[\text{Im}[f]] < \text{Re}\left[\frac{1}{b2}\right] \ \&\& \ (\text{Re}[f] > 0 \ || \ (\text{Re}[f] = 0 \ \&\& \ \text{Im}[f] > 0)), \frac{b2^2}{(1 + 4 b2^2 f^2 \pi^2)^{3/2}}, \text{Integrate}\left[e^{-\frac{r}{b2}} r \text{ BesselJ}[0, 2 f \pi r], \{r, 0, \infty\}, \text{Assumptions} \rightarrow \text{Re}[f] < 0 \ || \ (\text{Re}[f] \leq 0 \ \&\& \ \text{Im}[f] \leq 0) \ || \ 2 \pi \text{ Abs}[\text{Im}[f]] \geq \text{Re}\left[\frac{1}{b2}\right] \ || \ \text{Re}[b2] \leq 0\right]$ 

```

```

In[117]:= 
$$\frac{1}{2 b^2 \pi} a_2 * \frac{b^2}{(1 + 4 b^2 f^2 \pi^2)^{3/2}}$$

Out[117]:= 
$$\frac{a_2}{2 \pi (1 + 4 b^2 f^2 \pi^2)^{3/2}}$$


In[122]:= Term4 := a3 / (2 * Pi * b3^2) * 1 / ((1 + r^2 / (b3^2))^(3/2))
In[123]:= Integrate[Term4 * BesselJ[0, 2 f \pi r] * r, {r, 0, Infinity}]

Out[123]:= 
$$\frac{1}{2 b^3 \pi} a_3 \text{ If} \left[ \text{Abs}[\text{Im}[f]] == 0 \ \&\& \ \text{Re}[f] > 0 \ \&\& \ (b^3 \in \text{Reals} \ || \ \text{Re}[b^3] \geq 0), b^3 e^{-\sqrt{\frac{1}{b^3}} \frac{2 f \pi}{b^3}}, \right.$$


$$\left. \text{Integrate} \left[ \frac{r \text{ BesselJ}[0, 2 f \pi r]}{\left(1 + \frac{r^2}{b^3}\right)^{3/2}}, \{r, 0, \infty\}, \text{Assumptions} \rightarrow \text{Abs}[\text{Im}[f]] \neq 0 \ || \ (\text{Re}[b^3] < 0 \ \&\& \ b^3 \in \text{Reals}) \ || \ \text{Re}[f] \leq 0 \right] \right]$$


In[133]:= FullSimplify 
$$\left[ \frac{1}{2 b^3 \pi} a_3 * b^3 e^{-\sqrt{\frac{1}{b^3}} \frac{2 f \pi}{b^3}} \right]$$

Out[133]:= 
$$\frac{a_3 e^{-\sqrt{\frac{1}{b^3}} \frac{2 f \pi}{b^3}}}{2 \pi}$$


In[138]:= FullSimplify 
$$\left[ 2 * \text{Pi} * \left( -\frac{-1 + a_1 + a_2 + a_3}{4 \pi} + \frac{a_1 e^{-2 b^1 f^2 \pi^2}}{2 \pi} + \frac{a_2}{2 \pi (1 + 4 b^2 f^2 \pi^2)^{3/2}} + \frac{a_3 e^{-2 f \pi + b^3}}{2 \pi} \right) \right]$$

Out[138]:= 
$$\frac{1}{2} \left( 1 - a_3 + 2 a_3 e^{-2 b^3 f \pi} + a_1 \left( -1 + 2 e^{-2 b^1 f^2 \pi^2} \right) + a_2 \left( -1 + \frac{2}{(1 + 4 b^2 f^2 \pi^2)^{3/2}} \right) \right)$$


In[143]:= Simplify 
$$\left[ 1 / \left( \frac{1}{2} \left( 1 - a_3 + 2 a_3 e^{-2 b^3 f \pi} + a_1 \left( -1 + 2 e^{-2 b^1 f^2 \pi^2} \right) + a_2 \left( -1 + \frac{2}{(1 + 4 b^2 f^2 \pi^2)^{3/2}} \right) \right) \right) \right]$$

Out[143]:= 
$$\frac{2}{1 - a_3 + 2 a_3 e^{-2 b^3 f \pi} + a_1 \left( -1 + 2 e^{-2 b^1 f^2 \pi^2} \right) + a_2 \left( -1 + \frac{2}{(1 + 4 b^2 f^2 \pi^2)^{3/2}} \right)}$$


```

Solution of  $y_t$  and  $x_t$  is obtained by using the command below in Mathematica.

```

Solve[{yb - ya == dx, x3 *  $\frac{y_t/x_2}{\sqrt{1+(y_t/x_2)^2}}$  == ya, x3 *  $\frac{y_t/x_1}{\sqrt{1+(y_t/x_1)^2}}$  == yb}, {ya, yb, yt}]

```

This generates a ~20 page solution, which has not been included, but can be easily reproduced by the reader by entering the above command in Mathematica.